ABSTRACT

Title of Document: COMBUSTION AND HEAT TRANSFER IN MESO-SCALE HEAT RECIRCULATING COMBUSTORS

Vineeth Vijayan, PhD, 2010

Directed By: Distinguished University Professor,
Dr. Ashwani K. Gupta,
Department of Mechanical Engineering

Combustion in small-scale systems faces problems related to time available for chemical reaction to go to completion and the possible quenching of the reaction by the increased effects of interfacial phenomena (thermal quenching and radical quenching) that occur at the combustor walls due to higher surface to volume ratio. Heat recirculation, where in a portion of the energy from the products is fed back to the reactants through structural conduction is one of the strategies employed in meso-scale combustors to overcome the problems of thermal quenching of the flame. When liquid fuels are employed, structural conduction can help pre-vaporize the fuel and thereby removes the necessity for a fuel atomizer. This dissertation focuses on the design, development and operational characteristics of meso-scale combustors employing heat recirculation principle. Self-sustained combustion of propane-air and methanol-air flames were achieved in sub centimeter dimensions (32.6 mm^3). The effects of design and operational parameters like wall thermal conductivity, heat exchanger size/channel length, combustion chamber geometry, equivalence ratio, Reynolds number, and external heat transfer (loss) coefficient on the combustor performance were investigated experimentally and numerically. The experimental procedure involved fabrication of combustors with different geometric features employing materials of different thermal conductivities and then obtaining their operating limits. Thermal performance with respect to various flow conditions was obtained by measuring the reactant preheating and exhaust gas temperatures using thermocouples. Numerical simulations were performed for both reacting and non-reacting flow cases to understand the heat transfer characteristics with respect to various design and operational conditions. Both experiments and numerical simulations revealed that wall thermal conductivity is one of the most important parameters for meso-scale combustor design. For typical meso-scale dimensions wall materials with minimal thermal conductivity (< 1W/m-K), especially ceramics would yield the best performance. Results showed that the most thermally efficient operating condition occurs for fuel lean cases at higher Reynolds numbers. Flame dynamics inside the combustor were investigated through high-speed imaging and flame acoustic spectrum mapping. Due to the small length scales involved, hydrodynamic instabilities have negligible effect on meso-scale combustion. Flame was observed to be extremely stable with negligible fluctuations. However, a significant amount of thermoacoustic phenomena is present within the combustion regime. Chemiluminescence imaging was employed to correctly map the flame zone inside the combustor.

COMBUSTION AND HEAT TRANSFER IN MESO-SCALE HEAT RECIRCULATING COMBUSTORS

By

Vineeth Vijayan

Dissertation submitted to the Faculty of the Graduate School of the
University of Maryland, College Park, in partial fulfillment
of the requirements for the degree of
[Doctor of Philosophy]
[2010]

Advisory Committee:
Professor Ashwani K. Gupta, Advisor/Chair
Professor Ahsan Choudhuri
Professor Bao Yang
Professor Kenneth Yu
Professor Peter Sunderland

Acknowledgements

It is a challenging task to be concise and acknowledge the contributions of the various individuals I owe, for the successful completion of this dissertation, in a few words. I will start by thanking my advisor Prof. Ashwani Gupta for his guidance, understanding, and pushing to make me achieve my best and beyond. He has motivated me to believe in doing quality work and achieving success through hard work and perseverance.

I thank the other members of my advisory committee (Dr. Choudhuri, Dr. Sunderland, Dr. Yu and Dr. Yang) for their willingness to spare some time from their very busy schedules to help me achieve this dream.

My family has, of course, played a vital role in encouraging me and keeping me motivated not just during my graduate life but also throughout my life. The confidence they have in me is one of my main strengths and what keeps me going.

Next, I would like to remember my friends from Combustion Laboratory, all of whom had helped me in some way or the other. I have only good memories with all of them, which I will cherish through the rest of my life.

I would also like to thank Mr. Howard Paul Grossenbacher of Aerospace Machine Shop for his great help and valuable guidance in facility fabrication.

I am thankful to Kam for being there in my life and giving it a new purpose and direction in addition to the support she provided in editing the dissertation.

Finally, I wish to express my sincere gratitude towards Missile Defense AGENCY (MDA) who had supported this research. Thanks are also due to Alan

Hickling, Jim Kiessling, Paul Koskey and Richard Schwarz from the agency for their help, support and many useful suggestions.

Table of Contents

List of Tables

List of Figures

Chapter 1: Introduction

1.1 Motivation

Electronics miniaturization, which began during World War II, led to the ongoing miniaturization revolution, which is defined as the creation of ever-smaller scales of mechanical and electronic devices. Technology miniaturization translates to market share and competitive advantage for many commercial and scientific products. "Those companies and nations that can successfully develop and capitalize on miniaturization developments will reap handsome rewards. Personal computers, portable radios, and camcorders are examples of products that created massive new markets through miniaturization: they added billions of dollars to the GNP of countries where they were designed and built" (U.S. Congress, 1991. [1]). With the advancement of miniaturization of electro-mechanical devices, there came the need for micro-power generation (milli-watts to watts). Miniaturization of electronics also led to a reduction in the space and weight requirements of avionics previously required to operate a satellite. As a consequence, it is now possible to achieve the mission of a normal size satellite using a cluster of smaller spacecrafts whose overall size and weight are much smaller. Mission requirements of micro spacecrafts opened up the novel field of micro-propulsion. Over the past decade, there were considerable efforts to advance the field of micro-scale combustion as a means for achieving the demands put forward by micro-power generation and micro-propulsion industries. The main driving force behind these efforts is the much larger energy density of liquid hydrocarbon fuels (see Table 1.1) which can be extracted through combustion when compared with existing battery technologies.

Table 1.1. Energy density comparison

Energy Source	Energy Density (MJ/kg)	Energy Density (MJ/L)
Hydrogen	120	2.7
Liquid hydrocarbon	45	27
Lithium battery	1.2	0.828
Alkaline battery	0.6	1.152

1.1.1 Small scale power generation

Small scale power generation efforts employing combustion of hydrogen and hydrocarbon fuels can in general be divided into three different categories. Miniaturizing the existing conventional macro-scale heat engines (gas turbines, Wankel engines etc.) powered by the evolution of micromachining and fabrication technologies belong to the first category. Second group consists of novel engine technologies investigated for the first time for small scale power generation (for e.g. engines employing phase change of a working fluid). Third group comprises of small scale electrical power generators which convert chemical energy from the fuel directly into electricity. These are again subdivided into thermoelectric and thermo-photovoltaic power systems.

1.1.2 Small scale propulsion systems

Chemical rocket thrusters powered by micro-combustion are of great interest in the propulsion of small satellites. Chemical thrusters stand out amongst other micro-propulsion options due to their capability of generating much higher thrust values. Chemical rocket thrusters, which use combustion for chemical energy release, belong to two different classes; solid propellant rockets and liquid bipropellant rockets. A brief discussion on micro-propulsion is provided in section 1.3.

1.1.3 Small scale fuel reformers

Miniaturization trends in proton exchange membrane (PEM) fuel cell research have generated interest for small-scale fuel reformers. The aim is to develop a micro power generation device that consists of a fuel processor, which acts as a hydrogen source, coupled with a proton exchange membrane (PEM) fuel cell. Hydrogen production can be achieved through a number of methods. Usually it is produced from hydrocarbons or alcohols through steam reforming, partial oxidation or auto-thermal reforming. Cracking of ammonia can also yield hydrogen. Except for partial oxidation, all the aforementioned hydrogen production routes are endothermic. Therefore, energy must be supplied via an exothermic reaction, such as combustion. One of the important aspects of developing such a multifunctional microdevice is the thermal coupling between the micro-combustor and fuel reformer.

Some of the commonly employed hydrogen production reactions are:

Cracking of Ammonia

$2NH3 <==> N2 + 3H2$

Steam reforming of methanol

$CH_3OH + H_2O \Longleftrightarrow CO_2 + 3H_2$

$CH_3OH \Longleftrightarrow CO + 2H_2$

$CO + H_2O \Longleftrightarrow CO_2 + H_2$

Partial oxidation of methane

$CH_4 + 1/2O_2 \Longleftrightarrow CO + 2H_2$

1.2 Objectives and Approach

The main purpose of this dissertation is to develop meso-scale combustors for stable sustained combustion of propane-air and methanol-air mixtures using heat recirculation concept. Another objective is to determine the importance of design parameters, which include wall thermal conductivity, combustion chamber geometry and heat exchanger geometry on meso-scale combustion and heat transfer. Determining the effects of operating conditions (flow rate, equivalence ratio) on combustor performance is also important. It is aspired that this understanding will help in developing high performance micro-combustors depending on the type of application.

The following approach will be adopted

- Fabricate meso-scale combustors employing the Swiss-roll design concept with materials of different thermal conductivities and with different geometric features and investigate their combustion and heat transfer characteristics for propane-air mixtures and for methanol-air mixtures
- Experiments
  - Determine the operating limits of the combustors

  - Obtain the temperature distribution of the combustor walls at steady state using infrared camera
  - Obtain the reactant preheating temperatures and product exhaust temperatures to investigate the thermal performance
  - Perform high speed imaging and acoustic signature acquisition to study the flame dynamics
  - Perform chemiluminescence imaging to study the reaction zone features
- CFD simulations
  - Quantify the effect of material thermal conductivity, geometric parameters, equivalence ratio, Reynolds number and external heat transfer (loss) coefficient on the combustor performance

1.3 Micro-power generation

1.3.1 Micro heat engines

Several research groups have been exploring the development of miniature heat engines for power production. Miniature gas turbines, Wankel rotary engines, HCCI power systems and nontraditional heat engines are some of the concepts of interest.

For a number of years researchers at Massachusetts Institute of Technology were involved with micro gas turbine development [2, 3]. The goal was to develop a gas turbine the size of a shirt button. The turbine combined with an electrical generator was intended to produce 10-20W of power. This project is viewed by many as the pioneering research in MEMS-based micro-scale power generation [4].

However, the researchers faced several challenges during miniaturization related to fluid friction through small passages, bearings, close tolerance seals, and heat transfer within the engine. Figure 1.1 shows a schematic of the micro-gas-turbine, which includes a radial compressor/turbine unit, a combustion chamber and an electrical generator incorporated in the compressor. The device is constructed by bonding six silicon wafers to form the compressor, turbine, combustor, generator and other flow passages. Although the turbine, compressor and combustor had been demonstrated to operate independently, the engine as a whole has not operated. One of the major challenges was the lower overall efficiency of the micro-engine combustor. Despite the problems related to micro-engine operation, some major accomplishments of this research include the continuous operation of a silicon based microcombustor using H2/air mixtures and [5] hydrocarbon mixtures [6] and the achievement of rotation of the turbine at 1.3 million rpm by using air bearings.

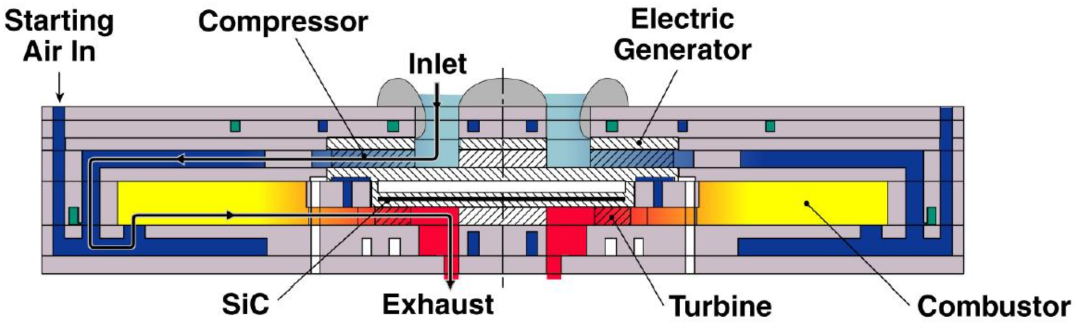

Figure 1.1 Schematic of the MIT micro-gas-turbine engine showing the radial compressor/turbine unit, combustion chamber and the electrical generator incorporated in the compressor. A photograph of the MEMS fabricated turbine blades is also shown [3]

Researchers at the University of California, Berkeley, focused on micro power generation using a small rotary engine (Wankel engine) [4, 7, 8]. Efforts were made to develop meso-scale 'mini rotary engine' and micro-scale 'micro rotary engine' (see Figurre.1.2). Similar to the micro gas turbine project, micro rotary engine project is also faced with problems relating to sealing, friction and internal heat transfer. The mini rotary engine was designed to deliver power on the order 30 W, and micro rotary engine designed to produce power in the mW range. The mini rotary engine was fabricated from steel through electro-discharge-machining (EDM). It had a rotor size of approximately 10 mm. Testing performed using hydrogen-air mixtures showed power output at very low efficiency (~0.2%). A major reason for the low efficiency of the engine is its low compression ratio, due to leakage between the rotor apex tip seals and the housing and over the rotor faces. MEMS fabrication is employed for the micro version of the rotary engine (rotor size ~ 1 mm) and is still in the initial stages of development. According to the researchers, the rotary engine is well suited for the MEMS fabrication techniques because of its planar construction, thus simplifying the overall production of the device. Other advantages include reduced number of engine parts and self-valving operation. Later on, researchers at Birmingham have also focused on micro Wankel engine development [9]. Their research involved two stages, the first stage being the development of a cryogenic CO_2 micro engine. The second stage will be the development of a micro combustion engine. The design of the CO_2 engine differed from the design of combustion engine in that the housing curve has been modified to eliminate the compression stage of the Otto cycle while keeping the expansion phase.

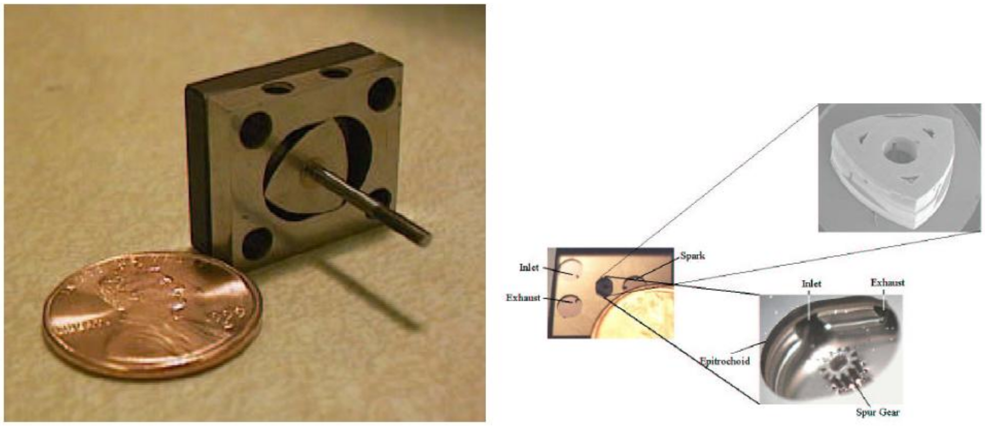

(a) Meso-scale prototype. (b) Micro-engine prototype.

Figure 1.2 Rotary engine prototypes under development at the University of California, Berkeley [7]

Yang et al. [10-12] proposed miniature free-piston engine generator using homogenous charge compression ignition combustion to minimize quenching effects. Based on this concept Aichlmayr and co-workers [13, 14] designed a homogenous charge compression ignition (HCCI) free piston micro-engine (Figure 1.3) with a power production capability of 10W. Unlike conventional compression and spark ignition engines, HCCI engines compress premixed fuel and air until it ignites spontaneously. Variations in charge composition and temperature cause ignition and combustion to be localized in reaction centers which are distributed throughout the chamber. Hence flame propagation in the traditional sense does not occur in HCCI and consequently. HCCI mode can result in considerable reduction of NOx emissions since operation at fuel lean conditions is possible. An ideal HCCI engine requires no external ignition system, which makes the design less complex, and more energy efficient. Power is generated by the motion of the free piston in the magnetic field induced by the permanent magnet generator.

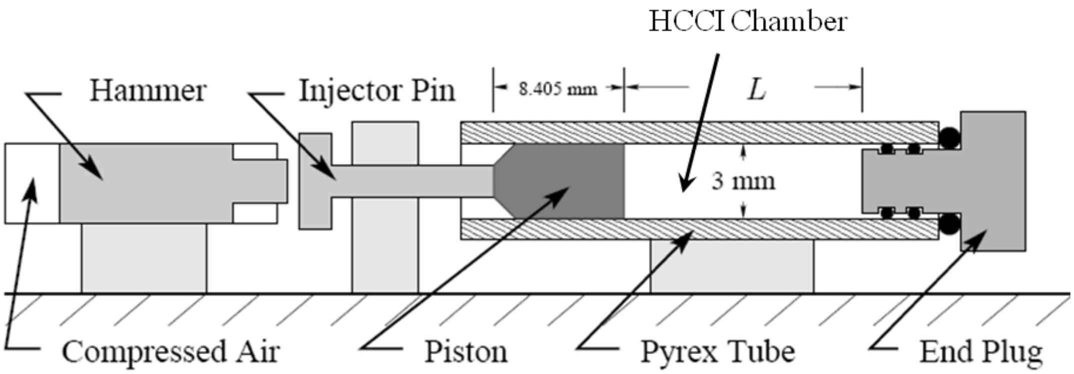

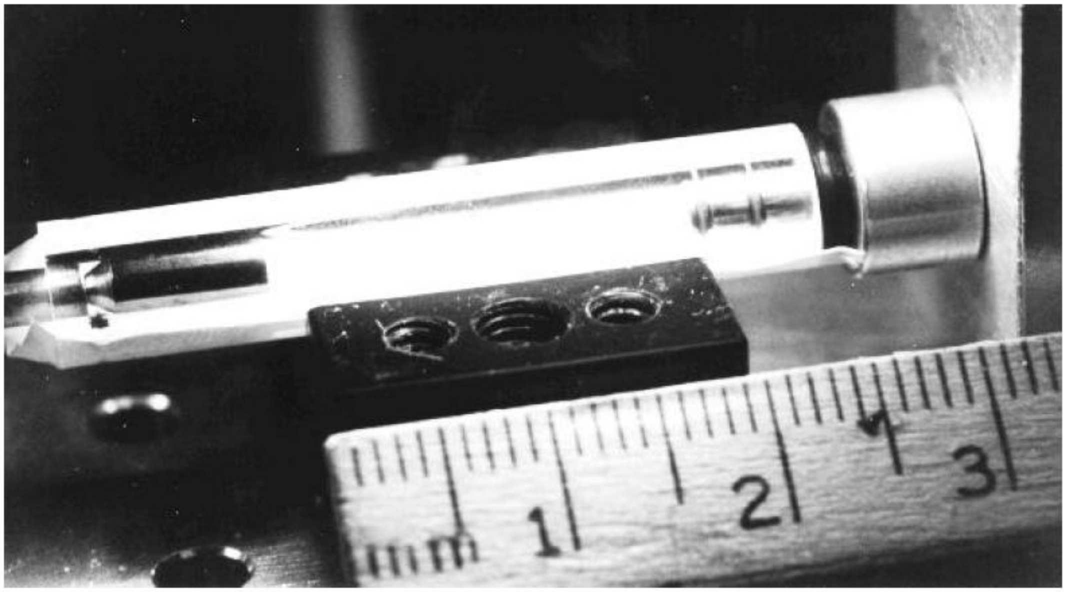

Figure 1.3 Schematic of Aichlmayr's single shot HCCI experiment along with a photograph of the piston-cylinder assembly. The piston is on the left and the end plug is on the right [13]

Dahm and coworkers [15] have developed an oscillatory rotating free-piston engine called Micro Internal Combustion Swing Engine (MICSE). The engine is intended to produce about 20 W with an overall efficiency of 14 % on butane fuel. The integrated assembly drawing of the non-fuel components of the MISCE engine is given in Figure 1.4.

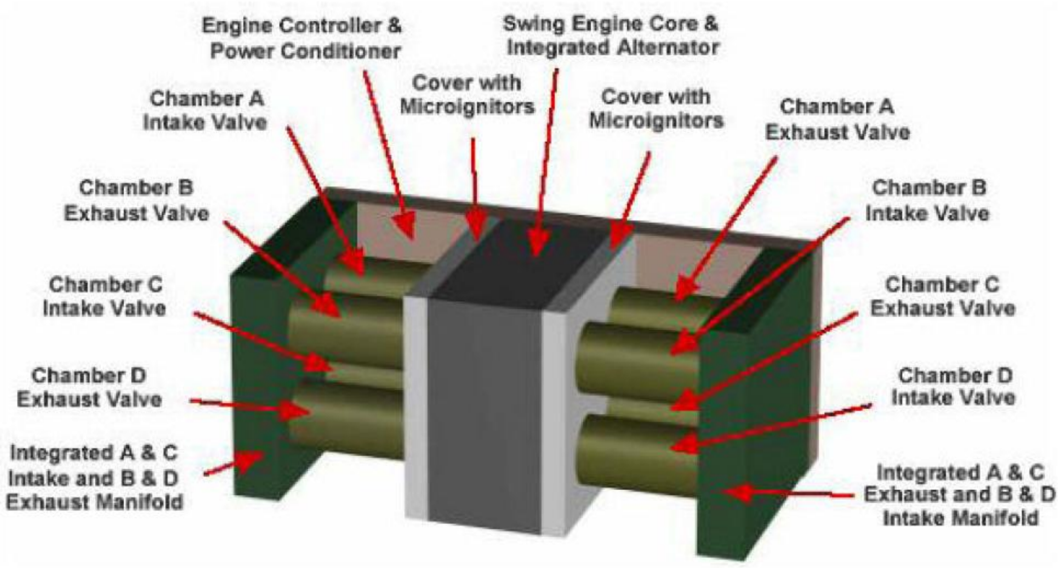

Figure 1.4 Dahm et al.'s assembly concept for all non-fuel components of the 20 W MICSE chemical-to-electrical energy conversion system indicating major system components. System volume is 17.6 cc (20x20x44 mm) and mass is 54 g [15]

In a swing engine, combustion occurs in four chambers separated by a single rotating swing-arm. Except for the swing-arm, there are virtually no other moving parts. The swing-arm creates four distinct combustion chambers in a single base structure. For the same power output, MICSE design permits lower weight and smaller size than linear free-piston engines. Figure 1.5 shows the swing arm and the valve ports of the engine.

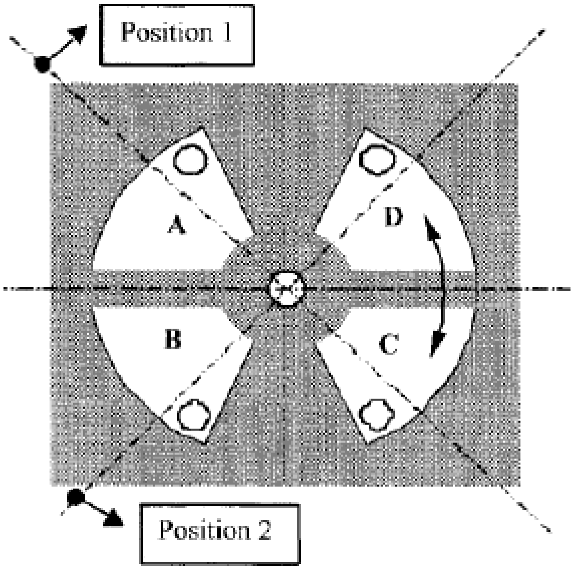

Figure 1.5 Base cavity, swing-arm, valve ports, and resulting four chambers (A-D) in the micro internal combustion swing engine (MICSE). The resulting arrangement produces inherent weight and volume efficiencies over conventional linear piston engines, while avoiding the mechanical complexities of rotary Wankel or turbine engines [15]

MISCE has lower vibration due to its rotating swing-arm when compared to the linearly translating piston of the free-piston engines. Unlike other internal combustion systems, the swing engine does not have any "dead point" in its operating cycle, and thus does not require an external starter. The mechanical power from the oscillatory motion of the swing engine is converted to electrical power with the aid of an inductive alternator.

Researchers at Washington State University [16, 17] have developed a heat engine that employs a novel thermodynamic cycle. This is in contrast to the common practice in the micro power generation research community of taking a traditional design for an engine and trying to shrink its size. The unique design uses flexible membranes, phase change of a working fluid, and the piezoelectric effect to create a miniature heat engine. An external combustion engine converts thermal power into mechanical power. Mechanical power is then converted into electrical power through a thin-film piezoelectric membrane generator. A unique aspect of this particular design is the capability to expand and compress a saturated two-phase working fluid. According to the researchers, no practical engine based on the expansion and/or compression of a two-phase mixture has been built previously. The advantage in employing a two-phase fluid in this manner is that it opens the possibility of approaching the ideal Carnot vapor cycle. This design is well suited for photolithography-based batch fabrication methods. Figure 1.6 shows the cross-sectional drawing of the engine.

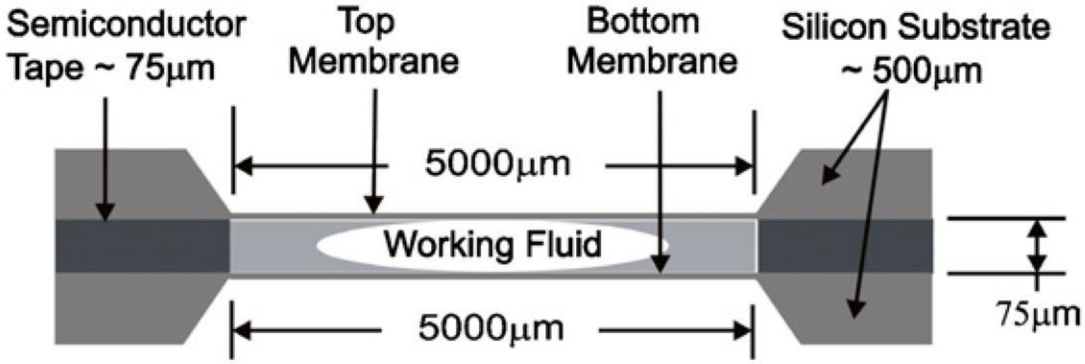

Figure 1.6 Schematic of the cross-section of the Carnot vapor cycle engine developed at Washington State University [16]

Researchers at Georgia institute of Technology have developed a self-resonant, MEMS-fabricated, air-breathing engine [18]. This device, which is also known as, a valveless pulsejet, converts chemical energy from the fuel into pulsatile thrust, which may be used for propulsion or converted into vibrational mechanical energy suitable for electrical power generation. Figure 1.7 shows a photograph of the self-resonant engine. A description of the valveless pulsejet operation cycle is provided in Figure 1.8.

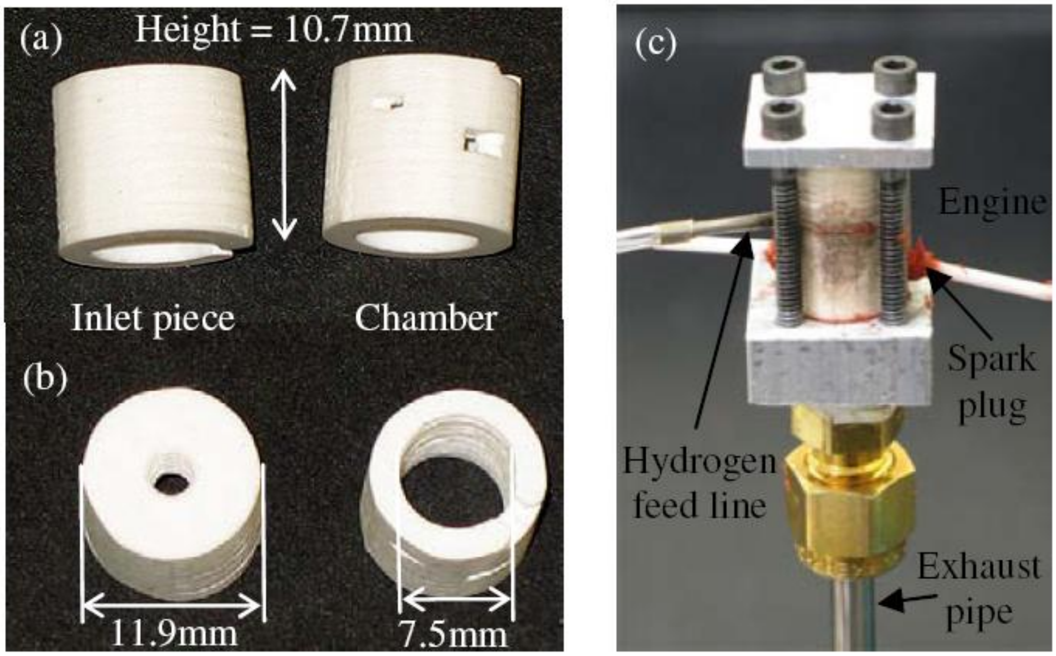

Figure 1.7 Self-resonant, combustion engine developed at Georgia institute of Technology: The air inlet piece has been fabricated separately to test different configurations with the same combustion chamber. (a) Side view (b) Top view and (c) Test set-up [18]

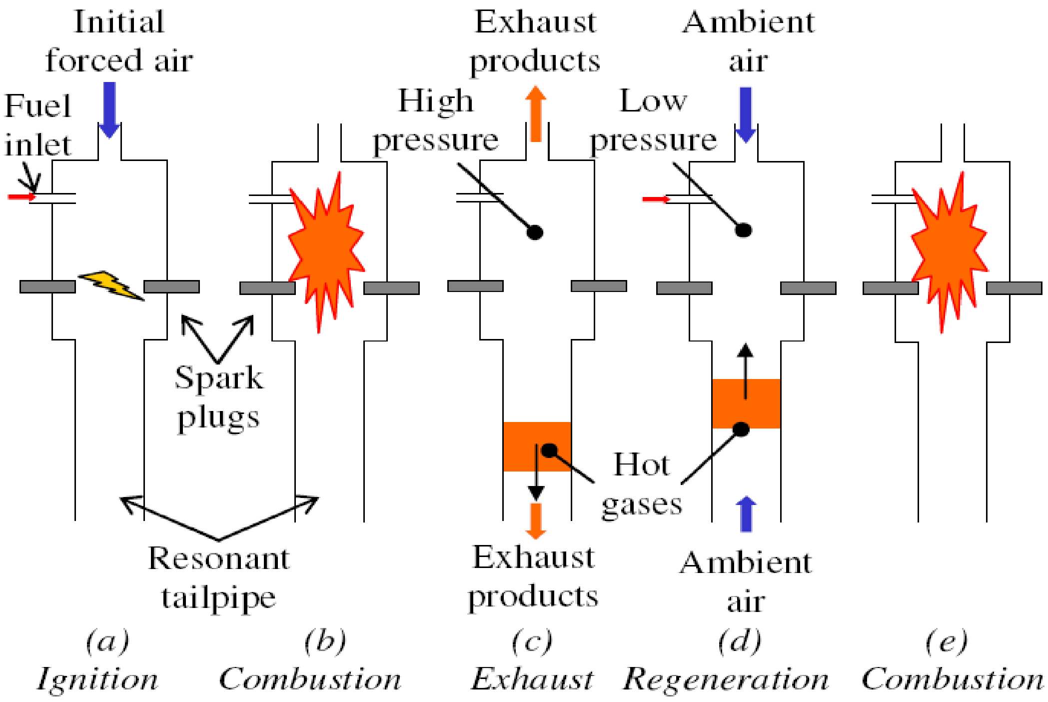

Figure 1.8 Conceptual schematic of typical valveless pulsejet operation [18]

Laser machined ceramic sheets were laminated and sintered for engine fabrication. The engine operation was successfully demonstrated using hydrogen fuel. Resonation frequency of the engine was in the range of 0.9-1.6 kHz with pressure differentials in the combustion chamber up to 10 kPa. Electric power is generated by employing a Lorentz-force type generator in fluidic contact with the engine exhaust. The generator membrane is mechanically driven by the oscillating thrust of the device. As a result, electrical power is delivered to an external load resistance. The first version of the air-breathing engine has been used for this experiment. The system delivered 2.5 μW to an external electrical load at a frequency of 1.5 kHz. Although the system had low overall efficiency and power output, it demonstrated potential for MEMS-scale, combustion-based fuel-to-electrical power generation.

More robust mechanical power transmission is expected to produce significantly higher electrical output.

1.3.2 Micro-thermoelectric (MTE) power systems

A typical thermoelectric power system comprises of four major components.

1. Micro-scale combustor
2. Thermal spreaders
3. Thermo electric device
4. Heat sink

The heat generated in the microcombustor is conducted through the spreaders to the thermoelectric device, which is connected to a heat sink. The thermoelectric device operates according to the Seebeck effect, where two semiconductor materials (p-type and n-type) with two different Seebeck coefficients are connected to support a thermal gradient (see Figure 1.9). Amongst the thermoelectric devices operating on Seebeck effect, semiconductor junctions are especially common in power generation devices, while metallic junctions are more common in temperature measurement. The heat source will drive electrons in the n-type element toward the cooler region, thus creating a current through the circuit. Holes in the p-type element will then flow in the direction of the current. The current can then be used to power a load, thus converting the thermal energy into electrical energy. Bismuth telluride compounds such as Bi_2Te_3 and Bi_2-XSbXTe_3 are commonly employed n-type and p-type materials respectively.

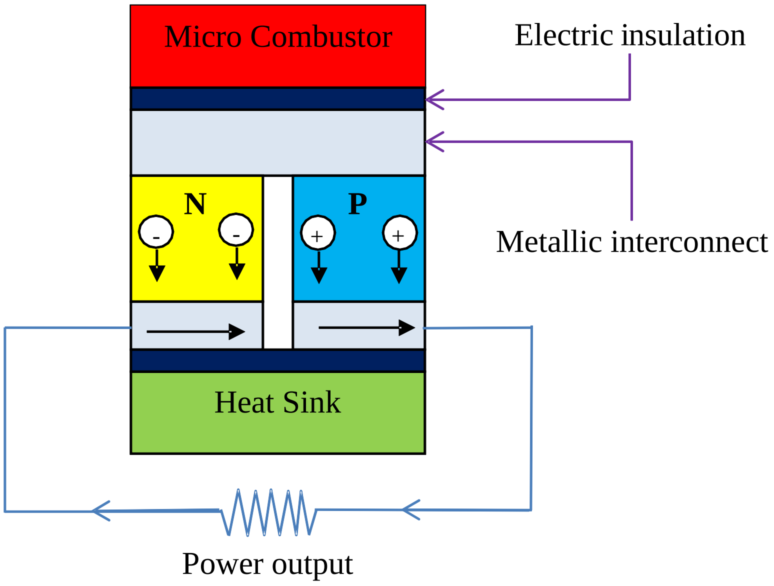

Figure 1.9 Schematic of a typical MTE power system

The power generated from thermoelectric devices is proportional to the square of the thermal gradient between the hot and cold sides. However, typical commercial thermoelectric devices have a practical limit of 300 °C. This is a result of the melting and degradation of materials in the devices, as well as migration of dopants in the semiconductor components of the devices [19]. Some state-of-the-art thermoelectric materials such as quantum-dot super lattices are capable of operations in the range 300–500 °C [20].

A mathematic model to estimate the overall efficiency of an integrated micro thermoelectric power system with a homogeneous microcombustion channel for pre-mixed gas was developed by Minaev and Fursenko [21]. They found that the highest efficiency could usually be reached near the flammability limits implying that the issues of flammability limits and flame stability are directly related to the efficiency of the micro thermoelectric system.

Cohen, Ronney, and others [22] published a patent on a microcombustion-based thermoelectric generator with a torroidal design. As shown in Figure 1.10, in their design (a variation of Swiss-roll type combustor) the reactant channel and exhaust channels were coiled around each other in a spiral configuration so that heat loss was reduced. The channel walls of the micro combustor are composed of thermoelectric materials (n-type and p-type). Some T-shaped or L-shaped fins made of thermally and electrically conductive materials were parts of the thermoelectric active wall. These fins were designed to act as a diffusion barrier between the n-type and p-type TE materials and to increase the thermal gradient.

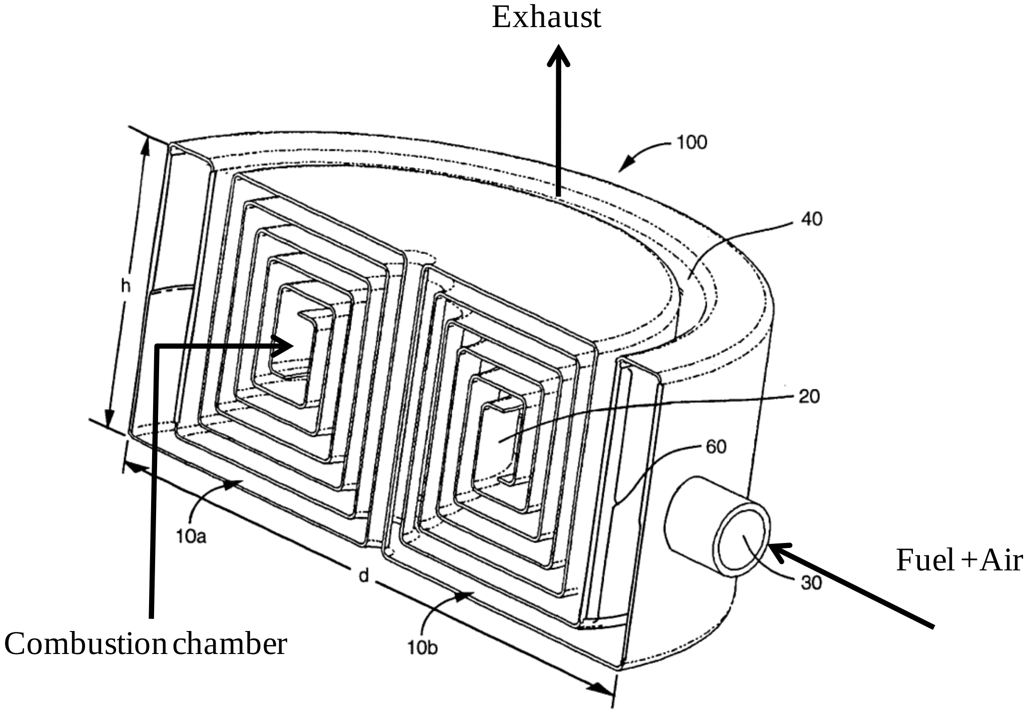

Figure 1.10 Torroidal microcombustor design with thermoelectric channel walls by Cohen et al. [22]

Yoshida et al. [23] have demonstrated that an integrated TE system can operate at total efficiency of 2.8% by installing two TE modules on both sides of a microcombustor. Microcombustion of butane was demonstrated with 100% combustion efficiency and uniform temperature distribution. However, resistive heating is required to ignite the fuel. In addition, only hydrogen combustion could be sustained when integrated with a TE device. Their integrated TE system was evaluated with hydrogen-air fuel combustion with a Pt catalyst and achieved power generation of 0.184 W at a total efficiency of 2.8%. It was suggested that a higher performance catalyst and an improved system design were needed to use butane in the integrated TE system.

Vlachos et al. [19, 24, 25] performed microcombustion experiments and fabricated an integrated TE system using hydrogen-air, propane-air, and methanol-air fuel mixtures at stoichiometric and fuel-lean conditions with Pt-alumina catalyst inserts in a stainless steel microcombustor. It was found that thermal properties of the microcombustor wall have a substantial effect on microcombustor thermal uniformity [25]. They applied thermally conductive metal (copper) spreaders to increase axial thermal uniformity along the microcombustor and to transport heat uniformly over the full footprint of the TE device. These studies also investigated the effects of fuel and flow rate on power generation, as well as heat removal from the cold side. Power generation was found to increase with fuel/air flow rate. When the load resistance matched with the internal resistance of the TE device, optimal power generation was obtained. The group also found that power generation was substantially improved by forced convection to augment heat removal from TE device. For the methanol integrated microcombustion-TE power system, maximum power generated was 0.65 W with maximum thermal efficiency of 1.1% [24].

1.3.3 Micro-thermophotovoltaic (MPTV) power systems

A typical thermophotovoltaic (TPV) power system comprises of three major components.

1. Micro-scale combustor
2. Thermal emitter
3. Photovoltaic(PV) diode cells

PV cells are arranged around the combustor or emitter in such a way that sufficient heat is transferred from the emitter to the PV cells by radiation [26]. PV cells convert the radiative heat to electricity directly. Gallium antimonide (GaSb) and indium gallium arsenide (InGaAs) are common PV cell materials. Polycrystalline Silicon Carbide (SiC) is the most commonly used emitter for TPV applications. The basic principle of operation of a TPV power system involves the use of a p/n junction to absorb optical energy from the radiation spectrum of the emitter, generate and separate charge carriers (electron/hole pairs), and in doing so convert that energy into electrical power. However, the TPV cells can only convert photons from the radiation if they have energies greater than the band gap of the p/n junction. Photons with energy above the band-gap can be absorbed, but the excess energy will be lost. Photons with lower energies cannot be absorbed and their energy is also lost. These losses can generate undesirable heating in the TPV cell.

In order to achieve the maximum efficiency, all photons should be converted to electrical energy. Selective emitters with emissivity over a narrow wavelength range, or optical filters that only pass a narrow range of wavelengths and reflect unusable radiation heat back to the combustor wall can be used to generate emission spectra that can be optimally converted by the PV converter [26]. This method can in principle, drastically increase the overall system efficiency. Xue et al. [26] have analyzed the energy conversion efficiency of a micro TPV system incorporating broadband emitter silicon carbide (SiC) and selective emitter materials (cobalt /nickel-doped magnesium oxide) and Gallium antimonide TPV cell. A backward-facing step was employed in the microcombustor to effectively create recirculation behind the step to prolong the gas residential time and enhance the mixing process of the fuel-oxidizer mixture. Consequently, the position of the flame can be effectively controlled, and the range of operation was widened. Experiments showed that the combustor can achieve uniform wall temperatures of around 1000 K. One of the TPV power systems developed by the researchers was able to produce electric power output ranging from 0.07 to 0.74 W with the hydrogen-air mixture [26]. This prototype used SiC as the material for the microcombustor and emitter, and a hexagonal GaSb TPV cell array.

Lee and Kwon [27] investigated a heat-recirculating microcombustor using a propane-air mixture for application in a micro-TPV system experimentally and computationally. The objective was to develop the micro-emitter as a thermal heat source for a 1-10 W power-generating micro-thermophotovoltaic system. The microemitter had cylindrical design with an annular-type shield (Figure 1.11). Heat recirculation concept was employed to achieve stable burning in small confinement, maximum heat transfer and uniform wall temperature distribution. Results showed uniform emissions from the microemitter walls. Based on experimental and computational results, thermal characteristics along the microcombustor wall were improved with decreasing wall thickness, as well as increasing ratios of the inner radius of the shield to the gap between the shield and microcombustor wall. Calculations made for a micro TPV system considering virtual PV cells under a typical test condition showed that the overall efficiency and the output power are 3.2% and 3.6 W, respectively. It was predicted that replacing the microemitter wall materials with SiC, the performance could be much improved: the overall efficiency and the output power of 4.3% and 4.2 W, respectively.

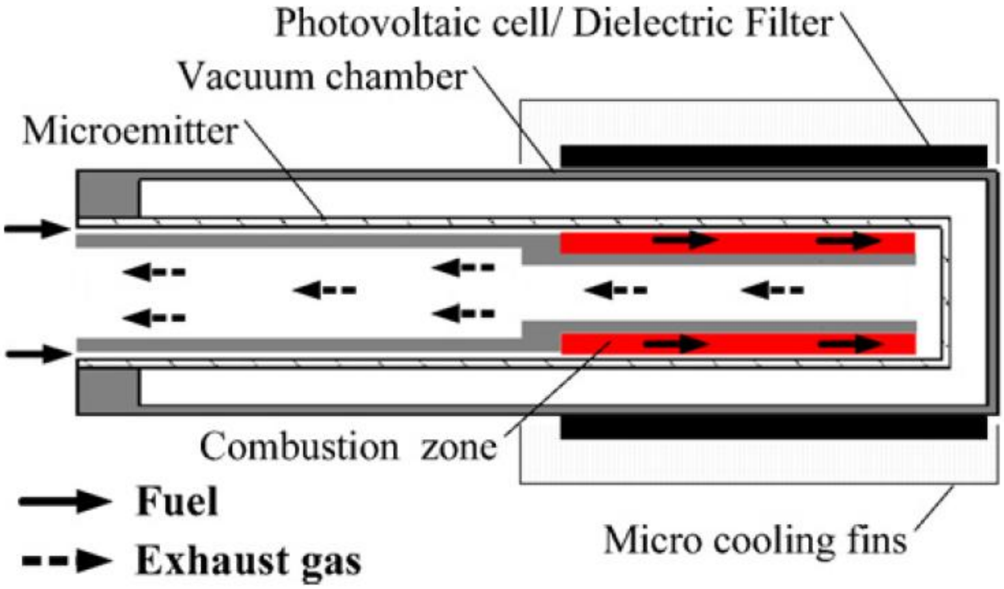

Figure 1.11 Conceptual design of micro-TPV system employed by Lee et al. [27]

1.4 Micro-propulsion

Since the early 1980s there has been an increasing interest within the Aerospace community in the development of micro (1-10kg) and pico (0.1-1kg) satellites. Several factors contributed for the satellite miniaturization trend. Miniaturization of electronics led to a reduction in the space and weight requirements of satellite avionics. As a consequence, it is now possible to achieve the mission of a normal size satellite using a cluster of smaller spacecrafts. Since it is estimated that about 30% of a space mission cost is usually from the launch costs, smaller satellites can reduce the overall mission expenditure. The concept of miniature satellites involves a cluster of many satellites flying in a certain formation and in constant communication with each other. The cluster could operate similarly to a parallel computer or each satellite could perform a single dedicated task. When put together, they perform all functions of a virtual satellite, which is much larger and expensive. Such microsatellite constellations offer increased reliability over larger conventional satellite because they are less prone to single point failures. MightySat-1 (U.S. Airforce), SNAP-1 (Surrey Space Centre, England), and Falconsat (U.S. Air Force Academy) are some examples of the microspacecraft programs [28]. However, there is still a lot of scope for improvement in the technology associated with microspacecrafts in order to fully utilize the possibilities offered by them. Such small satellites require small, lightweight propulsion systems that are adequately efficient, the development of which is one of the major challenges. Micropropulsion is still in its infant stage; development of many concepts is still required. Existing options include chemical thrusters, electro-thermal thrusters, cold gas thrusters, Hall thrusters, colloid thrusters, laser thrusters etc. Optimum thruster choice is subjective to the mission requirements. For high thrust and low weight missions, chemical thrusters are especially desirable. The following discussion on propulsion requirements and existing options is adapted from Rossi’s survey [29].

1.4.1 Propulsion requirements

Basic functions of a satellite propulsion module are

1. providing compensation for the external and internal forces acting on the satellite
2. orbital maneuvering
3. attitude control

These requirements are commonly expressed in terms of velocity increments (ΔV). From the mission specifications and spacecraft characteristics ΔV requirements are calculated which then translates to propellant need or consumption depending on the choice of the propulsion system.

1.4.1.1 ΔV Calculation

The thrust required to make a change in the spacecraft velocity, ΔV, is function of the mass of the spacecraft, $m_{S.}$

If a force F is applied on the aircraft, its velocity changes as follows

$$F = m_S a = m_S \frac{dV}{dt} \qquad [1.1]$$

where a is the spacecraft acceleration. However, thrust is produced by the consumption of propellant. Hence, the total mass of the satellite also changes during the maneuver.

$$Fdt = m_S d\,V + V dm_S \qquad [1.2]$$

For simplification, it can be assumed that the amount of propellant consumed during the maneuver is very small when compared with the total mass of the spacecraft such that,

$$Fdt = m_S d\,V \qquad [1.3]$$

Then the thrust needed for achieving a fixed ΔV in a fixed amount of time is given by the equation

$$\int F dt = m_S \Delta \quad [1.4]$$

The I_{sp} of the propulsion system is given by the equation (assuming constant thrust and mass flow rate),

$$I_{sp} = \frac{F}{\dot{m} g_0} \quad [1.5]$$

$$\int F dt = \int I_{sp} g_0 \dot{m} dt = m_S \Delta V \quad [1.6]$$

$$\int \dot{m} dt = m_P \quad [1.7]$$

where m_p is the total propellant consumption during the maneuver.

Assuming that the I_{sp} remains constant during the maneuver,

$$m_P = \frac{m_S \Delta V}{I_{sp} g_0} \quad [1.8]$$

Hence, if the ΔV required for a particular maneuver (which is a function of the mass of the spacecraft and type of maneuver), and the type of propulsion system (I_{sp}) which is employed to achieve the maneuver are known the amount of propellant required can be calculated from the above equation (1.8).

The propellant consumption mass fraction given by equation 1.9 is often used as a criterion of comparison for propulsion systems. A high value of η is desirable.

$$\eta = \frac{m_P}{m_S + m_P} \quad [1.9]$$

$$\eta = \frac{\frac{\Delta V}{I_{sp} g_0}}{1 + \frac{\Delta V}{I_{sp} g_0}} \quad [1.10]$$

$$\eta = \frac{\Delta V}{I_{sp} g_0 + \Delta V} \qquad [1.11]$$

1.4.1.2 ∆V Categories

The basic functions of a satellite propulsion module as described in the previous section can be divided into three ∆V categories.

1. primary ∆V, for orbit transfer and repositioning
2. secondary ∆V, for station keeping, external and internal force compensation
3. attitude control

Because of the lack of experience in ‘micro space field’ precise requirements of ∆V are not well defined by the space agencies for microsatellites. One paper discussed the propulsion requirements for very small satellites [30]. In general, micropropulsion thrust requirements range in between 1 µN and 10 N [30]. Table 1.2 gives some ∆V requirements of a 50 kg satellite depending on the type of space mission [31, 32].

Table 1.2 Table of estimated annual needs for a 50 kg satellite [29]

	Primary ∆V (m/s)	**Secondary ∆V (m/s)**	**Attitude control (m/s)**
Low orbit, <1000 km	<10	1–25	<10
Medium orbit	>100	<1	<1
Geosynchronous orbit	~1500	<5	~5

Micropropulsion devices or microthrusters can be subdivided into two main categories [33, 34]: electrical thrusters, which include electrothermal, electrostatic and electromagnetic devices, and chemical thrusters, which use the stored chemical energy in the propellant (liquid, solid, or gaseous).

1.4.2 Electrical thrusters

A typical electric propulsion device comprises of four components.

1. power source
2. power conversion system that converts the energy from the power source into electrical forms at the necessary voltage, frequency, pulse rate, and current level
3. propellant storage system
4. thruster to convert the electrical energy into kinetic energy

Electric thrusters can be again subdivided into the following three fundamental types:

1. Electrothermal thruster: the propellant is thermodynamically expanded through electrical heating and then accelerated to supersonic speeds through a nozzle. The ‘simplest’ electrothermal thrusters are resistojets. In resistojets, the propellant is heated by convective contact with a very hot metal. The propellant can be in gaseous (xenon) or liquid (water, hydrazine) form. Since liquid propellants vaporize on contact with the heating element they are also called vaporizing liquid thrusters (VLT). The advantages of VLT are its very small size and weight. The VLT can provide thrust in the range of milli Newtons with an input power of a few watts. Since it does not contain any moving parts, it has good reliability. The arc jet thruster also falls in the category of electrothermal thrusters.
2. Electrostatic thruster: power source is used to generate an electrostatic field. Thrust is produced by accelerating charged plasma through this field. However, this device can only operate under vacuum. Electrostatic thrusters are again subdivided based on the source of charged particles used.

    a. Electron bombardment thruster: Here, typically a noble gas (Xenon) is employed as the propellant. Plasma is generated by the application of electrical discharges in the gas, which is then accelerated in an electrostatic field.
    b. Field electrical emission propellant [35] (FEEP) or ion thruster: Uses liquid metal (cesium or indium) as propellant. Intense electrical field ionizes the liquid. The ions are then accelerated to very high speeds to generate thrust.
3. Electromagnetic thruster: power source is used to generate an electromagnetic field. Thrust is produced by accelerating charged plasma through this field. Two commonly used electromagnetic thrusters are:
    a. Pulsed plasma thruster (PPT): a capacitor is used to apply an electric arc at the surface of the propellant (usually Teflon) to create plasma. The electromagnetic field accelerates the plasma and generates thrust. The former operates in the transient mode.
    b. Hall thruster (HT): very similar to ion thruster except for the electromagnetic field. Compared to ion thrusters HT can accelerate the ions to higher exhaust velocities and generate higher thrust. Xenon is the commonly employed propellant.

1.4.3 Chemical thrusters

Chemical propulsion usually comprises of

1. a propellant tank

2. an ignition device
3. a nozzle to accelerate the gas stream

In addition to these, some chemical rockets may require intermediate parts such as valves, pumps, mixing parts, or feeding systems.

There are several chemical thruster options for micropropulsion.

1. Cold gas propulsion systems: Pressurized gas (usually an inert gas that do not contaminate the exposed spacecraft surfaces) propellant is ejected through a micro nozzle at high speed with the help of a valve (usually piezoelectric) [36, 37]. These thrusters can deliver thrust in the range of 0.1 to 10 mN and is suitable for fine attitude control and some secondary ΔV applications. The main drawbacks are the extremely low I_{sp} (~60 s) and the high leakage possibility reducing the reliability for long mission durations.
2. Solid propellant thruster: simplest propulsion system available. The solid propellant contains both fuel and oxidizer. Solid propellant thrusters are interesting for the generation of short impulses. The major drawback is the lack of restartability and hence cannot be used for station keeping because they cannot be repeatedly turned on and off. Hence, solid propellant rockets are employed as micro thruster arrays [38, 39].
3. Monopropellant (liquid) thruster: The hydrazine liquid monopropellant thruster has been widely employed for large spacecraft spacecraft propulsion. These thrusters have high I_{sp} (200–300 s) and are good candidates for primary ΔV propulsion applications. Drawbacks include problems associated with

liquid storage (valve failure), material compatibility, propellant safety and power required to pre-heat the system.

4. Bipropellant (liquid) thruster: Fuel and oxidizer (usually hydrazine and nitrogen tetroxide respectively) stored in separate tanks are burned in a combustion chamber to produce hot gases that are expanded out through a nozzle to produce thrust. They are capable of producing more thrust than any other existing propulsion system. Bipropellant thrusters usually have higher specific impulse than monopropellant ones (~ 350s). Hence, they are suitable for primary ΔV applications. However, there are difficulties involving obtaining good propellant mixing and stable combustion within the small combustion chamber. Propellant safety is another issue. Both hydrazine and nitrogen tetroxide are extremely toxic and they burn on contact (hypergolic).
5. Subliming Solid Micro Propulsion (SSP): It is based on the decomposition of solid propellant having a high sublimation pressure. Upon heating, the pressure in the propellant tank increases and the vapor is exhausted through a valve and nozzle to produce thrust force. The propellant usually employed is a heterocyclic nitrogen compound [40]. The theoretical performance for the compound as rocket propellant is I_{sp} ~ 250 s. The application of this type of technology could be in the attitude control of small satellites.

1.4.4 Thruster comparison

Of all the thruster options discussed in the previous sections, cold gas thrusters, subliming solid thrusters and solid propellant thrusters are relatively simple and less expensive. However, both of them have low specific impulse. In addition to this cold gas thrusters have the disadvantage of high leak rate. Miniaturized vaporizing liquid thrusters have higher I_{sp} than cold gas thrusters and subliming solid thrusters. However, they have a very complex design and require high power for operation. The same is the case with micro ion thrusters. They are complex and require high input power but have very high I_{sp}. Micro solid propellant thrusters are simple, inexpensive and have an acceptable performance but cannot be reused. Their good adaptability makes the pulsed plasma thruster a good candidate for low primary ΔV, secondary ΔV and attitude control. Each concept and option presents its own advantages and capabilities and has its own limitations. Table 1.3 summarizes the characteristics and performance of each option. In Tables 1.4 and 1.5 are reported the advantages and drawbacks of each micro thruster option. The chart of Figure 1.12 is a two-dimensional classification of the micro thruster operating performance: thrust force (N) over the total impulse (mN-s) space. The chart in Figure 1.13 is a two-dimensional classification of the micro thruster operating performance: thrust force (N) over the thruster efficiency (mN/W) space.

Table 1.3 Table of comparison of the micro propulsion systems characteristics and performance [29]

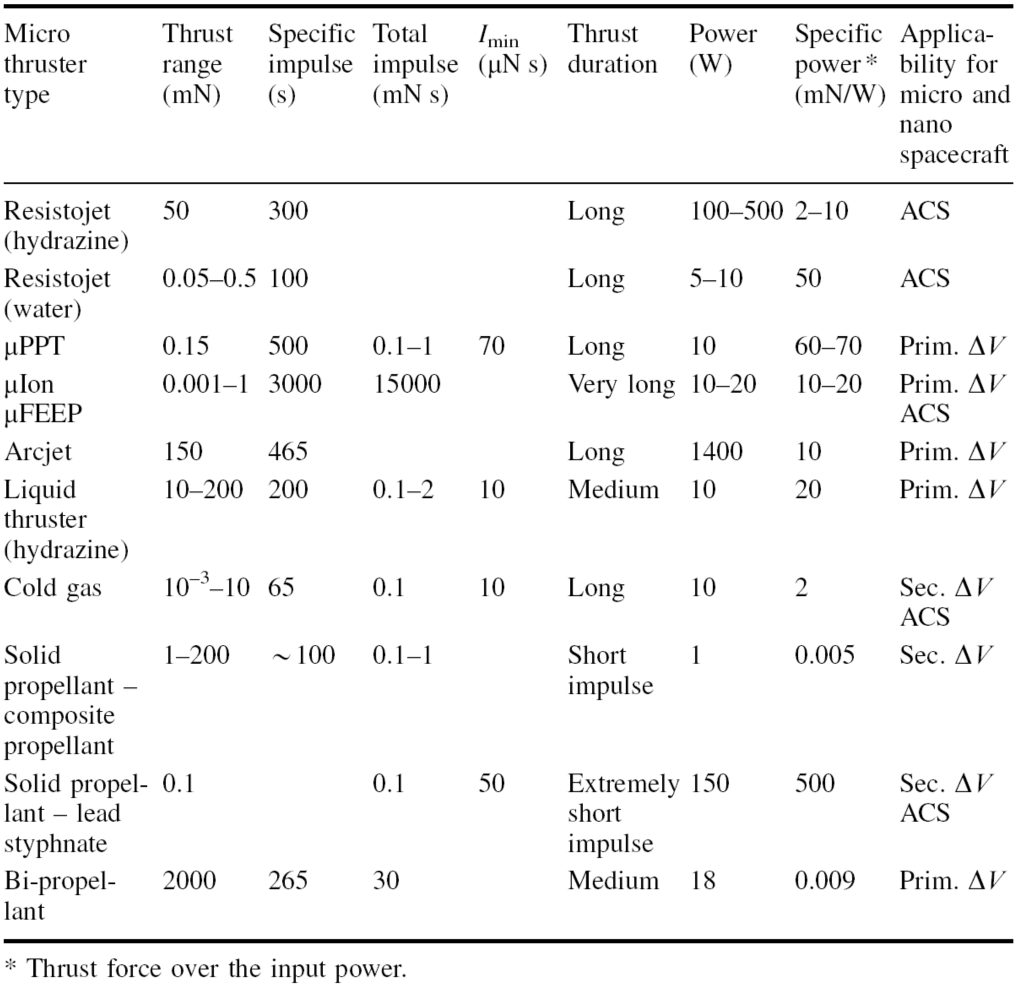

Micro thruster type	Thrust range (mN)	Specific impulse (s)	Total impulse (mN s)	$I_{\min}$ (μN s)	Thrust duration	Power (W)	Specific power* (mN/W)	Applicability for micro and nano spacecraft
Resistojet (hydrazine)	50	300			Long	100–500	2–10	ACS
Resistojet (water)	0.05–0.5	100			Long	5–10	50	ACS
μPPT	0.15	500	0.1–1	70	Long	10	60–70	Prim. ΔV
μIon μFEEP	0.001–1	3000	15000		Very long	10–20	10–20	Prim. ΔV ACS
Arcjet	150	465			Long	1400	10	Prim. ΔV
Liquid thruster (hydrazine)	10–200	200	0.1–2	10	Medium	10	20	Prim. ΔV
Cold gas	10^{-3}–10	65	0.1	10	Long	10	2	Sec. ΔV ACS
Solid propellant – composite propellant	1–200	~100	0.1–1		Short impulse	1	0.005	Sec. ΔV
Solid propellant – lead styphnate	0.1		0.1	50	Extremely short impulse	150	500	Sec. ΔV ACS
Bi-propellant	2000	265	30		Medium	18	0.009	Prim. ΔV

* Thrust force over the input power.

Table 1.4 Advantages and drawbacks of electrical propulsion systems [29]

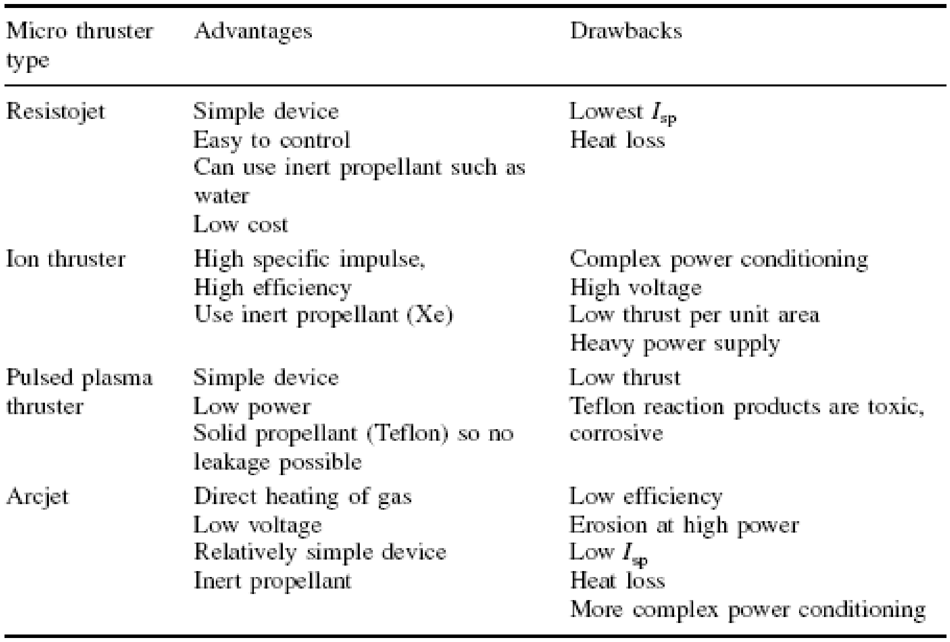

Micro thruster type	Advantages	Drawbacks
Resistojet	Simple device Easy to control Can use inert propellant such as water Low cost	Lowest I_{sp} Heat loss
Ion thruster	High specific impulse, High efficiency Use inert propellant (Xe)	Complex power conditioning High voltage Low thrust per unit area Heavy power supply
Pulsed plasma thruster	Simple device Low power Solid propellant (Teflon) so no leakage possible	Low thrust Teflon reaction products are toxic, corrosive
Arcjet	Direct heating of gas Low voltage Relatively simple device Inert propellant	Low efficiency Erosion at high power Low I_{sp} Heat loss More complex power conditioning

Table 1.5 Advantages and drawbacks of chemical propulsion systems [29]

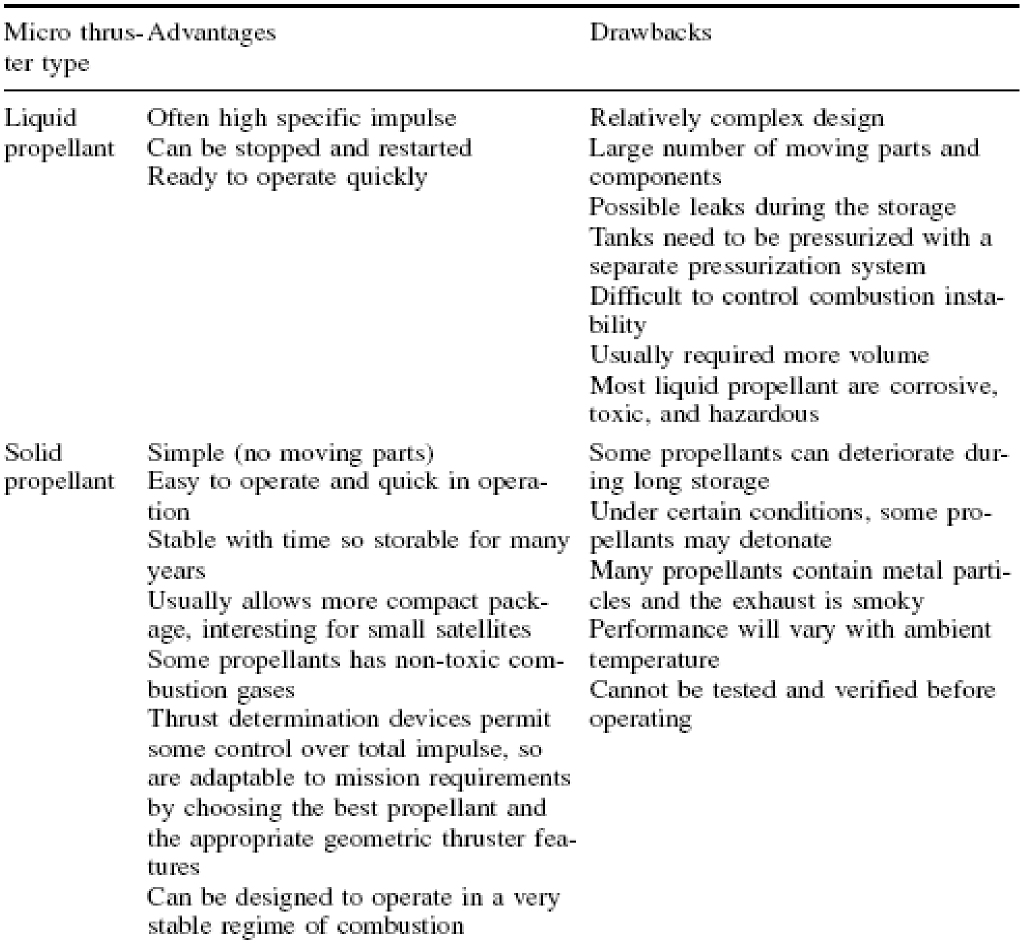

Micro thruster type	Advantages	Drawbacks
Liquid propellant	Often high specific impulse Can be stopped and restarted Ready to operate quickly	Relatively complex design Large number of moving parts and components Possible leaks during the storage Tanks need to be pressurized with a separate pressurization system Difficult to control combustion instability Usually required more volume Most liquid propellant are corrosive, toxic, and hazardous
Solid propellant	Simple (no moving parts) Easy to operate and quick in operation Stable with time so storable for many years Usually allows more compact package, interesting for small satellites Some propellants has non-toxic combustion gases Thrust determination devices permit some control over total impulse, so are adaptable to mission requirements by choosing the best propellant and the appropriate geometric thruster features Can be designed to operate in a very stable regime of combustion	Some propellants can deteriorate during long storage Under certain conditions, some propellants may detonate Many propellants contain metal particles and the exhaust is smoky Performance will vary with ambient temperature Cannot be tested and verified before operating

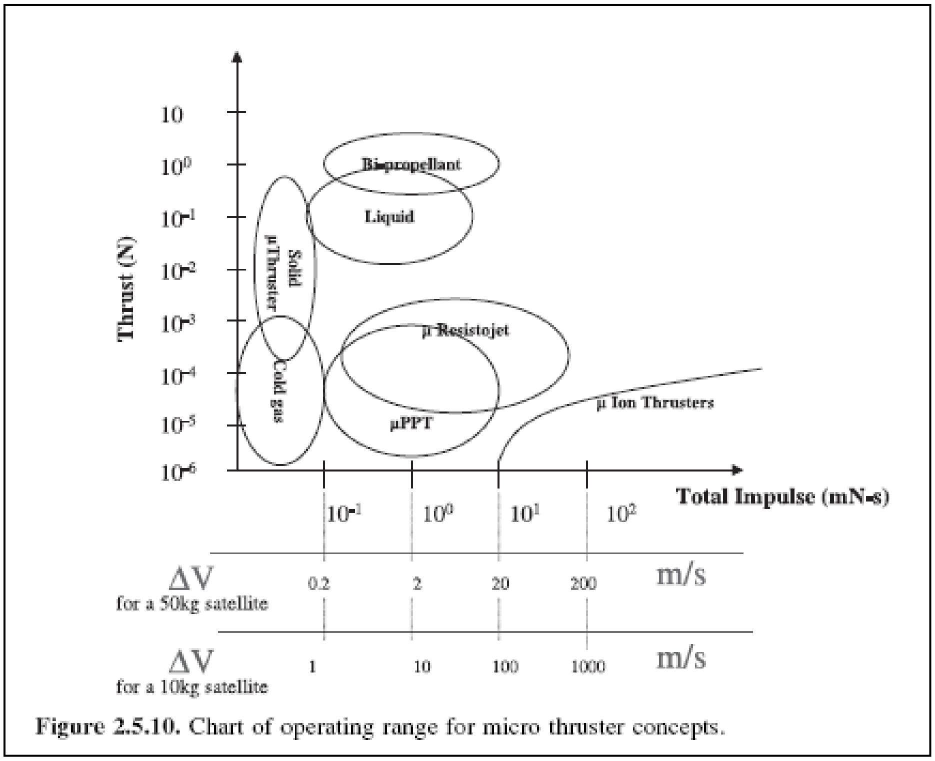

Figure 1.12 Chart of operating range for micro thruster concepts [29]

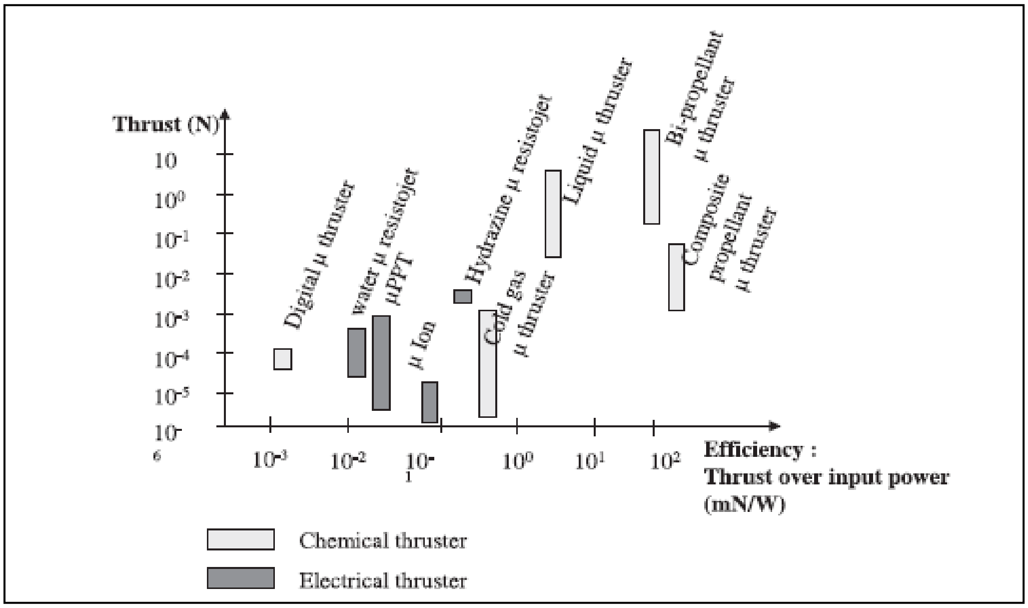

Figure 1.13 Chart of thruster efficiency (thrust force over input power) for the propulsion concepts [29]

The choice of a particular option (electrical or chemical) for the propulsion device is dictated primarily by the specific mission objectives. Then the selection of the propulsion systems for a specific mission is made after an analysis of the available propulsion system characteristics (F, Isp) and the mission requirements (altitude, duration, total mass, etc.). Many technological developments have been made and many micropropulsion devices have been demonstrated, characterized with respect to their capabilities, limits, advantages, drawbacks, and possible applicability. In conclusion, electric propulsion systems offer high Isp (500 s for the arcjet and 1000 s for others). For most of them the performance is directly linked to the input power, which is a limitation for their miniaturization. Compared to electric propulsion systems, chemical propulsion concepts can provide higher thrusts but at considerably lower I_{sp}s. Bipropellant chemical thrusters are capable of delivering high thrust required for primary ΔV applications.

1.5 Micro fuel reformers

A high-energy micro-scale power device that combines micro-combustor, combustion-driven fuel reformer and fuel cell has been developed at Pacific Northwest National Labs [42] to be employed as a power supply for microelectronics. The micro-scale fuel reformer extracts hydrogen from a hydrocarbon fuel (such as methanol) .The hydrogen-rich stream is then fed to a fuel cell to generate electrical power. The energy required for the operation of the fuel reformer is provided by the micro-combustor. Preliminary tests showed that the fuel reformer, utilizing methanol or butane, was able to provide up to 100 mW of hydrogen at an efficiency of up to 4.8%. The device was able to operate independent of any additional external heating, even during start-up. Analysis of the reformate stream revealed that it composed primarily of hydrogen (>73%). Approximately 26% carbon dioxide and 1% carbon monoxide are also present. The low level of carbon monoxide is acceptable for use with the related fuel cell technology.

1.6 Micro combustion: Characteristics and Scaling Issues

Combustion in small scales has several qualitative differences when compared with conventional scale combustion. As the size of the combustion chamber goes down the effects of interfacial phenomena (heat transfer and surface reactions) that occur at the combustor walls increases due to higher surface to volume ratio. The energy release in a combustor is proportional to its volume and the heat losses and surface reactions are proportional to its surface area. As the scale of the combustor is reduced, the surface area to volume ratio increases as the inverse of the characteristic length scale. This is illustrated in Figure 1.15 for different geometries.

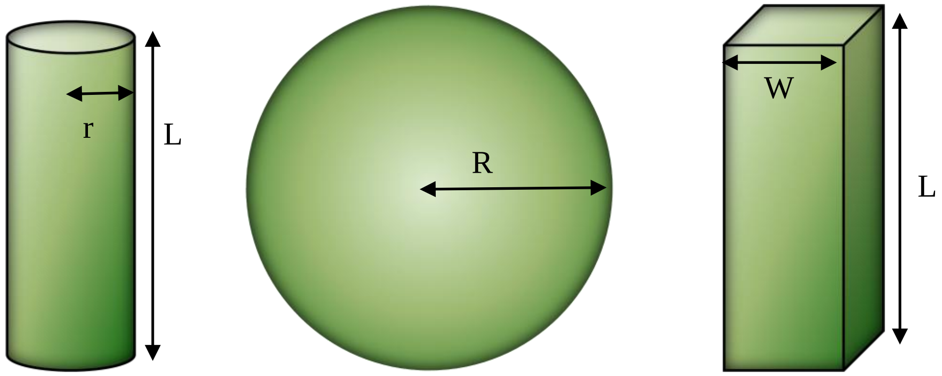

$$\left(\frac{A}{V}\right)_{cylinder} = \frac{2}{r} \qquad \left(\frac{A}{V}\right)_{sphere} = \frac{3}{R} \qquad \left(\frac{A}{V}\right)_{right\ cuboid} = \frac{4}{W}$$

Figure 1.15 Surface area by volume of a hollow cylinder, a sphere and a hollow right cuboid

The effect of this characteristic dimension on combustion as its value goes down can be understood by normalizing the conservation equations [4] and writing them in terms of thermo-physical non-dimensional numbers *Re* (Reynolds number), *Pe* (Peclet number), *Le* (Lewis number) and *Da* (Damkohler number).

$$\frac{L_c}{\tau_c u_c}\cdot\frac{\partial\bar{u}}{\partial\bar{\tau}}+\bar{u}\frac{\partial\bar{u}}{\partial\bar{x}}= -\frac{P_c}{\rho_c u_c^2}\frac{1}{\bar{\rho}}\frac{\partial\bar{P}}{\partial\bar{x}}+\frac{1}{Re}\bar{\vartheta}\frac{\partial^2\bar{u}}{\partial\bar{x}^2}+\frac{gL_c}{u_c^2} \tag{1.12}$$

$$\frac{L_c}{\tau_c u_c}\cdot\frac{\partial\bar{T}}{\partial\bar{\tau}}+\bar{u}\frac{\partial\bar{T}}{\partial\bar{x}}= \frac{1}{Pe}\bar{\alpha}\frac{\partial^2\bar{T}}{\partial\bar{x}^2}+Da\frac{Q}{\overline{C_p}T_c}\overline{\dot{w}''} \tag{1.13}$$

$$\frac{L_c}{\tau_c u_c}\cdot\frac{\partial\bar{y}_i}{\partial\bar{\tau}}+\bar{u}\frac{\partial\bar{y}_i}{\partial\bar{x}}= \frac{1}{LePe}\bar{D}\frac{\partial^2\bar{y}_i}{\partial\bar{x}^2}+Da\frac{1}{y_{ic}}\overline{\dot{w}''} \tag{1.14}$$

$$Da=\frac{\dot{w}''_c L_c}{\rho_c u_c} \tag{1.15}$$

$$Le=\frac{\alpha_c}{D_c} \tag{1.16}$$

$$Pe=\frac{L_c u_c}{\alpha_c} \tag{1.17}$$

$$Re=\frac{L_c u_c}{\vartheta_c} \tag{1.18}$$

Equations 1.21, 1.22 and 1.23 represent conservation of momentum, energy and species respectively. L_c, τ_c, u_c, P_c, ρ_c, $\dot{w}''_c$, α_c, D_c and ϑ_c are the characteristic values of length, time, velocity, pressure, density, reaction rate, thermal diffusivity, mass diffusion coefficient and viscosity respectively. y_{ic} is characteristic mass fraction of species i. $\bar{u}$, $\bar{\rho}$, $\bar{T}$, $\overline{\dot{w}''}$, $\bar{y}_i$, $\bar{\vartheta}$, $\bar{P}$ and $\bar{\alpha}$ are the normalized values of velocity, density, temperature, reaction rate, mass fraction of species i, viscosity, pressure and thermal diffusivity, normalized with respect to their characteristic values. $\bar{x}$ and $\bar{\tau}$ are the normalized spatial and time coordinates and Q = heat of the reaction.

For conventional length scales (macro scales), the Reynolds and Peclet numbers are large due to L_c being large. The flows are mostly in the turbulent regime and the viscous and diffusive effects are relatively small compared to the convective effects. In contrast, small-scale flows have small Re and Pe so that flows are laminar or transitional. This means that viscous and diffusive effects may dominate the system. In addition, for high flow rates, small characteristic length leads to small residence times. This might push the Damkohler number towards unity and sometimes below unity, thereby quenching the reaction.

The characteristic length scale for combustion systems is usually divided into three categories. Micro-scale, meso-scale and macro scale. When characteristic dimensions are in the range of one millimeter to one centimeter, it is usually accepted to be in meso-scale. Anything below millimeter scale can be considered micro and above centimeter scale can be considered macro. In the present research, we are dealing with combustion in the intermediate length scale or meso-scale.

1.6.1 Flame quenching

Flame quenching is defined as the failure of flame propagation in the presence of combustible substances. Flame quenching was first reported by Sir Humphry Davy [43] in 1817 when he was involved in preventing explosions in coal mines. He discovered that flame propagation could be stopped by fine wire gauze. Next contribution came hundred years later when Payman and Wheeller published their work on the propagation of flames through small diameter tubes [44]. In 1933 Holm [45], introduced the concept of quenching distance or quenching diameter based on his experimental studies of flame quenching. Since then several groups have performed extensive investigations on flame quenching by contact with the cold wall suggesting that it is impossible for a flame to pass through gaps of sub millimeter scale. The concept of quenching distance is often used to design explosion-proof devices. Due to its importance in industrial applications, several experiment methods to estimate the quenching distance for flame propagation in different mixtures were developed. Measurement of quenching distance was performed mainly using three different methods. They are 1) tube method 2) burner method 3) flange electrode method. The first method was developed by Holm and is commonly used for quenching distance estimation at atmospheric pressures [45, 46]. The second is mainly carried out at reduced pressures [47-49]. The third method was developed by Blanc et al.[50] and was later employed by other researchers Lewis and von Elbe [51], [52]. A review of all three methods is given in [53]. Andrews and Bradley [54] employed a constant volume bomb method to measure the quenching distance of methane air flames. They observed a U shaped dependence of quenching distance on the equivalence ratio with minimum quenching distance occurring near stoichiometric condition. Jarosinski et al.[55,56] carried out a series of experiments on methane-air and propane-air flames quenched by cold walls and showed that the quenching distance is a function of the fuel-air equivalence ratio with minimum located at the stoichiometric point. Another finding of this research was the nearly constant value of Peclet number at quenching conditions. Peclet number calculated using quenching distance and laminar burning velocity is around 39-41 for methane-air and 42 for propane-air over a broad range of mixture compositions. Experimental measurement of the heat flux from flame to the combustor wall during laminar flame quenching was performed by Vosen and Greif [57]. Results suggested that flame quenching occurs when the ratio of heat loss to heat generation is greater than 0.3. Studies that focused on assessing the effect of walls on the quenching distance found that the nature of the wall material hardly affected the quenching distance [46, 58]. From a thermal point of view, this can be explained by the higher (several orders of magnitude) heat capacity of a wall of finite thickness compared to that of the hot combustion products. However, some studies did observe a small effect of the properties of the wall [49] on the quenching distance. This was attributed to the residual catalytic activity of the wall surface, which was poisoned by the combustion products [59].

Several theories on flame quenching by walls were also developed. The most important contribution was made by Zel'dovich [60-62]. He demonstrated that at the quenching limit, $S_{L,lim}$, the laminar burning velocity, and the maximum value of the limit flame temperature, $(T_{b,max})_{lim}$ were related to their respective values under adiabatic conditions, S°_{L}, and T°_{b}, through the following relations.

$$\frac{S_{L,lim}}{S_L{}^0} = \sqrt{e} = 0.61 \qquad [1.19]$$

$$\Delta T_{b,lim} \equiv \left[T_b{}^0 - (T_{b,max})_{lim}\right] = \frac{b}{\left(S_{L,lim}\right)^2} = \frac{\left(T_b{}^0\right)^2 R}{E} \qquad [1.20]$$

where b is a parameter characterizing heat losses, R is universal gas constant and E is the activation energy.

In his theory, Zel'dovich also showed that the Peclet number, given by the expression remained constant at the flame quenching limit, where D_Q is the quenching diameter and α is the thermal diffusivity.

$$\mathrm{Pe} = \frac{S_L{}^0 D_Q}{\alpha} \qquad [1.21]$$

Later on, several group of theories based on the energy conservation equation for the flame, including heat loss [63–65] were developed to estimate quenching distance. Spalding [65] added the heat loss term to the 1D energy equation. His model predicted that both radiation and conduction losses are important for estimating flammability limits. However, conductive heat loss is more important as the combustor size is decreased. Mayer [64] considered the effect of heat loss by convection on flame temperature. He obtained an expression for quenching diameter and predicted the Peclet numbers at quenching conditions to be around 30-50. There are other simple models [66-68] dealing with the heat loss induced quenching, with expressions of the quenching distance explicitly given. One common feature of these theoretical models is that the wall is assumed to be cold (298 K) The reasoning behind this assumption is that the quenching process takes place in a very short time causing negligible increase in wall temperature.

There are several numerical simulations, which gave the results close to the experimental values. The results obtained by Karman and Milan [69], Westbrook et al. [70] and Popp and Baum [71] were in good agreement with the experimentally determined values. Aly et al. [72] simulated the quenching distance of the propane-air flames between two parallel plates by solving the 2D governing equations. The quenching limit was determined by iterating the solution with respect to the plate separation distance and approaching the limit state to within a specific criterion. Hackert [73] studied the effects of the wall thermal conditions on flame quenching. Flame shapes and heat transfer distributions to the wall have been presented for different wall thermal boundary conditions. Dou and Matalon [74] employed a diffusive-thermal model to examine the influence of conductive heat loss to the walls on the propagation of the premixed flames in 2D channels.

In all the aforementioned research on flame quenching, only thermal quenching mechanisms were extensively investigated by means of experimental, analytical, and numerical methods. During combustion, the internal surface of the combustor is heated and an adsorption reaction occurs between highly reactive radicals and surface defects through chemisorption. Radicals adsorbed on the surface tend to recombine to stable molecules then lead to desorption. A series of surface reactions cause the flame to be destabilized owing to excessive loss of reactive radicals. The effect of the surface reactions is amplified in the combustor particularly when the surface-to-volume ratio is high and can lead to flame quenching under certain circumstances. This mechanism of flame quenching known as chemical quenching or radical quenching had gained very little attention when compared to thermal quenching. Even though a few studies on the chemical quenching were done, their experimental verifications were rare. Masel et.al. [75] studied the effect of surface reactions on quenching by employing wall materials with varying surface activity. They concluded that for cold walls, thermal quenching is the dominant flame-quenching mechanism. However, as wall temperature approaches combustion temperatures, heterogeneously catalyzed radical recombination controls flame quenching.

It can be summarized that quenching distance is essentially an overall result of many factors. These include type of reactants, wall temperature, wall material, chamber pressure and geometry of the passage for flame propagation (higher quenching distance for circular tubes compared to parallel plates) The classical definition of quenching distance (the smallest possible length scale for combustion) applies only for the combustible mixture at 1 atm pressure and the wall temperature close to 298K. Quenching distance decreases with increasing the wall temperature due to reduction in heat loss from the flame. Similarly, as pressure increases quenching distance decreases [66]. Therefore, it is possible to achieve combustion inside much smaller scales than that predicted by the classical quenching theory.

1.6.1.1 Strategies to overcome quenching issue

There are three different ways to tackle the quenching issue. They are***:***

1. Catalytic combustion- although the increase of the surface-to-volume ratio of the combustor presents a problem for gas-phase combustion, it favors catalytic combustion [115].

2. Homogeneous charge compression ignition- HCCI is an alternative combustion mode in which a fuel-air mixture is compressed until it explodes. Ignition occurs at several locations in the combustion chamber. HCCI is essentially limited by kinetics. Traditional flame propagation is absent [14]. Since it is possible to burn the fresh charge without flame propagation, the flame-quenching problem is circumvented.

3. Preheating of the reactants through heat recirculation-Studies [116-121] have shown that quenching issue can be effectively dealt with through recirculation of thermal energy from the products to preheat the reactants without recirculating the combustion products themselves. They employed a Swiss-roll design utilized by

Weinberg et al. [113] for heat recirculation. This is the method which is employed in this dissertation for combustion inside meso-scale volumes.

1.6.2 Residence time

Time scaling effects are very important in small scale combustion. One of the basic requirements for stable sustained combustion is that the physical time available for the reactants to combust (residence time) should be larger than chemical reaction time and diffusion time. Otherwise, combustion will be incomplete resulting in reduced efficiency. This fundamental time constraint in combustion is quantified in terms of the Damkohler number. It is defined as the ratio of reactant residence time to the characteristic chemical reaction time. Damkohler number must be greater than unity to ensure complete combustion. For a given reactant feed rate, the reactant residence time decreases with the size of combustor. This implies that Damkohler number could be less than unity as the combustor size decreases. One way to achieve favorable Damkohler number is to decrease the chemical times by ensuring high combustion temperatures. This can be achieved by preheating the reactants, minimizing the heat losses and using highly energetic fuels. Another way is to effectively increase the residence time of a fraction of the reactants by inducing flow recirculations within the combustion chamber. This can be achieved by employing geometric flame holders [76], swirl injection [77] or dump combustors [27]. The present study employs reactant preheating using a Swiss-roll combustor design and geometric flame holder for sustaining combustion inside the meso-scale combustion chamber.

1.6.3 Liquid fuel considerations

It is to be noted that using liquid hydrocarbon fuels, there are additional challenges that include vaporization and mixing. Two methods available in literature to overcome this challenge include:

1. Electrosprays- since the available time for vaporization mixing and combustion is very small in a meso-scale combustor, liquid sprays with droplet sizes as small as few microns is required. For this purpose virtually the only candidate suitable at the small flow rate of interest is electrospray atomization [78, 79]. In electrosprays, atomization and dispersion of the liquid relies solely on its electrical potential of the liquid that is obtained via electrical charging. Such a system can be implemented by feeding a liquid with sufficient electric conductivity and moderate surface tension through a small orifice maintained at a high potential relative to a ground electrode that is located a short distance away. This approach offers enhanced vaporization and mixing because of the presence of net charge on the surface of the generated droplets.
2. Liquid Film Combustion - this method involves delivering the liquid fuel in the form of a film on inside surfaces of the combustor [80, 81]. This delivery exposes the fuel to rapid vaporization and simultaneously cools the combustor walls. Since the area/volume ratio of any wall film will grow as the volume of the combustors decreases, the liquid film can offer as high a liquid surface area for vaporization as a vaporizing spray in the sub centimeter-size range. Furthermore, the liquid film offers protection from heat losses and quenching that will not be present in vaporizing sprays. With the liquid film, the wall temperature will not exceed the boiling point of the liquid at the solid surface. In this research, a combination of heat recirculation and

liquid film evaporation has been employed for meso-scale combustion of methanol-air mixture.

1.6.4 Flame dynamics

Flame dynamics is intimately related to combustion instabilities and noise generation. In this section a brief discussion on combustion instability is presented which is mostly adapted from Searby's work in [82]. The discussion is intended to describe the effect of length scales on flame dynamics and provide an understanding on the type of instabilities that may be significant in small-scale combustion.

Combustion instability

Flame instability is one of the most disadvantageous aspects of combustion and is often detrimental to the operation of the system and can lead to serious consequences. Although combustion features a wide range of instabilities, they can be broadly divided into two general classes of instabilities: Intrinsic instabilities and thermo-acoustic instabilities.

In the first category, the instability is intrinsic to the combustion process. Such instabilities would occur even in the absence of a surrounding with which the combustion interacts. Darrieus–Landau hydrodynamic instability of premixed flame fronts and thermo-diffusive instabilities that arise when the Lewis number departs from unity are examples of intrinsic instabilities. Thermo-acoustic instabilities involve a coupling between combustion and the acoustics of the system. They can be distinguished to two different kinds. When the coupling is between combustion and the resonant modes whose wavelength is comparable with the total system longitudinal dimension, the instabilities that arise are generally characterized by low-frequency oscillations. These are thermoacoustic instabilities of the first kind. In thermo-acoustic instabilities of second kind, the coupling takes place between combustion and chamber resonances in the transverse or azimuthal direction. Since wavelength corresponding to this mode is related to the transverse dimension of the chamber, the frequency of oscillations are usually high.

1. Intrinsic instabilities

a. The Darrieus–Landau Hydrodynamic Instability: Due to the expansion of gas through the flame front, all premixed flames are unconditionally unstable to a hydrodynamic instability. George Darrieus [83] and Lev Landau [84] independently recognized this phenomenon and therefore is referred to as the Darrieus– Landau instability. Since the full derivation of the instability is beyond the scope of this dissertation, a simplistic explanation of the phenomenon is presented here to understand its influence in small scale combustion.

Figure 1.16 shows the velocity jump across a planar premixed flame front. For simplicity, it is assumed that, flame is an infinitely thin interface that transforms cold unburnt gas, at temperature T_0 and density ρ_0 into hot burnt gas at temperature Tb and density ρ_b. The flame speed is assumed to be a constant (S_L). For an observer whose in the reference frame of the flame front the unburnt gas enters the front at speed $U_0 = S_L$. The hot gases leave the front at a much larger velocity $U_b = S_L(\rho_0/\rho_b)$, because of thermal expansion. For standard hydrocarbon-air flames the density ratio ρ_0/ρ_b is typically of the order of 6-7. In order to conserve the momentum equation the velocity jump is accompanied by a small pressure jump which is roughly equal to $\delta = 1/2(\rho_b U_b^2 - \rho_0 U_0^2)$, typically of the order of 1Pa. When the flame front is inclined with respect to the incoming flow of unburnt gas as shown in Figure 1.17.a, the burnt gas deviates from the flow direction. This can be explained as follows. The incoming gas flow can be decomposed into two components that are parallel (U_{ll}) and perpendicular (U_n) to the flame front. For an observer in whose reference frame the flame front is stationary, the speed of the normal component must be equal to the flame velocity, $U_n = S_L$. The burnt gas leaving the flame will have a normal component equal to $U_n(\rho_0/\rho_b)$. However, the parallel component, U_{ll}, remains unaltered. This is because there is no parallel pressure jump that would be necessary to accelerate the parallel component of the flow. The burnt gas thus deviates toward the outgoing normal. This effect can be seen the figure which shows Figure 1.17.b a visualization of the streamlines through a Bunsen flame front. In most of the real situations, flame front is not planar. It is usually wrinkled at some wavelength λ. As discussed before at places where the streamlines are normal to the front, they will be accelerated, without any deviation as they cross the flame and at places where the front is inclined with respect to the incoming streamlines, they will be deviated toward the rear normal as in Figure 1.17.a. However, since it is not possible for stream lines to intersect each other, at locations downstream of the flame front the streamlines must curve to become parallel. Pressure gradients arise in the downstream sections due to the curvature in streamlines. The effect of gas expansion through a curved flame causes the flow to converge at places where the front is concave to the unburnt gas, and to diverge where the front is convex. Due to mass conservation principle the upstream flow is accelerated at places where the flame front is concave to the flow and decelerated at places where it is convex. Since the flame speed is assumed to be constant the situation is unconditionally unstable and the wrinkling will grow in time. This is called the Darrieus–Landau instability. Landau [84] derived an expression for the growth rate σ (dimensions s^{-1}). This expression is valid when the amplitude of wrinkling is small when compared with the wavelength.

$$\sigma \propto \frac{kS_L E}{E+1}\left(\sqrt{\frac{E^2+E-1}{E}}-1\right) \quad [1.22]$$

$$E = \frac{\rho_0}{\rho_b} \quad [1.23]$$

$$k = \frac{2\pi}{\lambda} \quad [1.24]$$

The growth rate of the Darrieus–Landau instability increases with the flame speed and with the wave number of wrinkling. This implies that wrinkles of short wavelength grow faster than wrinkles of long wavelength. However, the growth rate cannot increase indefinitely for small wavelengths. Short wavelength wrinkles that are comparable to the flame thickness may induce distortions of the flame structure that are not accounted for in the hydrodynamic stability description. Thermo-diffusive phenomena become more prominent when the wavelength of wrinkling is comparable with the flame thickness and may overcome the destabilizing effect of thermal expansion.

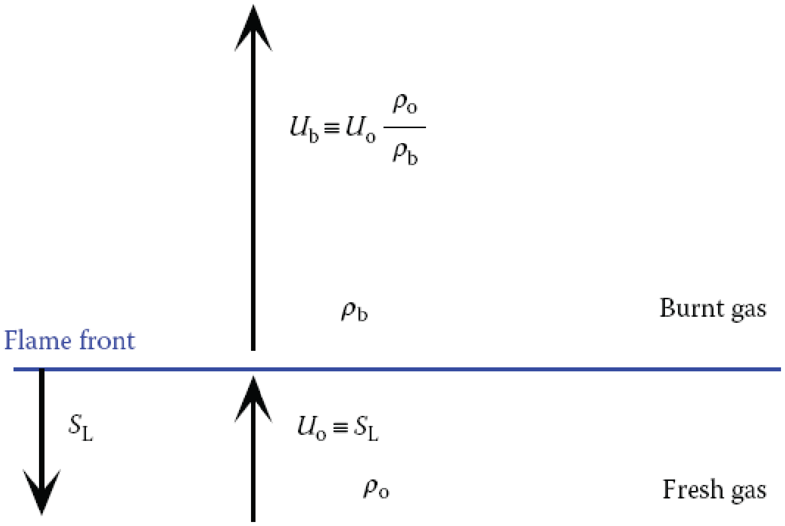

Figure 1.16 Gas expansion through a planar flame

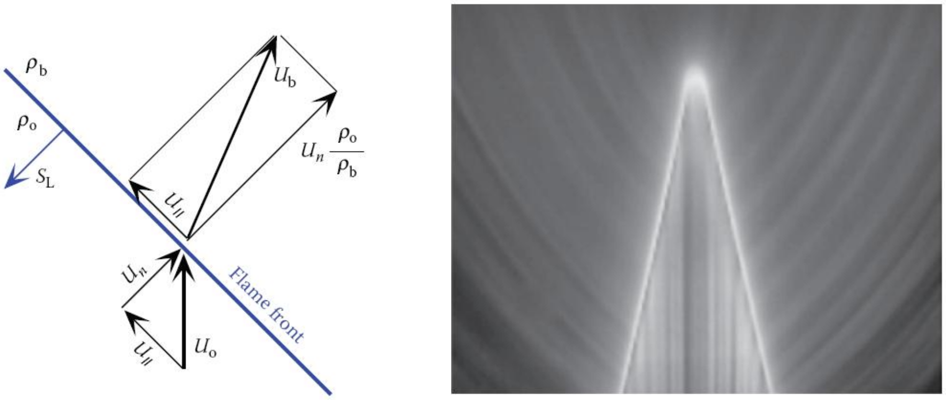

Figure 1.17 Deviation of streamlines through an inclined flame (left). Visualization of streamlines through an inclined Bunsen flame (right)

b. Thermo-diffusive instabilities: Similar to hydrodynamic instability, thermo-diffusive instability also arises due to wrinkles on the flame front. When the flame is curved or wrinkled, the gradients of temperature and species concentration are no longer parallel to the average direction of propagation and can cause the heat flux and species flux to converge or diverge. This can lead to a change in local flame velocity. The heat flux is convergent wherever the front is concave toward the unburnt gas. This leads to a rise in local flame temperature increases and hence the local flame velocity. The opposite is true for locations of the front that are convex. Clearly, a flame speed increases at places where flow is accelerated due to converging streamlines and vice versa. Hence, the effect of this heat or thermal diffusion is to stabilize a wrinkled flame. Unlike heat flux, the gradient of species concentration is in a direction opposite to the thermal gradient. The species flux becomes locally divergent at places where the front is concave toward the unburnt gas. The flux of reactive species into the reactive zone decreases, leading in turn to a decrease in the local flame velocity. Hence in a wrinkled flame, species diffusion leads to instability. Since both the diffusions occur simultaneously, the question of whether the flame is thermo-diffusively stable or not has to be answered based on the relevant Lewis number (usually that of the deficient species in the mixture). Lewis number is the ratio of the thermal, D_{th}, and species, D_{mol}, diffusion coefficients.

$$L_e = \frac{D_{th}}{D_{mol}} \qquad [1.25]$$

Based on the above discussion it is very tempting to assert that for Lewis number greater than unity, the effect of heat diffusion prevails over species diffusion and the flame is thermo-diffusively stable and vice versa. However, since there are additional effects that arise from the inclination of the streamlines within the preheat zone which can also lead to variations in local flame velocity, Le < 1 is not a sufficient criterion for flame stability. This was first recognized by Markstein [85] who formulated the equation for local flame velocity (S_n) based on flame curvature.

$$\frac{S_n - S_L}{S_L} = M_a \frac{\delta}{R} \qquad [1.26]$$

Where $\delta = D_{th}/S_L$ is a measure of the thermal thickness of the flame and M_a is a nondimensional number called Markstein number. If the Markstein number is positive, then the flame is thermo-diffusively stable. In fact, the Markstein number is generally positive for common hydrocarbon flames even though the Lewis number may be smaller than unity [86]. Dimensional analysis shows that the effect of diffusion on the growth rate of the wrinkling must scale as some effective diffusion coefficient, D, times the square of the wave number [87, 88]: Thus, it is globally expected that long wavelength wrinkling is unstable, because of the Darrieus–Landau instability, with a growth rate that increases linearly with wave number. But for wavelengths comparable with the flame thickness, thermo-diffusive effects become predominant and restabilize the flame through a term proportional to $-k^2$.

$$L_e = \frac{D_{th}}{D_{mol}} \qquad [1.27]$$

$$\delta = \frac{D_{th}}{S_L} \qquad [1.28]$$

$$\frac{S_n - S_L}{S_L} = \frac{L}{R} \qquad [1.29]$$

$$\frac{S_n - S_L}{S_L} = M_a \frac{\delta}{R} \qquad [1.30]$$

2. Thermoacoustic instabilities: Such instabilities are quite frequently observed in combustion chambers. They have been encountered during the development of

combustion systems such as rocket engines [89, 90], gas turbine engines [91, 92] and domestic boilers [93]. These instabilities are in general detrimental for the combustion device and can lead to mechanical failure. However, in some situations, they may be favorable for enhancing mixing and increasing burning rates. The phenomena were first observed by Mallard & Le Chatelier in 1883 [94]. It is a known fact that under normal conditions, combustion processes generate broadband incoherent noise usually referred to as “combustion roar.” The heat release fluctuations that are inherently present are responsible for this acoustic radiation. The relation between heat unsteady combustion and noise generation can be derived using the classical set of conservation equations. Assuming that the combustion takes place in a uniform medium at rest (Mach << 0), and writing the pressure, velocity and density variables as a sum of a mean value and a perturbed value, the linearized conservation equations for mass and momentum can be used to obtain a wave equation for the pressure in the presence of local heat release [82].

$$\frac{\partial^2 p\prime}{\partial t^2} - c^2\nabla^2 p' = \left(\frac{C_p - C_v}{C_v}\right)\frac{\partial \dot{q}}{\partial t} \qquad [1.31]$$

In the absence of fluctuations in the heat release rate, $\frac{\partial \dot{q}}{\partial t}$ = 0, Equation 1.40 reduces to the standard wave equation for the acoustic pressure. It can be seen that a fluctuating heat release then acts as a source term for the acoustic pressure.

The acoustics generated by combustion can in turn interact with the combustion zone, especially when the heat release rate is a function of the acoustic pressure ($\dot{q}$=f(p')). In that case, equation 1.40 describes a forced oscillator. The condition for coupling between the acoustic pressure and heat release rate leading to a positive feedback was first reported by Rayleigh [95]. “Rayleigh criterion” states that positive energy is transferred to the acoustic wave if the pressure fluctuation and heat release fluctuation are in phase. This integral form of the criterion is give below.

$$\int_0^V \int_0^{2\pi} p'\dot{q}'dtdv > 0 \qquad [1.32]$$

where $p'$and $\dot{q}'$ are the fluctuations in pressure and heat release rate respectively. The integration is carried out over the volume of combustion, V, and over one acoustic cycle.

However, it is to be noted here that the mechanism by which the acoustic wave modulates the heat release rate need not be always through pressure coupling. There are many other possible mechanisms [82]. These include

- Flame area oscillations induced by the acoustic acceleration
- Flame area oscillations induced by convective effects
- Equivalence ratio oscillations when the fuel is injected as a liquid

Chapter 2: Experiment: Theory and Apparatus

2.1 Experimental set-up

A schematic diagram of the experimental facility is shown in Figure 2.1. Propane and air flow were controlled using mass flow controllers because the required flow rates for propane and air are very small and it is difficult to control the flow rates manually. The flow controllers were remotely operated with the help of National Instruments Data Acquisition and Control box attached to the computer. Propane and air were premixed in the required ratio and fed to the combustor upstream of the combustion chamber. Combustion was started using spark electrodes placed at the center of the combustion chamber. A Bunsen burner was used for initial heat up of the combustor. Initial heating up of the combustor helps to reduce the amount of time required to reach the steady state for sustained combustion. Without this, the spark should be kept on for long enough time until the spark induced flame heats up the reactor sufficiently so that it preheats the reactants and sustains itself without the spark.

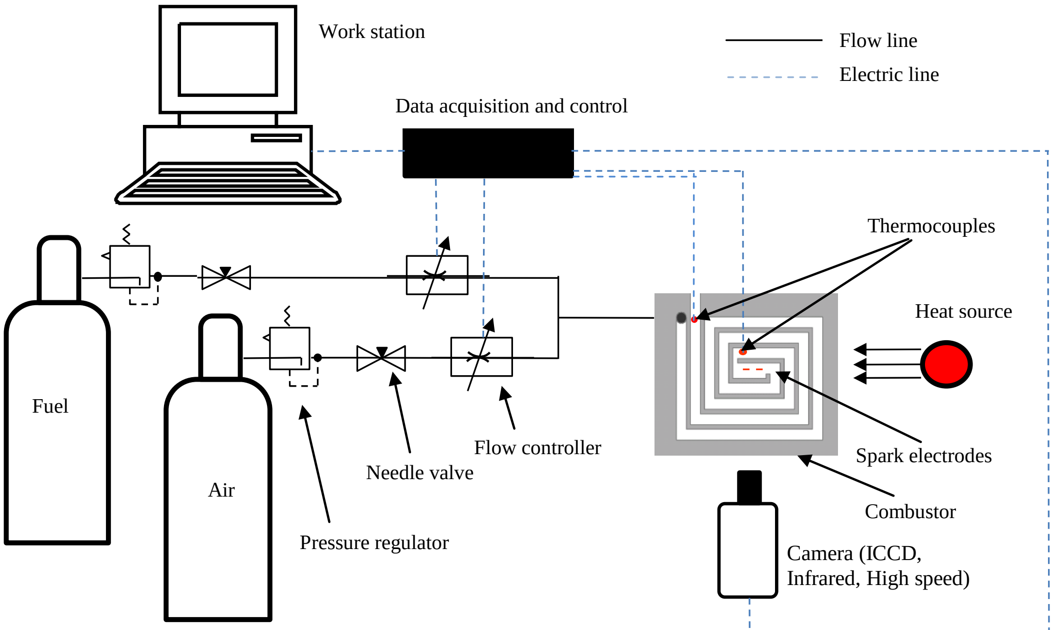

Figure 2.1 A schematic diagram of the experimental facility

2.2 Combustor fabrication

Combustor unit consists of a base material and an optical access window, which are held together by bolting two steel cover plates from both sides (see Figure). Quartz or calcium fluoride was chosen as the window material depending on the type of experiment. Four different materials were used for combustor base geometry fabrication; steel, aluminum, zirconium phosphate and macor. Table 2.1 provides details on the thermal conductivities of the materials discussed here. A three-axis micro CNC machine “Micro Mill” from “MicroProto Systems” (Figure 2.3) was employed for machining the meso-scale channels on to the base material. The machine has a high position increment resolution of 0.000125 inches and repeatability of 0.0005 inches. The G-code of the required geometry was written using “Mach 3” software, which was then fed to the milling machine through a controller. Of the four materials used, steel was the most difficult one to machine. Zirconium phosphate and macor are easily machinable ceramics.

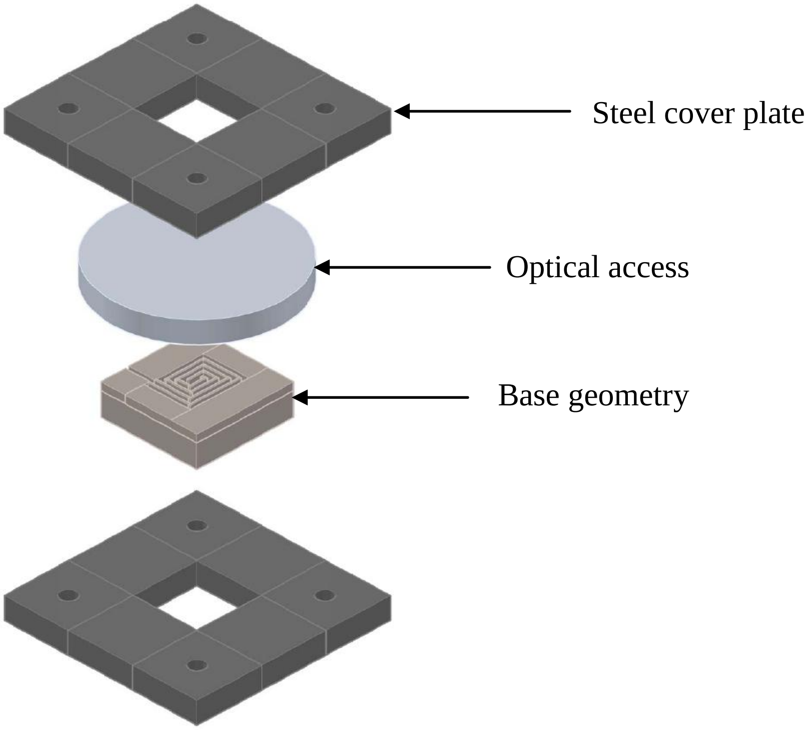

Figure 2.2 Combustor assembly

Table 2.1 Thermal conductivities of the different materials employed for the study

Material	Thermal conductivity (W/m/K)
Aluminum	202.4
Steel	16.27
Macor	1.46
Zirconium Phosphate	0.8
Calcium Fluoride	10
Quartz	1.4

Figure 2.3 Micro milling machine

2.3 Infrared Thermography

Thermal imaging of the combustor walls was carried out to determine the temperature distribution across the combustor surface. The infrared camera measures and images the emitted infrared radiation from the wall surface. The fact that radiation is a function of surface temperature makes it possible for the camera to calculate and display this temperature. The atmosphere has two bands of good transmission in the infrared range (i.e. short-wave band 2-5 nm and long-wave band between 8-14 nm). Most detectors and infrared (IR) cameras operate in the short-wave (SW) and long-wave (LW) regimes. The CCD and CMOS sensors used for visible light cameras are sensitive only to the nonthermal part of the infrared spectrum called near-infrared (NIR), but not to the part of infrared spectrum useful for thermal imaging (mid- and long-wavelength infrared). Most thermal imaging cameras use specialized focal plane arrays (FPAs) that respond to longer wavelengths. The most common types are InSb, InGaAs, HgCdTe and QWIP (Quantum well infrared photodetector) FPA. Their resolution is considerably lower than of optical cameras, mostly 160x120 or 320x240 pixels, up to 640x512 for the most expensive models. The infrared camera used in the present research is ThermaCAM SC 3000 from FLIR SYSTEMS, and the software is ThermaCAM Researcher 2001 (from FLIR).The technical specifications of the camera are:

- Sensor type: QWIP 320×240 pixels
- Field of view/minimum focus distance: 20°×15°/0.3 m
- Thermal sensitivity: 0.03 °C at 30 °C
- Spatial resolution (IFOV): 1.3 mrad

- Wavelength range: 8 – 9 μm

Figure 2.4 ThermaCAM SC 3000 from FLIR SYSTEMS

While performing flammability experiments, quartz window was used for optical access to the combustor. Since quartz will not allow the radiation in the range 8-9 microns to pass though, calcium fluoride window was used while performing thermal imaging. Calcium fluoride glass has good transmission in the range 0.2-9 microns [96]. The images presented here were captured at a frequency of 60 Hz, and they represent the average of 200 instantaneous images.

The radiation measured by the camera does not only depend on the object temperature but is also a function of its emissivity. The radiation that originates from the surroundings becomes reflected in the object. Moreover, radiation from the object and the reflected ambient radiation are influenced by the absorption in the atmosphere and in any external optics it passes through.

To measure temperature accurately, it is therefore necessary to compensate for the effects of a number of different radiation sources. The following object parameters must be supplied to the camera software:

- Emissivity
- Ambient
- Atmospheric temperature
- Distance
- Relative humidity of the air
- External optics transmission and temperature

Of the above parameters, emissivity is the most important. It is a measure of how much radiation is emitted from the object compared to that of it were a perfect blackbody. Normally, object materials and surface treatments exhibit emissivities ranging from approximately 0.1 to 0.95. Since emissivity of the ceramic materials which were employed in the present study is not available in literature, an alternative approach was used. A thermocouple was used to measure the wall temperature at a particular location. This temperature value was supplied to the corresponding location in the thermal image and the correct emissivity was calculated using the emissivity calculation function of ThermaCAM Researcher 2001. For the range of temperature measurements considered, the emissivity values of ceramics varied in the range 0.7-0.75.

2.4 Chemiluminescence imaging

Chemiluminescence is a non intrusive diagnostic method which has been widely used in combustion research because of the dependence of signal strength on fuel types, flow rate and equivalence ratio [97, 98]. Chemiluminescence is the radiation emitted from electronically excited molecules in the flame when these return to a lower energy state. The wavelength of radiation which is emitted is characteristic of the particular molecule and the particular transition the molecule undergoes. For some simple molecules, the spectrum exhibits one major peak and relatively few, weak secondary peaks. For complicated molecules, the radiation spectrum observed appears continuous. OH*, CH* and C2* are examples of molecules exhibiting a simple spectrum with major peaks, whereas CO2* is an example of a molecule with a radiation spectrum that appears continuous [97]. Chemiluminescence is intricately tied to the chemical kinetics that supports the combustion process. Chemiluminescence has therefore received renewed attention recently as a possible means of measuring unsteady heat release rate in unstable combustion systems [99, 100]. Also since the excited radicals especially the OH* is only observed in the reaction zone, can be employed as a flame marker [97, 98]. A reliable well understood measurement of chemiluminescence could provide quantitative insight into the details of the combustion process. Chemiluminescence measurement provides the ability to monitor the combustion system at a level of detail traditionally thought impossible.

2.5 High speed visual imaging

High-speed visual images of the flame were obtained to investigate the presence of flame fluctuations. The high-speed camera employed for the study was Photron Fastcam Ultima 1024, which is capable of recording up to 16,000 monochrome images per second. The maximum resolution of the camera is 1024×1024 pixels.

Figure 2.5 Photron Fastcam Ultima 1024

Photron Fastcam Ultima 1024 was employed for high speed flame imaging. After image acquisition further digital image processing has been applied to extract the flame dynamics with the intention of using the images (some examples can be found in figure 3) as a more quantifiable aid in understanding the combustion process. A two dimensional image of a flame can be regarded as an integration of the total light emission along the depth of the combustion chamber if an optical thin limit assumption is applicable. Image acquisitions were performed at a frequency of 4000 frames per second. Further increasing the frequency compromises the resolution of the camera and decreases the image contrast due to insufficient illumination of the sensor. Form the high speed images, time-resolved fluctuations of the total light emissions could be computed by integrating the entire grey-scale pixel values. The mean pixel intensity of each image was calculated by normalizing the total pixel value by the number of pixels in each image. A fast Fourier transform algorithm (FFT) was then applied to extract the frequency and amplitude information from the time-domain signals of the mean pixel intensity. The peak frequencies in the corresponding frequency spectrum represent the fluctuation frequencies of the flame.

2.6 Acoustic sampling

Acoustic measurements were performed using a microphone attached to “Terrasonde Audio Toolbox”. Sampling rate of the audio toolbox was higher than 40 kHz such that audio frequencies in the range of 20 Hz to 20 kHz could be acquired. The audio toolbox converts the time resolved voltage signal from the microphone to frequency spectra of sound pressure level (dB) using Fourier transform. Before starting the combustion experiments, background emissions were recorded to account for unwanted noise radiations. It was observed that noise emissions, with and without the presence of cold flow, had sound pressure levels below 60dB throughout the frequency spectra. However, flame acoustics can drive the sound levels at some particular frequencies to 90dB or above. The microphone was kept horizontally at a location of about six inches to the left side of combustor. It is to be noted here that the location of the microphone, although has some effect on the magnitude of sound pressure levels, did not affect the sound level distribution with respect to frequency. This was confirmed by acquiring data at different locations around the combustor.

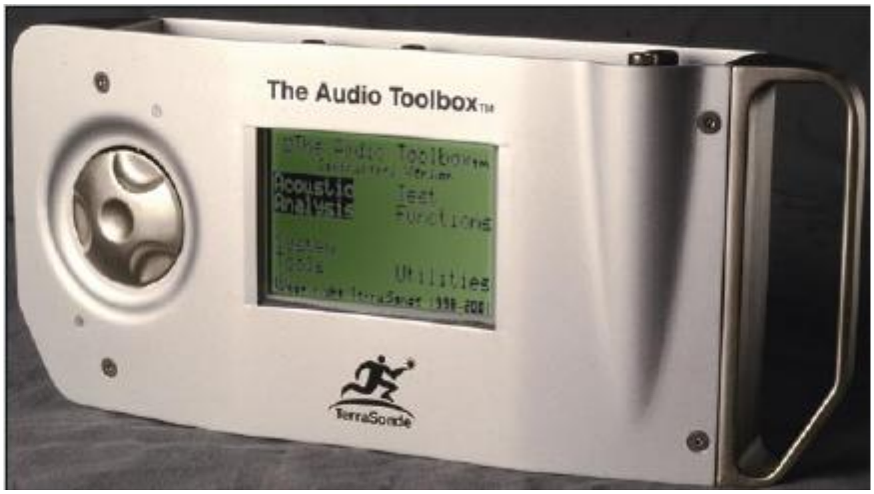

Figure 2.6 Terrasonde Audio Toolbox was employed for acoustic sampling

Chapter 3: Heat Recirculation

3.1 Heat exchanger theory and design

Heat exchangers are devices that are used to transfer thermal energy (enthalpy) between two or more fluids, between a solid surface and a fluid, or between solid particulates and a fluid which are at different temperatures. There are usually no external heat and work interactions. They find widespread applications in power generation, chemical processing, electronics cooling, air-conditioning, refrigeration and automotive industry. There are several different types of heat exchangers and are classified according to transfer processes, number of fluids, degree of surface compactness, construction features, flow arrangements, and heat transfer mechanisms [101]. For the present study, a recuperator type heat exchanger (in general recuperators are used to recover waste heat from exhaust gases of a heat engine to increase the overall efficiency) is employed and is operated in the counterflow mode. Based on its surface area density it can be classified as a compact heat exchanger and based on its construction it is a spiral heat exchanger.

Compact surface implies a large heat transfer surface area per unit volume of the heat exchanger, resulting in reduced space, weight, and energy requirements. A gas-to-fluid exchanger is referred to as a compact heat exchanger if it incorporates a heat transfer surface having a surface area density greater than 700 m^2/m^3 (or a hydraulic diameter less than 6 mm) for operating in a gas stream and greater than 400 m^2/m^3

operating in a liquid or phase-change stream [102]. In the present study, the surface area density of the heat exchanger is about 1920 m^2/m^3

The motivation for using compact surfaces is to gain specified heat exchanger performance, $Q/\Delta T_m$, within acceptably low mass and volume constraints.

The heat exchanger performance can in general be expressed as

$$\frac{Q}{\Delta T_m} = UA = U\beta V \qquad [1.33]$$

Here Q is the heat transfer rate, ΔT_m is the mean temperature difference, β is the surface area per unit volume and U the overall heat transfer coefficient. A is the area available for heat transfer and V is the heat exchanger volume. It is clear that the heat exchanger volume can be minimized by choosing high a degree of surface compactness. In addition to this, compact surfaces generally result in higher overall heat transfer coefficient U [101, 102] which helps further reduce the volume requirements.

3.1.1 Spiral Heat Exchangers

Amongst various forms of heat exchangers which are employed in industry, countercurrent spiral heat exchangers stand out due their high thermal performance, easy maintenance and compactness. Conventional spiral heat exchanger consists of two relatively long strips of sheet metal wrapped helically around a split mandrel to form a pair of spiral channels (Figure 3.1). These heat exchangers are commonly fabricated using carbon steel or stainless steel. Three different flow arrangements are usually employed:

1. both fluids in spiral counterflow

2. one fluid in spiral flow other in crossflow across the spiral
3. one fluid in spiral flow, the other in a combination of crossflow and spiral flow

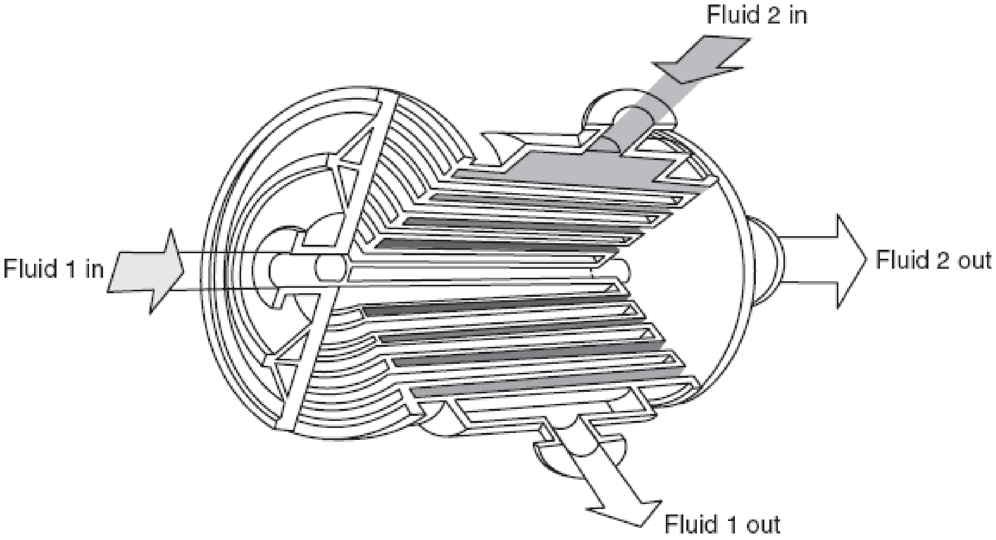

Figure 3.1 Conventional spiral heat exchanger. Adapted from [101]

The typical passage height is 5 to 25 mm with a surface compactness of up to 200 m^2/m^3 [101].

In industry, SHE is usually employed for applications such as pasteurization, gas cooling, condensing, heat recovery and effluent cooling. For sludge treatment, SHEs are generally smaller than other types of heat exchangers.

The advantages of this exchanger are as follows: Due to its wrapped cylindrical arrangement SHEs are amongst the most compact heat exchangers in the industry. The internal void volume is much lower (< 60%) than in a shell-and-tube exchanger. Hence it requires minimum installation space and servicing area. The curvature induced secondary flow effects result in turbulent flow conditions even at low Reynolds numbers and leads to enhanced heat transfer. SHEs are also self cleaning as the enhanced turbulence and shear due to the curved passages flush away deposits as they form.

3.1.2 Heat Exchanger Design

The goal of heat exchanger design is to relate the inlet and outlet temperatures, the overall heat transfer coefficient, and the geometry of the heat exchanger, to the rate of heat transfer between the two fluids.

Two commonly used approaches for heat exchanger design are the log mean temperature difference (LMTD) method [101] and the effectiveness-number of transfer units (ε-NTU) [101] method.

However, heat exchanger design theory employs several simplifying assumptions. Heat losses to or from the surroundings are often neglected. Longitudinal heat conduction in the fluids and in the wall is also usually not accounted for. These assumptions are adequate when used for designing conventional large scale heat exchangers. For applications, such as the present case, where heat losses and heat conduction in all directions are significant, the assumptions essentially render the conventional heat exchanger design theory ineffective.

3.2 Effect of longitudinal thermal conductivity

In a heat exchanger, since heat transfer takes place, temperature gradients exist in both fluids and in the separating wall in the fluid flow directions. This results in heat conduction in the wall and in fluids from the hotter to colder temperature regions, which may affect the heat transfer rate from the hot fluid to the cold fluid.

If a temperature gradient is established in the separating walls between fluid flow streams in a heat exchanger, heat transfer by conduction takes place from the hotter to colder region of the wall, flattens the wall temperature distribution, and reduces the performance of the exchanger.

For example, let us review typical temperature distributions in the hot fluid, cold fluid, and wall for a counterflow heat exchanger as shown in Figure 3.2.

Dashed lines represent the case of zero longitudinal heat conduction, and solid lines represent the case of finite longitudinal conduction. From the figure it is clear that longitudinal conduction in the wall flattens the temperature distributions, reduces the mean outlet temperature of the cold fluid, and thus reduces the exchanger effectiveness “from 90.9% to 73.1%. This in turn produces a penalty in the exchanger overall heat transfer rate

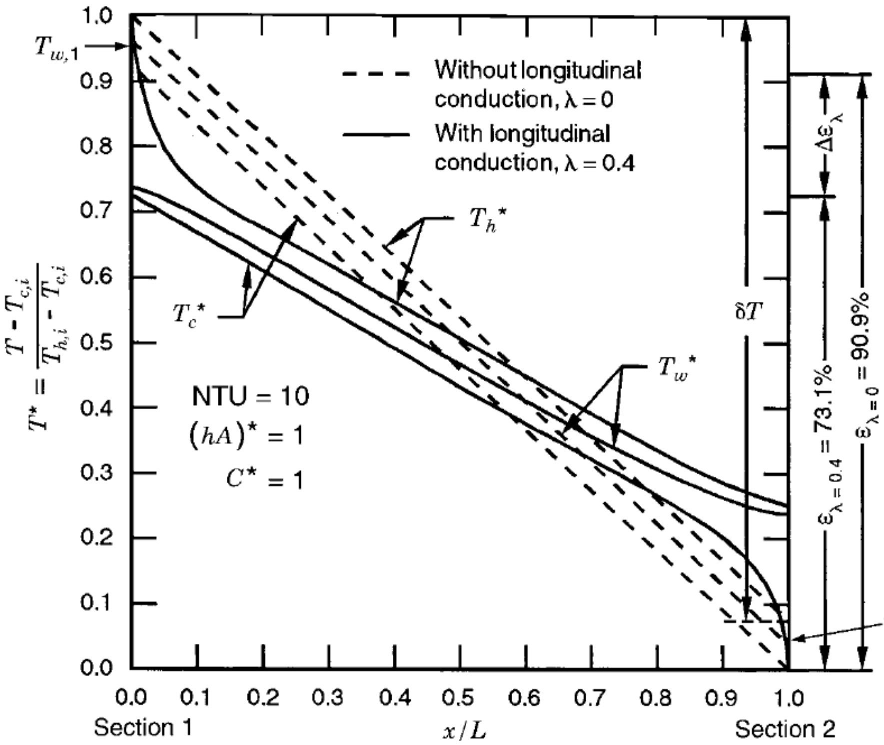

Figure 3.2 Fluid and wall temperature distributions in a counterflow exchanger having zero and finite longitudinal wall heat conduction. Adapted from [101]

3.3 Numerical simulation of counter flow heat exchanger

In the previous section we have seen that longitudinal conduction is detrimental for heat exchanger performance. Conduction in longitudinal direction can be minimized by decreasing the cross sectional area in the longitudinal direction, increasing the length of the heat exchanger or by decreasing the thermal conductivity of the walls. However, we cannot improve the exchanger performance by decreasing the thermal conductivity indefinitely since for zero thermal conductivity, there will be no heat transfer taking place in the heat exchanger. Hence there should be an optimum value for wall conductivity for which the heat exchanger performance will be maximized. It was mentioned before that existing heat exchanger design theories do not consider heat losses while evaluating performance. However, the effect of wall conductivity on exchanger performance and hence the optimum conductivity value is much dependent on the external heat transfer (loss) coefficient. This is crucial for designing meso-scale heat exchangers where external heat transfer coefficients can be very high [103]. In this section, results from numerical simulation of heat transfer in counter-flow rectangular heat exchanger performed using “Fluent 6.3.26” software will be presented. Simulations were carried out to determine the effects of wall thermal conductivity and external heat transfer coefficient on the heat exchanger performance. The 3-D geometry (Figure 3.3) was divided into 158500 structured cells. Grid size in all directions is 200 microns. 3-D simulations were employed mainly because the ‘shell conduction’ option in “Fluent” which accounts for heat conduction inside the walls in all directions is only available for 3-D cases. The rectangular flow paths have the same aspect ratio as the channels of the meso-scale combustors investigated experimentally. The length of the heat exchanger is similar to the length of preheating channel of the combustor shown in Figure 4.2.

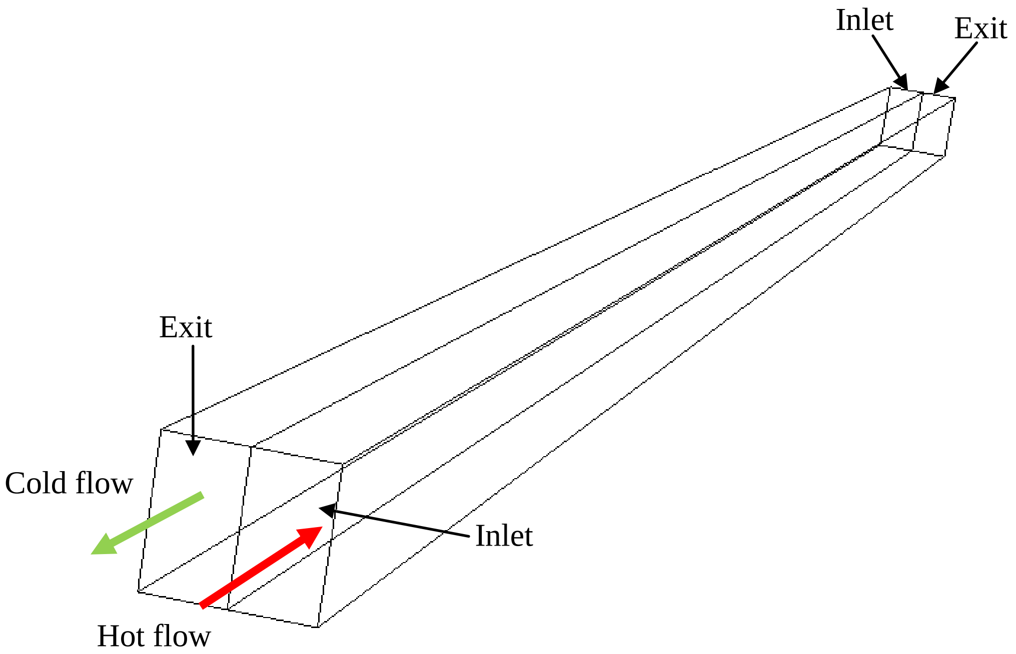

Figure 3.3 Counterflow heat exchanger

The input flow conditions are,

inlet Reynolds number = 300 (typical inlet Reynolds number for meso-scale combustors)

inlet temperature of hot flow = 1200 K

inlet temperature of cold flow = 300 K

Four different external heat transfer coefficients were considered (0, 1, 200 and 400 W/m^2/K). For the above set of input conditions, thermal conductivity was varied to achieve optimum performance. Simulations were performed for laminar flow since Reynolds number involved is quite low. Air was chosen as the working fluid for both cold and hot flows. Incompressible ideal gas properties were assumed. Viscosity, specific heat, gas thermal conductivity and wall thermal conductivity were assumed to be temperature independent. Convergence was assumed when the residuals of continuity and energy equations were below 10^{-10} and the mass weighted average of the hot flow and hot flow exit temperatures ceased to change.

3.3.1 Cold flow exit temperature

Cold flow exit temperature or the temperature at the cold flow outlet reported here, is the mass weighted average of temperature at the cold flow exit. It is a direct measure of the performance of the heat exchanger such that for a given set of input condition, the heat exchanger with the highest cold flow exit temperature can be considered to have the best performance. Figure 3.4 shows the cold flow exit temperature variation with respect to wall thermal conductivity for different heat transfer coefficients. As excepted, an optimum performance condition was observed for each heat transfer coefficient. For adiabatic walls and lower heat transfer coefficients (0, 1 W/m^2/K), the optimum performance occurs at wall conductivity of 1 W/m/K. However, as the heat transfer coefficient is increased to 400 W/m^2/K, which is a more realistic value in the meso-scale, the optimum conductivity value decreases to 0.04 W/m/K, which is closer to the thermal conductivity of air. What this implies is that, choosing low thermal conductivity ceramics (< 1W/m/K) as the heat exchanger material in meso-scale applications can improve the performance considerably. This is in contrary to that predicted by the existing heat exchanger design theories, since they do not account for the heat losses.

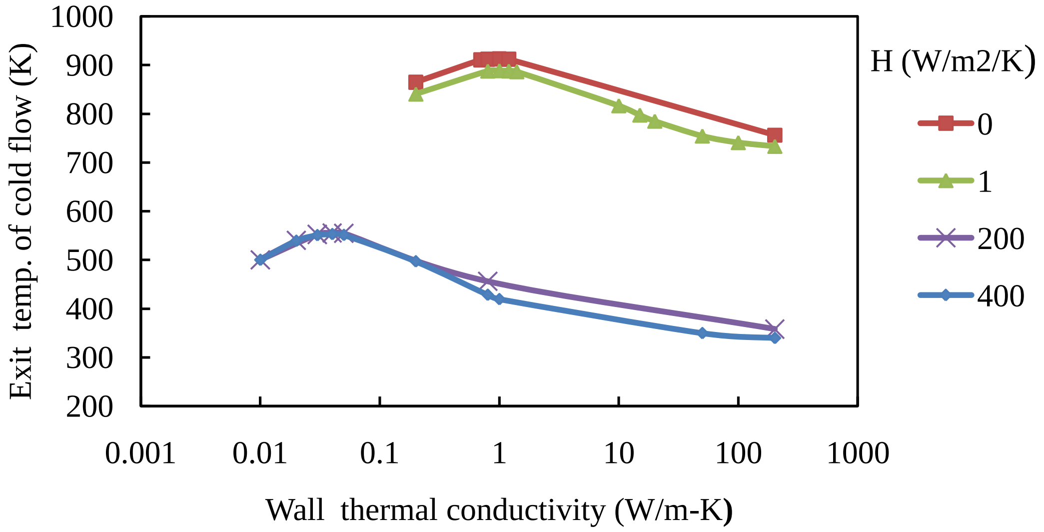

Figure 3.4 Cold flow exit temperature v/s wall thermal conductivity at various external heat transfer coefficients (H)

3.3.2 Hot flow exit temperature

Hot flow exit temperature reported here is the mass weighted average of temperature at the hot flow exit. Variation of hot flow exit temperature with conductivity is shown in Figure 3.5. For adiabatic and low heat transfer coefficient cases, the hot flow exit temperature has a strong dependency on conductivity throughout the range of conductivity values investigated. However, for higher heat transfer coefficient, the effect is significant only for values less than 1 W/m/K. Temperature remained almost a constant for conductivity values greater than 1 W/m/K.

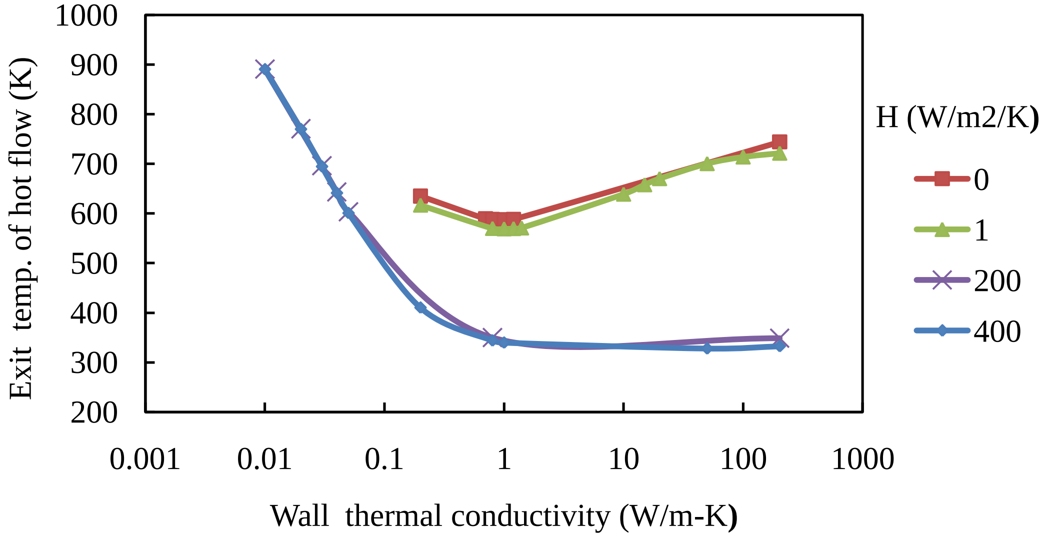

Figure 3.5 Hot flow exit temperature v/s wall thermal conductivity at various external heat transfer coefficients (H)

3.3.3 Heat loss

Figure 3.6 shows the variation of heat loss rate (as a percentage of input power) with respect to thermal conductivity. Clearly for H= 1/W/m^2/K there is negligible heat loss (~ 3%) and it is almost a constant throughout the range of conductivity values. For higher heat transfer coefficients, the effect is significant only for low thermal conductivities (< 1 W/m/K).

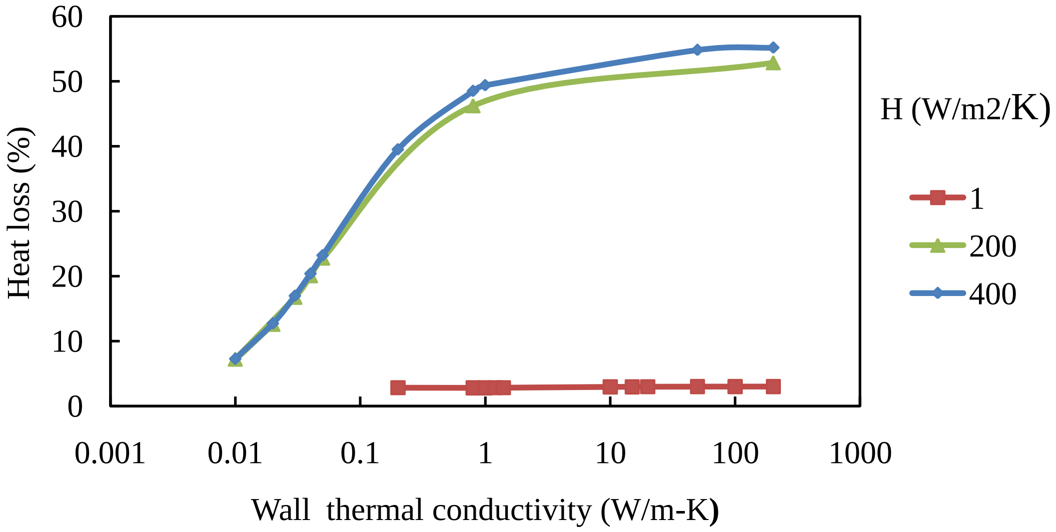

Figure 3.6 Heat loss (%) v/s wall thermal conductivity at various external heat transfer coefficients (H)

3.3.4 Discussion

From the above results it is clear that the effect of thermal conductivity on heat exchanger performance is much dependent on the external heat transfer coefficient. For the particular geometry considered, the variation in performance parameters (exit temperatures, heat loss) with conductivity at realistic external heat transfer coefficients (200-400 W/m^2/K), was more pronounced for lower conductivity values (< 1 W/m/K). For higher conductivity values, the performance parameters remained almost a constant. This is because, as the conductivity goes up, the rate of conductive heat transfer occurring inside the heat exchanger walls is much faster than the three convective heat transfer rates involved (hot flow to wall, wall to cold flow, and wall to surroundings). For such conditions, the heat exchanger behaves like a lumped body with a near-uniform wall temperature distribution.

3.4 Numerical simulations of spiral heat exchangers

In the previous section, the effect of thermal conductivity and heat transfer coefficient on the performance of a counter flow heat exchanger with straight channels was elaborated. However, in the present study, heat exchanger with spiral channels is employed for meso-scale combustor development. Hence it is important to determine the performance characteristics of meso-scale spiral heat exchangers with respect to various design and operational parameters like wall thermal conductivity, Reynolds number and heat transfer coefficient. There are several analytical models, correlations and design methods available for macro-scale spiral heat exchanger design [104-110]**.** Owing to the higher outer surface area to volume ratio of the small scale spiral heat exchanger, heat losses and the three dimensional thermal conduction inside the material have a very significant effect on its overall heat transfer as compared to the macroscopic counterpart. But there is a non availability of analytical models and correlations which consider the above two factors and which could be used for the sizing of meso-scale spiral heat exchangers. For the optimization of the heat exchanger it is very important to know the effects of several design parameters on its performance. The present section describes the numerical investigation performed to determine the effect of heat exchanger geometry, flow Reynolds number, thermal conductivity of the material and external heat transfer coefficient on the performance of meso-scale spiral heat exchangers.

The two specific geometries considered here are the Archimedean double spiral and the Rectangular double spiral. The two materials chosen for the detailed examination are aluminum (0.8 W/m/K) and zirconium phosphate (202.4 W/m/K).

1. Archimedean SHE made of aluminum (herein referred as: Arc-Al)
2. Archimedean SHE made of zirconium phosphate (herein referred as: Arc-Zirc)
3. Rectangular SHE made of aluminum (herein referred as: Rec-Al)
4. Rectangular SHE made of zirconium phosphate (herein referred as: Rec-Zirc)

The typical heat transfer paths inside a spiral heat exchanger are shown in the Figure 3.7. In a meso-scale SHE the relative heat transfer rates through each path vary significantly for various conditions making it difficult to predict its performance. A good heat exchanger will be one which offers least resistance to heat transfer to the cold flow and at the same time has a high resistance to heat transfer to the ambient. To compare the SHEs, five different performance parameters were investigated. These include: exit temperatures of the hot and cold flows, the percentage rate of heat loss to the ambient through the outer walls, the percentage rate of heat transfer to the cold flow and the percentage rate of heat loss of the hot flow. Here the percentage rates are defined with respect to the rate of enthalpy input due to the hot flow at its inlet. Also the exit temperatures mentioned here are mass weighted average temperatures.

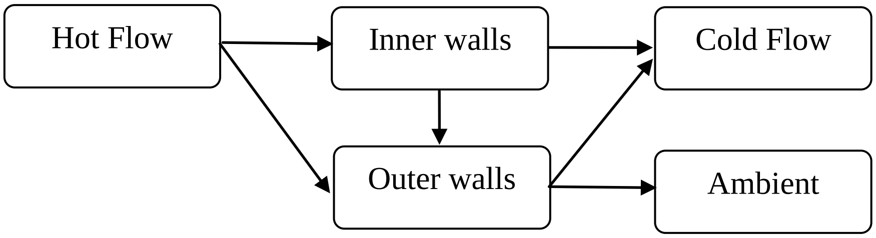

Figure 3.7 Heat transfer paths inside a spiral heat exchanger (It is possible for the heat to flow in the opposite direction of the arrow in some particular cases, for example, between outer walls and cold flow)

3.4.1 Exchanger Geometries

The specific geometric feature considered here was the type of spiral; Archimedean and rectangular. The two geometries considered are shown in Figure 3.8**.** The dimensions chosen were similar to that of meso-scale combustor A which was successfully developed for propane-air combustion, see Figure 4.2. The spiral channels had rectangular cross-section. The channel wall thickness, channel depth, channel width and outer wall thickness were kept the same for both the geometries. The channel aspect ratio and thicknesses do affect the heat transfer properties significantly. But to simplify the problem only the effect of the shape of the spiral is investigated here. The respective wetted surface areas of hot and cold flows were kept similar for the spirals. This was performed to achieve comparable inner heat transfer areas for both the spirals so that the resulting difference in heat transfer properties would only emanate from the type of flow field. Similar areas were achieved by performing a simultaneous minimization (with the aid of Matlab Optimization tool box) of differences between the respective hot and cold fluid wetted areas of the spirals. Rectangular SHE had two turns. To achieve similar areas the Archimedean spiral had to have higher number of turns (2.36 turns).

After minimization, the Archimedean SHE had 1.57% higher hot flow wetted surface area, 1.59% lower cold surface wetted area, 2.52% lower outer surface area and 1.76% lower material volume than the rectangular SHE.\

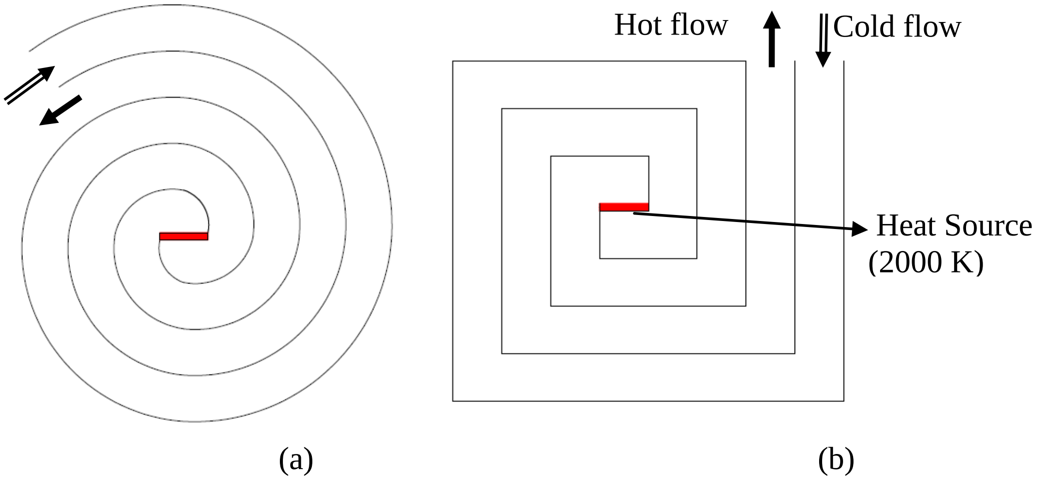

Figure 3.8 Geometry of the spiral heat exchangers (SHE). (a) Archimedean double spiral (2.36 turns), (b) Rectangular double spiral (2 turns)

3.4.2 Test matrix and simulation assumptions

In a real combustor-heat exchanger arrangement the combustion chamber will be located in the center of the double spiral heat exchanger. The hot flow through the heat exchanger will comprise of the combustion products and cold flow will be the premixed reactants. These two flows will have different thermodynamic properties based on their composition and temperature. The inlet temperature of the hot flow is the combustion temperature which is not a constant. It is extremely sensitive to the amount of heat losses, amount of preheating (heat transferred to the cold flow), mass flow rate, amongst other parameters. Since our goal is to characterize the heat exchanger, and not combustion, simulations were performed on non-reacting flow. Several simplifying assumptions were imposed so as to determine the effect of only a few key parameters. Air was chosen as the working fluid for both cold and hot flows. Incompressible ideal gas properties were assumed. Temperature independent viscosity, specific heat and thermal conductivity were assumed. Wall thermal conductivity value was also kept temperature independent. Structured grids were used for both the geometries. 3-D grid was used primarily because the wall thermal conduction model is available only for 3-D cases in the simulation code used here (Fluent). Another reason was that the flow through spiral geometries with rectangular cross-section is inherently three dimensional in nature. It could be considered as comprising of primary and secondary flows. Primary flow is the flow that occurs along a channel. Secondary flow is the flow across the channel. It is known from literature that these secondary flows affect the heat transfer coefficient significantly [111]. Only laminar flow cases were considered here because most of the meso-scale combustors work in the laminar flow regime [4]**.** To simulate the hot flow inlet a constant temperature (2000 K) source was kept at the center of the heat. The heat exchanger was operated in the counterflow mode. The hot flow starts from the center and exits the heat exchanger at its periphery. Cold flow starts at the periphery of the heat exchanger and exits just before the constant temperature source in the center. The cold flow inlet temperature was held at 300 K for all cases.

Convergence was assumed when the residuals of continuity and energy equations were below 10^{-10} and the mass weighted average of the hot flow exit temperature ceased to change.

The test matrix used for the simulations is shown in Table 3.1. Simulations were performed for three different Reynolds numbers and for four different external heat transfer coefficients. In all 48 cases were examined from the various combinations in simulations. Although a wide range of heat transfer coefficients were used, in real mesoscale combustors, external heat transfer coefficients are in the range 200-400 W/m^2/K [103]. The Reynolds number presented in this paper is the inlet Reynolds number for both hot and cold flows calculated with respect to the hydraulic diameter of the rectangular inlet.

Table 3.1 The test matrix

Geometry	**Material Thermal conductivity (W/m-K)**	**External Heat Transfer Coefficient (W/m^2-K)**	**Inlet Reynolds Number**
Archimedean SHE	202.4 (Aluminum)	0	300
Rectangular SHE	0.8 (Zirconium phosphate)	50	500
		200	700
		400	

3.4.3 Results and discussion

The heat transfer performance parameters are plotted with respect to external heat transfer coefficients for different Reynolds numbers (Figures 3.9-3.13**)** and with respect to Reynolds numbers for different external heat transfer coefficients (Figures 3.14-3.18). The variations observed in these parameters can be attributed to the SHE geometry, material thermal conductivity, external heat transfer coefficient and the inlet Reynolds number. The effects of each parameter are discussed below. Pressure drop across the channels was dependent only on the flow rate or the Reynolds number. Rectangular SHE had a higher pressure drop due to its sharp turns but the difference is negligible (Figure 3.19). The following nomenclature is used in all the figures.

- Arc-Al = Aluminum heat exchanger with Archimedean spiral geometry
- Arc-Zirc = Zirconium phosphate heat exchanger with Archimedean spiral geometry
- Rec-Al = Aluminum heat exchanger with rectangular spiral geometry
- Rec-Zirc = Zirconium phosphate heat exchanger with rectangular spiral geometry

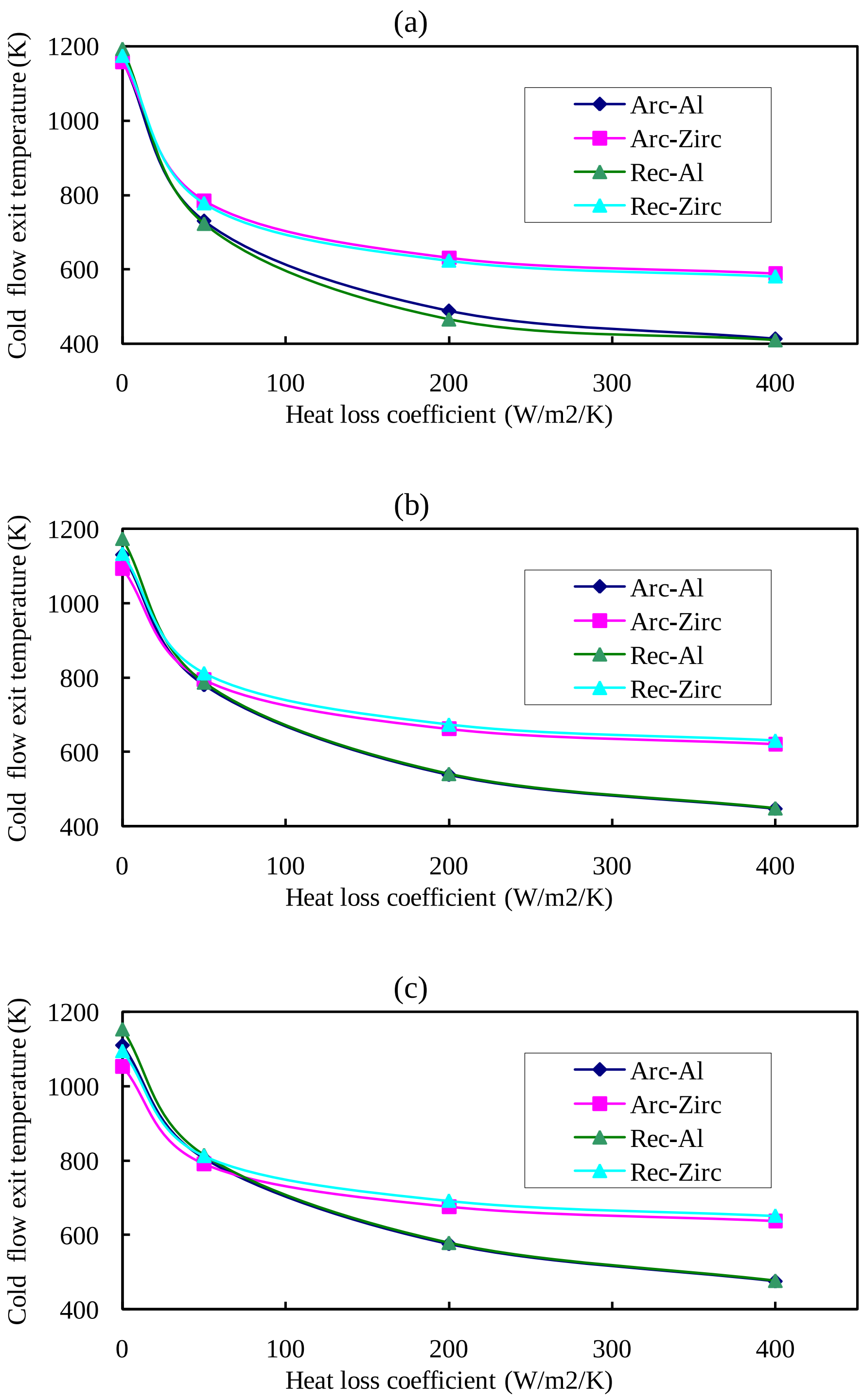

Figure 3.9 Variation of cold flow exit temperature with external heat transfer coefficient for three different inlet Reynolds numbers (a) Re = 300, (b) Re = 500 and (c) Re = 700

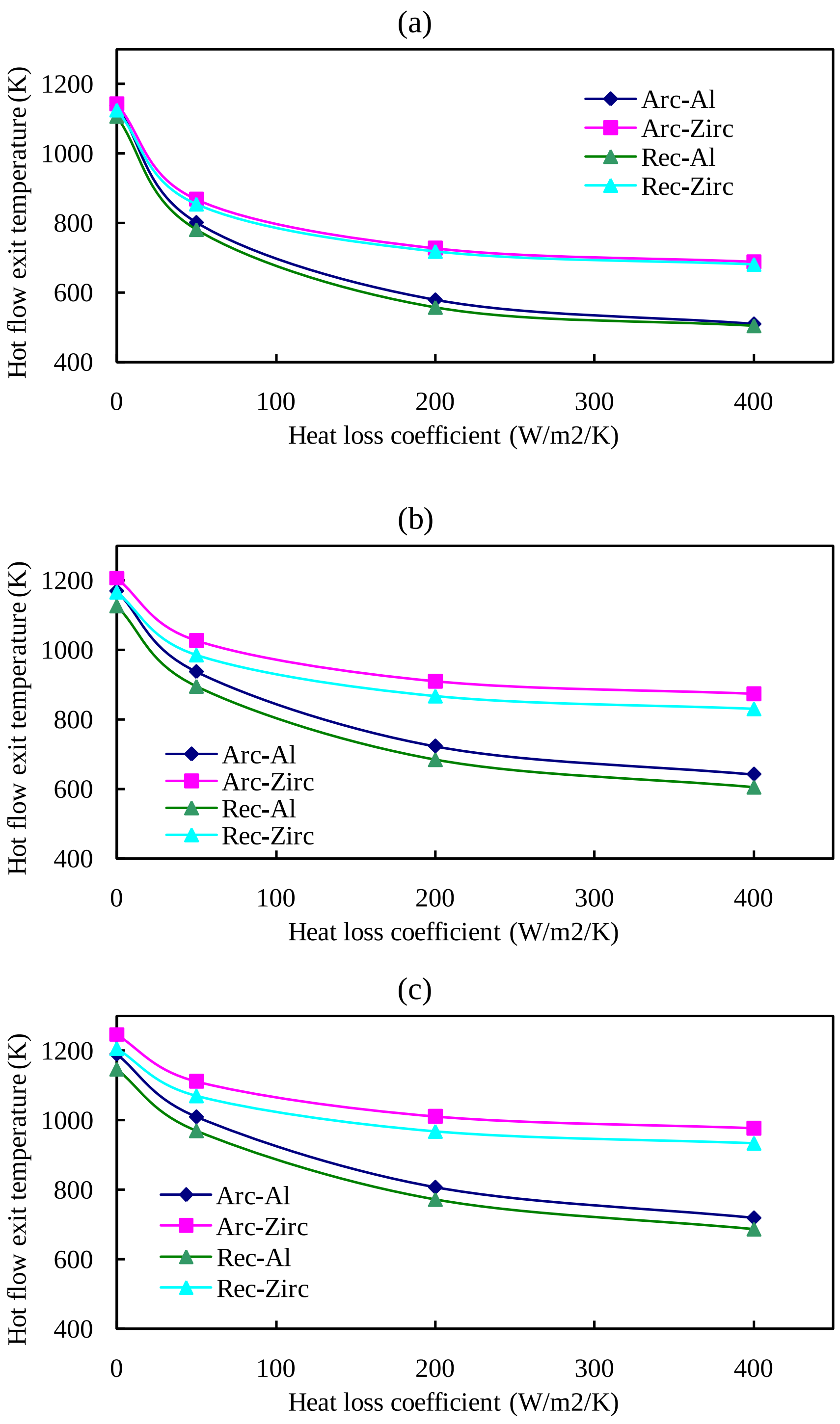

Figure 3.10 Variation of hot flow exit temperature with external heat transfer coefficient for three different inlet Reynolds numbers (a) Re = 300, (b) Re = 500 and (c) Re = 700

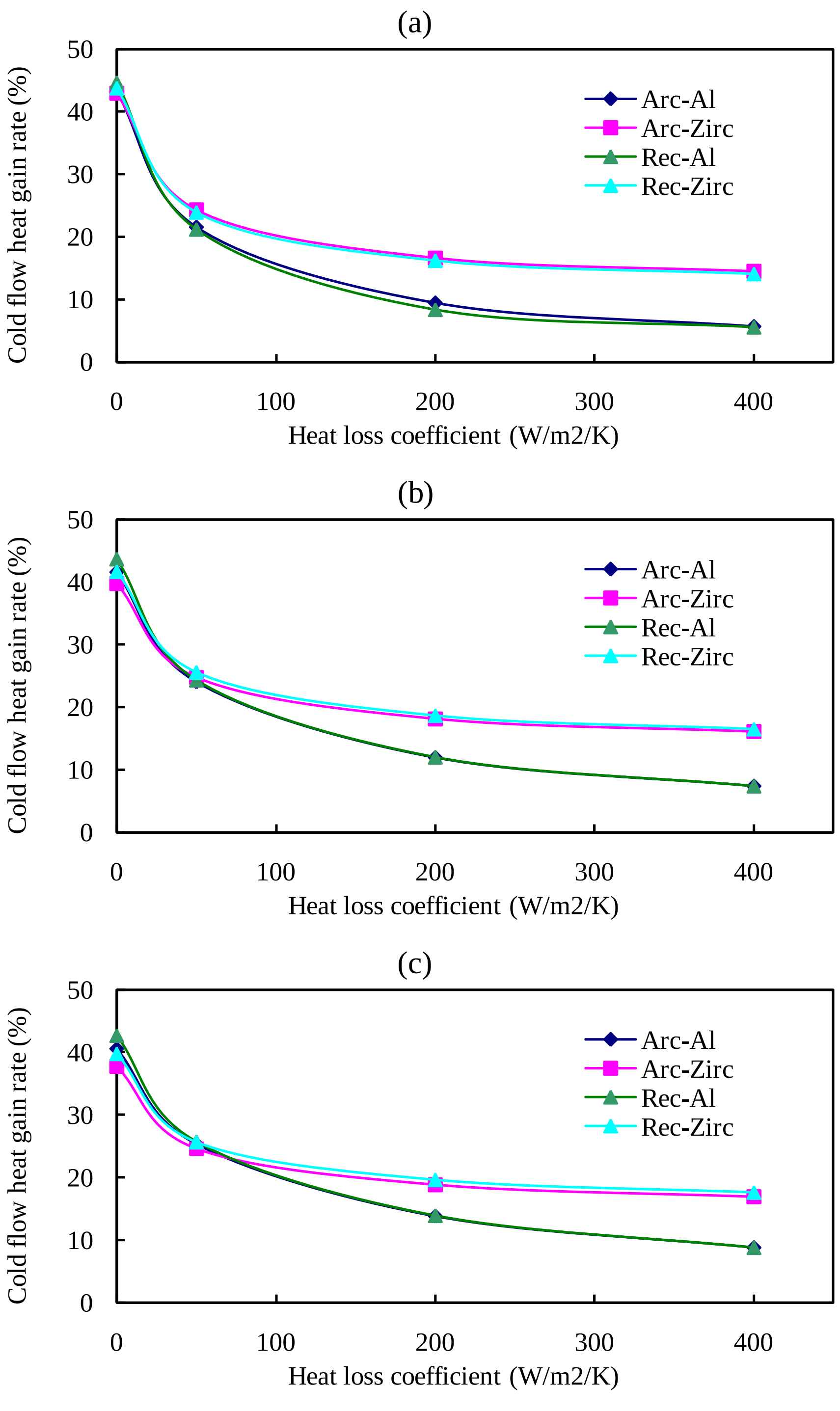

Figure 3.11 Variation of cold flow heat gain rate (%) with external heat transfer coefficient for three different inlet Reynolds numbers (a) Re = 300, (b) Re = 500 and (c) Re = 700

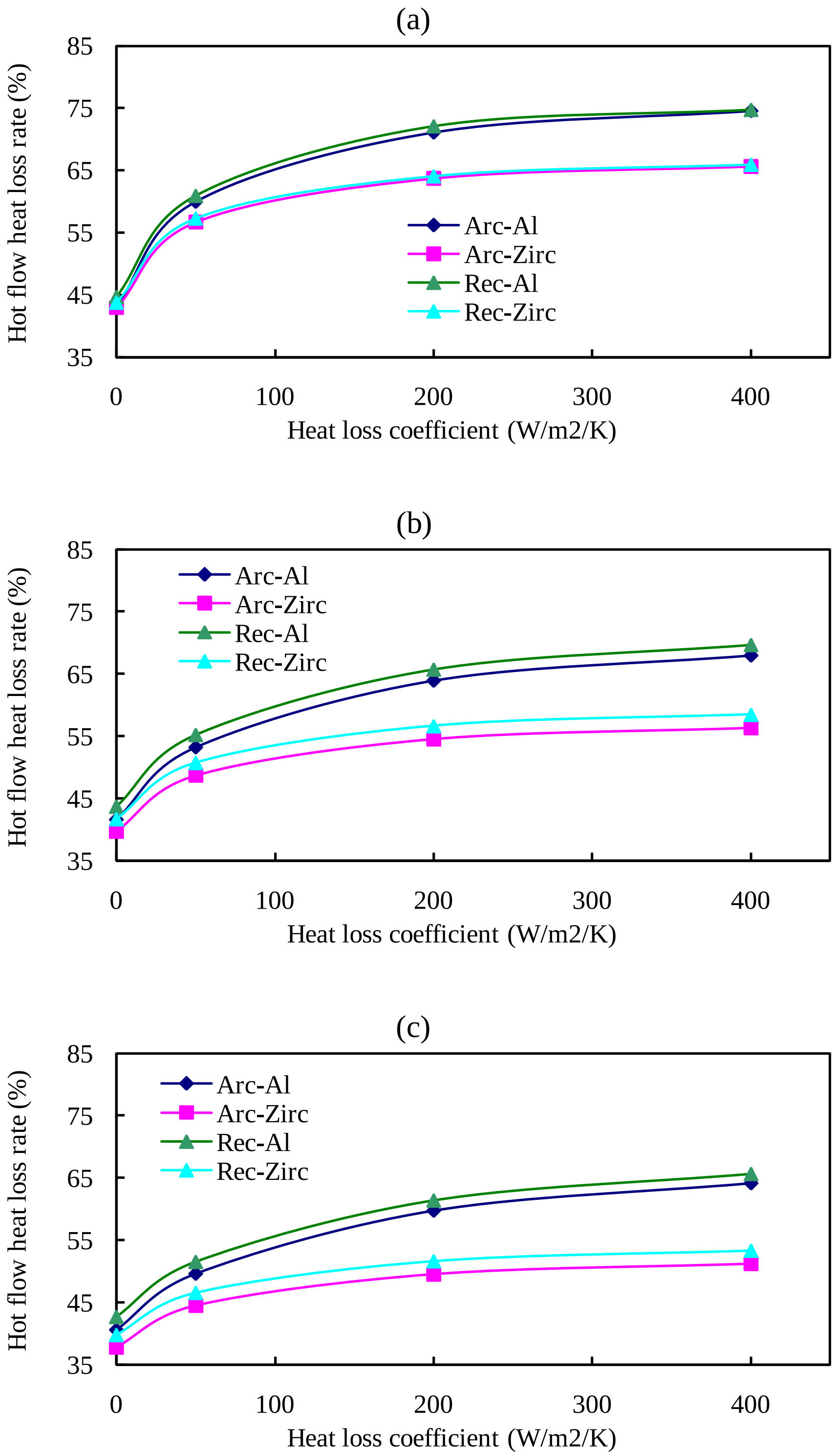

Figure 3.12 Variation of hot flow loss rate (%) with external heat transfer coefficient for three different inlet Reynolds numbers (a) Re = 300, (b) Re = 500 and (c) Re = 700

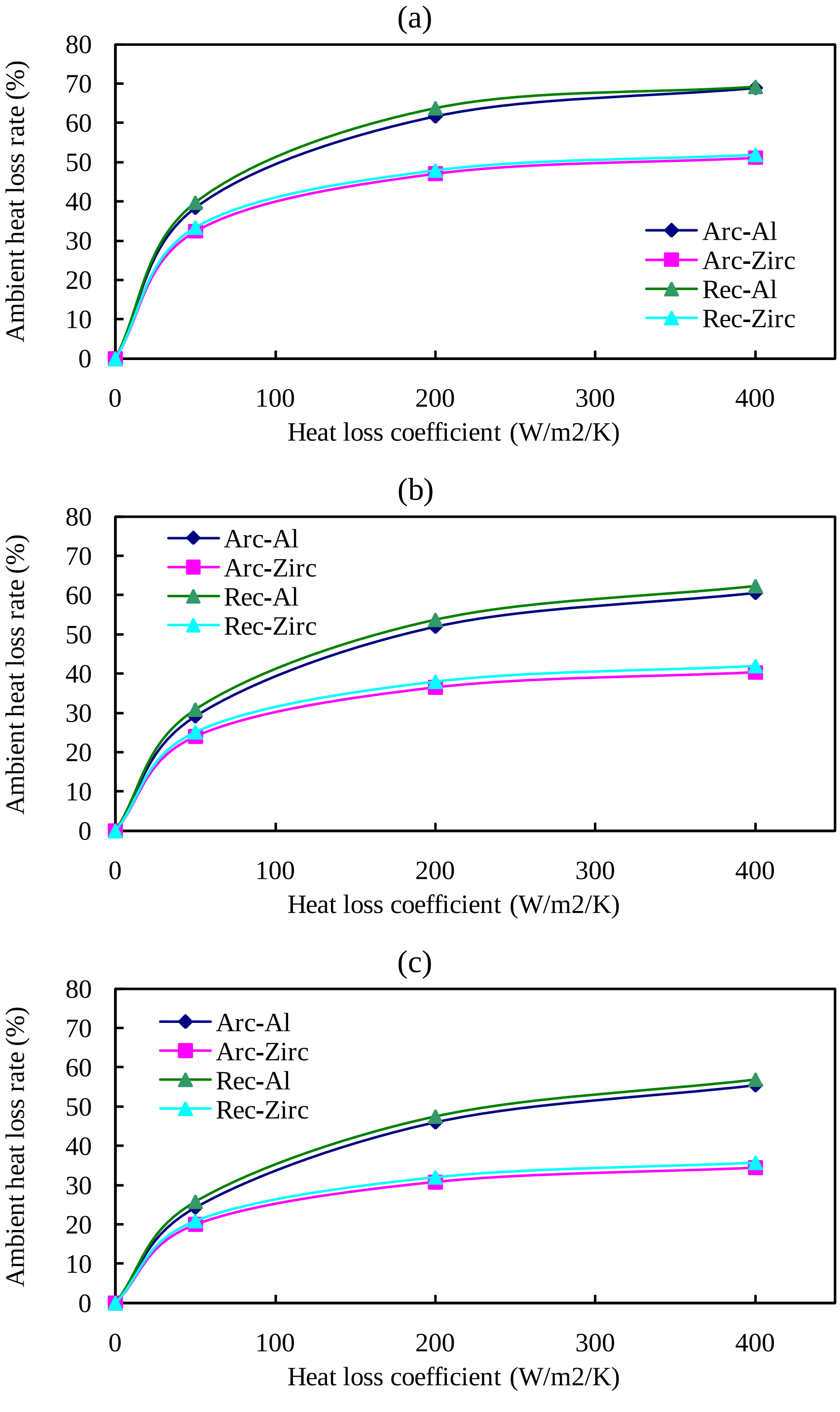

Figure 3.13 Variation of ambient heat loss rate (%) with external heat transfer coefficient for three different inlet Reynolds numbers (a) Re = 300, (b) Re = 500 and (c) Re = 700

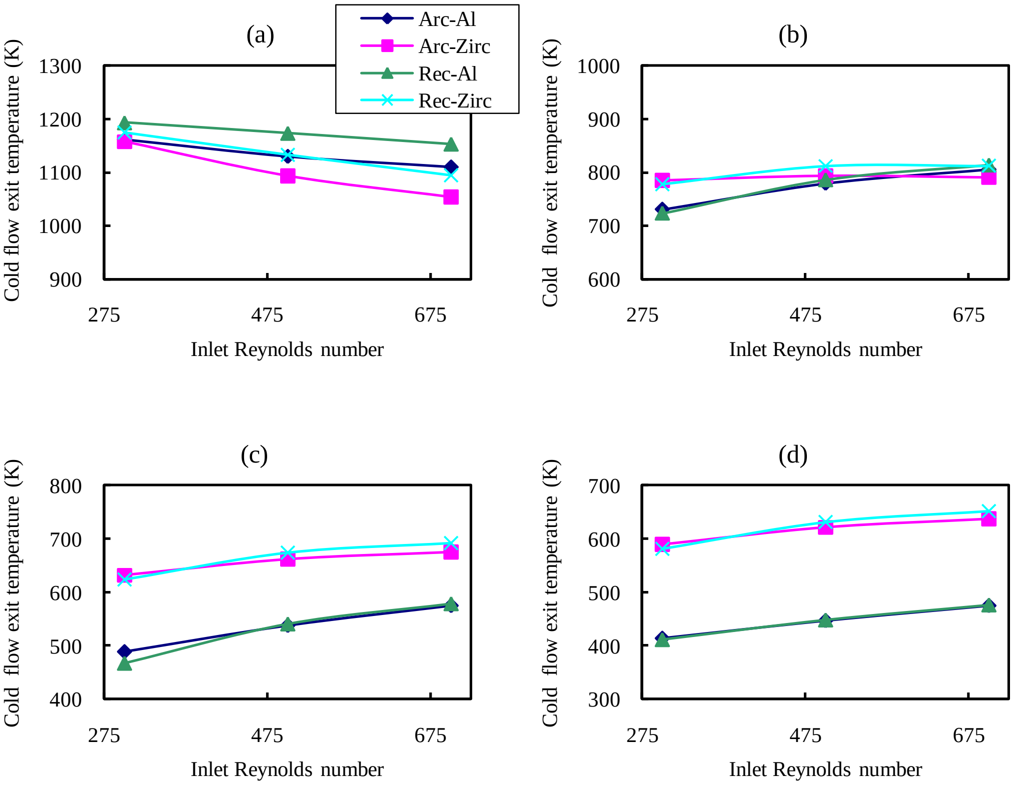

Figure 3.14 Variation of cold flow exit temperature with inlet Re for four different external heat transfer coefficients (W/m^2/K) (a) 0, (b) 50, (c) 200 and (d) 400

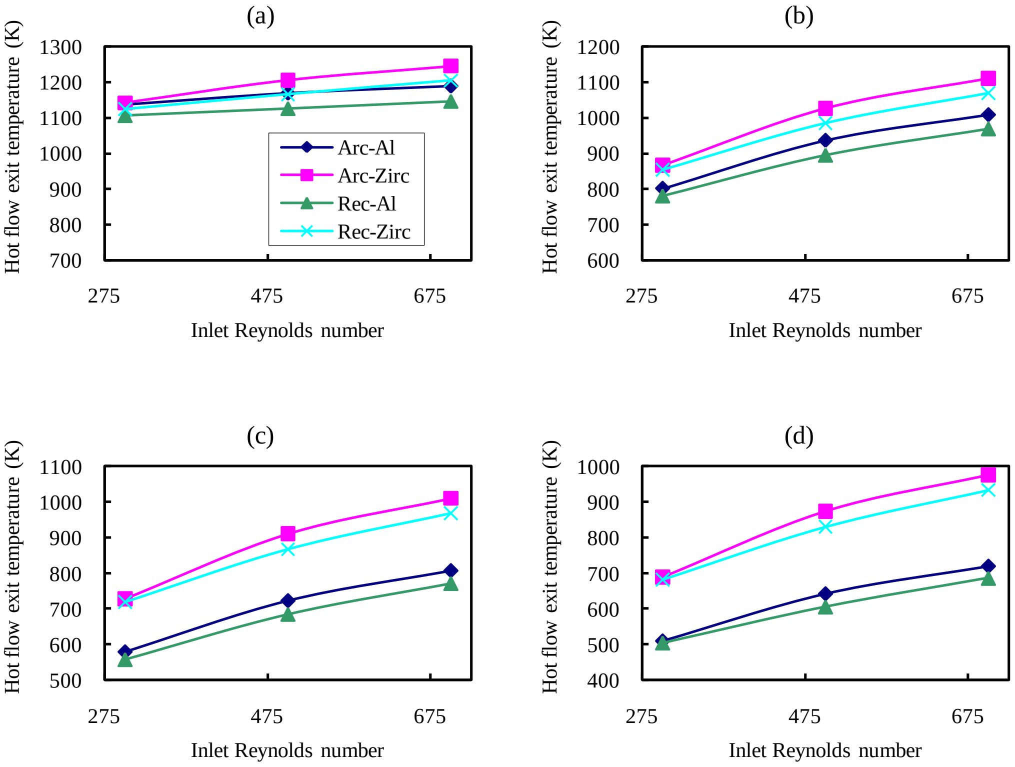

Figure 3.15. Variation of hot flow exit temperature with inlet Re for four different external heat transfer coefficients (W/m^2/K) (a) 0, (b) 50, (c) 200 and (d) 400

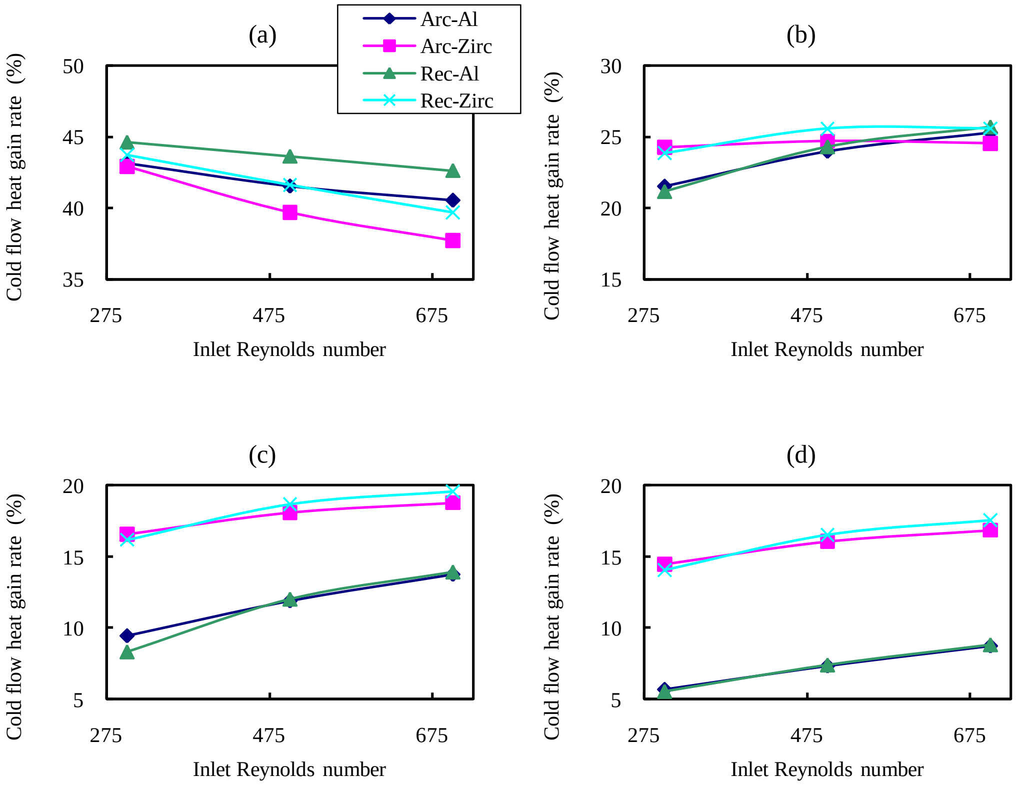

Figure 3.16 Variation of cold flow heat gain rate (%) with inlet Re for four different external heat transfer coefficients ($W/m^2/K$) (a) 0, (b) 50, (c) 200 and (d) 400

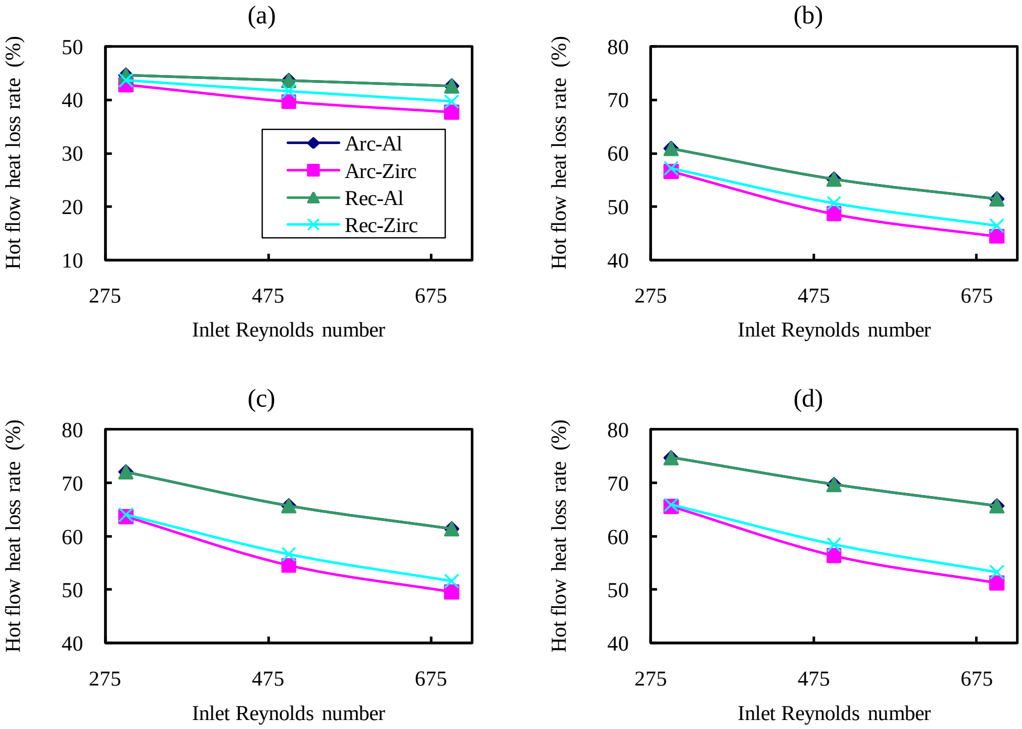

Figure 3.17 Variation of hot flow heat loss rate (%) with inlet Re for four different external heat transfer coefficients (W/m^2/K) (a) 0, (b) 50, (c) 200 and (d) 400

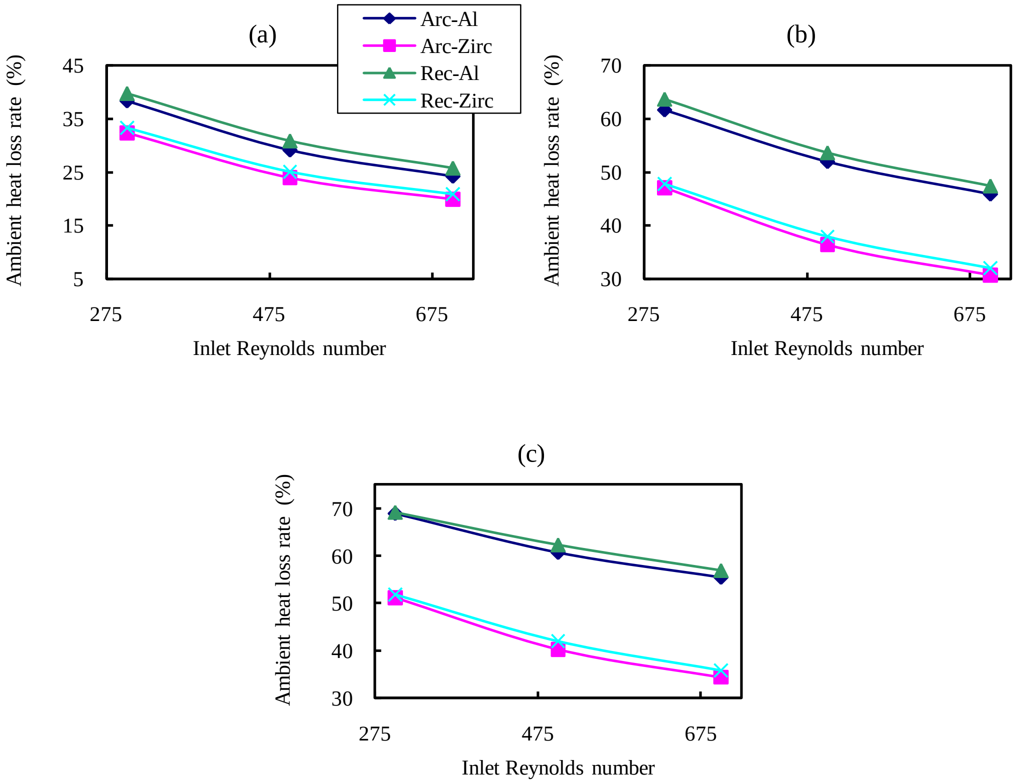

Figure 3.18 Variation of ambient heat loss rate (%) with inlet Reynolds number for three different external heat transfer coefficients (W/m2/K) (a) 50, (b) 200 and (c) 400

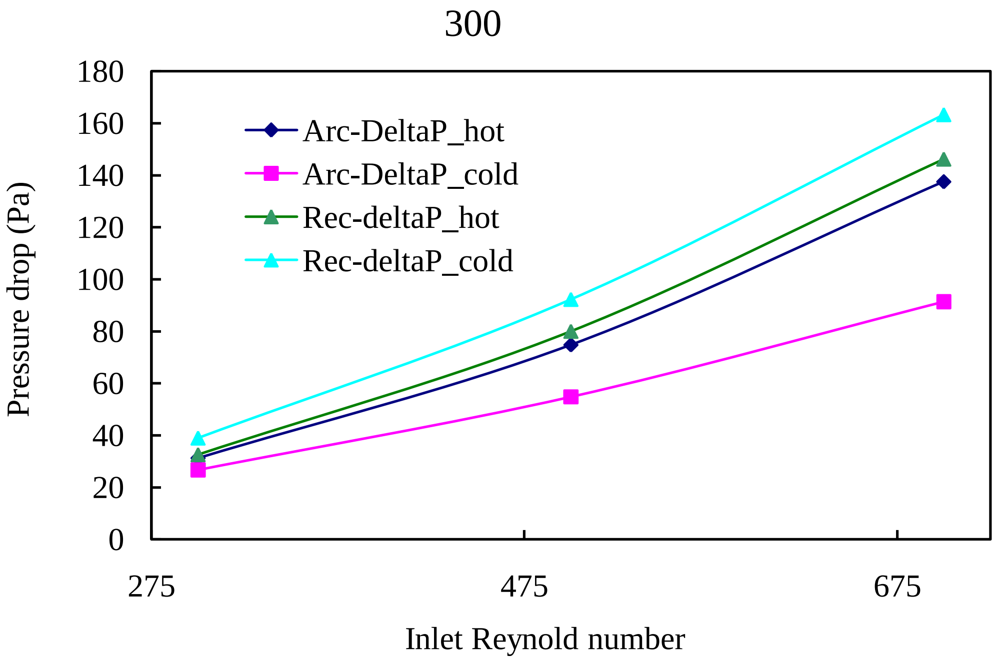

Figure 3.19 Pressure drop in the hot and cold flow sections of the two SHEs (only depends on Reynolds number and geometry)

3.4.3.1 Effect of the external heat transfer coefficient

For a given inlet Reynolds number the heat transfer characteristics (exit temperatures, heat transfer rates) of all the four different heat exchangers showed similar trends with respect to the heat transfer coefficient (Figures 3.9, 3.10, 3.11, 3.12 and 3.13**).** The trends observed were similar for different Reynolds number cases also. In general the cold flow exit temperature was found to asymptotically decrease with increase in heat transfer coefficient. The same was true for the hot flow exit temperature. These trends are easy to understand if the heat transfer rate plots shown in Figures 3.11, 3.12 and 3.13 are considered. As the heat transfer coefficient increases the total heat loss rate of the hot flow increases. The heat lost from the hot flow is distributed to the cold flow and the surroundings in an unequal manner as the heat transfer coefficient increases. Clearly, ambient heat loss increases with heat transfer coefficient because increase in heat transfer coefficient is analogous to reduction in the resistance to the heat transfer to the surroundings. Therefore with an increase in heat transfer coefficient, the percentage of ambient heat loss rate increases and that of cold flow heat gain decreases.

From the trends, it can be inferred that an increase in heat transfer coefficient results in the exit temperatures to asymptotically approach the ambient temperature. The total heat loss rate and the ambient heat loss rate are asymptotically approaching the heat input rate and the cold flow heat gain rate is asymptotically approaching zero. Therefore for better performance of the heat exchanger a reduction in heat transfer coefficient from 200W/m^2/K to 100W/m^2/K is much more beneficial than that from 300W/m^2/K to 200W/m^2/K.

3.4.3.2 Effect of the Inlet Reynolds number

The inlet Reynolds number has a varied effect on the heat transfer characteristics (exit temperatures, heat transfer rates) at different heat transfer coefficients. For the adiabatic boundary wall condition the cold flow exit temperature was found to decrease with inlet Reynolds number (Figure 3.14.a**)**. But as the heat transfer coefficient increases the temperatures gradually start to increase with Reynolds number (Figure 3.14. b, c and d**)**. Hot flow exit temperatures were found to increase with Reynolds numbers for all the heat transfer coefficients (Figure 3.15**)**. It is clear that the percentage of hot flow heat loss rate decreases with increase in Reynolds number. The same is the case for the ambient heat loss rate percentage. But the cold flow heat gain rate percentage was observed to increase with increase in

Reynolds number for all cases except for the adiabatic case (Figure 3.16). It could be inferred that in general the percentage heat transfer rate from the hot flow to the cold flow and the surroundings decreases with increase in Reynolds number. This is due to the higher mass flow rate at higher Reynolds numbers which causes comparatively smaller decrease in hot flow exit temperature. The decrease in percentage heat loss rate from the hot flow is directly responsible for the decrease in percentage heat loss rate to the ambient. But the ambient heat loss rate decreases at a much faster rate than the hot flow heat loss rate with increase in Reynolds number. This results in an increase in percentage heat gain rate of the cold flow with increase in Reynolds number for non-adiabatic cases.

3.4.3.3 Effect of heat exchanger geometry

Of all the parameters considered the heat exchanger geometry had surprisingly low effect on the heat transfer characteristics. The effect of geometry is most prominent at near adiabatic conditions and higher Reynolds numbers. Owing to the comparatively higher undeveloped nature of the flow field the rectangular SHE could be assumed to have higher internal heat transfer coefficient than the Archimedean SHE. This gives it a slight advantage over the Archimedean SHE at adiabatic boundary wall conditions. But as the external heat transfer coefficient increases the Archimedean SHE starts to perform almost as good as the rectangular SHE. This is because the lower external surface areas of the Archimedean SHE aids in having relatively lower ambient heat loss.

3.4.3.4 Effect of material thermal Conductivity

The effect of material thermal conductivity was observed to be significant on the heat exchanger performance for all the conditions investigated here. The effect is more prominent at higher Reynolds numbers. SHEs having the same material conductivity have similar heat transfer characteristics than the ones with the same geometry. Lower thermal conductivity ceramic SHE had 40% lower ambient heat loss rate and 100% higher heat transfer rate to the cold flow than the aluminum SHE when the external heat transfer coefficient was 400 $W/m^2/K$. The aluminum SHEs behaved analogous to a lumped body having a constant wall temperature. In contrast the ceramic SHEs provided considerable temperature gradients between its inner and outer walls.

Chapter 4: Combustion of premixed propane-air at meso-scale

4.1 Combustor Designs

The common feature of all the combustors investigated here is the Swiss-roll design which consists of a combustion region at the center and double spiral-shaped channels, the widths of which are smaller than the quenching distance of propane-air premixed flame at normal state conditions. The geometry and choice of material for the combustor were determined from extensive tests performed experimentally. Initially various combustor geometries were fabricated in aluminum and steel and examined for stable combustion over a wide range of flow rates and equivalence ratios (Figure 4.1). Table 4.1 provides details on some of the geometries and materials examined here. The parameters that differentiate these combustor geometries are the dimensions and shape of the channels and the combustion chamber itself. Thermal conductivity of the combustor material and the combustion chamber geometry were observed to be extremely significant to sustain flame in meso-scale. None of the metal combustors were able to self sustain a premixed propane-air flame. However, in the presence of an external heat supply some of them were able to sustain the flame. The geometry investigated in the present study (Figure 4.2) was arrived at based on the flammability experiments performed on these metal combustors in the presence of an external heat source. Ceramic combustors made of this geometry were able to self sustain the flame over a wide range of flow rates and equivalence ratios.

The combustion chamber design which was successfully able to hold the flame is shown in Figure 4.3. Even though some other designs with similar blockage area at the inlet of the combustion chamber were able to provide higher flow recirculation and hence lower residence time in the combustion chamber (as predicted by CFD results), they were never successful in flame holding. This will be later discussed in section. The only possible explanation for this counter-intuitive outcome is that even though there are sufficient ignition points or sources (locations were flame velocity is equal to flow velocity) present in all the designs only one of them have favorable velocity gradients around these points to sustain the flame. Global photographs of the flames obtained with aluminum, macor and zirconium phosphate combustors are given in Figure 4.4.

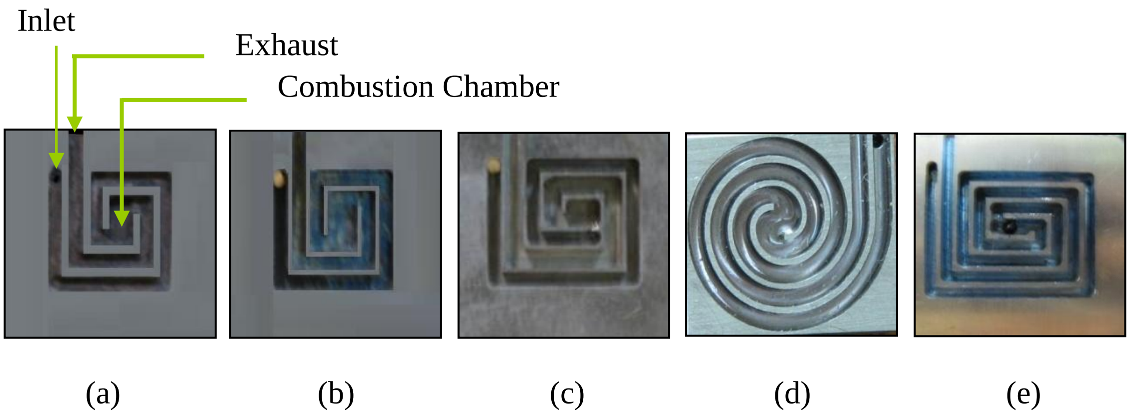

Figure 4.1 Sample photographs of Swiss-roll combustors. Geometries (a), (b) and (d) are made of steel while (c) and (e) are made of aluminum

Table 4.1. Design geometry and materials for the various combustors

Combustor Type	**Chamber volume (mm3)**	**Non-dimensionalized length* (inlet channel)**	**Non-dimensionalized length* (outlet channel)**	**Non-dimensionalized depth***	**Material**
Rectangular spiral	15.2	30.49	14.30	0.69	Steel
Rectangular spiral	56.7	31.37	15.05	1.89	Steel, Al
Rectangular spiral	56.7	40.95	22.67	1.89	Al
Rectangular spiral	18	43.34	24.28	1.89	Steel, Al
Rectangular spiral	34.8	59.50	40.73	1.89	Al
Archimedean spiral	61.76	48.84	31.50	1.89	Steel
Rectangular spiral ✓	32.6	70.87	47.50	1.89	Steel, Al, Macor, Zirconium phosphate

* Non-dimensionalized with respect to channel width

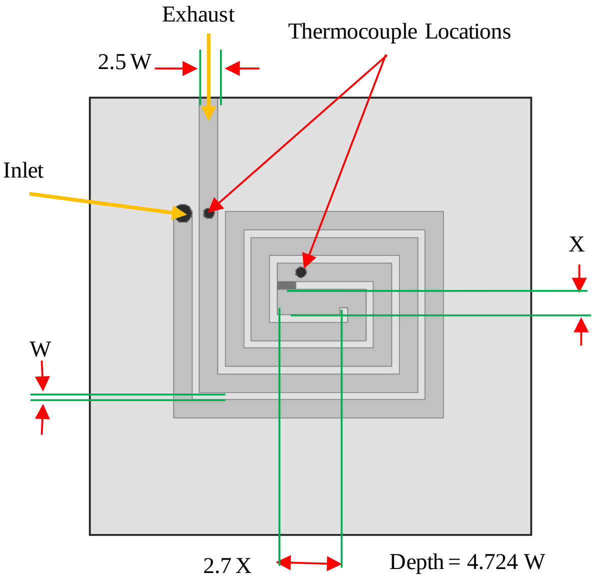

Figure 4.2 Combustor geometry

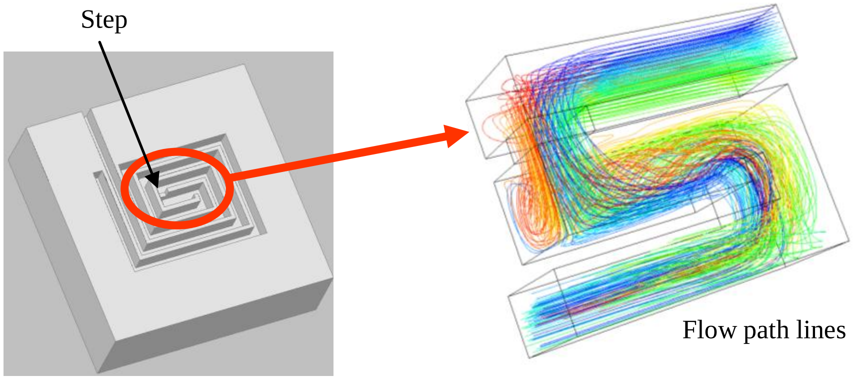

Figure 4.3 Combustion chamber geometry with step at the inlet and path lines showing the 3-D recirculation zone induced by this step

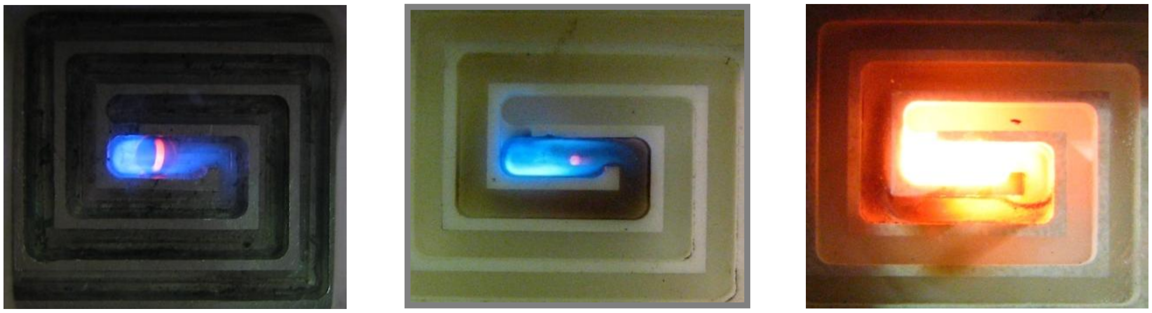

(a) **(b)** **(c)**

Figure 4.4 Propane flame inside various combustors: (a) Aluminum, (b) Macor, (c) Zirconium phosphate. The flame inside aluminum was sustained using external heating

4.2 Operating Limits

It was observed from the experiments that only the ceramic combustors could sustain combustion in the meso-scale dimensions. Both aluminum and steel required continuous heating at the outer wall to sustain combustion. Extinction limits were obtained for both of the ceramic combustors (Figures 4.5 and 4.6). The results are plotted for equivalence ratio against inlet Reynolds number and mean flow velocity. The errors associated with the measurements are reported in Appendix A. Inlet Reynolds number was calculated based on the hydraulic diameter at the inlet of the combustor. The errors associated with measurement of equivalence ratio, Reynolds number and inlet velocity originates from the flow controllers. Since the flow controllers have a measurement error of 1.5% of the maximum flow rate, the error increases while operating at lower flow rates. It was observed that the combustors had a rich operating limit and a lean operating limit and both of them were well within the reported flammability limits of propane flame at the normal state [112]. Many researchers have reported extra lean combustion or the so-called super adiabatic flame, using large-scale Swiss-roll combustors [113] or using porous materials but no such observation could be made in the meso-scale conditions. For macor combustor, rich operating limit was found to increase with increase in inlet Reynolds number. However, the lean operating limit was found to be more or less a constant. In the case of zirconium phosphate combustor, rich and lean operating limits both increased with increase in inlet Reynolds number. There was no upper limit for the mean flow velocity through the zirconium phosphate combustor that will sustain a flame within the experimental range of conditions examined. However in the case of the macor combustor, there was an upper limit for the velocity and was set by the material limitation. Macor combustor was not able to cope with the thermal stresses at higher Reynolds numbers (higher energy release rate due to higher fuel-air flow rate). Also, for a particular inlet flow condition, macor combustor was observed to crack due to resonance from the flame induced acoustics (see section 4.6). For both combustors, the minimum mean flow velocity required to sustain a flame was larger than the laminar burning velocity of the propane flame, about 0.383 m/s [114]. The minimum mean inlet velocity for which the flames could be sustained was found to be more than two times the laminar flame speed for macor combustor and around five times for the zirconium phosphate combustor. The difference between the minimum mean flow velocities can be explained due to the higher amount of heat recirculation and thereby preheating which is possible in the zirconium phosphate combustor as compared to the macor combustor. This implies that for the same inlet flow conditions the burning rate inside the zirconium phosphate combustor is higher as compared to macor combustor. This enhanced burning rate causes the minimum mean flow velocity for sustained combustion (without flashback or extinction) in the zirconium phosphate combustor to be higher than that of macor.

The fact that very high mean flow velocities could be sent through the inlet of the combustor and still have a stable, self sustained flame in the central chamber shows that the flame speed of propane air mixtures is not laminar any more. The flame speed might have got enhanced due to the following two factors.

1. Aerodynamic effects of the highly non-uniform flow field in the central chamber due to the flame holder (step)
2. Increased reaction rate due to increased enthalpy of the incoming reactants

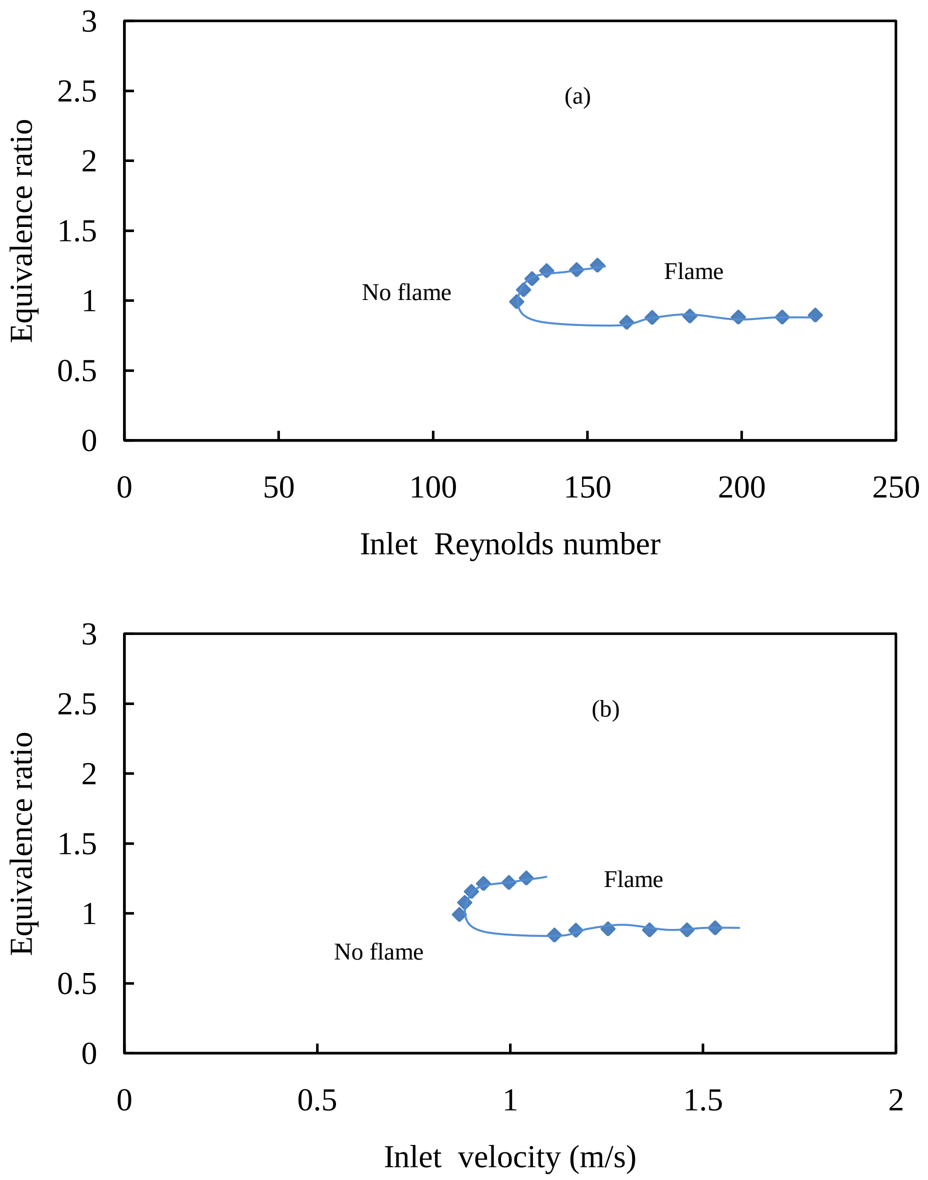

Figure 4.5. Extinction limits of macor combustor (a) with respect to inlet Reynolds number (b) with respect to mean inlet velocity

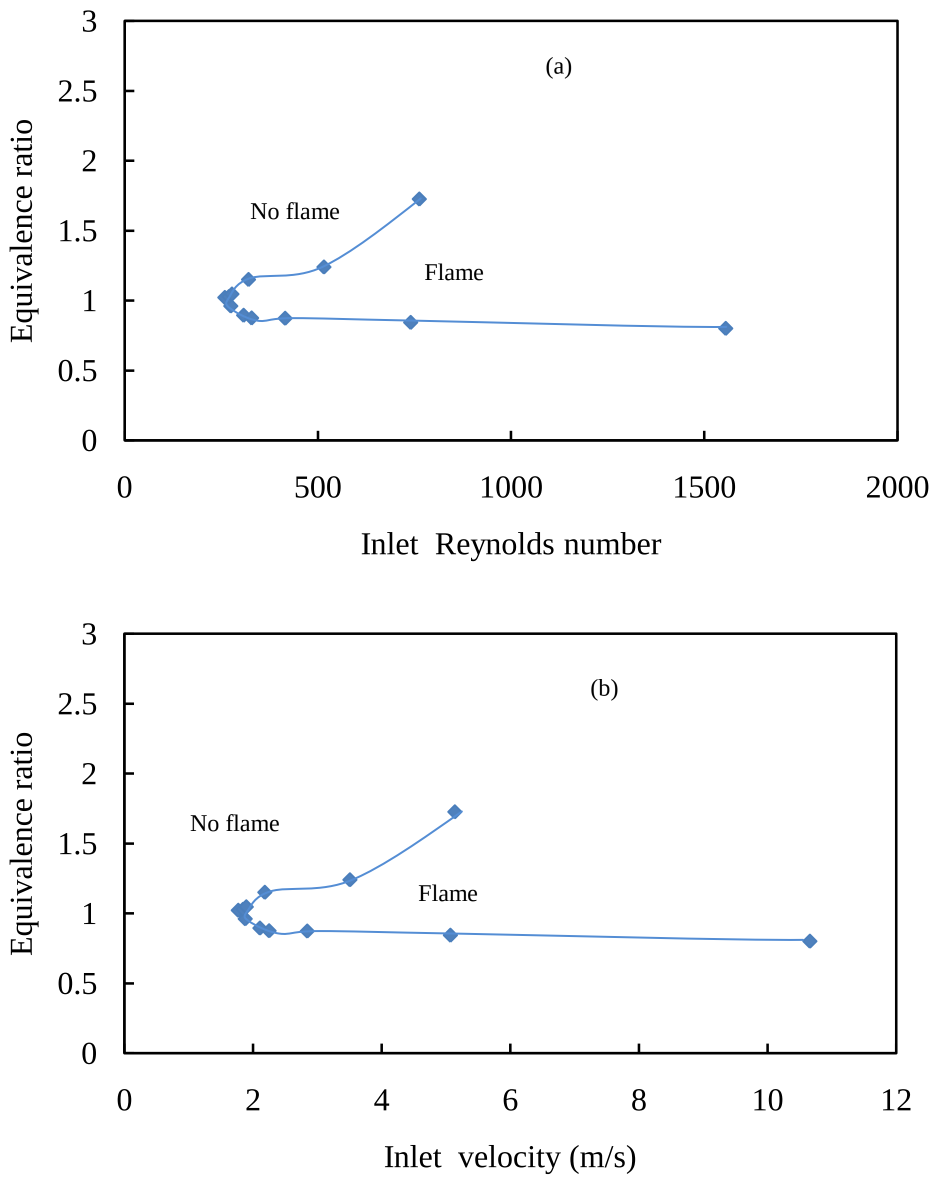

Figure 4.6 Extinction limits of zirconium phosphate combustor (a) with respect to inlet Reynolds number and (b) with respect to mean inlet velocity

4.3 Wall temperature distribution

Thermal imaging of the combustors was carried out to determine the temperature distribution across the combustor surface. While performing flammability experiments, quartz window was used for optical access to the combustor. Since quartz will not allow the radiation in the range 8-9 microns to pass though, calcium fluoride window was used for thermal imaging. Calcium fluoride glass has good transmission in the range 0.2-9 microns [96]. But the thermal conductivity of calcium fluoride is seven times higher than that of quartz (Table 2.1). Hence while using calcium fluoride instead of quartz; it was not possible to sustain combustion due to higher heat losses from the combustion chamber. Therefore to sustain flame, a spark was switched on continuously. It was observed from the thermal images that the presence of spark has little to no affect on temperature distribution. Although the presence of calcium fluoride changes the temperature distribution of the combustor as compared to quartz, the thermal images helps to get some idea on the kind of thermal gradients that can develop inside the combustor between the central chamber and the outer walls. This also can be used for CFD code validation. It should be noted here that the thermal camera sees only the temperature of the walls since the infrared radiation from the hot gases is negligible as compared to that from the hot walls.

Figure 4.7 shows a comparison of the thermal images obtained from the macor and zirconium phosphate combustor walls for similar inlet conditions. The fuel flow rate for all these cases was 0.46 mg/s. Equivalence ratio was varied by varying the air flow rate. It was observed that the zirconium phosphate combustor was able to maintain a higher temperature in its combustion chamber as compared to the macor combustor for the same heat load. This basically implies that the heat loss from the combustion chamber is lower for the zirconium phosphate combustor. Equivalence ratio was also found to have a significant impact on the steady state wall temperature.

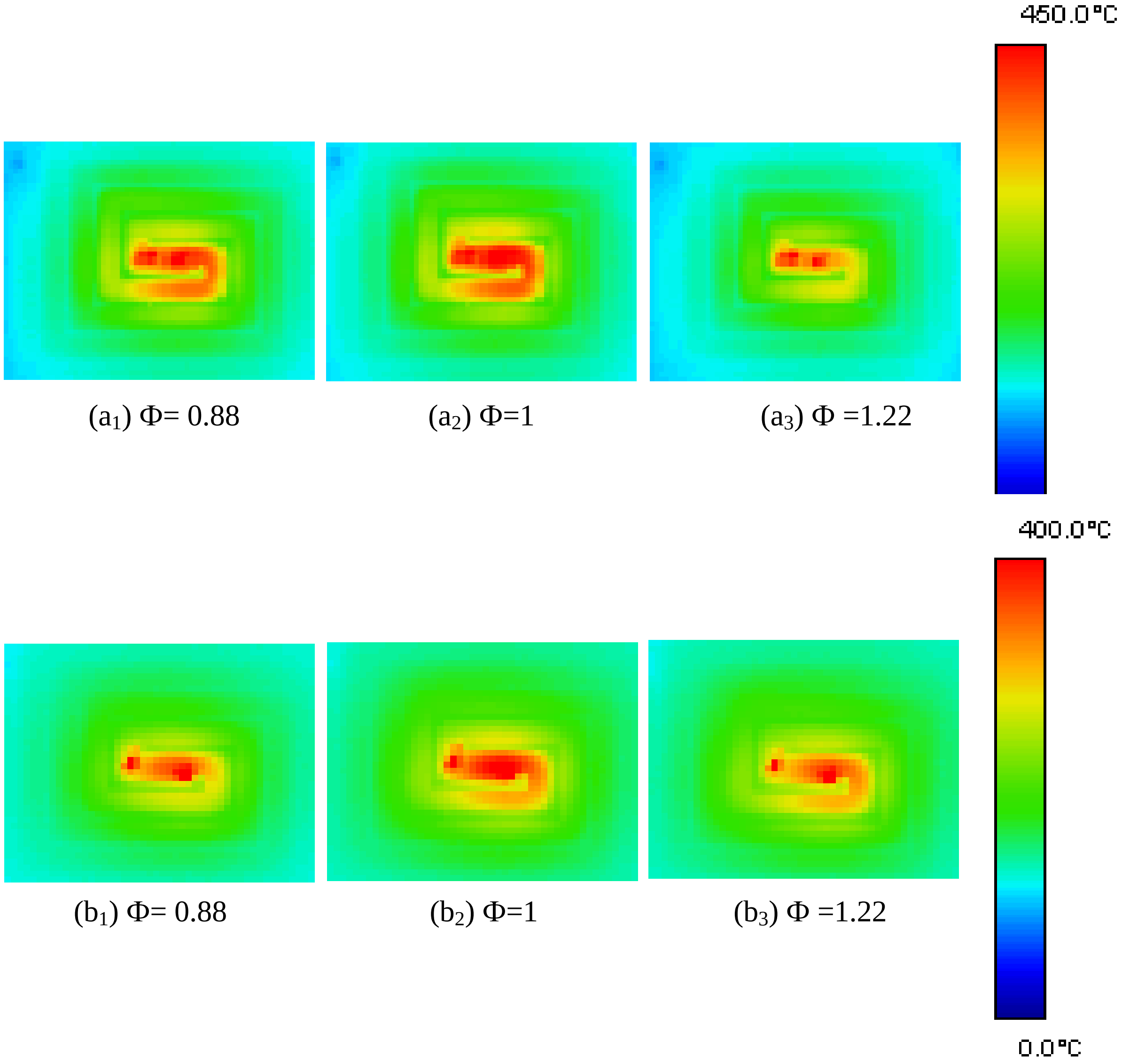

(a$_1$) Φ= 0.88 (a$_2$) Φ=1 (a$_3$) Φ =1.22

(b$_1$) Φ= 0.88 (b$_2$) Φ=1 (b$_3$) Φ =1.22

Figure 4.7. Thermal images of (a) Zirconium phosphate combustor, and (b) Macor combustor at various equivalence ratios for a constant fuel flow rate of 0.46 mg/s.

4.4 Numerical simulations

In a previous section results were presented on numerical simulations performed on spiral heat exchangers. A constant inlet temperature was chosen for the hot flow (2000 K) in those simulations. However, when the spiral heat exchanger is integrated with a combustor, the hot flow exit temperature which is now equal to the combustion temperature is directly dependent on the cold flow exit temperature or the preheating temperature of the reactants. Hence numerical simulations were performed on the actual combustor geometry for reacting flow conditions. These CFD simulations were not performed for studying combustion and flame characteristics but rather the heat transfer characteristics through the walls of the combustor. They helped to obtain a better understanding of heat transfer through the walls of the combustor as this is difficult to determine experimentally. The parameters varied were thermal conductivity of the combustor material and inlet flow velocity or heat load and were found to have a strong impact on the heat transfer inside the combustor.

In the Swiss-roll combustor, when the reactants combust at the central chamber of the combustor, the following observations can be made. The products lose heat to the channel walls and to the outer walls by convective heat transfer as they travel from the central chamber to the exit and out to the exhaust. A part of this heat reaches the reactants through the channel walls and the outer walls and preheats them before they reach the combustion chamber. A significant amount of heat is lost to the surrounding through the outer walls. Heat conduction along the walls is detrimental for the performance of a meso-scale combustor because it removes the thermal enthalpy from the combustion zone. However, conduction across the channel walls should be high enough for heat recirculation. This optimization problem naturally gives rise to the following questions:

- How much is the heat loss in the combustion chamber?
- How much is the overall heat loss?
- What is the degree of preheating of reactants before reaching the combustion chamber?
- How much of this preheating occurs through channel walls?
- How much of preheating occurs through outer walls?
- How does wall thermal conductivity and inlet velocity affect all of the above parameters?

Simulations were able to provide some estimates to the above questions. It also provided some information on how to design heat recirculating combustors with maximum recirculation of heat to the reactants and minimum reduction in the enthalpy of products by the time they reach the exhaust.

The following non dimensional parameters were examined using the simulation results.

i) HL_cc/ Heat Load
ii) HL_tot/ Heat Load
iii) HR_CW/ Heat Load
iv) HR_OW/ Heat Load
v) HR_tot/ Heat Load
vi) HR_OW/ HR_CW

where, HL_cc = rate of heat loss in the combustion chamber, HL_tot = rate of total heat loss from the combustor, HR_CW = rate of heat recirculation to the reactants through the channel walls, HR_OW = rate of heat recirculation to the reactants through the outer walls and HR_tot = total rate of heat recirculation to the reactants. Simulations for the 3-D Swiss-roll geometry (Fig. 3) were performed with the aid of Fluent software. Steady segregated solver was used. Laminar flow was assumed. No radiation model was employed in the simulations. Only convection heat losses were considered. The heat transfer coefficient to account for the heat losses from the external walls was obtained by comparing the simulations with the wall thermal images obtained experimentally. Here the simulations (similar to the experiments) were also performed by keeping calcium fluoride as the material for one of the outer walls. The same problem encountered during the experiments was also experienced in the simulations. The flame will not sustain itself in the presence of calcium fluoride window. During experiments this problem was overcame by using a continuous spark source in the combustor. During simulations this was achieved by reducing the activation energy of the reactions. For a wall heat transfer coefficient of 400 W/m^2/K, the temperature contours obtained with the CFD compared favorably with the thermal images (Figure 4.8).

Different thermal conductivity values chosen for simulations correspond to different combustor materials (see Table 2.1). Calcium fluoride and quartz were chosen as one of the outer walls in some simulations for comparing with experimental results because as mentioned before, these two materials were used for optical access. It was observed both experimentally and from the CFD simulations that a propane flame could not be sustained inside the metal combustors. Hence to compare the heat transfer in different materials in the same scale, the flame was sustained artificially by reducing the activation energy of the reactants.

Three different cases were considered for examining the effect of inlet Reynolds number (Re) on combustor performance. These were: (a) combustor made of macor with quartz window, (b) combustor made of zirconium phosphate with quartz window, and (c) combustor made completely of zirconium phosphate. Cases (a) and (b) are the same as the experiments conducted. Case (c) was considered to quantify the advantages of using a combustor made fully of zirconium phosphate as compared to the one that incorporated use of quartz window.

Simulation results compared well with the wall thermal images obtained experimentally for a wall heat transfer coefficient of 400 $W/m^2/K$. Figure 16 shows a comparison of the CFD simulations results (A1 and B1) with the experimental results (A2 and B2) obtained from the macor and zirconium phosphate combustors, respectively at stoichiometric condition. The results show good comparison between simulations and experimental data. The large difference in the central chamber temperatures of the macor and zirconium phosphate combustors is evident from these results.

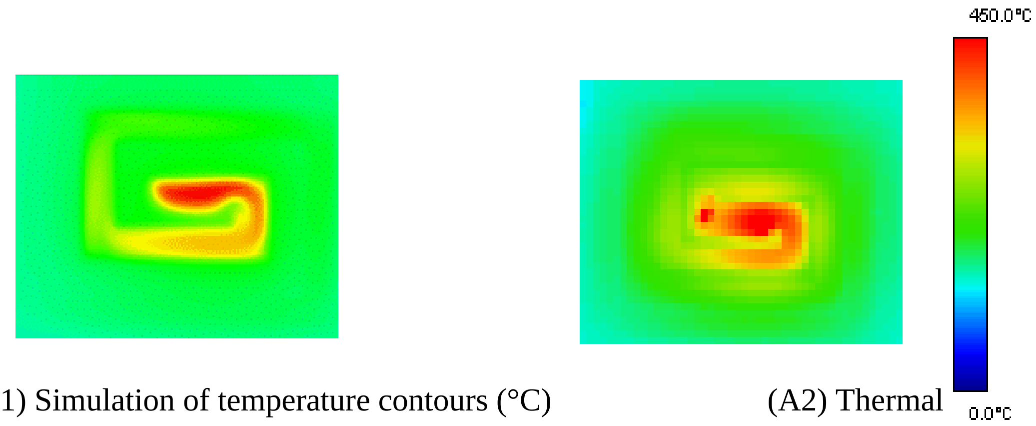

(A1) Simulation of temperature contours (°C) (A2) Thermal

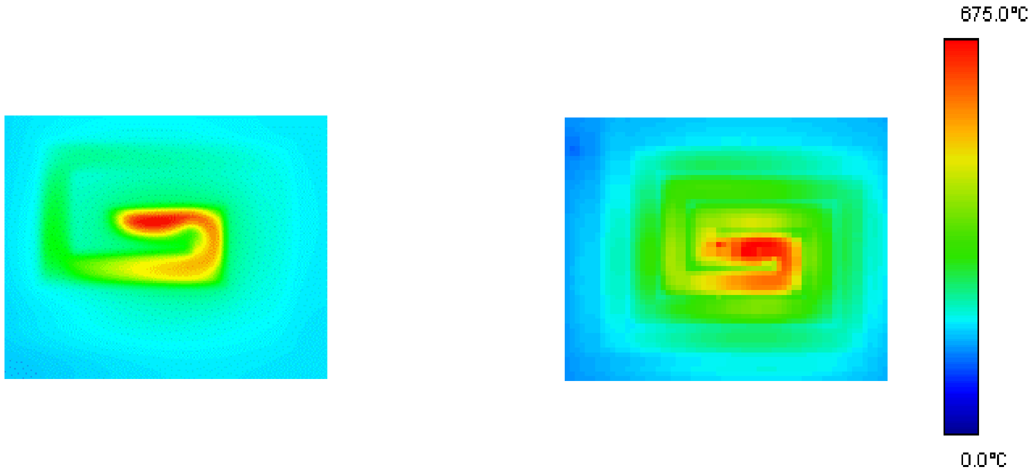

(B1) Simulation of temperature contours (°C) (B2) Thermal image

Figure 4.8 A comparison of CFD simulation results on wall temperature contours with the thermal images for (A) Macor combustor, and (B) Zirconium phosphate combustor for a fuel flow rate of 0.69 mg/s and equivalence ratio, Φ=1

Simulations showed the importance of material thermal conductivity in meso-scale combustion. They also showed the range of thermal conductivity which is important for successful combustor operation. Figure 4.9 shows that heat loss from the combustion chamber is lower for lower thermal conductivity.

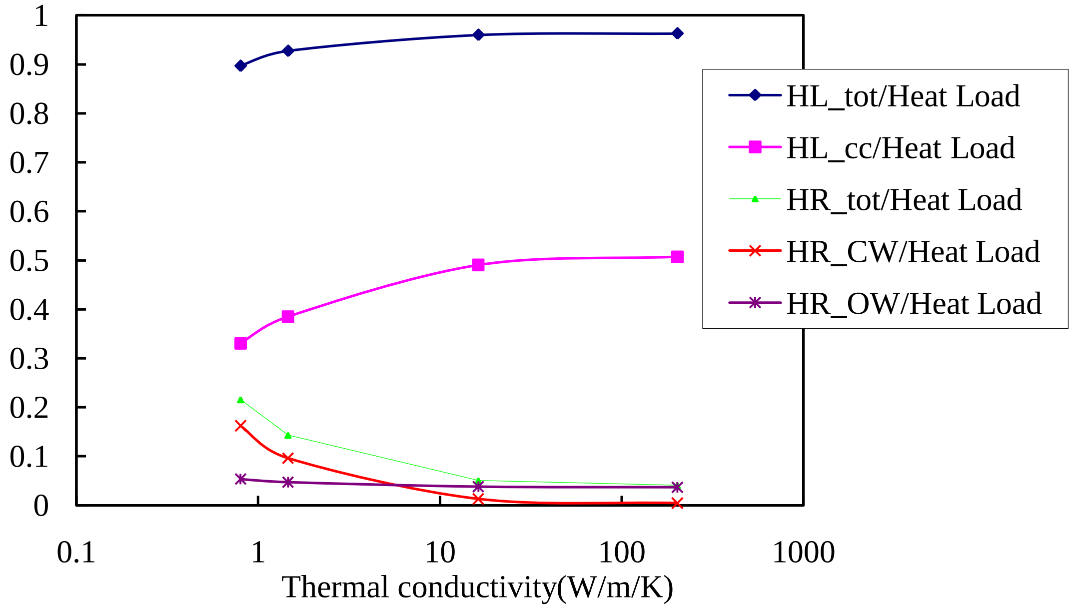

Figure 4.9 Effect of thermal conductivity on heat transfer rates for a heat load of 29W (HL_cc = Rate of heat loss in the combustion chamber, HL_tot = Rate of total heat loss from the combustor, HR_CW = Rate of heat recirculation to the reactants through the channel walls, HR_OW = Rate of heat recirculation to the reactants through the outer walls and HR_tot = total rate of heat recirculation to the reactants)

Chamber heat loss increases with increase in thermal conductivity rapidly in the beginning (<15 W/m/K) and at a lower rate for higher thermal conductivities (> 15 W/m/K). The overall heat loss from the combustors also increased with increase in thermal conductivity, but at a very slow rate. In fact the total heat loss from zirconium phosphate combustor and aluminum combustor were comparable. This shows that even though using lower thermal conductivity material helped to sustain combustion by reducing heat losses from the combustion chamber and increasing the heat recirculated to the reactants, the overall heat loss from the combustor still remained high. By the time the products reach the exit, they were found to possess, at best, only 10% of the heat load. Total heat recirculated to the reactants decreased as the thermal conductivity increased. The rate of decrease in heat recirculation was higher at lower thermal conductivities and lower at higher thermal conductivities. The heat recirculated to the reactants though the channel walls showed the same trend. It was observed that for metal combustors, most of the heat recirculation to the products occurred though the outer walls and not through the channel walls. In fact at steady state, metal combustors were found to have about the same temperature throughout their surface. It can be inferred that, for higher thermal conductivity (>15W/m/K) the combustor material behaves like a lumped body so that the conductive heat transfer inside the body is much faster than the convective heat transfer. Hence the heat loss from the central chamber is very high. In the low thermal conductivity case (< 15W/m/K) the material no longer behaves as a lumped mass and is capable of sustaining huge thermal gradients between the central chamber and the outer walls. Heat loss from the central chamber is minimized. Figure 4.10 shows the variation in the ratio of rate of heat recirculation to reactants through outer walls to that through the channel walls as a function of the thermal conductivity. It can be seen that the ratio is lower than 1 for low thermal conductivities and increases very rapidly and reaches close to 9 for a thermal conductivity of 202.4 W/m/K. This does not mean that an increase in thermal conductivity will increase the heat recirculated through the outer walls.

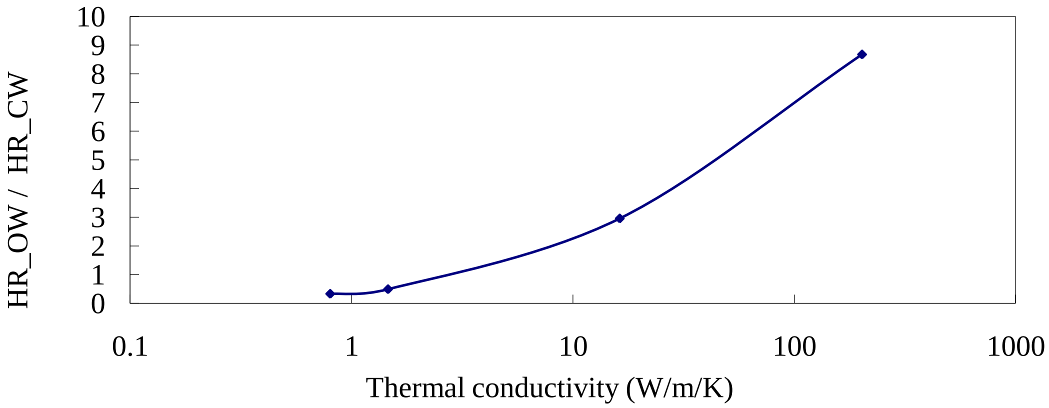

Figure 4.10 Effect of thermal conductivity on ratio of heat recirculation rate through outer walls to that through channel walls for a heat load of 29W. (HR_CW = Rate of heat recirculation to the reactants through the channel walls, HR_OW = Rate of heat recirculation to the reactants through the outer walls)

In fact this is almost constant (see Figure 4-10). However, the heat recirculated through the channel walls decreases tremendously with increase in conductivity. In short, these results imply that zirconium phosphate combustor is most favorable for flame stabilization from heat transfer point of view. Increase in the Reynolds number at constant equivalence ratio was found to have a favorable affect on combustor performance (see Figures. 4.11 – 4.14). As the Re increased the ratio of rate of heat losses from the combustor to heat load was found to decrease substantially. Same trend was found for the ratio of overall heat loss rate to heat load. The ratio of heat recirculation rate to the reactants through channel walls to heat load was found to increase with increase in Re. The ratio of total heat recirculated to the reactants to heat load also showed a similar trend.

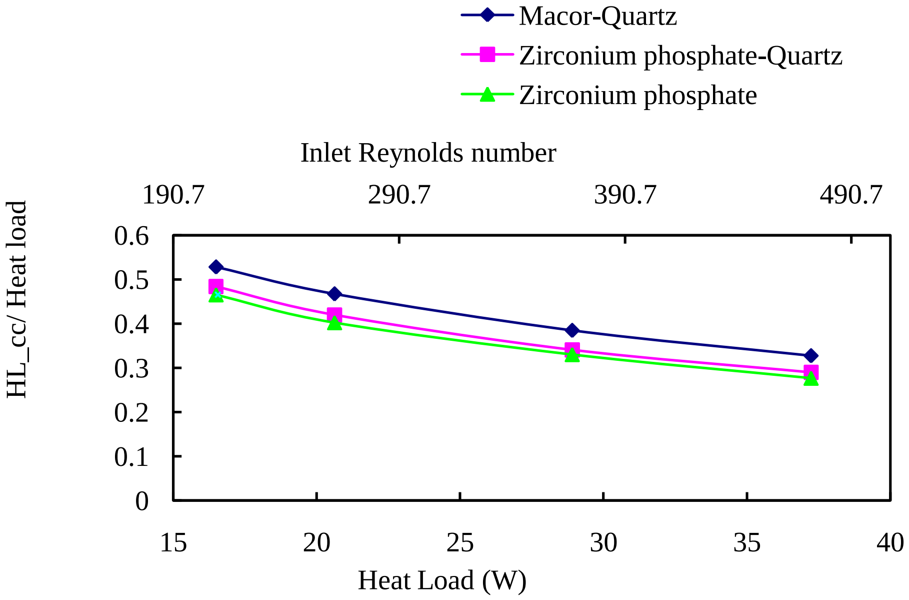

Figure 4.11 Effect of Heat Load on the ratio of rate of heat loss from the combustion chamber (HL_cc) to heat load

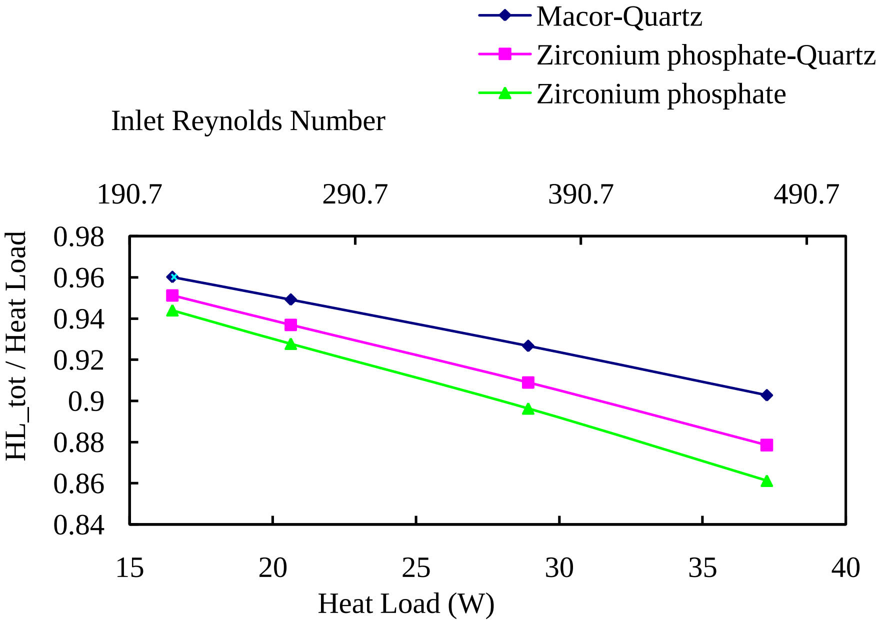

Figure 4.12 Effect of Heat Load on the ratio of rate of total heat loss from the combustor (HL_tot) to heat load

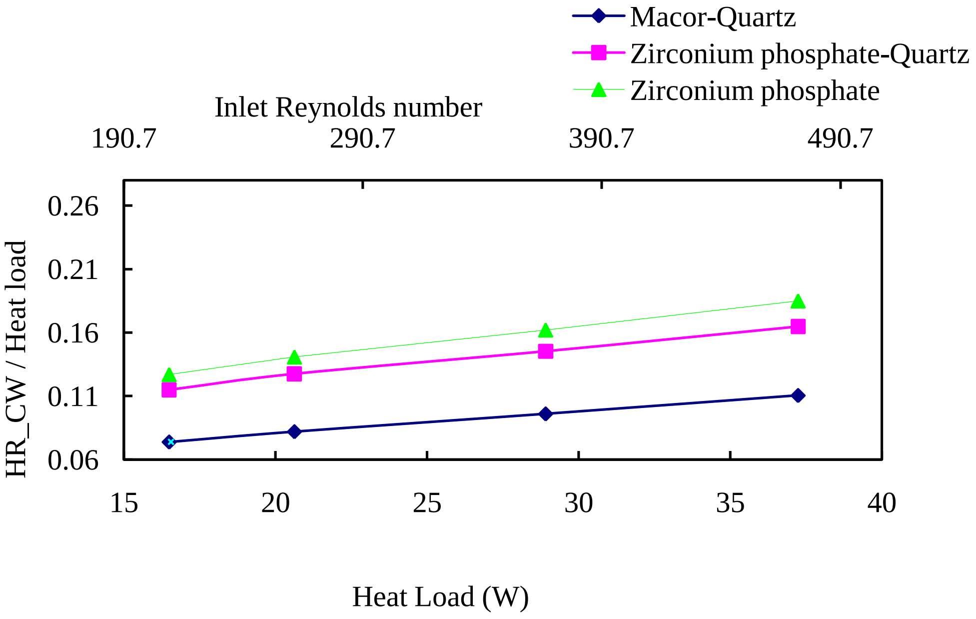

Figure 4.13 Effect of Heat Load on the ratio of rate of heat recirculated to the reactants through channel walls (HR_CW) to heat load

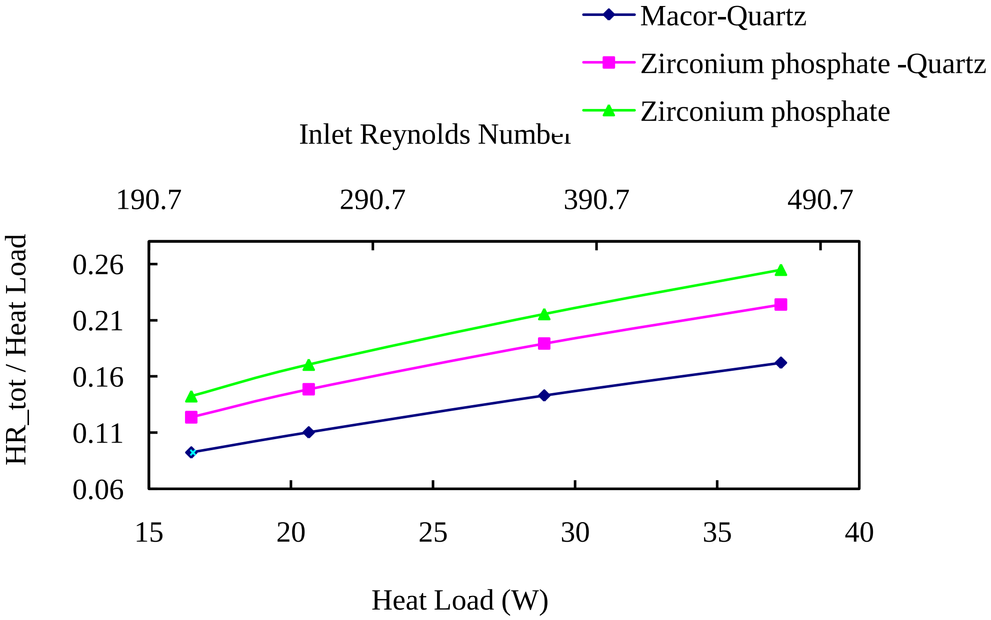

Figure 4.14 Effect of Heat Load on the ratio of rate of total heat recirculated to the reactants (HR_tot) to heat load

4.5 Chemiluminescence

In this section the variation of the chemiluminescence strength of OH* CH* and C2* emissions from propane-air flame is presented with respect to fuel flow rate, air flow rate and equivalence ratio keeping anyone of them constant and varying the other two. For a constant equivalence ratio it was observed that the chemiluminescence emission strength in all wavelengths increased with increase in flow rate. The variation was almost linear for all the wavelengths observed. However, for a constant air flow rate different trends were observed when equivalence ratio was varied. The emission of OH* increased with equivalence ratio and reached a maximum and then decreased whereas CH* and C2* emissions showed a continuous increase with equivalence ratio. It was also observed that the reaction zone size as depicted by the OH* chemiluminescence decreases with equivalence ratio. For slightly rich flames at higher fuel flow rates, the OH* chemiluminescence images showed that the flame shifts to an upstream location of the combustion chamber. This is possibly due to the pre-ignition of the reactant mixture at high preheating temperatures. It was not possible to detect this state with both naked eye and from C2* or CH* images due to the high luminosity of the flame (Figure 4.4c).

4.5.1 Global Chemiluminescence

Figures 4.15-4.18 show intensity images of chemiluminescence of OH*, CH* and C2* obtained at an air flow rate of 900 ml/min at various equivalence ratios of 0.9 (fuel lean) to 1.3 (fuel-rich). The results show a monotonic increase in strength of CH* and C2* chemiluminescence with increase in fuel flow rate. For OH* the strongest emission was at the stoichiometric condition (Figure 4.18). The size of the emitting region increases with increase in equivalence ratio for CH* and C2* chemiluminescence. The trend observed for OH* chemiluminescence was contrary to that observed for CH* and C2*. For OH* at the most fuel-rich condition examined here (Φ=1.3) the region of detectable signal regime was the smallest for any air flow rate. The OH* chemiluminescence represent flame marking radical in flames and at the low wavelengths it is unaffected by the presence of any thermal radiation from heated walls of the combustor and/or carbon particles. The results infer that the reaction zone inside the meso-scale combustor shrinks as the flame is allowed to proceed from lean to rich condition. The increase in emission intensity in the visible part of the spectrum with increase in equivalence ratio is attributed to two factors. Firstly, an increase in C2* and CH* radicals as the flame is made fuel rich. C2* and CH* emissions are known to increase with increase equivalence ratio [97, 98]. The second more probable factor is increase in thermal radiation as the mixture becomes fuel rich. However, the flame temperature is lower for fuel rich premixed combustion. The temperature measurements made at upstream location of the combustor using a thermocouple showed reactant preheat temperature to decrease with increase in equivalence ratio. Therefore, it can be expected that the resulting combustion temperature inside the meso-scale combustor must decrease rapidly with increase in equivalence ratio. This suggests that the thermal radiation from the walls next to the flame must decrease with increase in equivalence ratio. So the increase of thermal emission must stem from an increase in the amount of carbon or soot particle concentration with increase in equivalence ratio.

For a few particular conditions (high flow rate and slightly fuel rich) flame was observed to stabilize at an upstream location of the combustion chamber. This combustion mode is accompanied by high acoustic signatures. The prevailing high background thermal radiation precluded our observation on relative location of the flame inside the combustor. Close observation with C2* or CH* images did not assist us in locating the relative flame position from within the combustor. In contrast the OH* images clearly indicated the presence of the flame in the narrow channel upstream of the combustion chamber (see Figure 4.19).

Image intensity integration technique was used to calculate total global emission of the chemiluminescence signal strength emanating from the flame surface. This was performed only for OH* images (Figures 4.20-4.22**).** The rationale for not performing such calculation for C2*and CH* images is the complex nature of such images that incorporate thermal radiation from the combustor walls as well as the carbon particles present. Each plot is normalized with the respective highest emission value observed. For constant air flow rate the total emission strength was highest for the stoichiometric flame (Figure 4.20). The same trend was observed for the case of constant fuel flow rate (Figure 4.21). A continuous increase in emission strength was observed with fuel flow rate at constant equivalence ratio (Figure 4.22). The results clearly show that strongest emissions of OH* occurs at stoichiometric condition and it increases with increase in the heat load (fuel flow rate). The OH* emission decreases on both fuel rich and fuel lean operation.

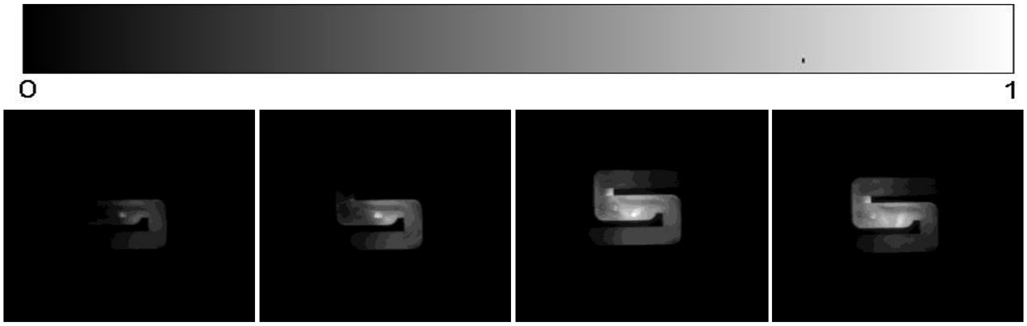

Φ=.9 Φ=1 Φ =1.2 Φ =1.3

Figure 4.15 C2* Chemiluminescence images at 470 nm for different equivalence ratios at air flow rate =900 ml/min

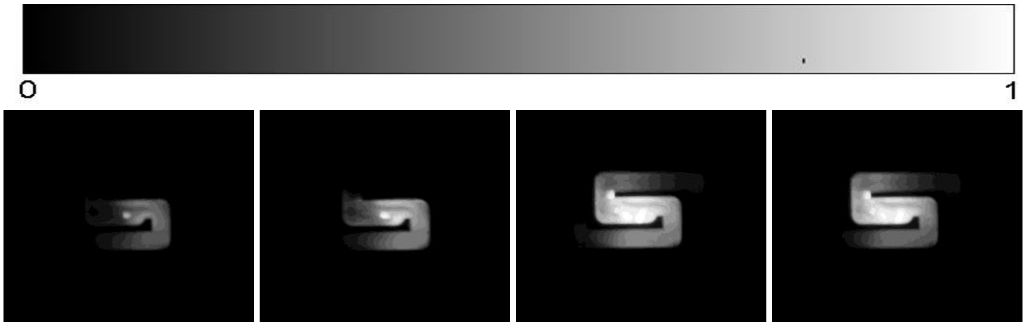

Φ=.9 Φ=1 Φ =1.2 Φ =1.3

Figure 4.16 C2* Chemiluminescence images at 430 nm for different equivalence ratios at air flow rate =900 ml/min

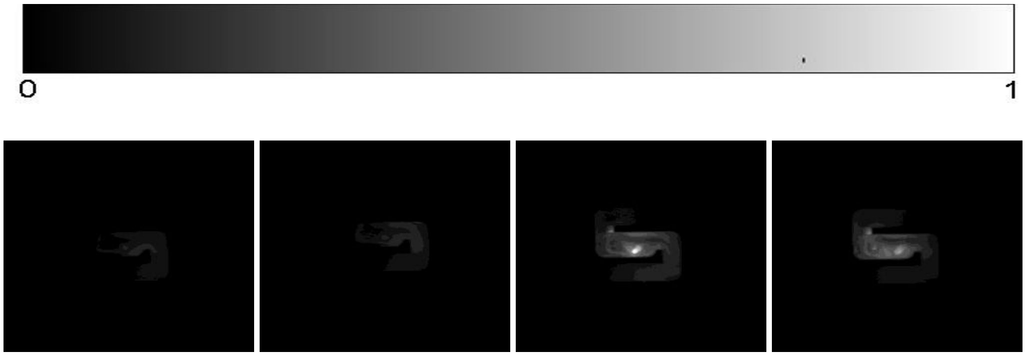

Φ=.9 Φ=1 Φ =1.2 Φ =1.3

Figure 4.17 CH* Chemiluminescence images at 515 nm for different equivalence ratios at air flow rate =900 ml/min

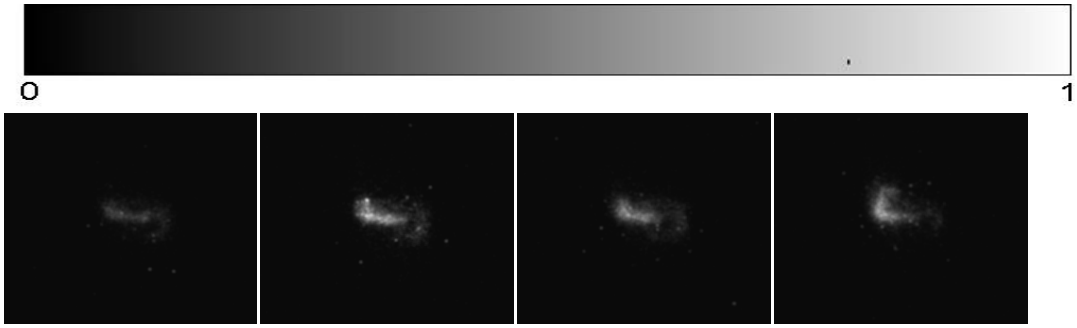

Φ=.9 Φ=1 Φ =1.2 Φ =1.3

Figure 4.18 OH* Chemiluminescence images at 515 nm for different equivalence ratios at air flow rate =900 ml/min

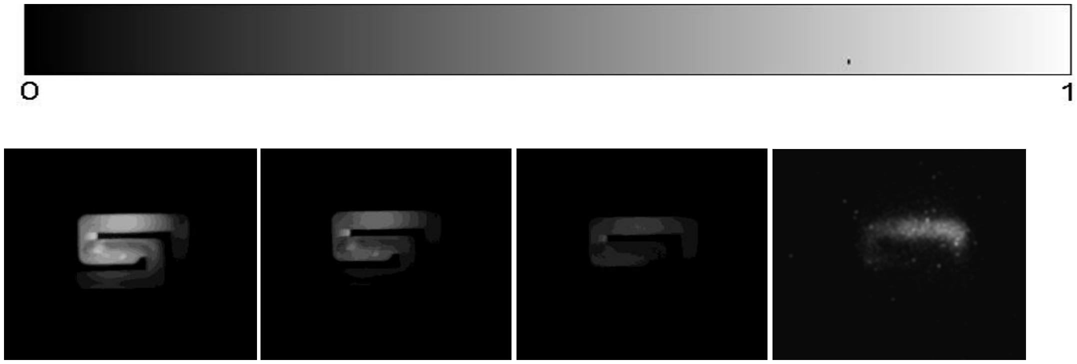

Φ=.9 Φ=1 Φ =1.2 Φ =1.3

Figure 4.19 Chemiluminescence images of flame stabilized at upstream location. Only the OH* image predicts the reaction zone correctly

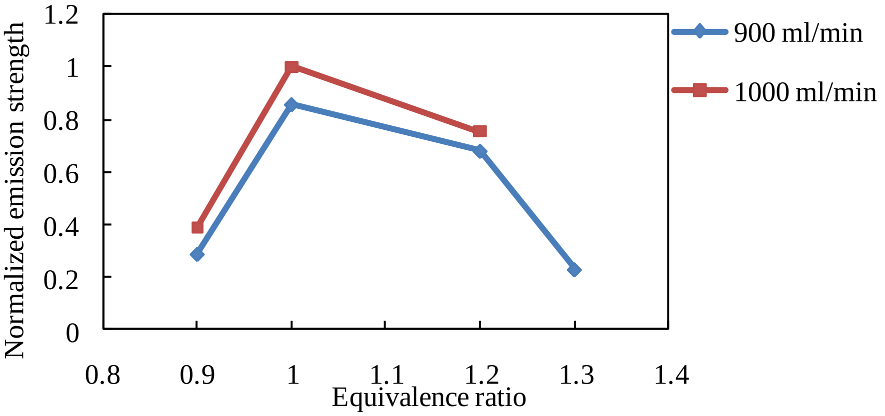

Figure 4.20 OH* global chemiluminescence yield at 307 nm as a function of equivalence ratio at two air flow rates

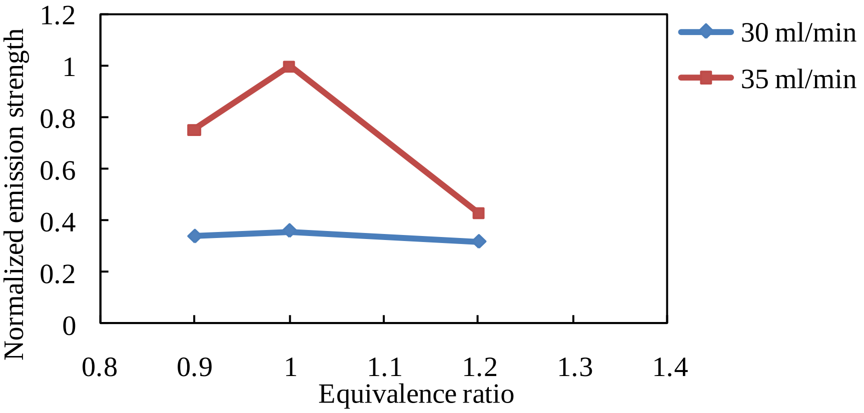

Figure 4.21 OH* global chemiluminescence yield at 307 nm as a function of equivalence ratio at two fuel flow rates

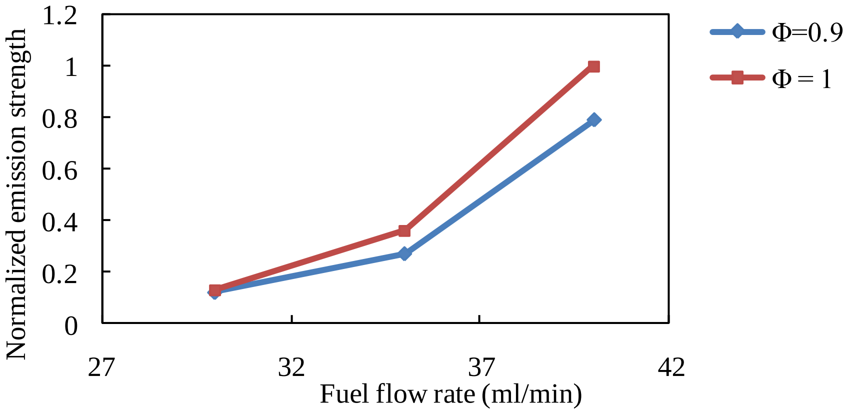

Figure 4.22 OH* global chemiluminescence yield at 307 nm as a function of fuel flow rate at two equivalence ratios (Φ)

4.5.2 Local Chemiluminescence

Local chemiluminescence measurements have been performed by carefully selecting a suitable location in the flame from the 2-D images**.** Figures 4.23-4.34 show the variation in strength of chemiluminescence signal as a function of equivalence ratios and flow rates. Each plot is normalized with the respective highest emission value detected. It should be noted that the local chemiluminescence emission values plotted for CH* and C2* are qualitative values since they incorporate background thermal radiation from sources other than the chemiluminescence signal.

4.5.3 CH* Chemiluminescence:

Figure 4.23 shows the variation of CH* emissions as a function of equivalence ratio at two different air flow rates. The results show a steady increase in CH* emission with increase in fuel flow rate. However, a different trend for CH* was observed when the fuel flow rate was held constant as shown in Figure 4.24.

Maximum emission occurs at the stoichiometric condition. The emission decreases when the air flow is increased or decreased on either side of stoichiometric condition. Figure 4.25 shows the variation of CH* as a function of fuel flow rate at two different equivalence ratios. A continuous increase in emission strength was observed with increase in fuel flow rate.

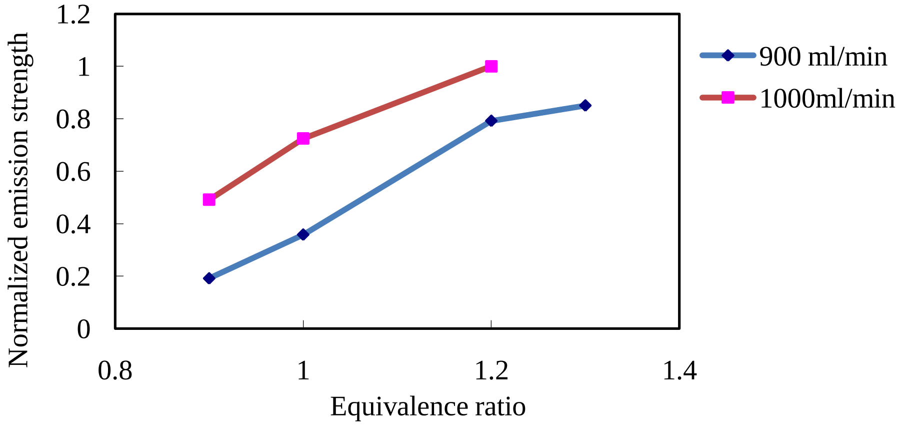

Figure 4.23 CH* chemiluminescence yield at 430 nm as a function of equivalence ratio at two air flow rates

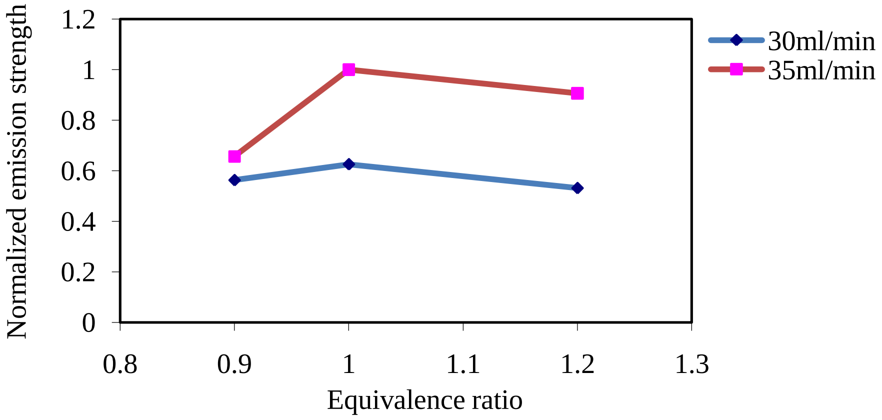

Figure 4.24 CH* chemiluminescence yield at 430 nm as a function of equivalence ratio at two fuel flow rates

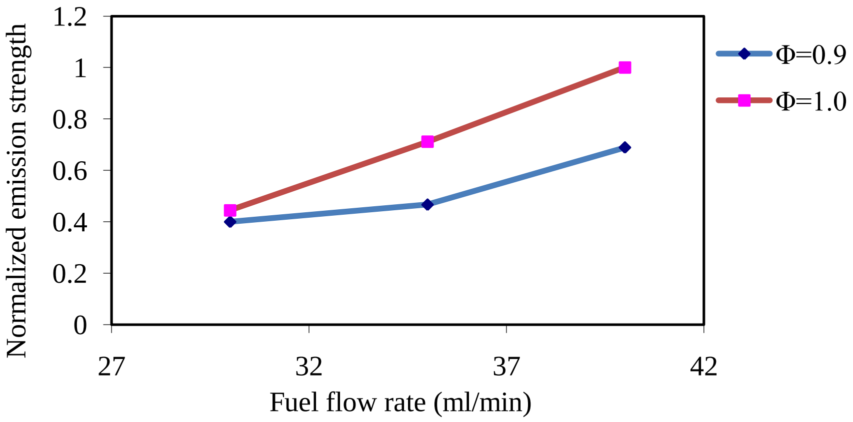

Figure 4.25 CH* chemiluminescence yield at 430 nm as a function of fuel flow rate at two equivalence ratios (Φ)

C2* Chemiluminescence:

The two wavelengths of C2* emissions (470 and 515nm) showed similar trends with variation in air or fuel flow rates and equivalence ratios. Figures 4.26 and

4.27 show the variation of C2* emissions as a function of equivalence ratio at two different air flow rates. The results clearly show an increase in emission with increase in equivalence ratio. However, the rate of increase decreases at fuel rich condition. The variation of C2* with equivalence ratio for a fixed fuel flow rate showed trends similar to CH* emission (see Figure 4.28 and 4.29). Similar to that found for CH*, the peak emission intensity of C2* was found to peak at the stoichiometric condition and decreased on either side of this condition. Figures 4.30 and 4.31 show the variation of C2* with air flow rate at two different equivalence ratios. A continuous increase in emission strength was observed with increase in fuel flow rate.

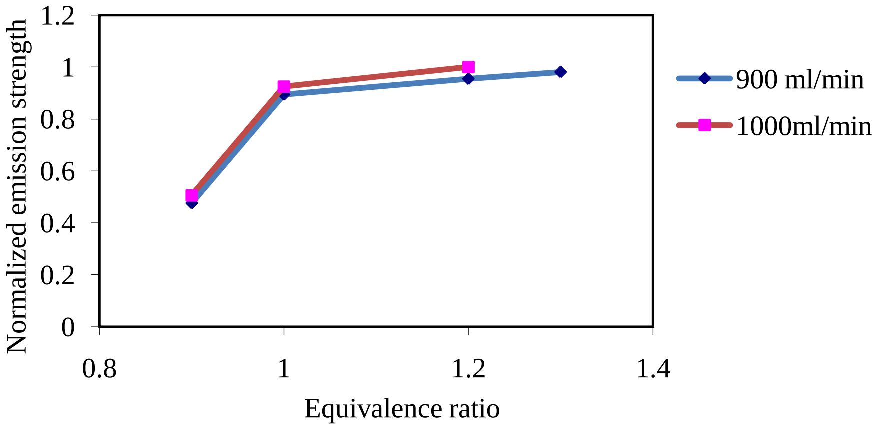

Figure 4.26 C2* chemiluminescence at 515 nm as a function of equivalence ratio at two air flow rates

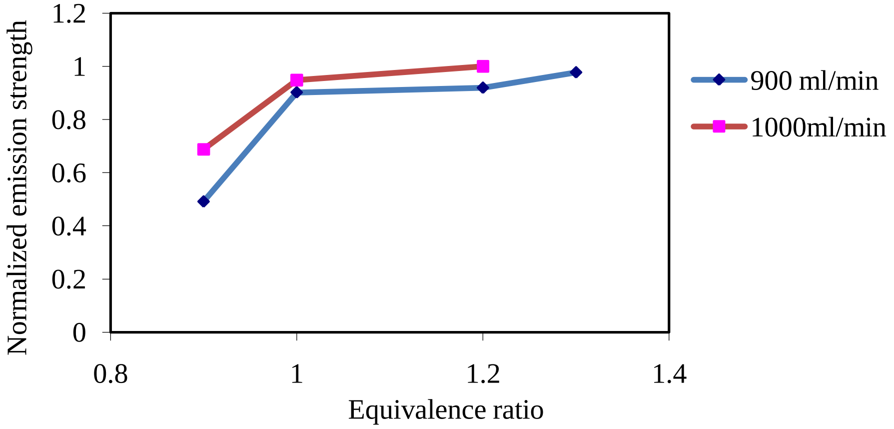

Figure 4.27 C2* chemiluminescence at 470 nm as a function of equivalence ratio at two air flow rates

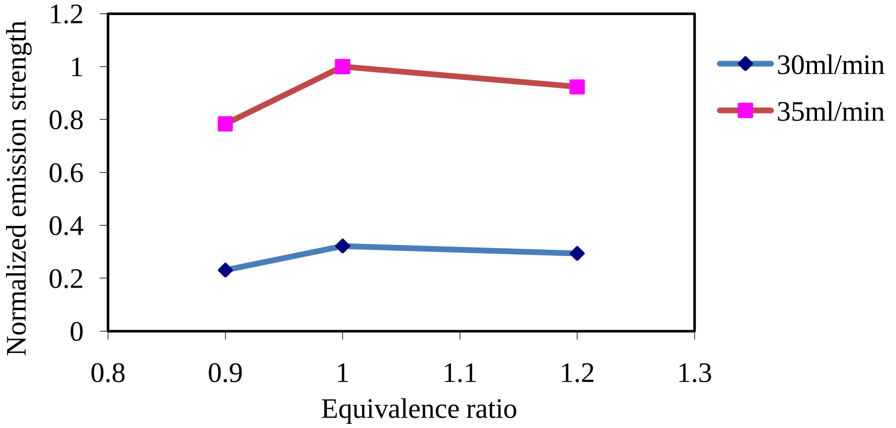

Figure 4.28 C2* chemiluminescence yield at 515 nm as a function of equivalence ratio at two fuel flow rates

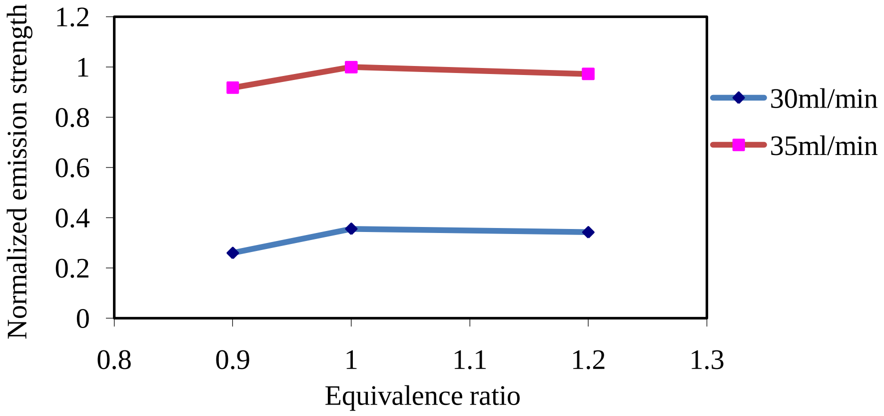

Figure 4.29 C2* chemiluminescence yield at 470 nm as a function of equivalence ratio at two fuel flow rates

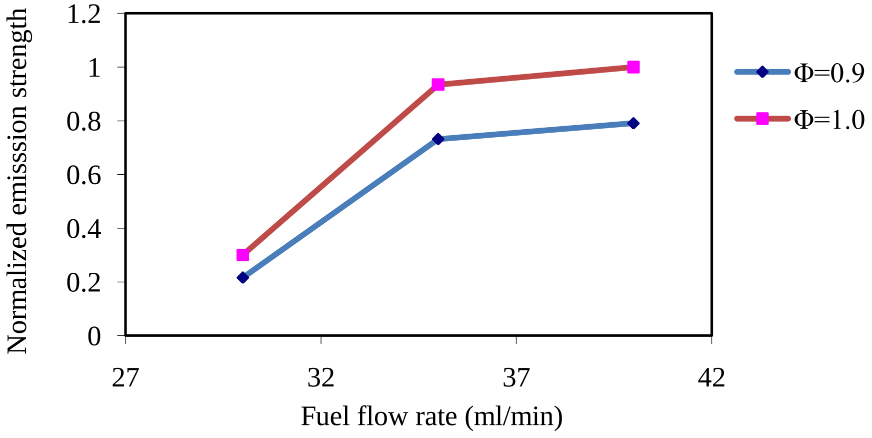

Figure 4.30 C2* chemiluminescence yield at 515 nm as a function of fuel flow rate at two equivalence ratios (Φ)

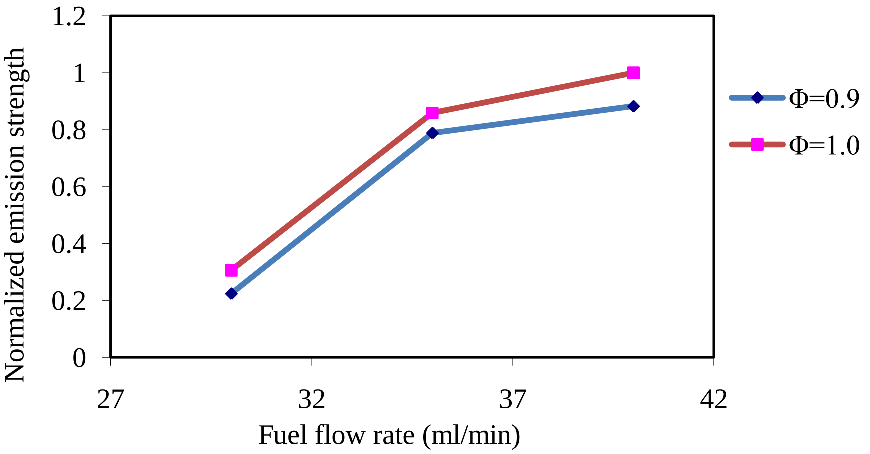

Figure 4.31 C2* chemiluminescence yield at 470 nm as a function of fuel flow rate at two equivalence ratios (Φ)

4.5.4 OH* Chemiluminescence:

The local chemiluminescence values of OH* showed trends similar to those obtained on global chemiluminescence values. Figure 4.32 shows the variation of OH* emission as a function of equivalence ratio at two different air flow rates. Unlike CH* and C2* emission, the OH* emission peaked at the stoichiometric condition. Figure 4.33 shows the variation of OH* with equivalence ratio at two different fuel flow rates. The emission strength is negligibly impacted by the increase in equivalence ratio for fuel rich conditions. For a constant equivalence ratio a continuous increase in emission strength was observed with increase in fuel flow rate (Figure 4.34).

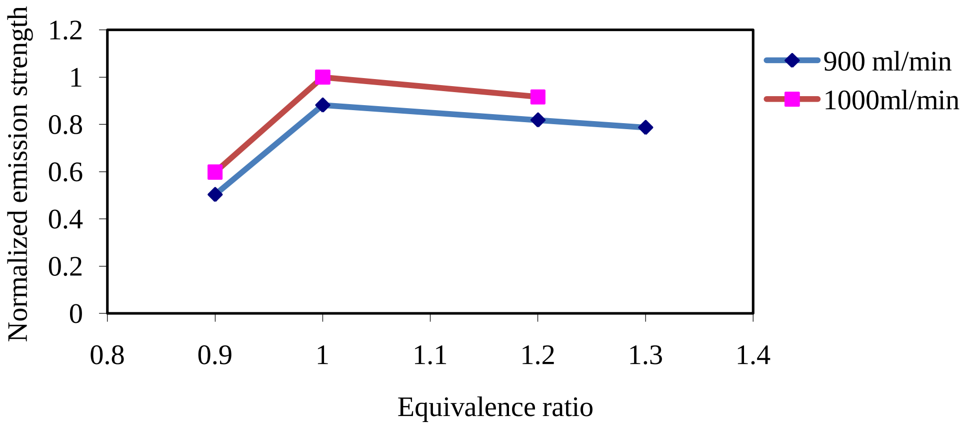

Figure 4.32 OH* chemiluminescence yield at 307 nm as a function of equivalence ratio at two air flow rates

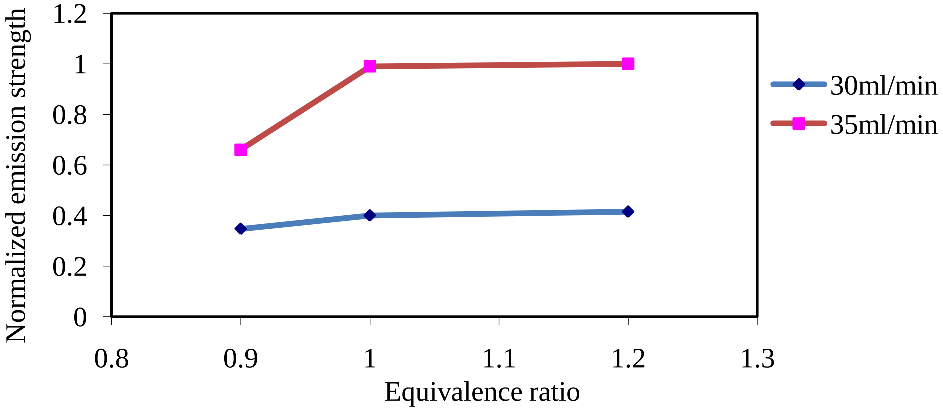

Figure 4.33 OH* chemiluminescence yield at 307 nm as a function of equivalence ratio at two fuel flow rates

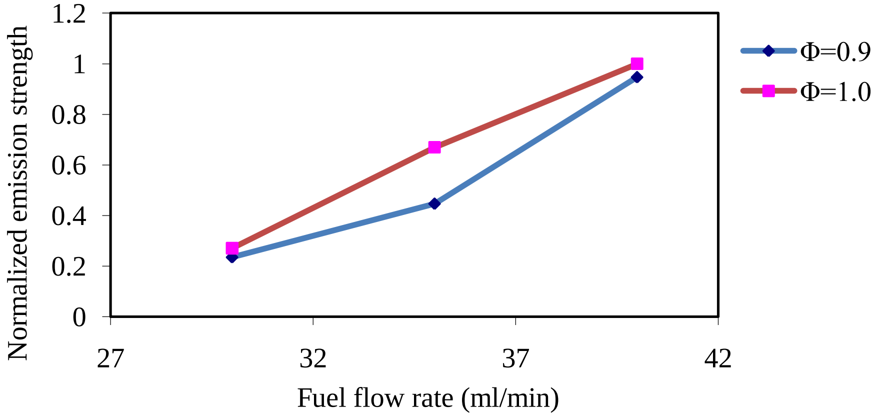

Figure 4.34 OH* chemiluminescence yield at 307 nm as a function of fuel flow rate at two equivalence ratios (Φ)

Chemiluminescence emissions from a propane-air flame inside a meso-scale combustor have been investigated at four different wavelengths for several air and fuel flow rates and equivalence ratio. The emission from the excited OH radicals was different than those obtained from C2 and CH excited radicals. The OH* emissions were confined to a narrow region. The reaction zones predicted by CH* and C2* emissions were rather large. At higher heat loads under slightly fuel rich condition the flame was observed to pre-ignite and stabilize in a narrow channel upstream of the combustion chamber. The OH* images were successfully able to capture the flame location of this combustion mode. In general for a given equivalence ratio, the emission strength increases with increase in flow rate. It can be inferred that for meso-scale combustion with heat recirculation OH* chemiluminescence signal provided good and effective means to detect the presence of flame zone in the combustor. In the combustion zone at the thermal radiation emanating from high temperatures zone of the combustor walls as well as combustion generated particles can adversely impact the chemiluminescence signal in visible part of the spectrum. Further efforts are in progress to help foster the OH* chemiluminescence diagnostics in determining the fate of flame from various types of meso-scale combustors operating under various conditions.

4.6 Effect of Channel length

Three different combustors (A, B & C) were considered here in the present investigation, see Figure 4.35. Of these, we had already presented some results from combustor C in the previous sections (see Figure 4.2). The combustion chamber geometry was identical for all the combustors examined here. They differed only in the lengths of the inlet and outlet channels leading to the combustor section. The non-dimensionalized lengths of the inlet and exhaust channels considered here are given in Table 4.2. Combustor C had the longest inlet and outlet channel lengths while combustor A had the smallest inlet and outlet channel lengths.

Extinction limit map of the three combustors have been obtained experimentally. Variation of reactant preheating and product gas stream temperatures with equivalence ratios and flow rates were investigated. The approach used was to measure the gas stream temperatures using two K-type thermocouples installed at two different locations in the combustor. The temperature measurements reported are average values at the measured location and not the actual temperature profile in the channel cross-section, which is rather challenging to measure experimentally due to very small size of the channel. Having higher reactant preheat temperature helps to reduce the ignition delay and improves combustion efficiency. However, it is to be noted that high preheat temperatures could also mean that the combustion temperature is high which can be detrimental for longevity of the combustion chamber. On the other hand, exhaust temperature is a direct indicator of the combustor thermal efficiency. Global images of the flames obtained inside the combustors are shown in Figure 4.36.

Experimental results revealed significant effect of the channel length on the operating limit map and thermal performance of the combustor. Furthermore, it was confirmed that in the absence of any preheating of the channel, flame could not be sustained at any equivalence ratio or flow rate to the combustor. The operating regime of the combustor was observed to broaden with an increase in channel length. In spite of its ability to broaden the operating limits, combustor with larger channel length was unable to sustain flames at lower mean flow rates. The higher amount of preheats accompanying the longer channel lengths increases the flame speed considerably, thus setting a lower limit on the amounts of flow that can be sent through the combustor to sustain a flame. On the other hand, combustors with smaller channel length could sustain flames at very low mean flow rates. However, for the lowest channel length considered here, combustor could sustain only fuel rich flames, which are not favorable in terms of energy efficiency. It was observed that, for all three cases, the exhaust temperature increased monotonically with decrease in equivalence ratio until the blow-off condition was reached which suggests that the maximum thermal efficiency of the combustor occurs at its lean blow-off limit. For a given fuel flow rate, preheating of the reactant was highest for fuel-rich condition. It decreased monotonically on either side of this condition.

Table 4.2 Non-dimensionalized lengths of the combustor channels (normalized using channel width)

Combustor	Length of inlet channel (non-dimensionalized)	Length of outlet channel (non-dimensionalized)	Total length (non-dimensionalized)
A	19.3	8.1	27.4
B	36	19.2	55.2
C	70.4	45.2	115.6


(a) (b) (c)

Figure 4.35 Combustor geometries investigated for (a) Combustor A, (b) Combustor B, and (c) Combustor C

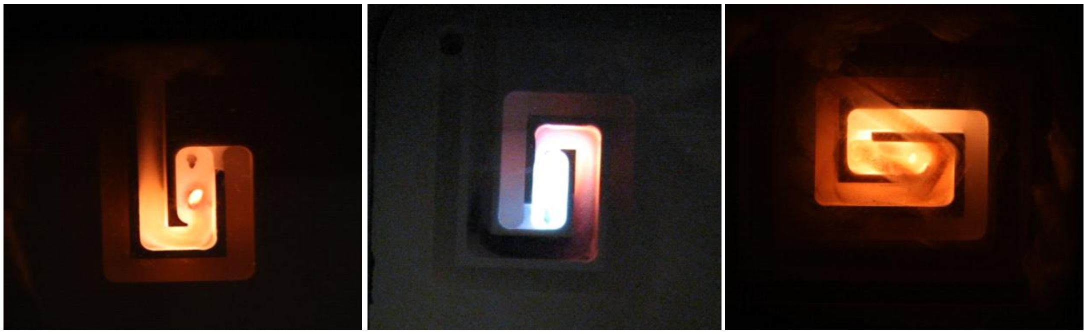

(a) (b) (c)

Figure 4.36 Global image of the propane air flame inside the meso-scale combustors for (a) Combustor A, (b) Combustor B, and (c) Combustor C

4.6.1 Operating Limits

The flame stability and extinction limits of the combustors are shown in the Figure 4.37. The errors associated with the measurements are reported in Appendix A. As expected, the combustors had a fuel-rich extinction limit as well as a fuel-lean extinction limit. The data shows that both of them lie well within the reported flammability limits of propane-air flame at the normal state condition [112]. Several researchers have reported extra lean combustion or the so-called super adiabatic flame in large-scale Swiss-roll combustors [113]. However, this was not observed for the meso-scale combustors investigated here. This is attributed to the higher heat loss in smaller scale combustors. For all three combustors investigated here, maximum possible flow rate for sustained combustion could not be determined with the existing experimental facility. This implies that stable flames were observed in all three combustors for mean flow velocities as high as 12 m/s which is around thirty times the laminar flame speed of propane-air mixture at standard conditions [114].The minimum mean flow velocity which was observed to be 0.66 m/s (for combustor A) was also higher than the laminar flame speed of propane-air. The presence of high flame speeds (high burning rates) due to preheating of the reactant led to very high power densities (~ 4.3 GW/m^3) inside the combustion chamber. This high power density is one of the unique features of meso-scale combustors.

For combustor A, the operating limits (especially the fuel-rich limit) narrow with increase in total flow rate, see Figure 4.37.a. In addition, this combustor was never able to sustain a flame under fuel-lean conditions. This implies that due to its smaller inlet channel length, the amount of preheating achieved is not sufficient to overcome the heat losses at fuel-lean conditions.

The fuel-rich extinction limit of combustor B shows a similar trend as that observed for combustor A, see Figure 4.37.b. However, with increase in flow rates, the lean extinction limit was observed to broaden. This is due to the relatively higher preheating possible in combustor B as compared to combustor A. The minimum mean flow velocity required for sustained combustion inside this combustor is 0.68m/s.

Combustor C behaved quite differently from combustors A and B (see, Figure 4.37.c). Operating limit map is narrowest at the lowest flow rate, which is contrary to that observed for A, and B. Operating limits broaden considerably with increase in flow rate of the reactants to the combustor. Furthermore the minimum possible mean flow velocity for sustaining the flame inside this combustor was much higher (1.78 m/s) when compared to A and B (that was only 0.66 and 0.68 m/s, respectively), see Figure 4.38.

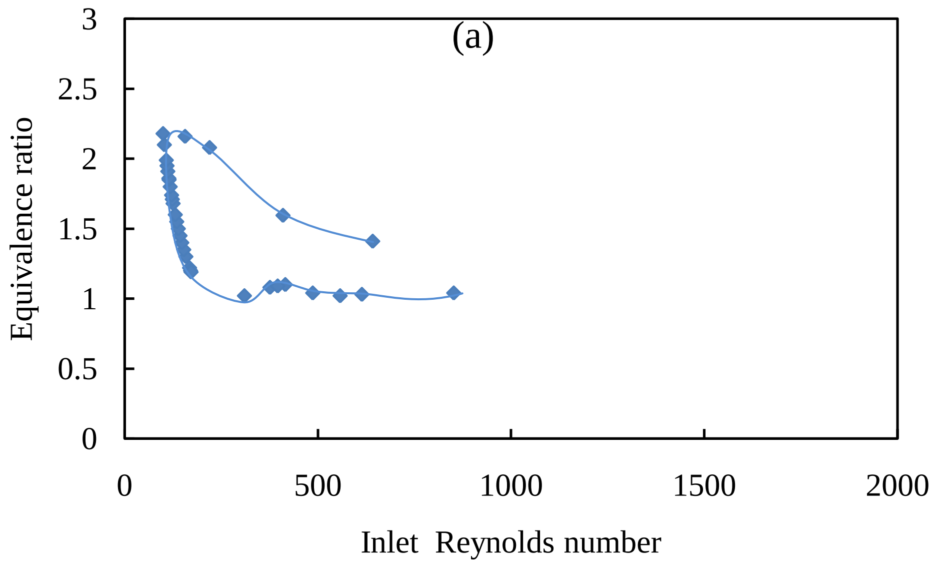
(a)
Equivalence ratio
3
2.5
2
1.5
1
0.5
0
0
500
1000
1500
2000
Inlet Reynolds number

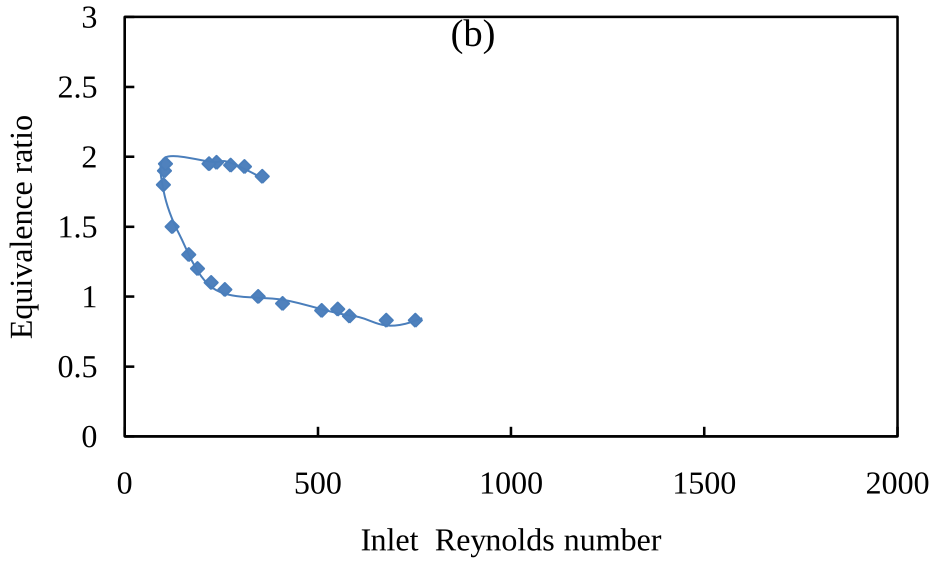
(b)
Equivalence ratio
3
2.5
2
1.5
1
0.5
0
0
500
1000
1500
2000
Inlet Reynolds number

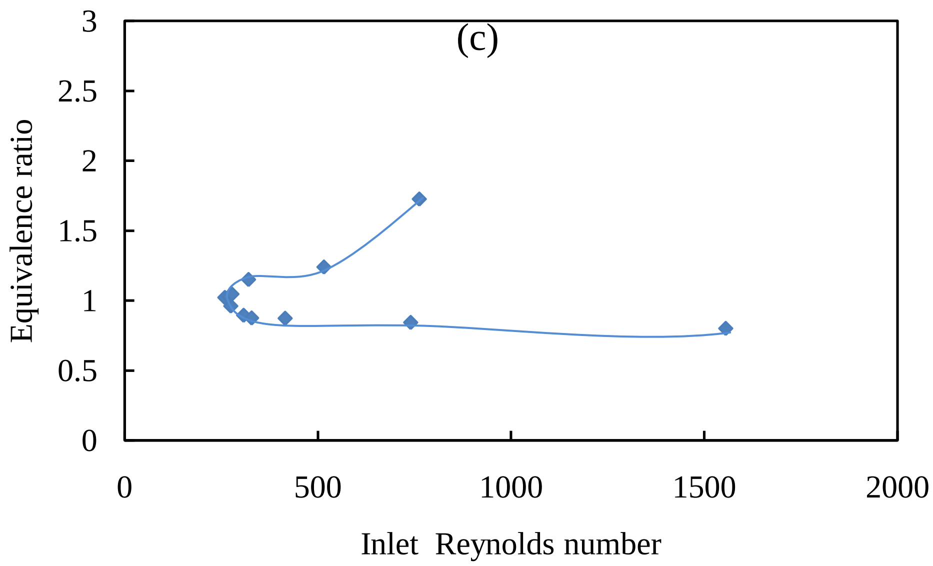

Figure 4.37. Extinction limits of combustors with respect to inlet Reynolds number (a) Combustor A, (b) Combustor B, and (c) Combustor C

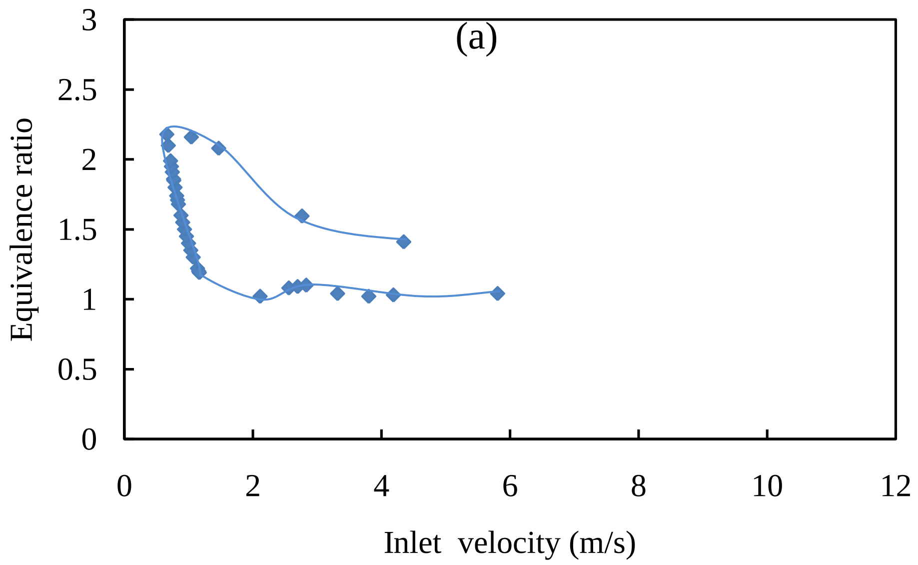

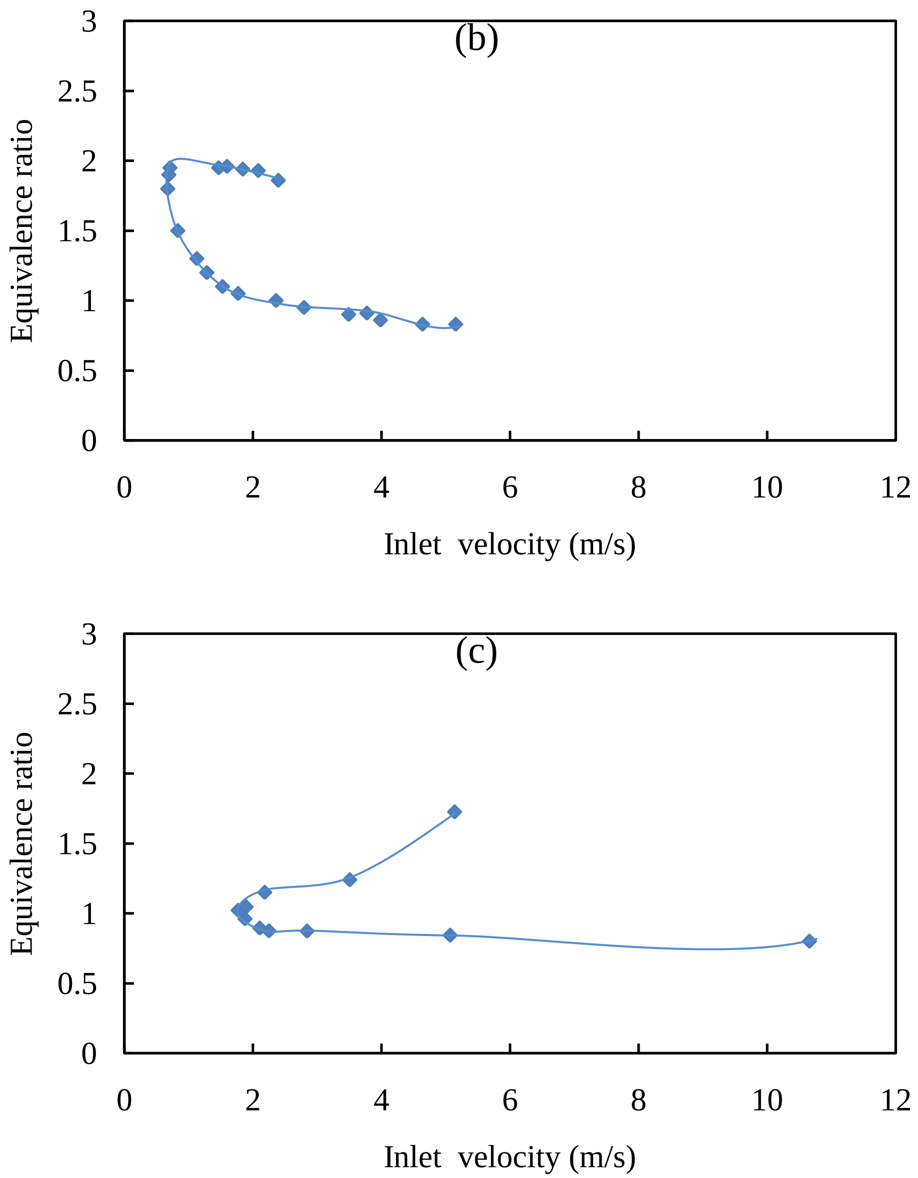

Figure 4.38. Extinction limits of the combustors (with respect to mean inlet velocity (a) Combustor A, (b) Combustor B, and (c) Combustor C

4.6.2 Preheat Temperature

Figure 4.39 shows the variation of preheat temperature with equivalence ratio at different fuel flow rates. As expected, the temperatures observed for combustor A were the lowest (590 K-775 K). For combustor B the temperatures observed were in the range 625 K-845 K. Combustor C had the highest amount of preheating (700 K-1060 K). For all the three cases, the preheating temperature peaked at a particular equivalence ratio and decreased monotonically on either side of this peak value. For combustors A and B, equivalence ratio at the peak value was close to 1.3. For combustor C however, this was close to stoichiometric condition and slightly towards the fuel-rich side. For a given equivalence ratio, the preheat temperature increased with increase in fuel flow rate. This was true for all three combustors examined here. In general, the minimum preheat temperature was observed at the fuel-rich extinction limit for all the combustors. The behavior of preheat temperature with equivalence ratio can be explained based on two competing phenomena. For a constant fuel flow rate, as the equivalence ratio is increased beyond the stoichiometric condition, the amount of fuel which burns and releases energy decreases to result in lower combustion temperature which in turn decreased the preheat temperature. However, an increase in equivalence ratio implies a lower mass flow rate of air that needs to be heated up. Therefore, this effect tends to increase the preheat temperature. On the right side of the peak equivalence ratio, the latter effect dominates the former and vice versa.

In the case of combustor C, it was observed that for slightly fuel-rich conditions ($1.03 < \Phi < 1.26$) when the preheat temperature is high (> 1000 K) the flame goes into a noisy mode and was also accompanied with a shift of the flame position to an upstream location. Figure 4.40 shows the OH chemiluminescence image obtained during this mode. This location coincides with the thermocouple location and therefore during this mode the preheat temperature of the reactant could not be measured, see Figure 4.39.c. This mode starts because of the pre-ignition of the mixture before reaching the combustion chamber due to high preheats temperature. High levels of acoustic emissions (noise levels) observed imply the presence of flame instability associated with this mode.

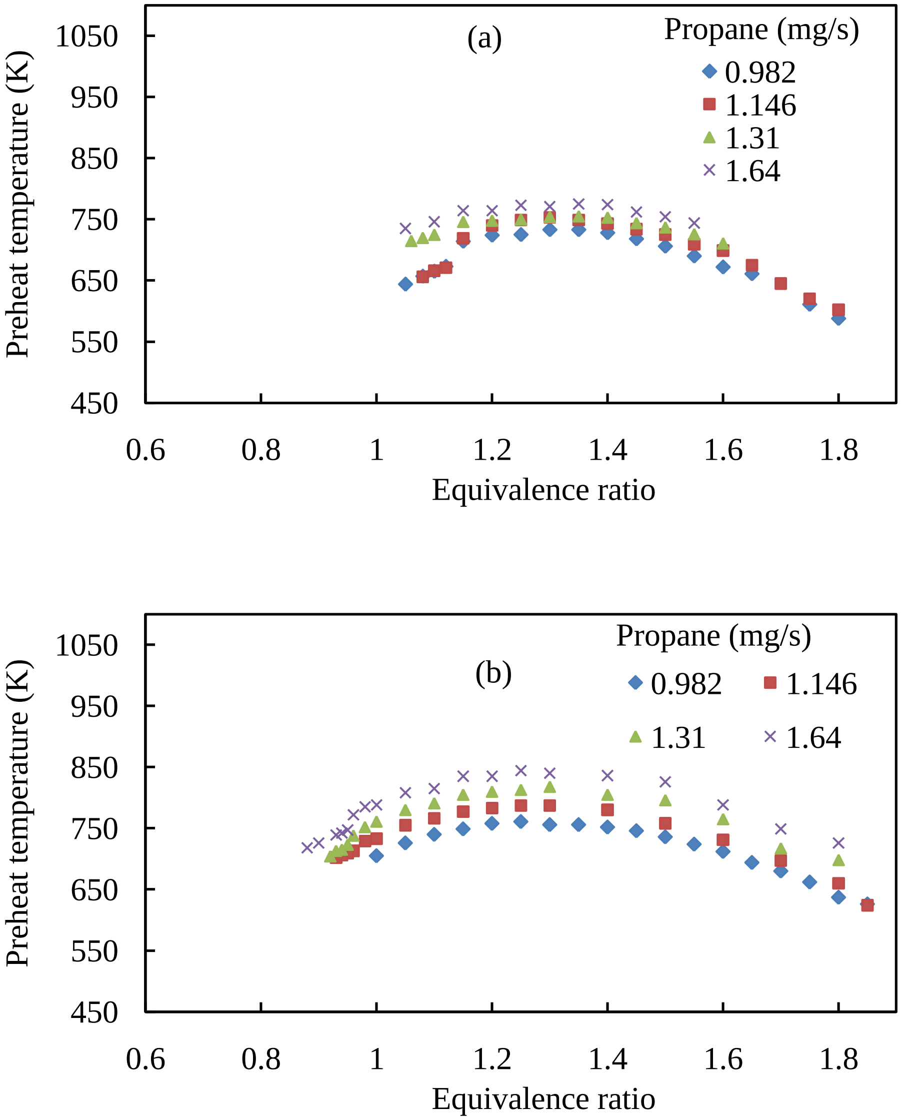

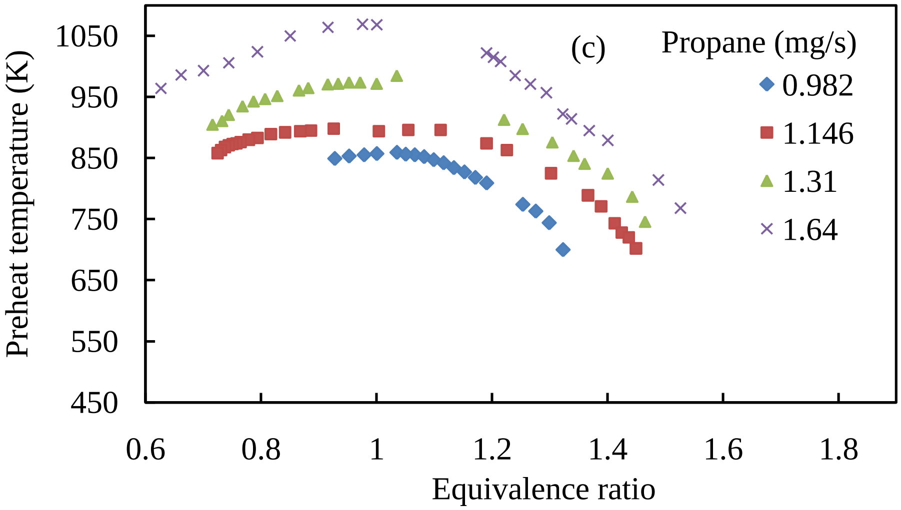

Figure 4.39 Preheat temperature vs. equivalence ratio at various propane flow rates for (a) Combustor A, (b) Combustor B, and (c) Combustor C

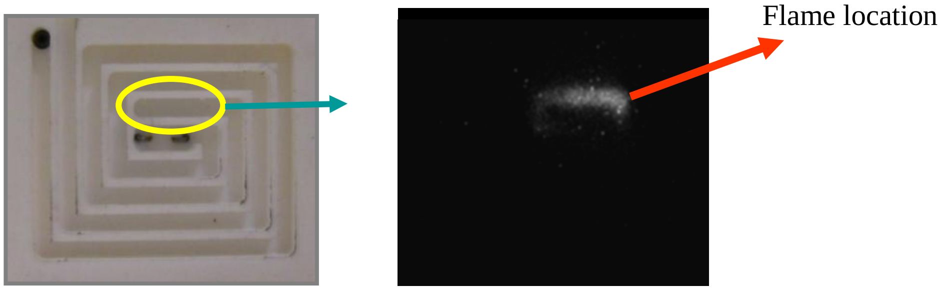

Figure 4.40 OH chemiluminescence image of the pulsating flame mode in combustor C

4.6.3 Exhaust Temperature

Figure 4.41 shows the variation of exhaust temperature with equivalence ratio at different fuel flow rates. The temperatures observed were in the range 740-1070 K for combustor A, 585-915 K for combustor B and 500-750 K for combustor C. Clearly, having longer channel lengths is unfavorable for achieving higher exhaust temperatures. For all the three combustors, the exhaust temperature decreased monotonously with increase in equivalence ratio for a constant fuel flow rate. The trend for fuel-rich cases is as expected. Here, the decrease in exhaust temperature with increase in equivalence ratio is due to lower combustion temperatures. However, for fuel-lean cases (Figures.4.41 b and c) the trend is counter-intuitive. As the airflow rate is increased from stoichiometric condition, the combustion efficiency increases, reaches a maximum value and then starts to decrease. The combustion temperature is lower for fuel-lean condition as compared to the stoichiometric condition. Also, there is a higher mass flow rate of air at lower equivalence ratios that needs to be heated up. Despite these factors, the exhaust temperature increases with the increase in air flow rate. This implies that the heat losses to the ambient decreases considerably with decrease in the equivalence ratio. Therefore, one can conclude that lean premixed combustion is the most thermally efficient condition for meso-scale combustor. This is particularly significant in the case of combustor C.

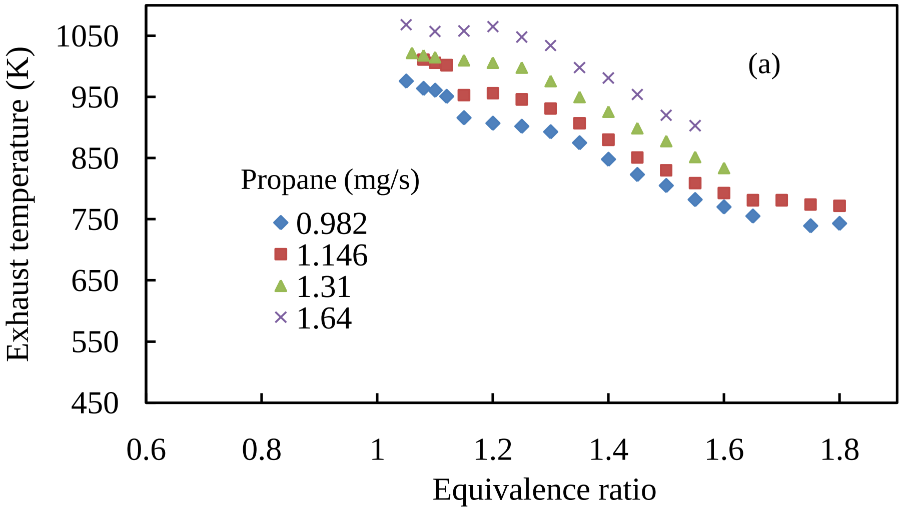

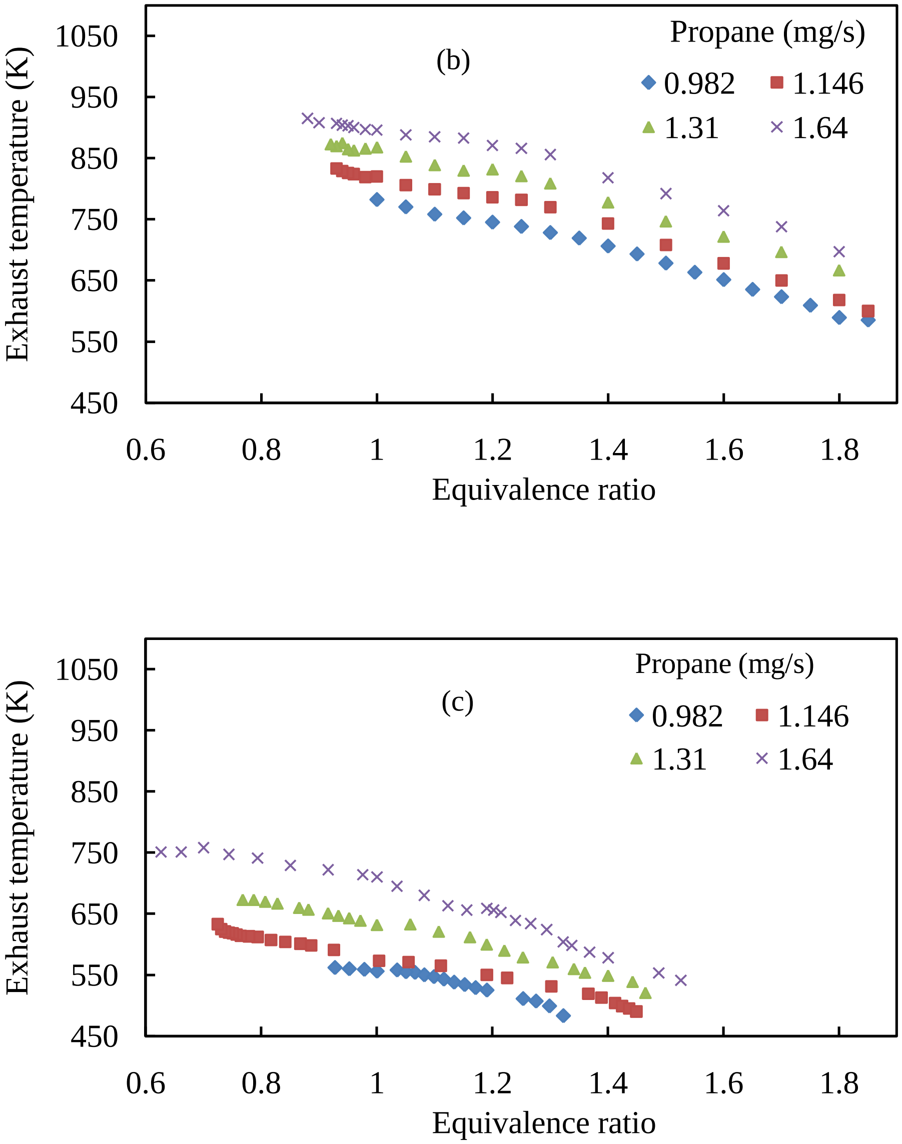

Figure 4.41 Exhaust temperature vs. equivalence ratio for various propane flow rates for (a) Combustor A, (b) Combustor B, and (c) Combustor C

4.6.4 Efficiency

The output power from the combustors was calculated using exhaust temperature. For calculating the specific heat at the exhaust it was assumed that after combustion, species composition remains frozen till it reaches the exhaust. Product species were calculated assuming that the reactions reach equilibrium condition. Equilibrium calculations were performed (using CEA software) combustion by considering 150 species. Of these only 11 species (CO, CO2, H, H2, H2O, NO, N2, O, OH, O2, Ar) which had a significant presence after the reaction were chosen for specific heat calculations. Temperature dependent isobaric specific heat values of the above ten species were employed for the calculations. This data was obtained from the NIST online database [122]. The output power was calculated using the product mass fraction, specific heat values and mass flow rate. The energy at the exhaust was calculated using the product mole fraction and specific heat values.

Figure 8 shows the output power of the products at exhaust (normalized using the corresponding heat load) as a function of the equivalence ratio at different fuel flow rates. For a constant fuel flow rate, the variation of output power with equivalence ratio was similar to that of the exhaust temperature. However, the rate of decrease in output power with increase in equivalence ratio was higher than the rate of decrease of exhaust temperature. This can be attributed to the net decrease in the specific heat of the mixture with increase in equivalence ratio. From the calculations it was observed that for a constant temperature the specific heat of the products increases with the increase in equivalence ratio. Similarly for a constant mixture composition the specific heat increases with increase in temperature. In the present case variation of specific heat with temperature was much more significant than that with mixture composition. The net effect is the drop in specific heat value with increase in equivalence ratio.

The energy efficiency was observed to vary in the range of 15% to 50% for the set of conditions considered here. Combustors were observed to operate at higher efficiency at higher fuel flow rates for a given equivalence ratio. When the equivalence ratio and fuel flow rate were held constant, combustor A was observed to have the highest efficiency and combustor C the lowest. Combustors A and B operate mostly in fuel rich conditions unlike combustor C which could operate well in fuel-lean and fuel-rich conditions. Since efficiency of the combustor increases with decrease in equivalence ratio, combustor C was able to attain better efficiency than combustors A and B under fuel-lean conditions at higher fuel flow rates, see Figure 4.42. This is despite the fact that the exhaust temperatures measured for combustor C is considerably lower than those measured for combustor A and B.

It can be thus inferred that reducing the channel length reduces the surface area available for heat loss and thereby increases the thermal efficiency of the combustor. However, smaller channel length also implies that there is insufficient preheating of the reactants for sustained combustion under fuel-lean condition. Since highest thermal efficiency occurs at the leanest condition, having higher channel length could be beneficial in some cases.

Since the heat losses to the ambient decreases with the decrease in equivalence ratio, it is not recommended to operate fuel lean when the combustor walls are used as a heater or a thermal source. In this case higher heat losses through the walls are preferable. Figure 8 shows that high heat transfer through the walls (as high has 85% of heat load) is achievable while operating under fuel-rich conditions.

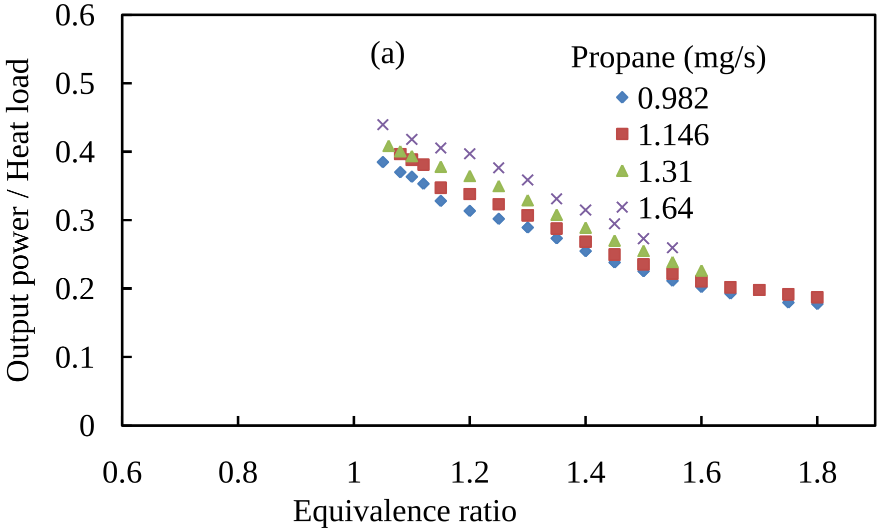
0.6
0.5
0.4
0.3
0.2
0.1
0
Output power / Heat load
(a)
Propane (mg/s)
0.982
1.146
1.31
1.64
0.6
0.8
1
1.2
1.4
1.6
1.8
Equivalence ratio

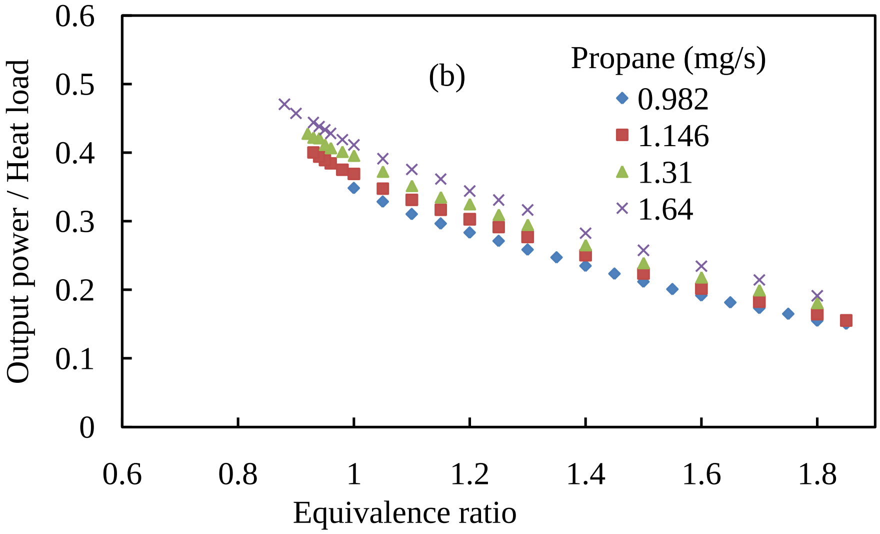
0.6
0.5
0.4
0.3
0.2
0.1
0
Output power / Heat load
(b)
Propane (mg/s)
0.982
1.146
1.31
1.64
0.6
0.8
1
1.2
1.4
1.6
1.8
Equivalence ratio

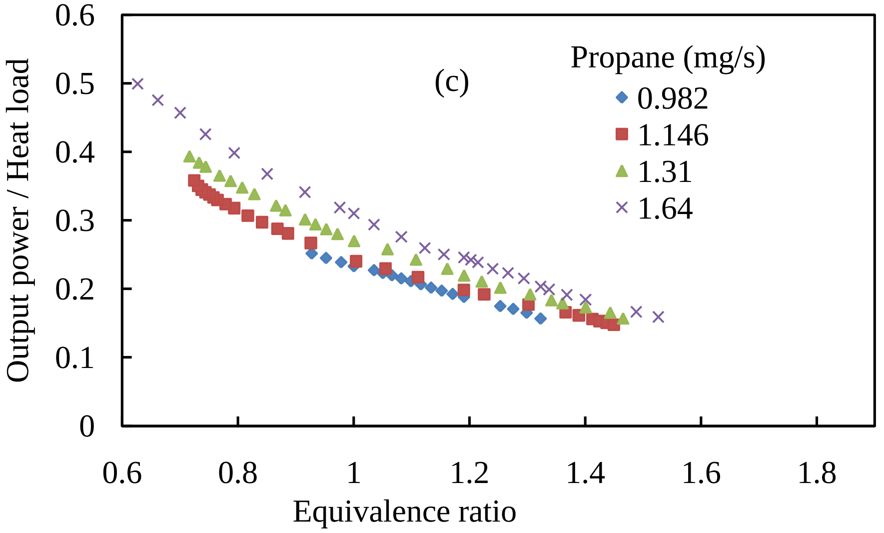

Figure 4.42 Normalized output power (thermal efficiency) vs. equivalence ratio for (a) Combustor A, (b) Combustor B, and (c) Combustor

4.7 Numerical Simulations

Temperature measurements reported in the previous section had shown some trends which need to be explained.

For a given propane flow rate,

1. The exhaust temperature continuously decreases with increase in equivalence ratio
2. The reactant preheating temperature peaks at a particular equivalence ratio and decreases monotonically on either side of this condition.
3. The peak equivalence ratio is observed to move towards the richer direction as the channel length decreases

For a conventional combustor, variation in combustion temperatures with respect to equivalence ratio can be explained based on combustion efficiency. However, for the present case, variation in equivalence ratio and flow rates affects both combustion efficiency and heat transfer simultaneously. Since they are coupled together it is difficult to explain the trends showed by the exhaust and preheat temperatures. This section describes numerical simulations performed by keeping combustion efficiency to be 100%. An attempt is made to isolate the effect of heat transfer through the spiral heat exchanger on the thermal performance. Two different combustors with geometries similar to combustor A and C were investigated (Figure 4.43). The assumptions and wall boundary conditions used for these simulations are same as those employed in section 4.4. 100% combustion efficiency was achieved by decreasing the activation energy of the reactants. Keeping the propane flow rate constant (1.146 mg/s), parametric study on equivalence ratio was performed.

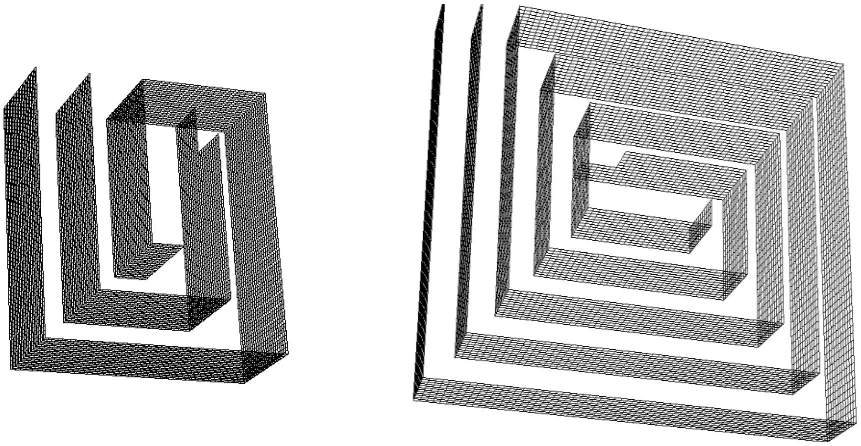

Figure 4.43 Combustor geometries investiagated (a) Combustor A (shorter channels), (b) Combustor C (longer channels)

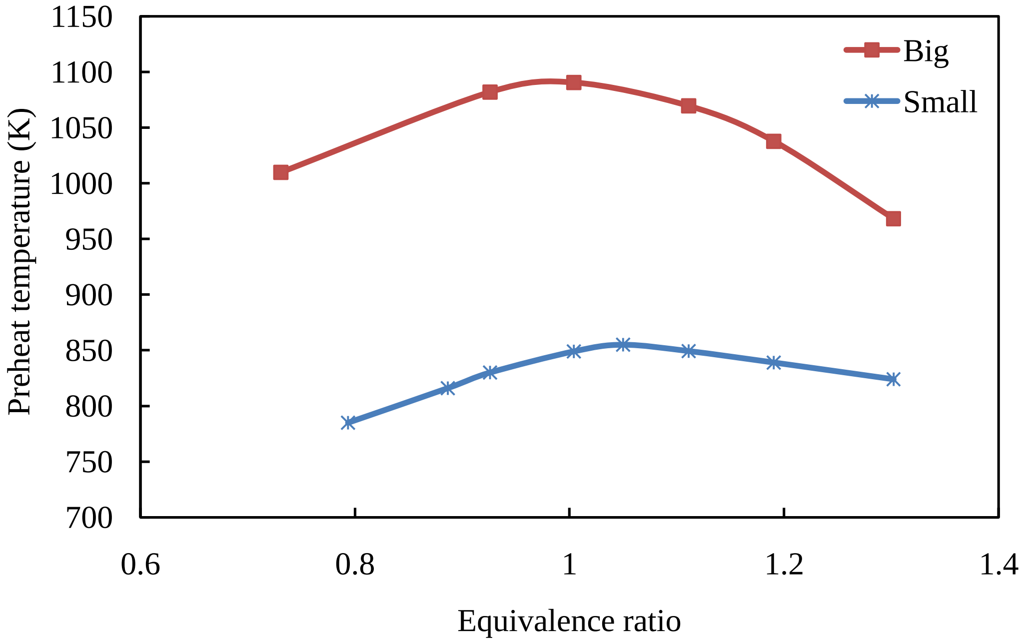

Figure 4.44 Preheat temperature vs. equivalence ratio for propane flow rate of 1.146 mg/s

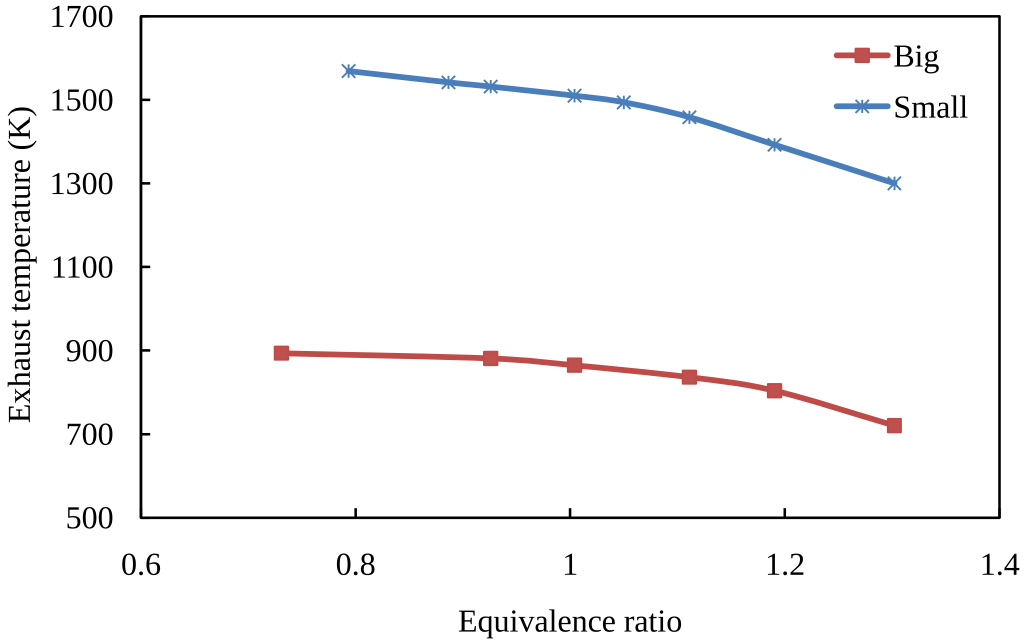

Figure 4.44 Exhaust temperature vs. equivalence ratio for propane flow rate of 1.146 mg/s

Clearly, the numerical simulations over-predict the temperatures compared to experimental values. However, the important thing to note here is that the simulations were able to capture the trend with respect to equivalence ratio. For both the combustors, the exhaust temperature decreased continuously with increase in equivalence ratio for a given fuel flow rate (Figure 4.44). Preheat temperature was observed to peak for a particular equivalence ratio and decrease monotonically on either side (Figure 4.43). The peak equivalence ratio for Combustor C occurs at stoichiometric condition. However, in the case of combustor A, the value shifted to slightly towards the rich side (1.05). Even though this is not close to the value obtained experimentally (1.3), it is clear that the equivalence ratio value for highest preheating temperature shifts towards the rich side as the size of the heat exchanger decreases.

4.8 Flame Dynamics

The combustors showed a wide range of flame dynamics. Several transient phenomena were observed when the inlet flow conditions were varied. However, the flame regimes presented in this paper where those exhibiting limit cycle behavior in the sense that they were self sustaining once initiated. FREI oscillations which were reported by researchers in small scale combustion [123-125] were not observed in the present case. However, since the combustion occurs in a confined space the flame is accompanied by significant acoustic emissions. The flame was observed to excite the harmonics of the hot gases inside the combustor. For some conditions, the flame is affected by the acoustics and oscillates at high frequencies. Though it has some effect on flame stability, the acoustics associated with the flame did not lead to flame extinction. This is evident from the significant acoustic emissions observed over a wide region within the operating regime. The high intensity acoustical oscillations can lead to mechanical failure of the combustor through self excited and sustained resonance. The natural frequency of combustor is related to the mass and stiffness of the material. Combustors machined from Macor ceramic were the only ones which failed due to this effect. Figure 4.48 shows a combustor that was fractured due to acoustical interactions between the flame and the combustion chamber. For the particular combustor shown in Figure 4.48 the crack propagated at a specific equivalence ratio, and the wall temperature was far below the maximum working temperature of the material.

The present section describes the flame dynamics observed in combustor C (Figure 4.35.c) made of zirconium phosphate. Several transient phenomena were observed when the inlet flow conditions were varied. However, the flame regimes presented here are those exhibiting limit cycle behavior in the sense that they are self sustaining once initiated. Five flame regimes were determined based on acoustic signature, reactant preheating temperature and high-speed imaging of the flames. To distinguish between flow noise and flame acoustics, acoustic signals were acquired for non-reacting conditions. Results showed that in the absence of combustion there are no acoustic emissions from the combustor above 60 dB. The distribution of five flame modes across the operatingregime is shown in Figure 4.49. The five regimes are (1) Harmonic regime (whistling flame), (2) Rich limit instability, (3) Lean limit instability, (4) Silent regime and (5) Pulsating flame. Four of the five modes presented here are accompanied with acoustic emissions. Regime #4 was completely silent mode of combustor operation. Regime (1) can be considered as the combustor's base flame mode since this mode is the easiest to achieve. This mode occurs for lower heat loads where the reactant preheating temperature is low (< 1000 K). The acoustic emission from this mode was characterized with the presence of a base frequency (ν_b) and its harmonic modes ($n\nu_b$, where n = 0,1,2,…). The base frequencies were observed to be in the range of 1500-1700 Hz. Clearly, this implies that the combustion is exciting the standing wave modes of the hot gases in the combustor as observed in Rijke tube [126]. Since only the harmonics are excited, the flame acoustics of this mode could be considered as whistling mode. High-speed imaging performed on this regime at 4000 fps showed no flame oscillations. However, it can be assumed that there is some fluctuation in heat release rate since only unsteady heat addition can excite the standing waves. The only multiples of the base frequency observed were 2, 3, 4, 5, 6 and 7. The acoustic signature of the flame in regime (1) at an equivalence ratio of 1.2 for three different flow rates is shown in Figure 4.50. For propane flow rate of 0.976 mg/s the frequencies observed were at a frequency of 1510 Hz and its harmonics (at frequency of 2970, 4460, 5950, 7550, 8910, 10590 Hz). Those observed for 1.068 mg/s and 1.159 mg/s were at a frequency of 1600 Hz and its multiples (3150, 4720, 6300, 8000) and 1700 Hz and its harmonics (3340, 5000, 6670, 8480 and 10000), respectively.

Figure 4.51 shows the variation of base frequency emitted from the combustor (in harmonic regime) vs. input equivalence ratio to the combustor at various propane flow rates. For a given fuel flow rate, the base frequency remains constant as equivalence ratio is varied except when they reach the extremes. The base frequency is more dependent on fuel flow rate than equivalence ratio. When closer to the extinction limits the base frequency decreases to a lower value. For a given equivalence ratio the base frequency is observed to increase with increase in heat load (fuel flow rate). This is due to the increase in the sonic velocity of the gaseous mixture due to increase in temperature distribution throughout the combustor. The acoustic signals observed for regime (1) are clearly due to the excitation of the longitudinal modes of the combustor volume since transverse modes would produce frequencies, which are two orders of magnitude higher due to the small dimensions in the transverse directions. This was confirmed by approximate acoustic calculations performed on a rectangular pipe whose dimensions were comparable to that of the spiral combustor volume. Since all the harmonics were observed, the length of the reactant feed line pipe can be considered open at both ends. For an open-open pipe the first harmonic is ν_b = c/2L where c= sonic velocity and L = total length. Sonic velocity of the combustor can be calculated using the first harmonic ($c=2L\nu_b$). The sonic velocities obtained using this method (experimentally observed base frequencies) were compared with those obtained by approximate calculations performed on propane-air mixture under similar conditions. The calculations were based on several simplifying assumptions. The fluid inside the pipe was assumed to be a homogeneous mixture with uniform temperature. The mixture properties (composition, sonic velocity) were assumed to be that of an equilibrium composition of propane-air mixture calculated for a particular temperature and pressure. In reality, the combustor volume is characterized by a temperature distribution instead of a single temperature. However, an average temperature was used for equilibrium calculations. Several assumptions were made for calculating the average temperature of the combustion chamber. The temperature variation was assumed to be one-dimensional (i.e. along the flow direction). Both preheating and exhaust channels were assumed to have linear variation in temperature, see Figure 4.52. The combustion chamber was a constant temperature (T_{chamb}), which was chosen to be the adiabatic flame temperature of propane-air for the corresponding preheat temperature and equivalence ratio. The average temperature (T_{avg}) was then calculated using a length weighted average.

$$T_{avg} = \frac{(T_{in} + T_{pre})*0.5*L_{pre} + T_{chamb}*L_{chamb} + (T_{chamb} + T_{out})*0.5*L_{out}}{L_{pre} + L_{chamb} + L_{out}} \quad [4.1]$$

Here T_{in} ,T_{pre} and T_{out} are the inlet, reactant preheating and exhaust temperatures, respectively, and L_{pre}, $L_{chamb,}$ L_{out} are the lengths of the preheating channel, combustion chamber and exhaust channel, respectively. $T_{pre\ and}$ T_{out} are dependent on the fuel flow rate and equivalence ratio. These values were obtained experimentally. The comparison of sonic velocities estimated experimentally and from calculations is shown in Figure 4.53. Sonic velocities were plotted with respect to equivalence ratios for three fuel flow rate cases. The calculations compared well with the experiments especially for a fuel flow rate of 1.068 mg/s. The velocities obtained were in the range 550-700 m/s.

The flame was unstable when approaching the lean and rich extinction limits (regimes 3 and 2). The acoustics at the rich and lean extinction limits were noisy as indicated by the presence of a broad band of emission. However, these instabilities were self-sustaining and did not quench the flame. Figure 4.54 shows the acoustic signature obtained at the rich limit for two different propane flow rates. The sound levels observed were low owing to the low intensity of combustion. Figure 4.55 shows the acoustic signature obtained at the lean limit for two different propane flow rates. Sound levels were much higher than that observed at the rich limit.

Regime 4 (silent flame) occurs when the preheat temperature is high (> 1000 K). The flame is extremely steady in this regime. High-speed imaging performed on this regime at 4000 fps showed no flame oscillations. Figure 4.56 shows the acoustic signature of this mode as compared with the background noise levels. Both are very similar implying near zero acoustic emission from the combustor. Here the heat release rate is highly constant such that the acoustic modes are not excited at all.

Pulsating flame mode (regime 5) occurs at high preheat temperatures (> 1000 K) when the equivalence ratio is slightly above unity ($1.03 < \Phi < 1.26$). This mode starts because of the pre-ignition of the mixture due to high preheat temperatures. The flame shifts to an upstream location where the acoustics generated by the flame in turn affects the stability of the flame. The flame was observed to fluctuate at frequencies around 1000 Hz, see Figure 4.57. Since the regular instability phenomena cannot cause the flame to oscillate at this high frequencies it can be safely assumed that this perturbation is a thermoacoustic one. It is possible that the flame location is near a velocity antinode of the standing wave. This is further confirmed by the good comparison between the acoustic signature and high-speed imaging of the flame. The acoustic emissions of this regime are shown in Figure 4.58. The emission spectrum is rather continuous except for the presence of a peak frequency. The peak frequency value matched well with the flame fluctuation frequency obtained from the Fourier transform of high-speed images, see Figure 4.59. As the mixture gets richer the frequency of oscillation decreases (Figure 4.59), until it riches a critical value and the flame shifts back to the combustion chamber and burns in silent mode (Regime 4). As the equivalence ratio increases the flame temperature and the heat release rate decreases. This decreases the resonant frequency of the standing waves of the gaseous mixture inside the combustor, which explains the decrease in the flame fluctuation frequency.

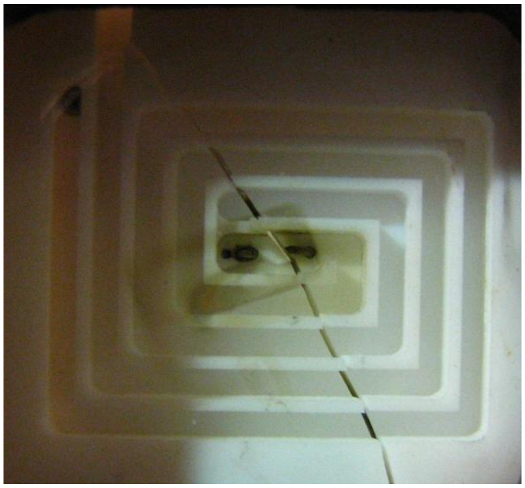

Figure 4.48 Macor combustor that has fractured due to acoustic interactions between the flame and the combustor

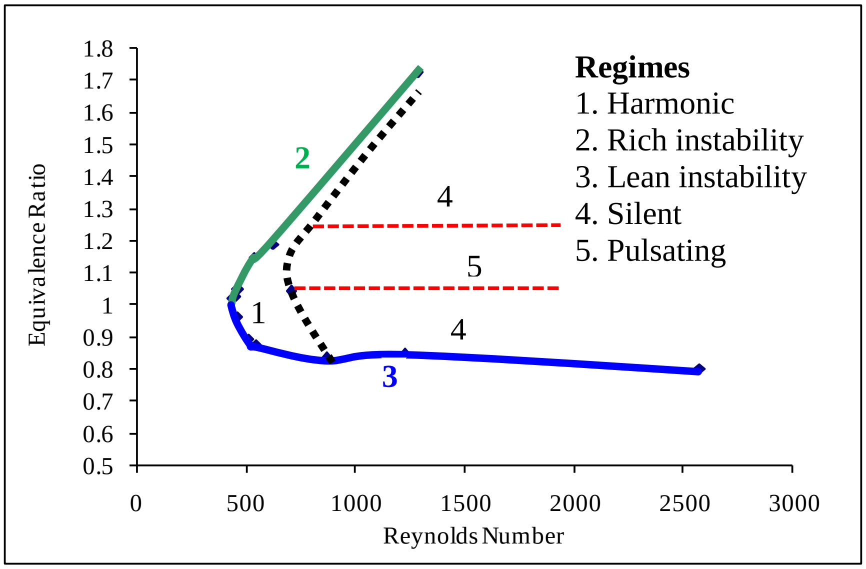

Figure 4.49 Distribution of five flame regimes across the operating regime

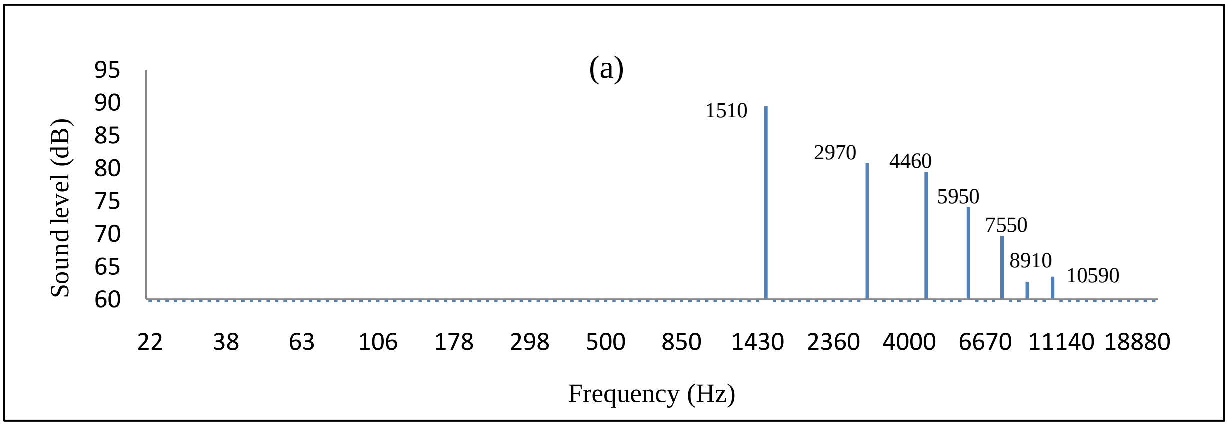

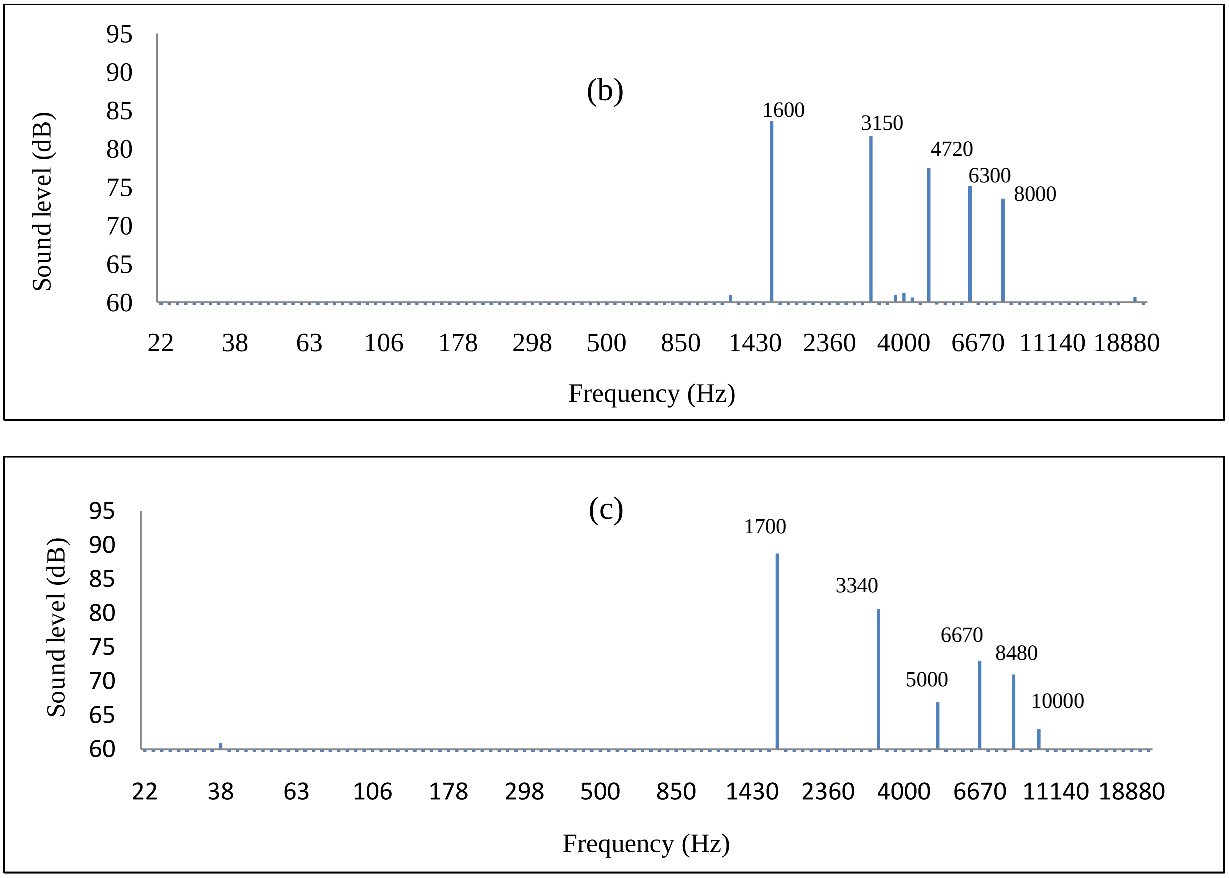

Figure 4.50 Acoustic signature of the flame at equivalence ratio 1.2 for propane flow rate (a) 0.976 mg/s (b) 1.068 mg/s and (c) 1.159 mg/s

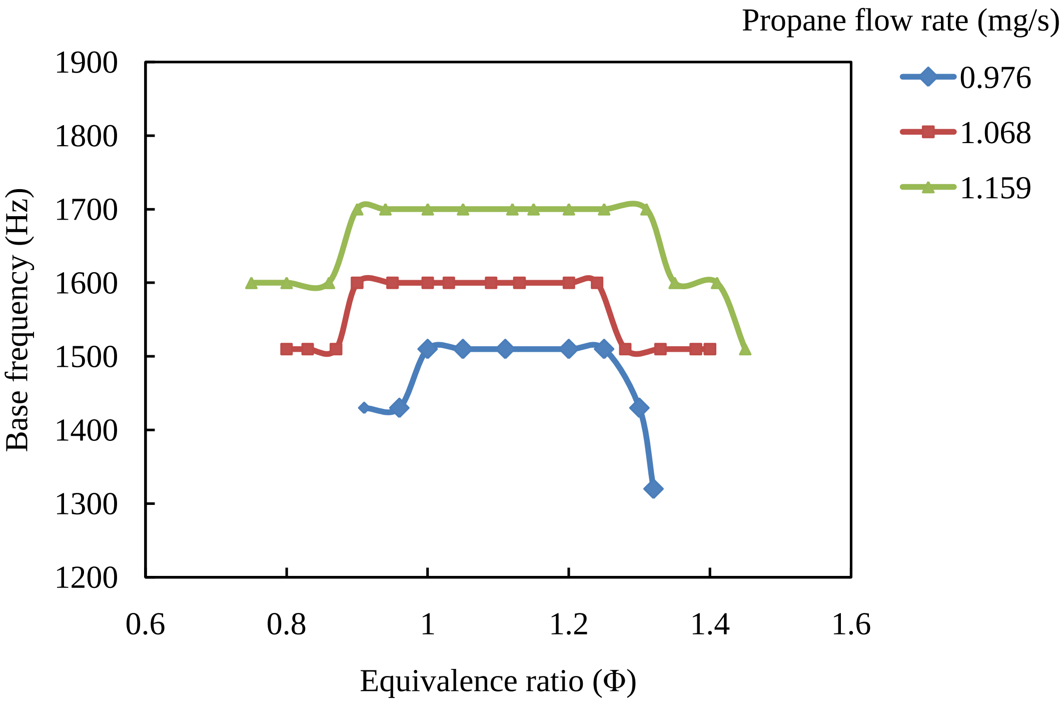

Figure 4.51. Base frequency (First harmonic) emitted by the combustor (in harmonic regime) vs. equivalence ratio at various propane flow rates

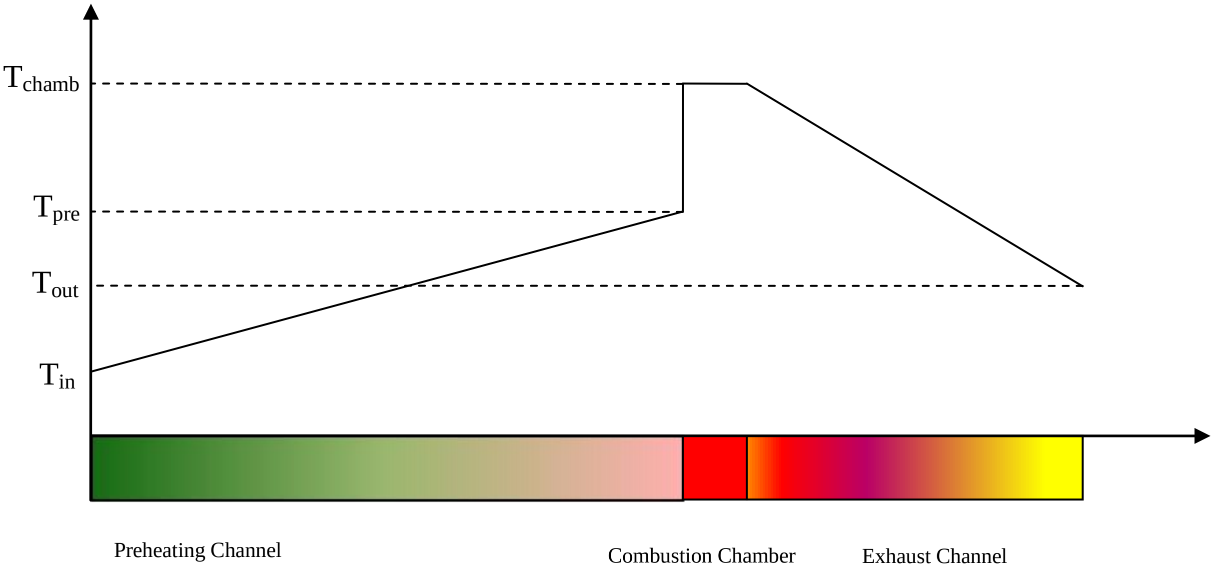

Figure 4.52 Assumed temperature variation along the length of the combustor

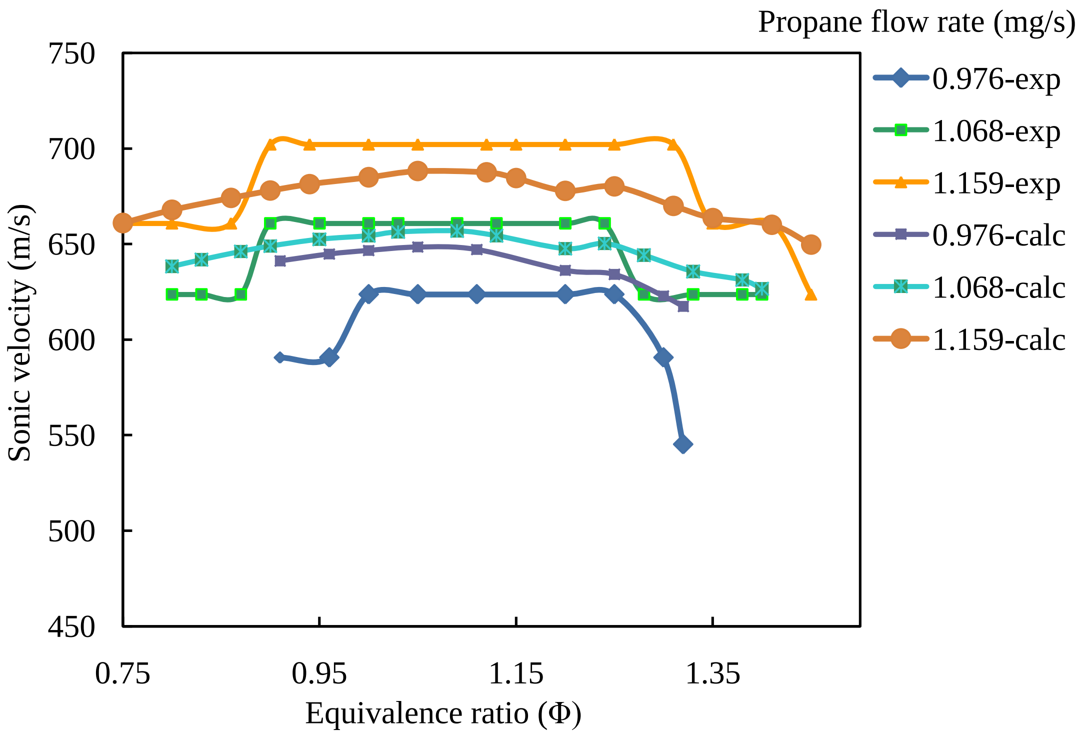

Figure 4.53 Comparison of sonic velocity obtained experimentally and through calculations

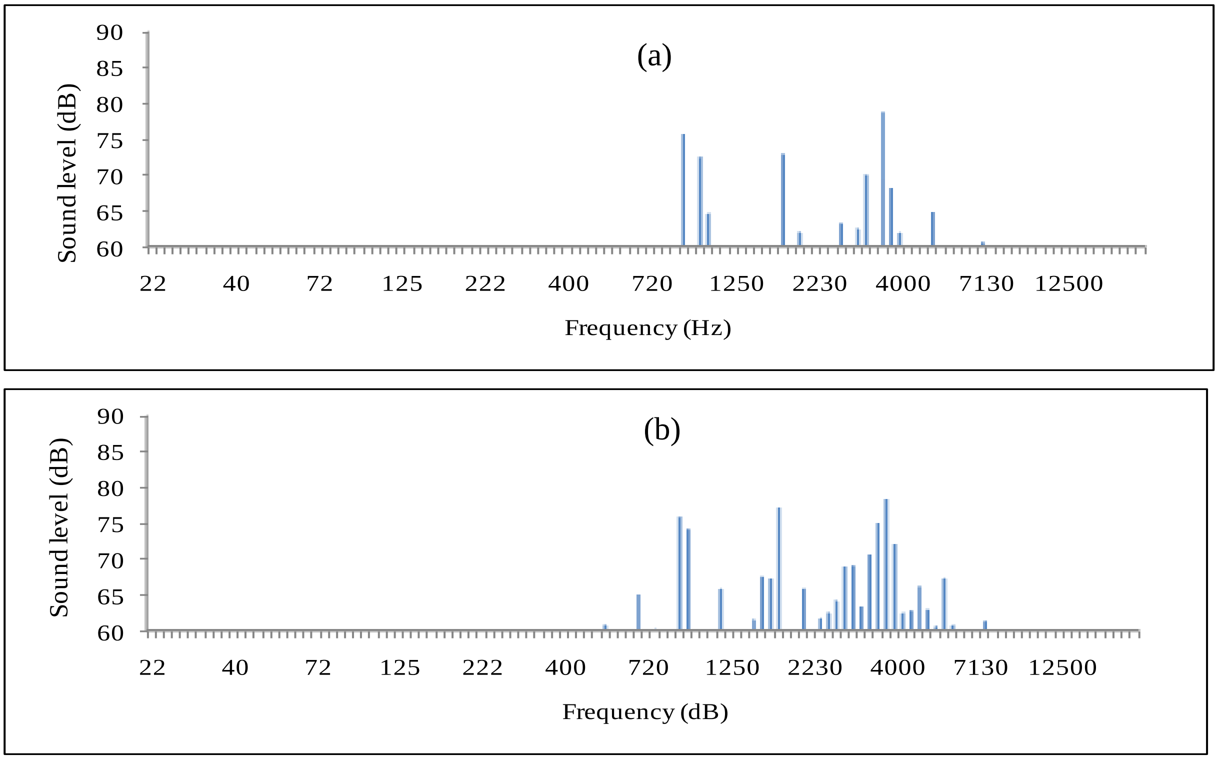

Figure 4.54 Acoustic signature of the rich instability obtained at two propane flow rates (a) 0.982 mg/s and (b) 1.146 mg/s

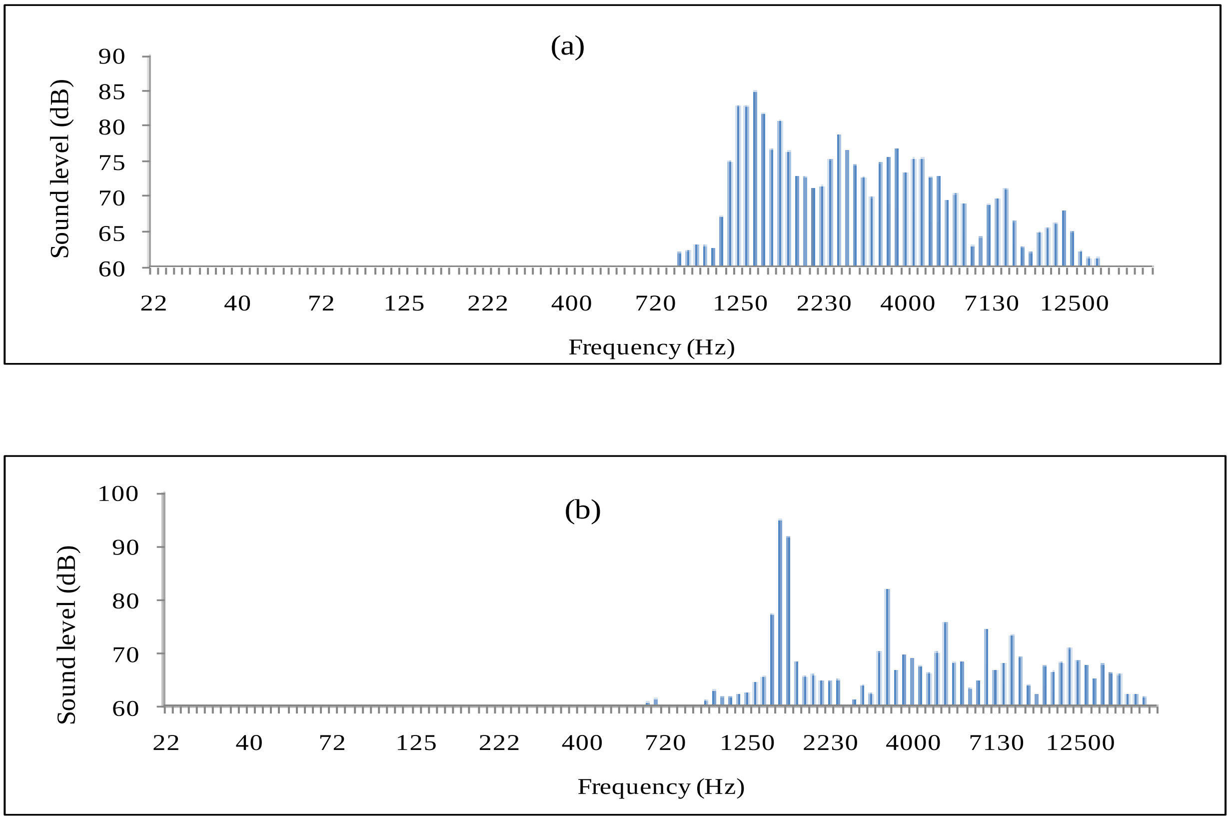

Figure 4.55 Acoustic signature of the lean instability obtained at two propane flow rates flow rates (a) 1.146 mg/s and (b) 1.31 mg/s

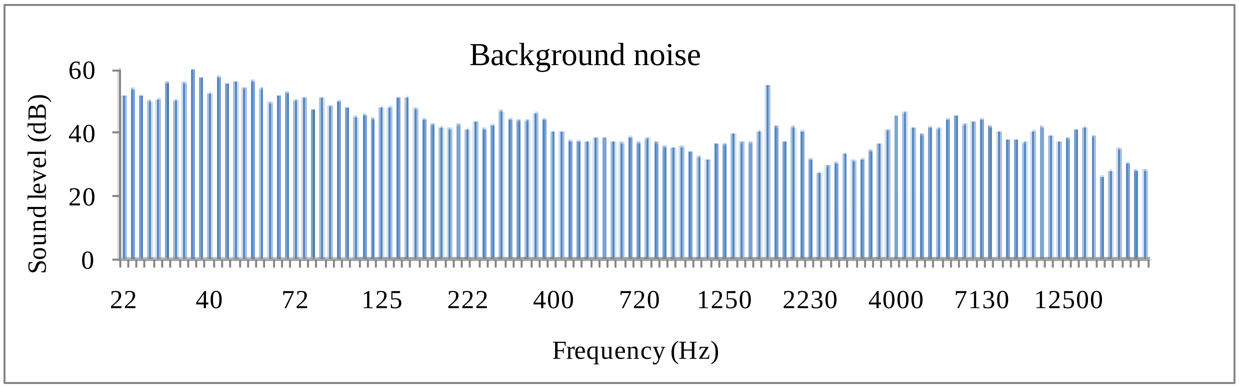

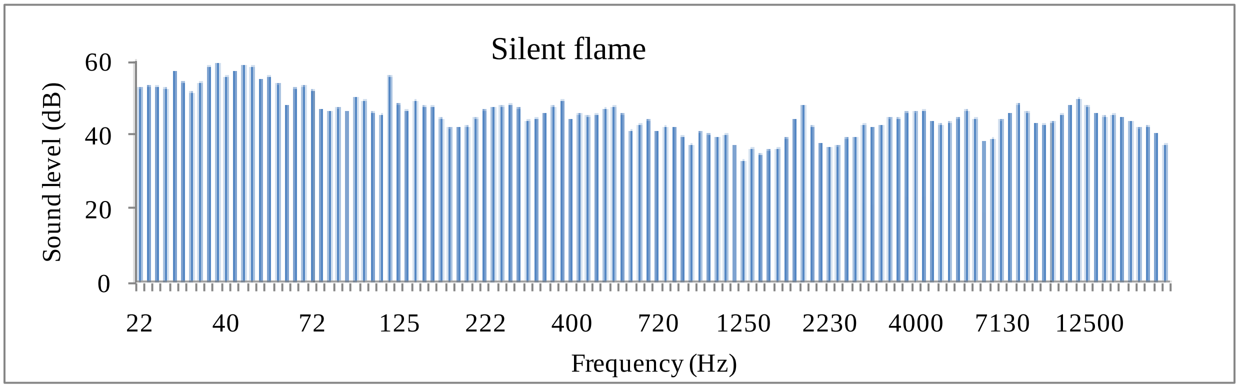

Figure 4.56 Comparison of acoustic signature of background noise with that of the silent flame. Sound levels are below 60dB for both the cases

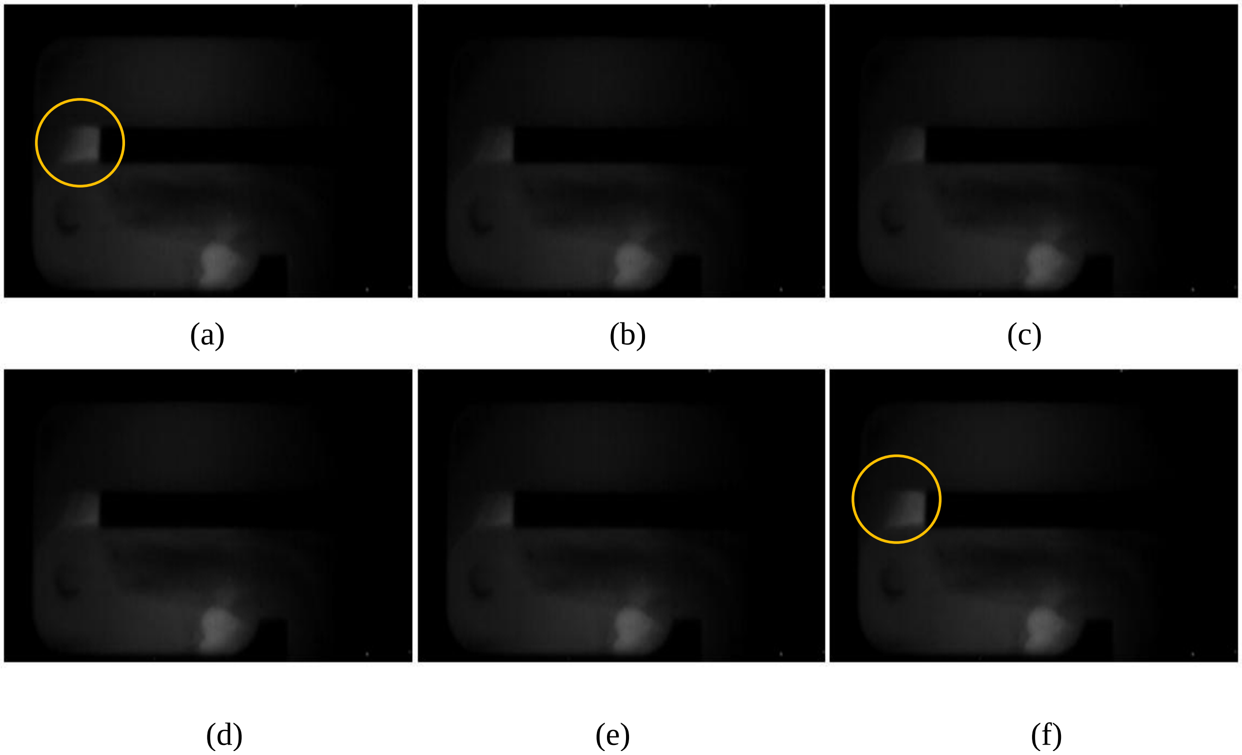

(a) (b) (c)

(d) (e) (f)

Figure 4.57 High speed images of the pulsating flame acquired at 4000 frames per second. The time difference between adjacent images is 2.5 ms. Figures (a) to (f) shows once complete cycle of the oscillation with (a) and (f) having peak intensity values

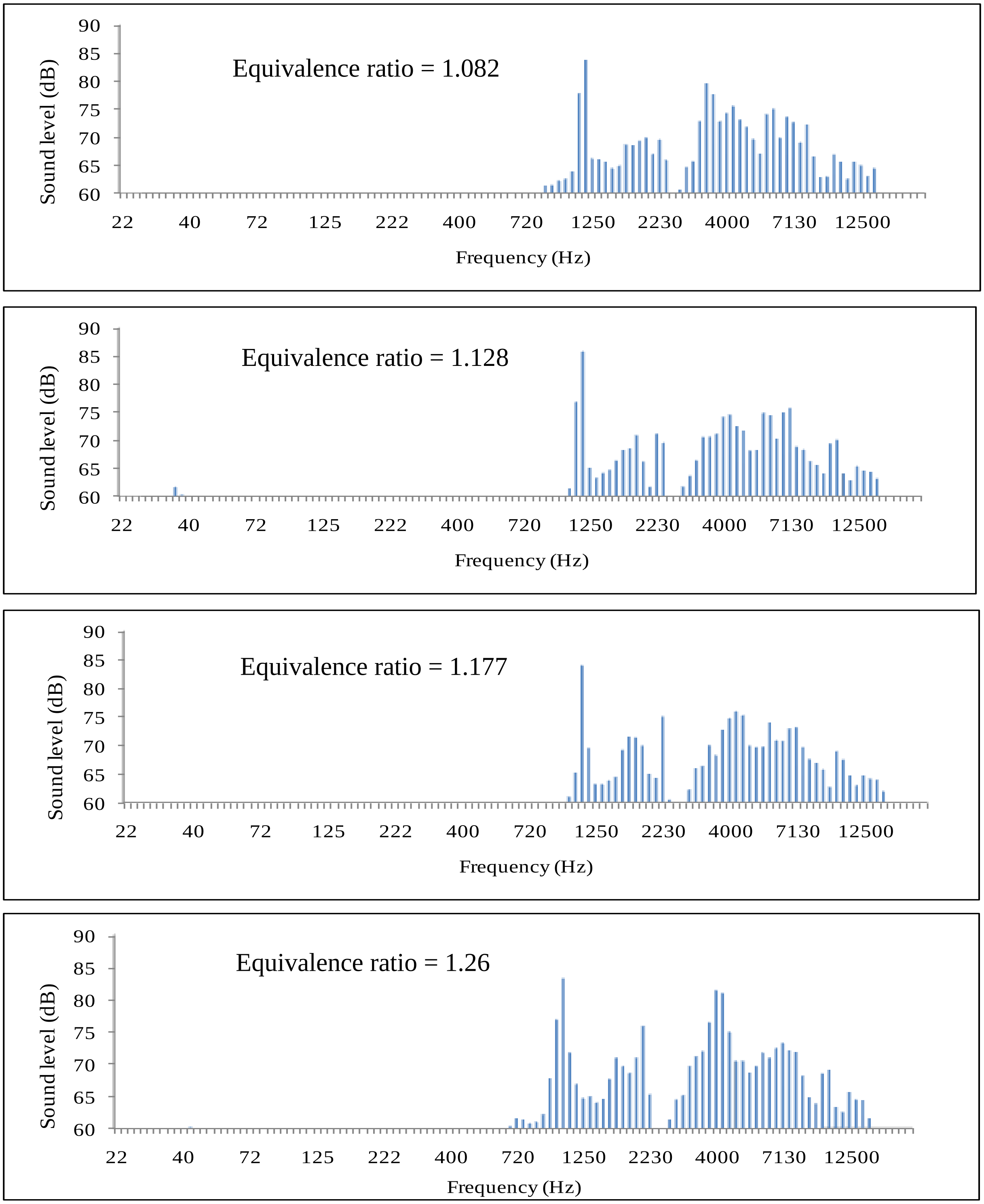

Figure 4.58 Acoustic signature of the pulsating flame obtained at four equivalence ratios for propane flow rate of 1.48 mg/s

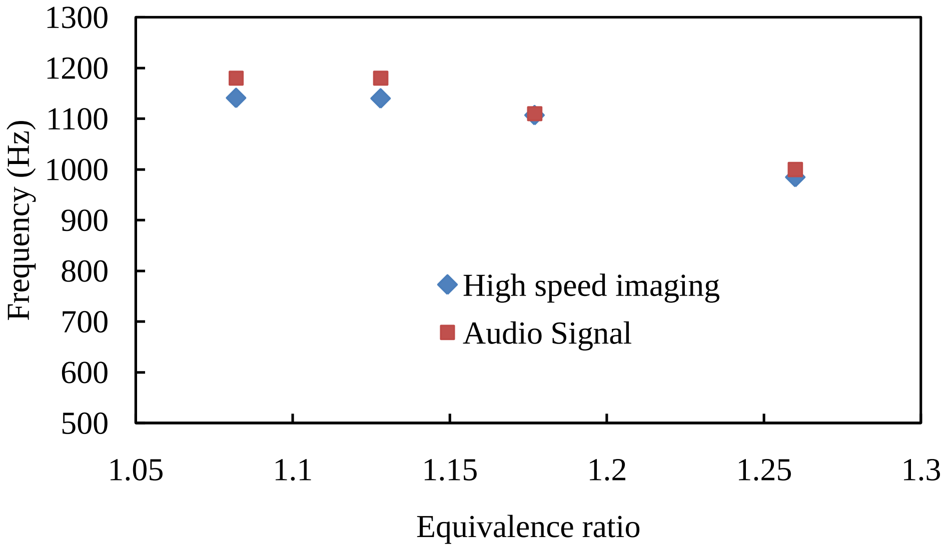

Figure 4.59 Comparison between the dominant acoustic frequency obtained using microphone and the flame fluctuation frequency obtained using high speed imaging for four different equivalence ratios at a propane flow rate of 1.48 mg/s

4.9 Effect of geometric flame holder

Six different flame holder designs were tested for flame holding capability. The common feature of these designs is the blockage ratio (50%). All flame holders induce flow recirculation in the combustion chamber but with different magnitudes and in different directions.

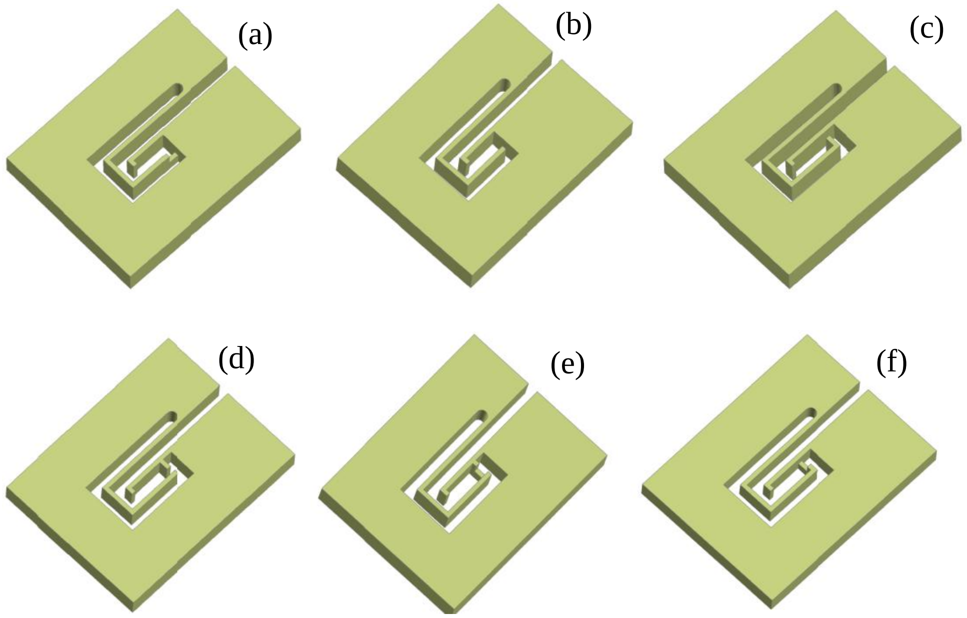

Figure 4.60 Comparison between the dominant acoustic frequency obtained using microphone and the flame fluctuation frequency obtained using high speed imaging for four different equivalence ratios at a propane flow rate of 1.48 mg/s

Since the dimensions involved are extremely small, it is quite easy to assume that the effect on combustion might not vary significantly. However, the results showed the contrary. Only designs ‘a’ and ‘c’ were able to hold the flame. Other designs were not able to hold the flame for any of the flow and equivalence ratio conditions tested. Of the designs ‘a’ and ‘c’, a’’ outperformed ‘c’ by a good margin. The flame sustained in the presence of ‘a’ was quite stable and no visible fluctuations were observed. On the contrary, design ‘c’ resulted in noisy fluctuating flame. The operating regime in the presence of ‘a’ was much broader when compared to that of ‘c’. To understand the difference in the flame holding property of these designs, numerical simulations of the flow field was performed for cold flow case (using Fluent software). Figure 4.61 shows the flow recirculation in the direction opposite to the mean flow direction inside the combustion chamber with respect to axial distance beginning from the inlet to the chamber. Clearly, design ‘a’ has the lowest recirculation in every plane except for a location close to the inlet. Design ‘c’ and other designs showed almost similar behavior.

For comparing the residence time distribution (RTD) the “step method” using tracer injection was employed. In this approach, the species concentration, will be set to a particular value (C_{in}) at the inlet for time t=0, and maintained at this level over subsequent time steps. The species concentration at the outlet will be monitored as a function of time. The variation of concentration-time will follow an F-curve shape (see Figure 4.62). In general it can be assumed that the faster the concentration at the outlet approaches the maximum value, the smaller is the average residence time inside the chamber. From the Figure 4.60 it can be seen that the flow path of the designs ‘a’ and ‘b’ are shorter when compared to the rest. So the RTD comparison is made between ‘a’ and ‘b’ separately from the rest of the designs. Simulations were performed for inlet Re = 150. Figure 4.62 shows the RTD distribution in ‘a’ and ‘b’. Clearly when compared to ‘b’, ‘a’ has unfavorable residence time distribution. Figure 4.63 shows the RTD distribution in the rest of the designs. All the designs showed almost similar trend except for design ‘e’ which was marginally better than the rest. In short design ‘c’ although was able to hold the flame during experiments, does not have any advantage over other designs when it comes to residence time distribution.

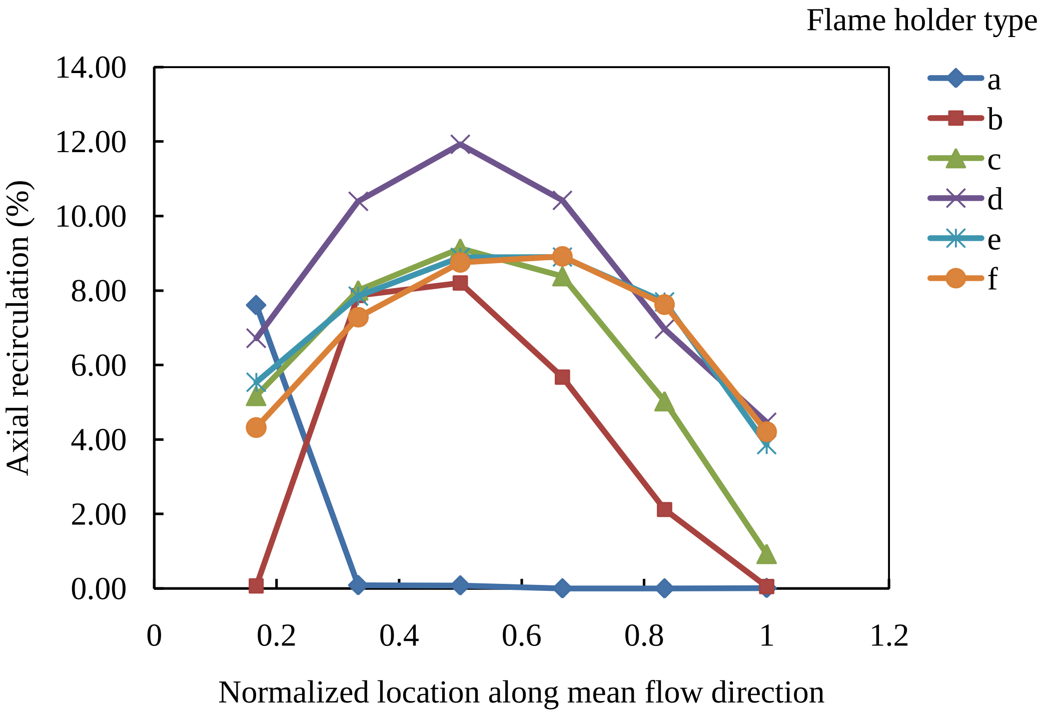

Figure 4.61 Flow recirculation in the axial direction v/s normalized axial location inside the combustion chamber for various flame holder designs

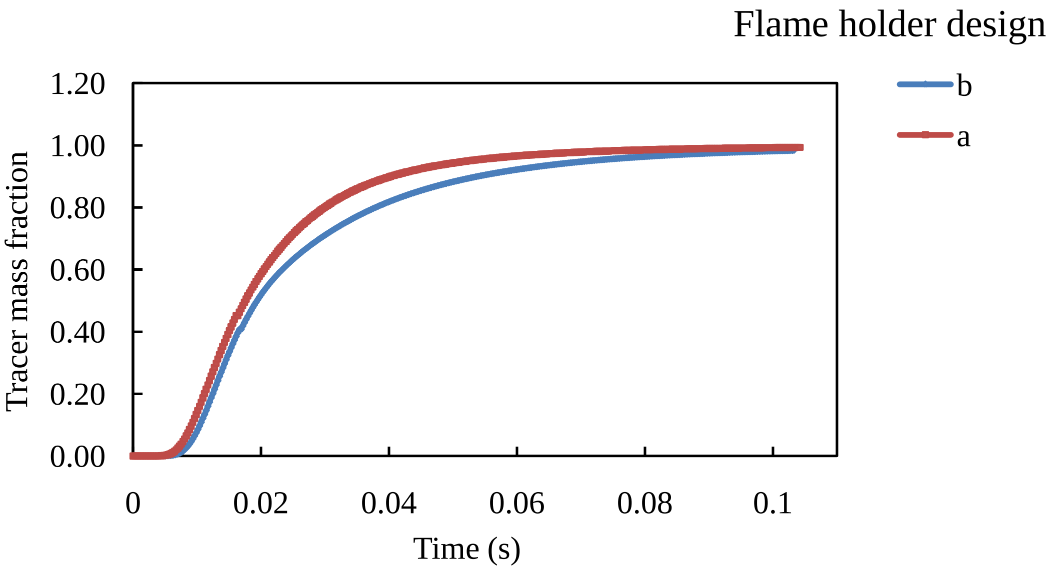

Figure 4.62 Residence time distribution of flame holder designs ‘a’ and ‘b’

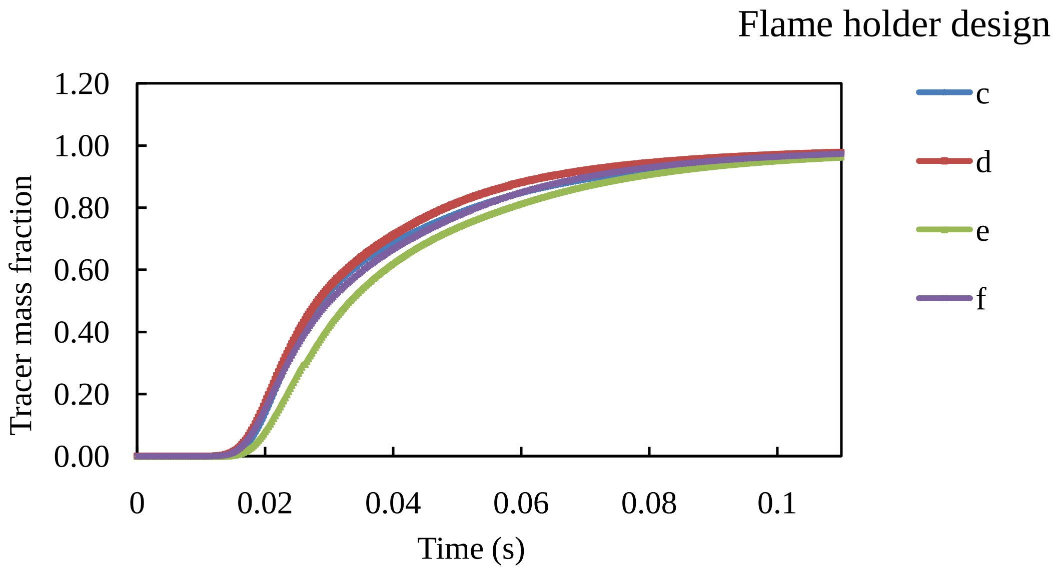

Figure 4.63 Residence time distribution of flame holder designs ‘c’, ‘d’, ‘e’ and f’

It can be sufficed that the amount of recirculation and residence times are not sufficient enough criteria to design and compare flame holder geometries in meso-scale. The possible reasons are the following,

Proximity to the walls means that, flow recirculation in the wrong direction can perhaps lead to reactive species being convected towards the wall and quenched. The second reason is flame stretch. Flame holder designs which can induce good recirculation might also lead the flame to stretch in an undesirable way leading to quenching.

Chapter 5: Methanol-air combustion at meso-scale

As mentioned previously, a combination of heat recirculation and liquid fuel film evaporation concepts has been employed for meso-scale combustion of methanol-air mixture. Self sustained combustion of the mixture was achieved in an extremely small volume (~32.6 mm^3). The combustor employed for this purpose had the same geometry as combustor C. Combustion was initiated using spark electrodes placed at the center of the combustion chamber just like in the case of propane-air combustion discussed in chapter 4. An external thermal heat source was used for initial heat up of the combustor. Initial heat up of the combustor helps to reduce the amount of time required to reach the steady state condition for sustained combustion. Without this, the spark should be kept on for long time duration until the spark induced flame heats up the reactor sufficiently so as to preheat and vaporize methanol and sustain the flame itself without the spark. Liquid methanol gets vaporized in the millimeter size channels due to the recirculated heat. Operating limits were obtained for the combustor experimentally. The meso-scale combustor was demonstrated to operate with methanol fuel for prolonged time duration. A general feature of the methanol-air flames examined here was the high luminosity (Figure 5.1). Combustion was also accompanied with high acoustic emissions for all the conditions investigated. Methanol is introduced to the air flow in the form of a T-junction and the subsequent methanol-air mixture is then fed to the combustor upstream of the combustion chamber through a six-inch long tube, see Figure 5.2. It was observed that the two phase flow inside the reactant feeding tube has a significant impact on combustion stability. Intermittency in fuel flow accompanying a given amount of airflow results in the emergence of multiphase flow regimes (plug, slug, annular and dispersed bubble flows) that is not favorable for achieving steady state combustion conditions. Only stratified flow (Figure 5.3) which ensures a continuous and steady mass flow rate of liquid fuel could stabilize the flame. The two phase flow instabilities which can quench the flames are more prone to be initiated with the variation in air flow than liquid flow. Therefore, in the experiments conducted here, the flame stability limits were obtained by keeping the air flow rate constant and varying the fuel flow rates till the extinction limits were reached.

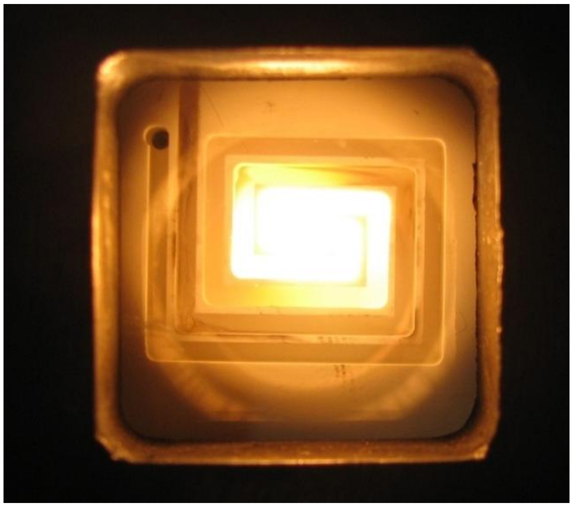

Figure 5.1 Methanol-air flame inside the Swiss-roll combustor

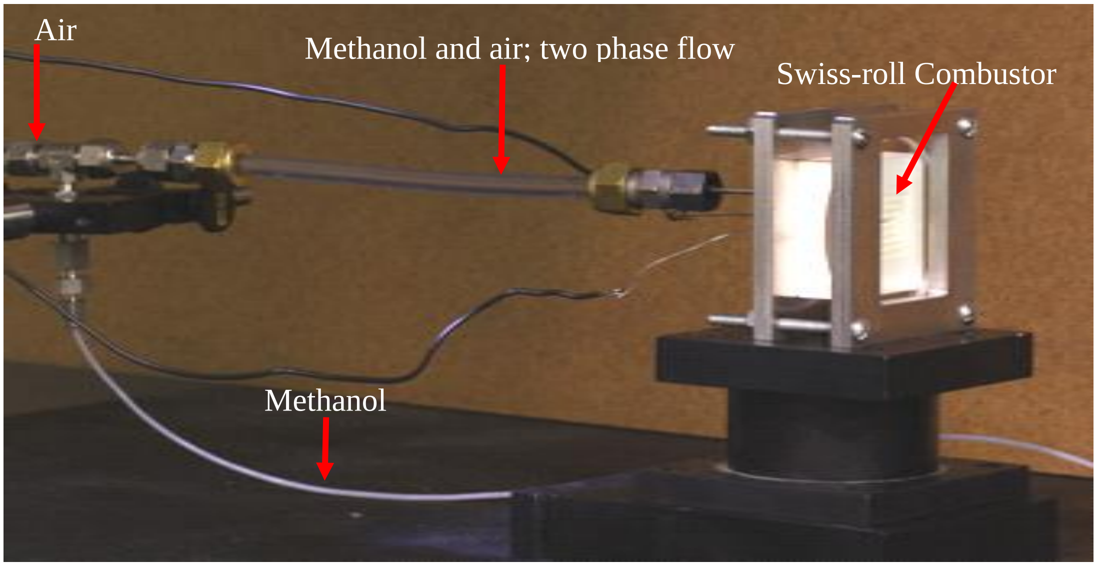

Figure 5.2 Methanol and air injection lines

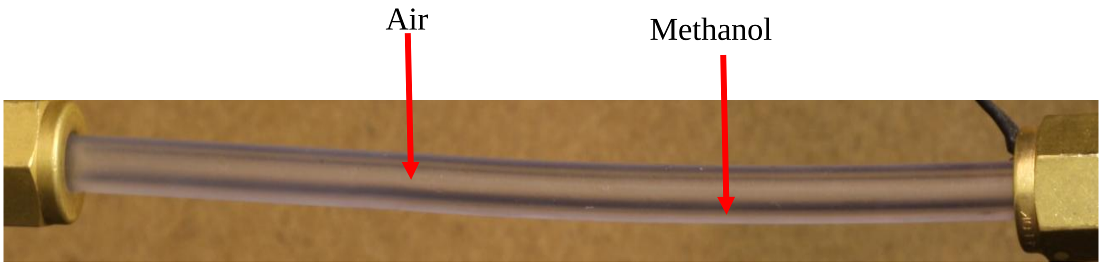

Figure 5.3 Stratified two phase flow inside the reactant feed tube carrying methanol and air

5.1 Liquid Fuel Film Concept

There are several benefits of employing liquid fuel film concept in small-scale heat recirculating combustion. Firstly, there is higher heat transfer rate to the fuel as compared to injecting droplets. This can be explained as follows. A portion of the energy released in the combustion chamber is recirculated to the reactants through the combustor walls. Hence adjacent wall surfaces are always at a higher temperature than the reactants. If the fuel is injected as droplets, most of the heat transfer to the fuel takes place through air because not all the droplets will come in direct contact with the walls. Since air has much lower temperature than the walls, heat transfer rate to the droplets will be lower. If the inlet channel is having a perfect annular multiphase flow, the recirculated heat will be used to completely vaporize the liquid fuel before raising the temperature of the co-flowing air above the boiling point of the liquid. It is clear that if the surface area of the liquid fuel is kept constant, more heat transfer occurs in liquid films when compared to droplets. Now the question is how much surface area/volume is available for liquid to vaporize when it is in the annular flow regime as compared to droplet regime.

$$\left(\frac{Area}{Volume}\right)_{film} = \frac{\pi \cdot d \cdot L}{\pi \cdot d \cdot L \cdot t} = \frac{1}{t} \qquad [5.1]$$

$$\left(\frac{Area}{Volume}\right)_{droplet} = \frac{4 \cdot \pi \cdot R^2}{\frac{4}{3} \cdot \pi \cdot R^3} = \frac{3}{R} \qquad [5.2]$$

$$\left(\frac{Area}{Volume}\right)_{film} \Big/ \left(\frac{Area}{Volume}\right)_{droplet} = \frac{R}{3 \cdot t} \qquad [5.3]$$

It was previously claimed that liquid film will have as much or more surface area/volume as compared to droplets if the combustor diameter is sufficiently small [127]. This work predicted fuel film thickness to be of the order of few microns for tube diameters close to a millimeter. Typical fuel sprays would have droplet sizes in the range 10 microns to 100 microns. Since surface area per volume ratio of liquid film and droplets $=R/(3\times t)$, having a liquid film inside millimeter size tube diameters can be highly advantageous in terms of area available for vaporization according to this work. However, several simplifying assumptions were made while arriving at these conclusions. For example, the velocity slip ratio ($S=V_G/V_L$) was kept a constant, of the order of 10. In the present work slip velocity is calculated based on an existing correlation. This correlation called the CISE correlation [128] was developed independently of flow regimes. Calculations based on this correlation showed that due to the simplifying assumptions, fuel film thickness is severely under predicted in [127].

Slip ratio can be obtained from CISE correlation as follows.

$$S = 1 + E_1 \cdot \sqrt{\frac{y}{1+y \cdot E_2} - y \cdot E_2} \qquad [5.4]$$

Where

$$y = \frac{\rho_L \cdot X}{\rho_G \cdot (1-X)} \qquad [5.5]$$

$$X = \frac{m_G}{m_G + m_L} \qquad [5.6]$$

For steady state $X = \frac{\dot{m}_G}{\dot{m}_G + \dot{m}_L}$ [5.7]

$$E_1 = 1.578 \cdot \left(\frac{F \cdot d_h}{\mu_L}\right)^{-0.19} \cdot \left(\frac{\rho_L}{\rho_G}\right)^{0.22} \qquad [5.8]$$

$$E_2 = 0.0273 \cdot \left(\frac{F^2 \cdot d_h}{\sigma \cdot \rho_L}\right)^{-0.19} \cdot \left(\frac{F \cdot d_h}{\mu_l}\right)^{-0.51} \cdot \left(\frac{\rho_L}{\rho_G}\right)^{0.08} \qquad [5.9]$$

$$F = \frac{\dot{m}_G + \dot{m}_L}{A} \qquad [5.10]$$

Once the slip ratio is obtained, the film thickness is calculated as follows.

$$\rho_G \cdot A_G \cdot V_G = \dot{m}_G \qquad [5.11]$$

$$\rho_L \cdot A_L \cdot V_L = \dot{m}_L \qquad [5.12]$$

$$S = \frac{V_G}{V_L} \qquad [5.13]$$

$$A = A_G + A_L \qquad [5.14]$$

$$V_G = \frac{1}{A \cdot S} \cdot \left(\frac{\dot{m}_L}{\rho_L} + \frac{\dot{m}_G \cdot S}{\rho_G} \right) \qquad [5.15]$$

$$t = \frac{1}{2 \cdot \pi} \cdot \left(\pi \cdot d - \sqrt{\pi^2 \cdot d^2 - 4\pi \cdot A_L} \right) \qquad [5.16]$$

For methanol-air flow, the slip ratios calculated were in the range 100-250 which is quite different from that assumed in the previous study [127]. It was observed that film thickness is mainly dependent on the tube diameter. For a given tube diameter, the mass flux had negligible effect on the film thickness in the range where flow is incompressible. For a constant gas-liquid mass ratio, film thickness increases almost linearly as the diameter of the tube increases, see Figure 5.4 Film thickness was also found to increase with equivalence ratio when mass flux and tube diameter are kept constant, see Figure 5.5. For tube diameters in the range 1mm-5mm the film thickness was calculated to be in the range of 10 micron-1900 micron.

In the present study it was not possible to experimentally investigate the characteristics of the multiphase flow regime inside the combustor channels. However, steady sustained combustion indicate that the two phases have no intermittency in mass flow rate which would be the case if the flow regime was slug, plug or dispersed flow. Hence it is safe to assume that the flow is in annular or stratified flow regimes. Based on the hydraulic diameter of the channels of the present combustor (2mm) the film thickness was estimated to be in the range 40-100 microns. Previously, simple one dimensional analysis had shown that methanol droplet sizes of the order of 20 microns or less is required for complete vaporization inside the preheating channels of the same combustor [129]. Even with an estimated film thickness of 40-100 microns, which has much lower surface/volume ratio as compared to a 20 micron droplet, the combustor was observed to operate successfully over a wide range of conditions. This suffices the advantage of liquid fuel film over droplet spray due to the higher heat transfer rates possible in the former.

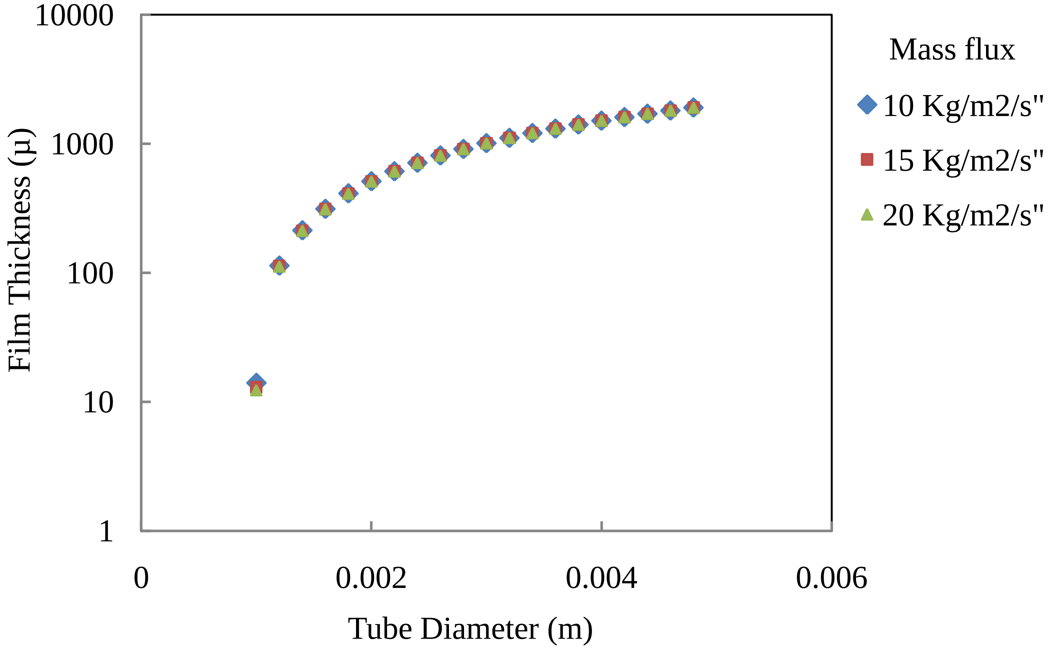

Figure 5.4 Film thickness vs. tube diameter for stoichiometric methanol-air annular flow at different mass flux conditions

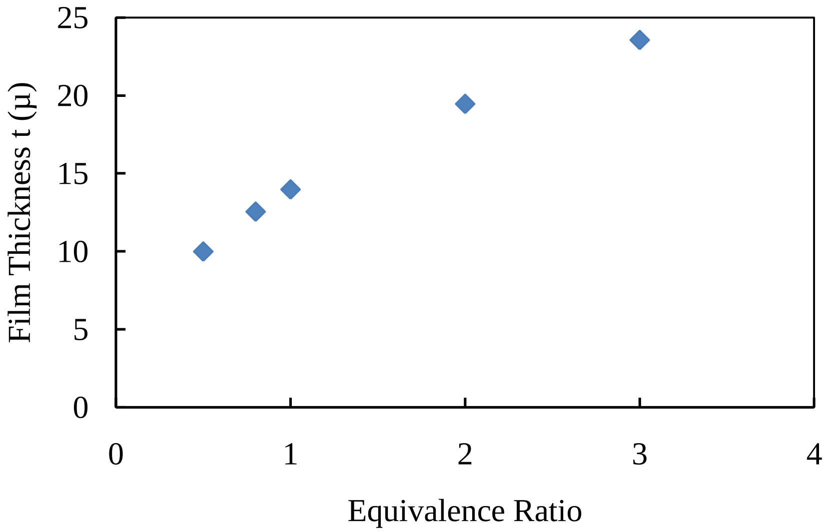

Figure 5.5 Film thickness vs. equivalence ratio of methanol-air annular flow for tube diameter of 1mm and a constant mass flux of 10kg/m2/s

5.2 Operating Limits

The extinction limits of the combustor are shown in Figure 5.6. Note that the equivalence ratio shown on the y-axis is not the actual equivalence ratio of the flame. The value shown is the ratio calculated based on the inlet flow rates of methanol and air. The errors associated with the measurements are reported in Appendix A. Similar to the propane-air combustion results obtained previously inside the same combustor, it was observed that the methanol-air combustion had an upper and lower extinction limit. However, in the present case both these limits were on the fuel-rich side. This implies that the combustion is incomplete with a significant amount of unburnt fuel. This could be due to incomplete mixing of the vaporized fuel with air. The minimum and maximum inlet equivalence ratios achieved were 1.14 and 3.5, respectively. Both occur at high air flow rate. Increase in air flow rate was observed to broaden the flame extinction limits. This suggests better mixing and vaporization at higher air flow rates. Hence for more efficient combustion it is recommended to operate the combustor at higher air flow rates. The inlet equivalence ratio at the minimum air flow rate possible was found to be around 1.5 as compared to 1 in the case of propane air combustion. For estimating the heat load of the combustor, air was assumed to be the limiting reactant. This predicted the heat load range of the combustor was found to be between 50W and 280W. This was higher than that observed for propane air combustion (30W-140W). Even though the power density of methanol is almost one half of that of propane the stoichiometric combustion of propane requires 4.67 times more air than that for methanol. This explains why the heat load of methanol air combustion was higher than that of propane air combustion considering the fact that both had almost similar air flow rates. Under the assumption that complete reaction occurs inside the combustion chamber volume (32.6 mm^3), the combustor was observed to have a maximum power density of 8.5 GW/m^3 (corresponding to maximum heat load of 280W) which is very high compared to that of conventional macro-scale combustors. Higher power density of the heat recirculating meso-scale combustor is a direct consequence of enhanced burning rates due to the preheated reactants.

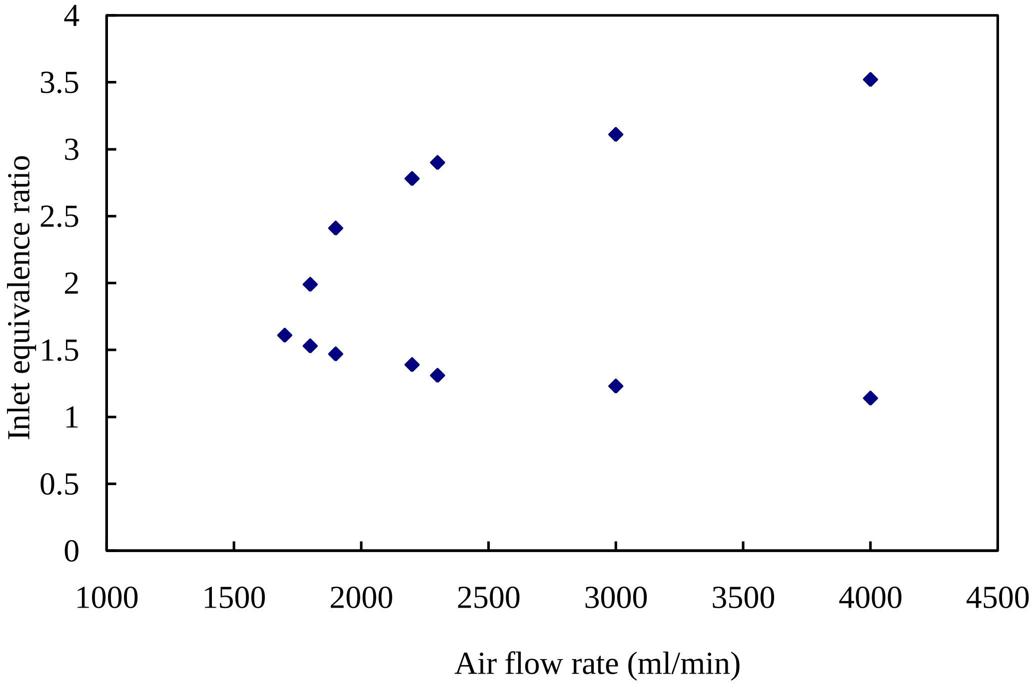

Figure 5.6 Extinction limits of methanol-air combustion

5.3 Thermal Performance

5.3.1 Preheating and Exhaust Temperatures

Investigation of the effect of equivalence ratio and flow rates on the amounts of preheating of the reactants and product exhaust temperatures was performed using two K-type thermocouples installed at two different locations in the combustor. The temperature measurements reported are approximate average values and not the actual temperature profile in the channel cross-section which can be quite a challenge to measure experimentally with good spatial resolution.

Figure 5.7 shows the variation of preheat temperature with equivalence ratio at different fuel flow rates. The temperatures observed were in the range of 675K-825K.

This high amount of preheating increases the combustion temperature which explains and supports the observed high power density. However the high heat exchange between reactants and exit products is necessary to pre-vaporize the reactants. Alternatively, a combination of longer mixing distances and preheats could be used to better fuel air preparation of the mixture to sustain efficient mixing between the reactants and support efficient near stoichiometric combustion.

The experimental results showed that for a given air flow rate the preheat temperature initially increases with increase in equivalence ratio until it reaches a peak value and then decreases. The minimum preheat temperature occurs at the lower extinction limit.

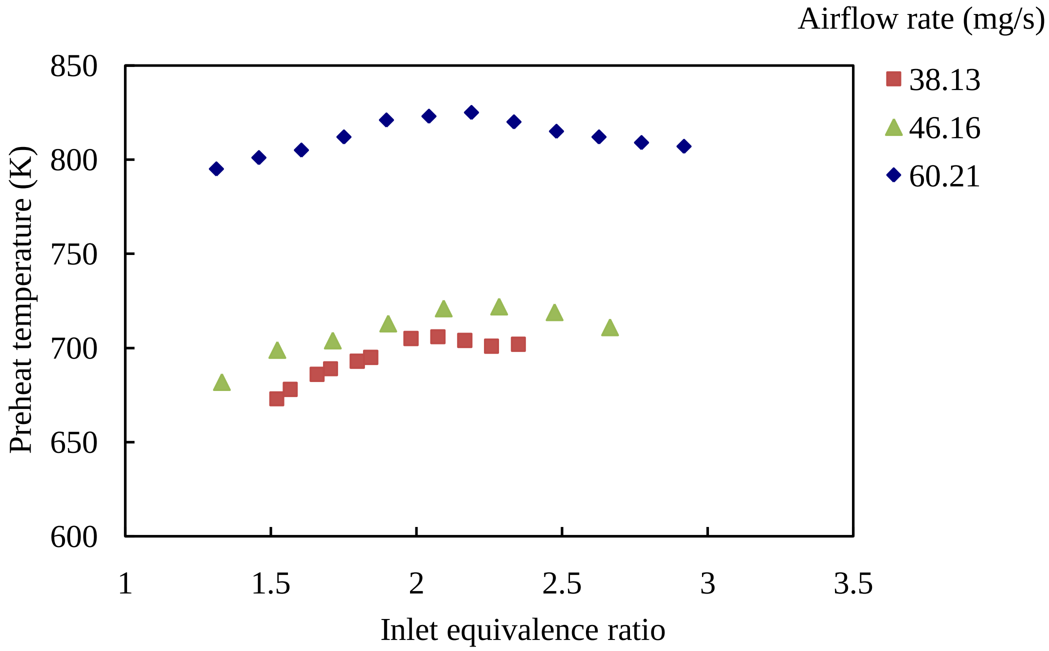

Figure 5.7 Preheat temperature vs. inlet equivalence ratio for three different air flow rates

Figure 5.8 shows the variation of exhaust temperature with equivalence ratio at different air flow rates. The trend observed is similar to that of reactant preheat temperature. Exhaust temperature increases with increase in equivalence ratio until it reaches a peak value and then decreases. The temperatures observed were in the range of 475K-615K.

Due to incomplete mixing in the combustor excess methanol is required to consume all the oxidizer present. It can be inferred that for a given air flow rate as the equivalence ratio increases from lower fuel flow limit, the consumption of oxidizer increases with an accompanying increase in combustion temperature. Once the complete consumption of oxidizer is achieved, further increase in the fuel flow rate results in a reduction of the combustion temperature. This effect of equivalence ratio on combustion temperature also causes a change in the preheat temperature and exhaust temperature; all showing a similar trend.

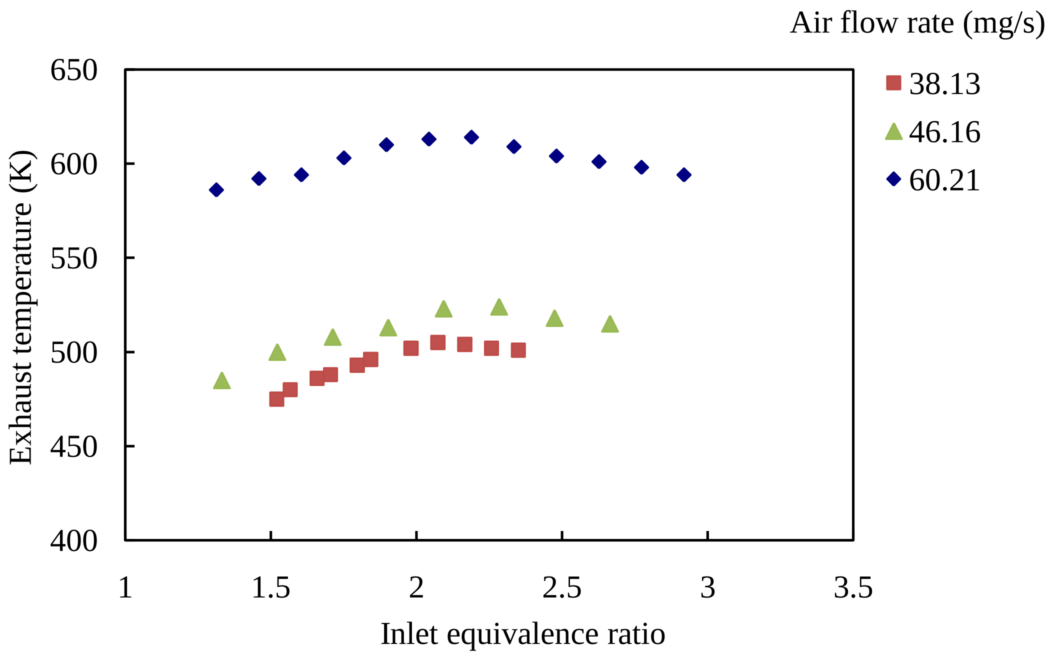

Figure 5.8 Exhaust temperature vs. inlet equivalence ratio for three different air flow rates

Figure 5.9.a shows the variation of preheat temperature along both the lower and upper extinction limits for three air flow rates. For both the cases the temperatures were found to increase with increase in air flow rate. The increase in reactant preheat temperature at the extinction limit can be attributed to a reduction in ignition delay time required to support the smaller residence times at higher flow rates. The variation is higher at the lower extinction limit. Figure 5.9.b shows the variation of exhaust temperature along the lower and upper extinction limits at various air flow rates. The exhaust temperature was also observed to increase with increase in air flow rate. The increase in the exhaust temperature can be directly attributed to the increase in reactant preheat temperatures.

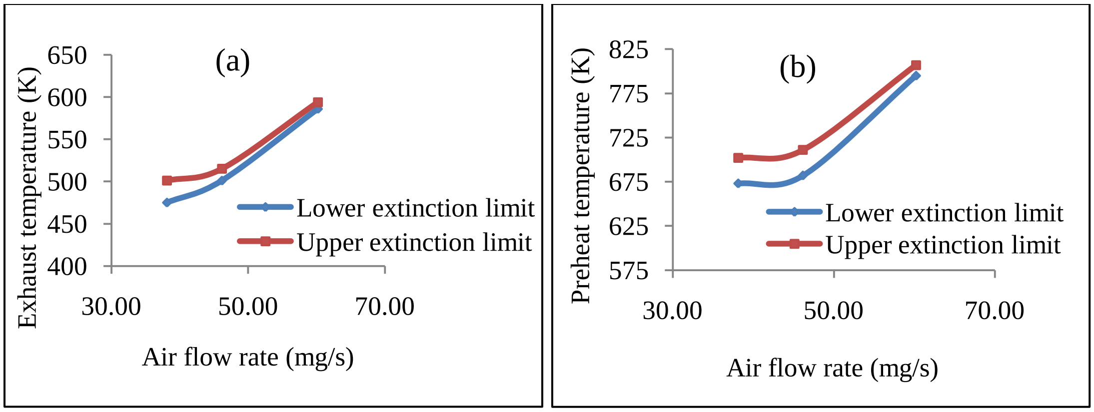

Figure 5.9 Preheat (a) and exhaust (b) temperature variation at extinction limits

5.3.2 Efficiency

Exhaust enthalpy was calculated based on the exhaust temperature. For calculating the specific heat at the exhaust it was assumed that after combustion, species composition remains frozen till it reaches the exhaust. Product species were calculated assuming that the reactions reach equilibrium condition. Equilibrium calculations were performed (using CEA software) for fuel-rich methanol-air combustion by considering 160 species and 10 species (CO, CO2, H, H2, H2O, NO, NH3, N2, OH, O2) which had a significant presence after the reaction were chosen for specific heat calculations. From the above, NO, OH, NH3 and O2 together accounted only for less than 0.04% of the total mass flow rate. Temperature dependent isobaric specific heat values of the above ten species were employed for the calculations [122]. The output power was calculated using the product mass fraction, specific heat values and mass flow rate.

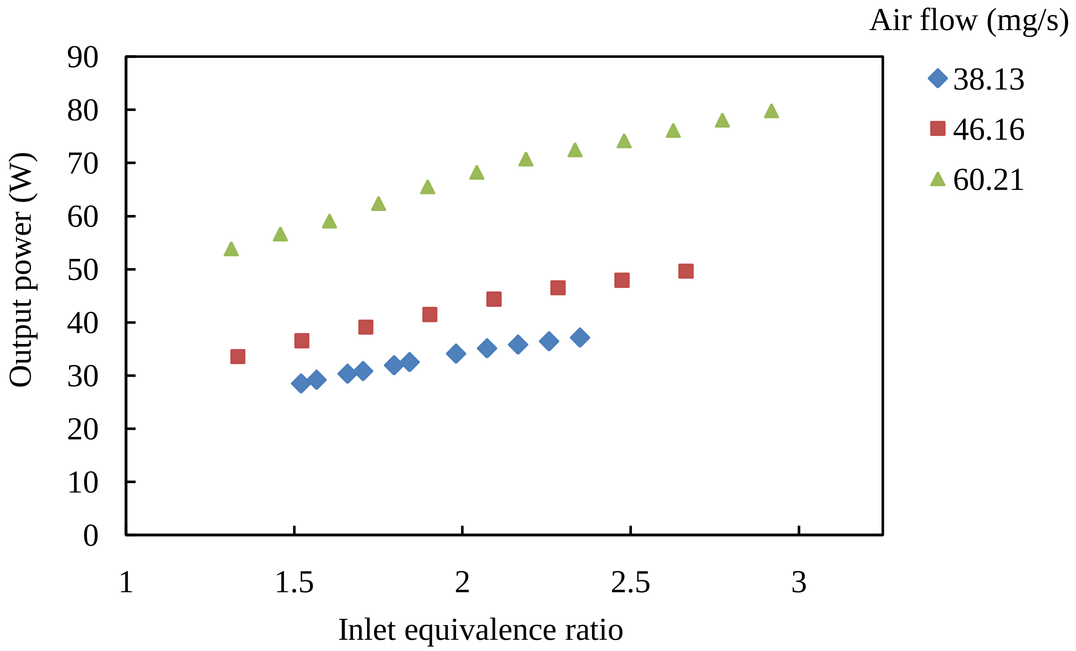

Figure 5.10 Output power vs. inlet equivalence ratio for three different air flow rates

Figure 5.10 shows the output power measured at the exhaust as a function of equivalence ratio for the three different air flow rates. The variation was observed to be in the range of 30W to 80W. It is clear that increasing the equivalence ratio results in higher output power for a constant airflow rate. This is despite the fact that the exhaust temperature peaks at a particular value of equivalence ratio and decreases monotonically on either sides. This is because both mass flow rate and specific heat values dominate temperature in output power calculations.

Figure 5.11 shows the variation of normalized output power (using the corresponding input heat load) as a function of the equivalence ratio at three air flow rates. It was observed that for the set of conditions considered, energy efficiency (output power/input power) varied in the range of 12% to 20% (very low). This is much lower than that observed in the case for propane-air combustion. For a given air flow rate, decrease in fuel flow rate results in an increase in the overall efficiency. Also for a given equivalence ratio, higher air flow rates ensures more energy efficient operation of the combustor.

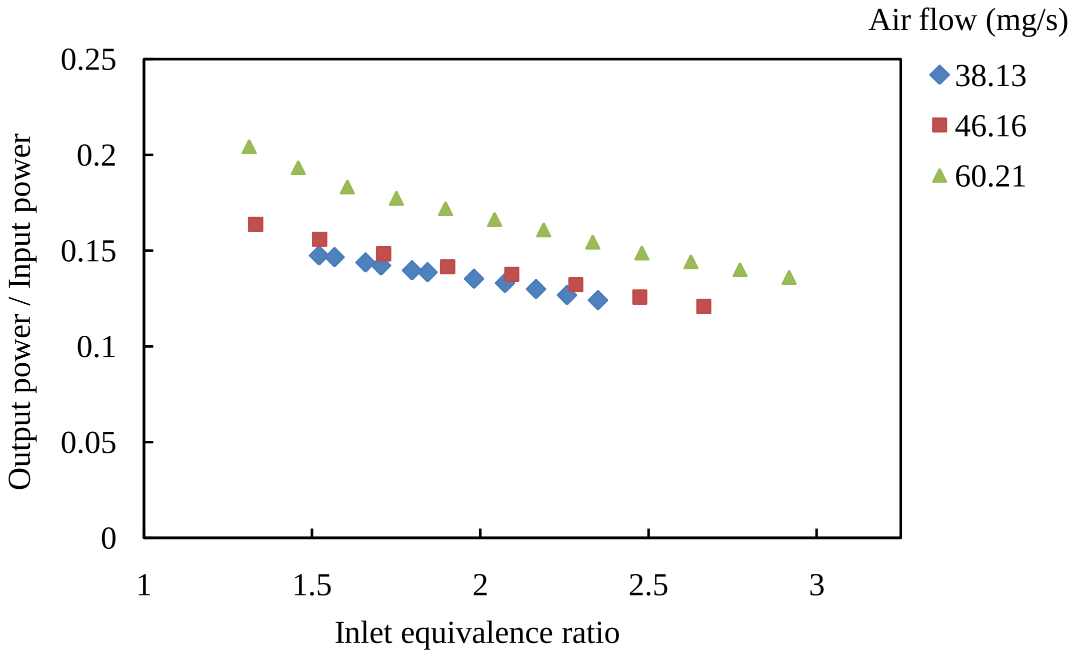

Figure 5.11 Combustor efficiency vs. inlet equivalence ratio for three different air flow rates

The thermal heat loss rate through the outer walls can be considered as the difference between the rate of energy release in the combustion chamber and the exhaust enthalpy flow rate. Since the combustor operates only in fuel-rich conditions it should be noted that the rate of energy release in the combustion chamber is different from the input power. Input power is directly proportional to the inlet fuel flow rate. However, the rate of energy release in the combustion chamber is assumed to be equal to the maximum power that can be extracted with the amount of oxidizer available. Figure 5.12 shows that wall heat loss rate decreases with increase in equivalence ratio. The wall thermal heat loss rate varied from 20% to 60% of the total input power. Also for a given equivalence ratio the losses are lower for higher air flow rates. It can be inferred that for a given air flow rate wall heat losses decrease with increase in the equivalence ratio. However, for overall energy efficiency operating in the lower equivalence ratio limit is beneficial.

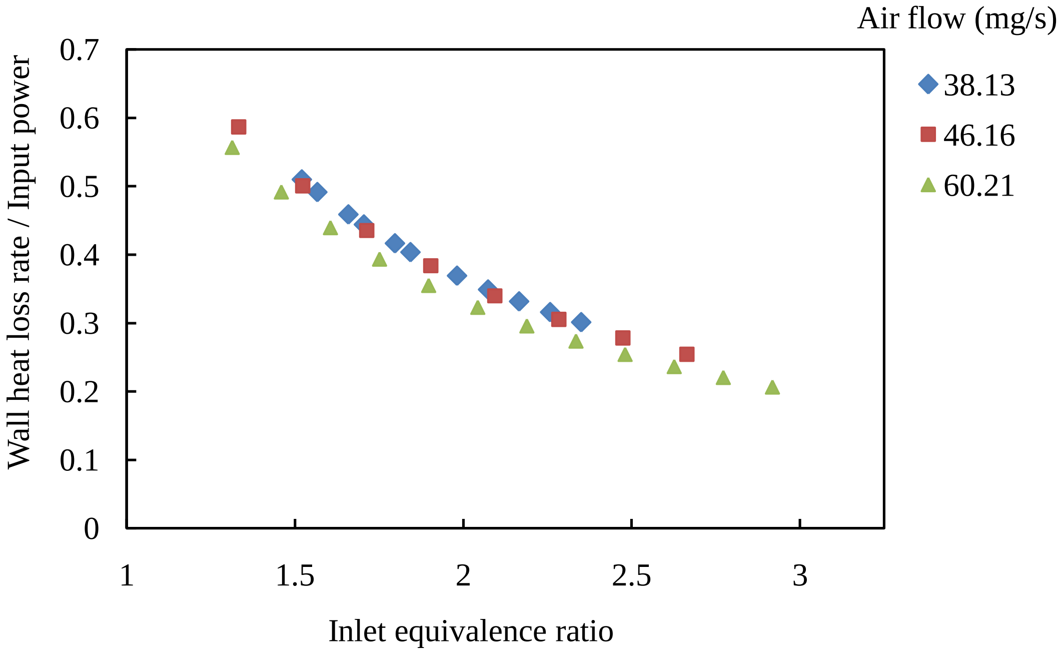

Figure 5.12 Normalized wall heat loss rate vs. inlet equivalence ratio for three different air flow rates

Chapter 6: Contributions and Recommendations for Future Work

6.1 Contributions

This dissertation has investigated the combustion and heat transfer characteristics inside meso- scale heat-recirculating combustors experimentally and through numerical simulations. The research resulted in the successful development of meso-scale combustors that are capable of sustaining the flames of propane-air and methanol-air mixtures inside a chamber volume as small as 32.6 mm^3. Employing a very low thermal conductivity material for combustor fabrication and an efficient choice of flame holder design are the two most important criteria for combustion in millimeter dimensions. The key findings and contributions of the research are given below.

Effect of wall thermal conductivity

Wall thermal conductivity is one of the most important parameters for meso-scale combustor design. Experiments and simulations showed that at typical meso-scale dimensions wall materials with minimal thermal conductivity (< 1W/m-K), especially ceramics would yield the best performance. Employing lower thermal conductivity materials for heat recirculating combustor fabrication have the following benefits.

1. Higher amount of reactant preheating
2. Lower heat losses from the combustion chamber resulting in higher combustion temperatures and hence broader flammability regime

3. Lower overall heat loss from the combustor (combustion chamber + heat exchanger) with higher power available at the exhaust

It was observed that due to the high amount of reactant preheating, the burning velocities inside the combustor can reach around thirty times the corresponding laminar burning velocity at standard temperature and pressure conditions. This led to a very high power density inside the combustion chamber.

However, as the thermal conductivity of a meso-scale combustor's wall is reduced the ability of the combustor to operate at lower flow rates is compromised. This can be attributed to the higher amount of reactant preheating which causes the minimum mean flow velocity that is required to operate the combustor (without the flame flashing back) to increase.

Effect of Heat exchanger size/Channel Length

The advantages of having longer heat exchanger channels are the following,

1. Higher preheating of the reactants
2. Ability to combust fuel-lean mixtures
3. Broader operating regime

However, there are some disadvantages also.

1. Longer channel length also means an increase in the outer surface area of the combustor leading to higher over all heat loss resulting in lower power at the combustor exit
2. It also adversely affects the combustor's ability to operate at low mean flow rates. The higher amount of preheating accompanying the longer channels

increases the flame speed considerably. This then sets a lower limit on the amount of flow that could be sent through the combustor to sustain a flame.

Effect of Reynolds number and equivalence ratio

It was observed that keeping all the other parameters constant, the thermal efficiency (output power / input power) of the combustor increases with increase in inlet Reynolds number. This implies that operating at higher Reynolds numbers decreases the percentage of heat lost. It was also observed that for a given fuel flow rate the thermal efficiency of the combustor increases monotonically with decrease in equivalence ratio. Maximum thermal efficiency occurs at the lean blow off limit. This effect is so pronounced that the combustor with longer channel length was able to operate at better thermal efficiencies (due to its capability to operate in the lean regime) compared to the one with shorter channel length for the same amount of input fuel flow rate. It can be concluded that for applications requiring higher power output in the exhaust flow, operating lean at higher Reynolds numbers will provide the optimum thermal efficiency.

Flame dynamics

Due to the small length scales involved, hydrodynamic instabilities have negligible effect on meso-scale combustion. Flame was observed to be extremely stable with negligible fluctuations. There is a broad region within the flammability regime where the flame is completely silent with no fluctuations perceivable. However, a significant amount of thermoacoustic phenomena is present within the flammability regime. It was observed that the flame excites the longitudinal resonance modes (1500-1700 Hz) of the combustor for several lower heat load conditions. For certain conditions, the flame-generated acoustics in turn affected the flame leading to flame oscillations in the range of 1 KHz.

Flame holding

The amount of flow recirculation and mean residence time are not sufficient criteria to design and compare flame holder geometries in meso-scale. The following could be the possible reasons,

- Proximity to the walls means that, flow recirculation in the wrong direction can perhaps lead to reactive species being convected towards the wall and quenched.
- The second reason is flame stretch. Flame holder designs, which can induce good recirculation, might also lead the flame to stretch in an undesirable way leading to quenching.

Liquid fuel combustion

Methanol-air combustion was achieved inside the meso-scale combustor without the application of fuel atomizer. Methanol was vaporized through liquid fuel film concept. One important requirement for sustained combustion of the liquid fuel is that there should be no intermittency in the fuel feed rate. Hence it is important to operate in stratified or annular two phase flows.

6.2 Recommendations for Future Work

This research has analyzed multiple aspects and parameters that are significant in meso-scale combustion and heat transfer and had yielded results that contribute significantly to the understanding of the problem. Nevertheless, some details still require further substantiation and are thus recommended for future work, as summarized below.

Investigation of different fuel oxidizer mixtures

The present study has employed propane-air and methanol-air as reactants. For microthruster applications in space, it is necessary to investigate the combustion characteristics of a bipropellant for example a mixture of methanol and hydrogen peroxide.

Flame temperature

Flame temperature is an indicator of thermal and combustion efficiencies and can give information on the burning rates inside the chamber. In the present study it was not possible to measure the flame temperatures with a thermocouple due to the extremely small dimensions involved (installing the thermocouple in the chamber can significantly distort the flow field and can quench the flame) and the presence of extremely high flame temperatures. Non-intrusive optical methods like two-color pyrometry should be employed to obtain the temperature distribution inside the chamber.

Flow field

Flow field is very important when analyzing flame stabilization. Due to the extremely small dimensions involved, flow field mapping was not performed in the present study. This is especially important in understanding the experimental observations made on the flame holder designs in the present study.

Thruster performance

To obtain the thruster performance values, a nozzle should be attached to the combustor and thrust measurements should be performed inside a vacuum chamber using a load cell.

Exhaust gas composition

Exhaust gas composition can give information on combustion efficiency. Analysis of the exhaust gases using a gas chromatograph is recommended to characterize combustion.

Investigation of pressure effects

The chamber pressure is extremely dependent on the exhaust nozzle geometry employed. It is recommended to investigate the effect of chamber pressure on the operating limits, combustion efficiency, and thermal efficiency.

Appendix A

Uncertainty in flow measurements

The errors associated with measurement of equivalence ratio, Reynolds number and inlet velocity originates from the flow controllers. The propane and air flow controllers have an accuracy of ±1.5% of the maximum flow rate. These flow controllers have a repeatability/precision of ±0.5% of full scale. The temperature coefficient is 0.15% of full scale/°C and pressure coefficient is 0.01% of full scale/psi. Since the operating conditions reported in this dissertation, have a temperature variation of ±2 °C and ±2 psi, minimum accuracy is estimated to be ±1.82% of full scale (±1.5% ± 0.15×2% ± 0.01×2%).

Hence, the minimum accuracy (worst case) of propane and air flow controllers are ±3.64 ml/min and ±182 ml/min. The repeatability/precision are ±1 ml/min and ±50 ml/min respectively for propane and air flow controllers.

The accuracy of methanol flow controller is ±1% of full scale, which is equivalent to ±3 g/hr. It has a precision of ±0.2%, which is equivalent to ±0.6 g/hr.

Errors present in the measurement of equivalence ratio, Reynolds number and inlet velocity are calculated as follows. Equivalence ratio, inlet Reynolds number and inlet velocity are functions of fuel and air flow rates. Hence r= r (f_1, f_2) where f_1=fuel flow rate, f_2=air flow rate and r = equivalence ratio, inlet Reynolds number or inlet velocity.

The error associated with the measurement is then given by the following second power equation [130].

$$\Delta r = \sqrt{\left[\left(\frac{\partial r}{\partial f_1}\Delta f_1\right)^2 + \left(\frac{\partial r}{\partial f_2}\Delta f_2\right)^2\right]}$$

Here Δr = error in the measurement of quantity r, Δf_1 =error associated with fuel flow rate and Δf_2 =error associated with air flow rate. If the error in flow rate measurement is assumed 1.82% of full scale, the percentage error in the flow rates increases with decrease in flow rate. However, it is quite clear that the error given by 1.82% of full-scale value will imply negative flow when the flow rates are sufficiently small. Hence, this value cannot be employed while operating at lower flow conditions. As a first approximation, the error occurring at lower flow rates is estimated based on the precision (0.5% of full scale). The above assumption yields the following results. Error associated with inlet Reynolds number and inlet velocity vary in the range 6 to 25% and 6 to 26% respectively for the range of flow rates reported in this dissertation. The error in equivalence ratio (of propane-air mixture) measurement varies in the range of 7 to 30%. For the case of methanol-air mixtures, the error in equivalence ratio measurements varies in the range 8-16.2%. For all the cases reported above, the higher values of error (%) occur at lower flow rates.

Appendix B

List of publications

1. Vijayan, V., Gupta, A.K., “Combustion and Heat Transfer at Meso-scale with Thermal Recuperation", accepted for publication by Applied Energy, March 2010
2. Vijayan, V., Gupta, A.K., “Flame Dynamics of a Meso-scale Heat Recirculating Combustor”, submitted to Applied Energy, February 2010
3. Vijayan, V., Gupta, A.K., “Thermal Performance of a Meso-scale Liquid Fuel Combustor”, submitted to Applied Energy, March 2010
4. Vijayan, V., Gupta, A.K., “Experimental Investigation of a High Power Density Ceramic Mesoscale Combustor”, 6th International Energy Conversion Engineering Conference (IECEC), Cleveland, OH, July 28-30, 2008, AIAA-2008-5660
5. Vijayan V, Gupta A.K., “Combustion and Heat Transfer at Meso Scale with Thermal Energy Recirculation” 47th AIAA Aerospace Sciences Meeting, Orlando, Florida, January 5–8, 2009, AIAA 2009-443
6. Vijayan, V., Gupta, A.K., “Heat Transfer Comparison between Archimedean and Rectangular Spiral Heat Exchangers for Mesoscale Combustor Application” 47th AIAA Aerospace Sciences Meeting, Orlando, Florida, January 5–8, 2009, AIAA-2009-254
7. Vijayan, V., Gupta, A.K., “Flame Dynamics of a Mesoscale Combustor” 7th International Energy Conversion Engineering Conference, Denver, Colorado, Aug 2–5, 2009, AIAA-2009-4604
8. Vijayan, V., Gupta, A.K., “Thermal Performance of a Mesoscale Heat Regenerating Combustor” 7th International Energy Conversion Engineering Conference 2 - 5 Aug 2009, Denver, Colorado, AIAA-2009-4605
9. Vijayan, V., Gupta, A.K., “Experimental Investigation of a Mesoscale Liquid Fuel Combustor”, 45th AIAA/ASME/SAE/ASEE Joint Propulsion Conference & Exhibit, Denver, Colorado, Aug 2 – 5, 2009, AIAA-2009-5244
10. Vijayan, V., Gupta, A.K., “Chemiluminescence Study of Propane-Air Flame Inside a Mesoscale Combustor”, 45th AIAA/ASME/SAE/ASEE Joint Propulsion Conference & Exhibit, Denver, Colorado, Aug 2–5, 2009, AIAA-2009-5245
11. Vijayan, V., Gupta, A.K., “Thermal Performance of a Mesoscale Liquid Fueled Combustor”, 48th AIAA Aerospace Sciences Meeting, Orlando, Florida, January 4-7, 2010, AIAA-2010-1601

References

[1] U.S. Congress, Office of Technology Assessment, “Miniaturization Technologies”. Government Printing Office, Washington DC. 1991

[2] Epstein, Senturia, Al-Midani, Anathasuresh, Ayón, Breuer, Chen, Ehrich, Esteve, Fréchette, Gauba, Ghodssi, Groshenry, Jacobson, Kerrebrock, Lang, Lin, London, Lopata, Mehra, Mur Miranda, Nagle, Orr, Piekos, Schmidt, Shirley, Spearing, Tan, Tzeng, and Waitz, 1997, Micro-Heat Engines, Gas Turbines, and Rocket Engines”, 28th AIAA Fluid Dynamics Conference, 97-1773, 1997

[3] Mehra, X. Zhang, A. A. Ayon, I. A. Waitz, M. A. Schmidt, and C. M. Spadaccini, “A Six-Wafer Combustion System for a Silicon Micro Gas Turbine Engine”, Journal of MicroElectroMechanical Systems, 2000, 9(4), pp. 517 – 527

[4] Fernandez-Pello, A.C, “Micro-Power Generation using Combustion: issues and approaches” 29th Int. Symposium on Combustion, The Combustion Institute, Pittsburgh, PA, 2002, pp. 1–45

[5] Mehra, A., and Waitz, I. A, “Development of a Hydrogen Combustor for a Microfabricated Gas Turbine Engine”, Solid State Sensor and Actuator Workshop, Hilton Head, GA, 1998

[6] Spadaccini, C.M., Zhang, X., Cadou, C. P., Miki, N., and Waitz, I. A. "Development of a Catalytic Silicon Micro-Combustor for Hydrocarbon-Fueled Power MEMS”, MEMS 2001, Las Vegas NV, Jan 2002

[7] Fu, K., A.J. Knobloch, F.C. Martinez, D.C. Walter, C. Fernandez-Pello, A.P. Pisano, D. Liepmann, K. Miyasaka, and K. Maruta. "Design and Experimental Results of Small-scale Rotary Engines." Proceedings of 2001 ASME International Mechanical Engineering Congress and Exposition. New York, NY, ASME, 41, pp. 295-302

[8] Fu, K., A.J. Knobloch, F.C. Martinez, D.C. Walther, C. Fernandez-Pello, A.P. Pisano, and D. Liepmann. "Design and Fabrication of a Silicon-based MEMS Rotary Engine." Proceedings of 2001 ASME International Mechanical Engineering Congress and Exposition. New York, NY, ASME, 41, pp. 303-308

[9] Lee, C. H., Jiang, K. C., Jin, P. D., and Prewett, P. D., Design and Fabrication of a Micro Wankel Engine using MEMS Technology. Microelectronic Engineering. 2004, 73-74, pp.529-534

[10] Yang, W. “Liquid Piston Microengine." Technical Proposal, DARPA BAA01-09 Micro Power Generation (MPG). Honeywell Technology Center, 12001 State Highway 55, Plymouth, MN. 2001

[11] Yang, W., and Bonne, U. “MEMS Free-Piston Knock Engine." Technical Proposal, DARPA Contract F30602-99-C-0200. Honeywell Technology Center, 12001 State Highway 55, Plymouth, MN. 1999

[12] Yang, W., Bonne, U., and Johnson, B. R.,“Microcombustion Engine/Generator." U. S. Patent 6,276,313. 2001

[13] Aichlmayr, H. T., Kittelson, D. B. and Zachariah, M. R. “Miniature Free-piston Homogeneous Charge Compression Ignition Engine-compressor Concept- Part I: Performance Estimation and Design Considerations Unique to Small Dimensions”,Chemical Engineering Science, 2002, 57, pp. 4161-4171

[14] Aichlmayr, H. T., Kittelson, D. B. and Zachariah, M. R. “Micro-HCCI Combustion: Experimental Characterization and Development of a Detailed Chemical Kinetic model with Coupled Piston Motion”, Combustion and Flame, 2003, 135, pp. 227-248

[15] Dahm, W. J. A., Ni, J., Mijit, K., Mayor, J. R., Qiao, G., Dyer, S. W., Benjamin, A. G. , Gu, Y., Lei, Y., and Papke, M.L., “Micro Internal Combustion Swing Engine (MICSE) for Portable Power Generation Systems”. AIAA Paper 2002-0722, AIAA, Reno, NV. 2002

[16] Whalen, S., Richards, R., Bahr, D., Richards, C., “Operation and Testing of a Micro Heat Engine”. Nanotech. 2003

[17] Weiss, L. W., Cho, J. H., McNeil, K. E., Richards, C. D., Bahr, D. F., and Richards, R. F. “Characterization of Dynamic Micro Heat Engine with Integrated Thermal Switch” J. Micromech. Microeng. 2006, 16, S262–S269

[18] Herrault, F., Crittenden, T., Yorish, S., Birdsell, E., Glezer, A., and Allen, M. G. “A self-resonant MEMS-fabricated, Air-breathing engine” Solid-State Sensors, Actuators, and Microsystems Workshop, South Carolina, 2008

[19] Federici, J. A., Norton, D. G., Bruggemann, T., Voit, K. W., Wetzel, E. D., and Vlachos, D. G. “Catalytic Microcombustors With Integrated Thermoelectric Elements for Portable Power Production” Journal of Power Sources 2006, 161, pp.1469–1478

[20] Venkatasubramanian, R.; Watkins, C., Caylor, C., and Bulman, G. “Microscale Thermoelectric Devices for Energy Harvesting and Thermal Management”. Technical Digest, Power MEMS, 2006

[21] Minaev, S. S., and Fursenko, R. V. “Estimates of Efficiency of a Small-size Thermoelectric Channel in Terms of Conversion of Heat Produced by Gas Combustion to Electric Power”. Combustion Explosion & Shock Waves 2007, 43, pp.384–390

[22] Cohen, A L., Ronney, P., Frodis, U., Sitzki, L.; Meiburg, E., and Wussow S. “Microcombustion and Combustion-Based Thermoelectric Microgenerator” U.S. Patent 6,613,972 B2, September, 2003

[23] Yoshida, K., Tanaka, S., Tomonari, S., Satoh, D., and Esashi, M. “High Energy Density Miniature Thermoelectric Generator Using Catalytic Combustion”. J. Microelectromech. Syst. 2006, 15, pp. 195-203

[24] Karim, A. M., Federici, J. A., and Vlachos, D. G. “Portable Power Production from Methanol in an Integrated Thermoeletric/Microreactor System”. Journal of Power Sources 2008, 179, pp.113–120

[25] Norton, D. G., Wetzel, E. D., and Vlachos, D. G. “Thermal Management in Catalytic Microreactors”. Ind. Eng. Chem. Res. 2006, 45, pp.76-84

[26] Xue, H., Yang, W. M., Chou, S. K., Shu, C. and Li, Z. W. “Microthermophotovoltaics power system for portable mems devices”. Microscale Thermophysical Engineering 2005, 9, pp.85-97

[27] Lee, K. H., and Kwon, O. C. “Studies on a Heat-recirculating Microemitter for a Micro thermophotovoltaic System”. Combustion & Flame 2008, 153, pp. 161-172

[28] Micci, M.M., and Ketsdever. A., “Micropropulsion for small spacecraft”, Progress in Astronautics and Aeronautics, AIAA, Chapters 1-3, 2000

[29] Rossi, C. “Micropropulsion for Space- A survey of MEMS-based Micro Thrusters and Their Solid Propellant Technology. Wiley Inter Science. 2002, 10, pp.257-292.

[30] De Groot, W. A., “Propulsion Options for Primary Thrust and Attitude Control of Microspacecraft”. NASA/CR-1998-206608

[31] Mueller, J., Leifer, S.D., Muller, L., and George, T. “Design, Analysis and Fabrication of a Vaporizing Liquid Micro-Thruster” AIAA Paper 97-3054, Seattle, 1997

[32] LAAS Report No. 96304, 1996

[33] Jonson, S.W. The 30th AIAA/ASME/SAE/ASEE Joint Propulsion Conference, Indianapolis, IN, June, 1994

[34] Mueller, J., The 33rd AIAA/ASME/SAE/ASEE Joint Propulsion Conference, Seattle, WA, July 1997

[35] Marcuccio, S., Genovese, A., and Andrenucci, M., Journal of Propulsion and Power, 1998, 14, pp.774–781

[36] Köhler, J., Simu, U., Bejhed, J., Kratz, H., Jonsson, K., Nguyen, H., Bruhn, F., Hedlund, C., Lindberg, U., Hjort, K. and Stenmark, L., “A Hybrid Cold Gas Microthruster System for Spacecraft”, 11th Int. Conf. Solid-State Sensors & Actuators, pp 886-889, (Transducers '01), Munich, Germany, June, 2001

[37] Köhler, J., Bejhed, J., Kratz, H., Lindberg, U., Hjort, K., and Stenmark, L., “A hybrid cold gas microthruster system for spacecraft, Sensors & Actuators” A 97-98, pp 587-598, 2002

[38] Rossi, C., Estève, D., Larangot, B., Orieux, S., Smart Mater. Struct. 2001, 10, pp. 1–7

[39] Lewis, D.H., Janson, S.W., Cohen, R. B., Antonsson, E. K., Sens. Actuators A 80 2000, pp. 143–154

[40] Mueller, J., Muller, L., and George, T. "Subliming Solid Micro-Thruster for Microspacecraft" New Technology Report NPO-19926/9525

[41] Jack Mattingly "Elements of Propulsion: Gas Turbines and Rockets" American Institute of Aeronautics and Astronautics, 2006

[42] Holladay, J.D., Jones, E.O., Phelps, M., and Hu, J. "High-efficiency Microscale Power using a Fuel Processor and Fuel Cell", SPIE Micromachining & Microfabrication. Paper 4559-20, San Francisco, October, 2001

[43] Davy, H. "On the Fire-damp of Coal Mines and the Methods of Lighting the Mines so as to Prevent Explosions" Phil. Trans. Roy. Soc., 106: 1, 1816

[44] Payman, W. and Wheeler, R.V. "The Propagation of Flame Through Tubes of Small Diameter" J. Chem. Soc., 113: 656, 1918Holm, J.M. "On the Initiation of Gaseous Explosions by Small Flames" Phil. Mag.. 1932, 14, pp. 18-56

[45] Holm, J.M., On the initiation of gaseous explosions by small flames, Phil. Mag., 14: 8, 1932; ibid. 15: 329, 1933

[46] Friedman, R. "The Quenching of Laminar Oxy-hydrogen Flames by Solid Surfaces" Proc. Comb. Inst., 1949, 3, pp. 110-210

[47] Gardner, W.E. and Pugh, A. "The Propagation of Flame in Hydrogen-oxygen Mixtures" Trans. Faraday Soc. 1939, 35, pp. 283-335

[48] Simon, D.M., Belles, F.E., and Spakowski, A.E. " Investigation and Interpretation of the Flammability Region for some Lean Hydrocarbon-air Mixtures" Proc. Comb. Inst. 1953, 4, pp. 126-148

[49] Potter, A.E., Jr., and Anagnostou, E. "Reaction Order in the Hydrogen-bromine Flame from the Pressure Dependence of Quenching Diameter" Proc. Comb. Inst. 1959, 7, pp. 347-360

[50] Blanc, M.V., Guest, P.G., von Elbe, G., and Lewis, B. "Ignition of Explosive Gas Mixtures by Electric Sparks" Proc. Comb. Inst. 1949, 3, pp. 363-399

[51] Lewis, B. and Von Elbe, G. "Combustion, Flames and Explosions of Gases" 3rd edition, Academic Press, New York, 1987

[52] Calcote, H.F., Gregory, C.A., Jr., Barnet, C.M., and Gilmer, R.B. "Spark Ignition: Effect of Molecular Structure" Industr. Eng. Chem., 1952, 44, pp. 2656-78

[53] Potter, A. E., “Flame quenching”, Progress in Combustion Science and Technology, 1960, pp. 145-181

[54] Andrews G.E. and Bradley D.,“The Burning Velocity of Methane-air Mixtures” Combust. Flame 19, 1972, pp. 275-289

[55] Jarosinski, J. “Flame Quenching by a Cold Wall” Combust. Flame, 1983, 50, pp.167-190

[56] Jarosinski, J., Podfilipski, J., and Fodemski, T. “Properties of Flames Propagating in Propane-air Mixtures near Flammability and Quenching Limits” Combust. Sci. Tech. 2002, pp.167-174

[57] Vosen, S.R., Greif, R. and Westbrook C.K., “Unsteady Heat Transfer during Laminar Flame Quenching”, Proc. Combust. Inst. 1984, 20, pp. 75–83

[58] Lewis, B. and von Elbe, G. “Stability and structure of burner flames” J. Chem. Phys., 11: 75, 1943

[59] Lafitte, P. and Pannetier, G. “The Inflammability of Mixtures of Cyanogen and Air; the Influence of Humidity” Proc. Comb. Inst., 3: 210, 1949

[60] Zel’dovich, Ya.B. “Theory of Limit Propagation of Slow Flame” Zhur. Eksp. Teor. Fiz., 11: 159, 1941

[61] Zel’dovich, Ya.B. “Theory of Combustion and Gas Detonation” Akad. Nauk SSSR, Moscow, 1944

[62] Zel’dovich, Ya.B., Barenblatt, G.I., Librovich, V.B., and Makhviladze, G.M. “The Mathematical Theory of Combustion and Explosion” Nauka Publishing House, Moscow, 1980

[63] Von Elbe, G. and Lewis, B. “Theory of Ignition, Quenching and Stabilization of Fl ames of Nonturbulent Gas Mixtures” Proc. Comb. Inst., 3: 68, 1949

[64] Mayer, E. “A theory of Flame Propagation Limits due to Heat loss” Combust. Flame, 1: 438, 1957

[65] Spalding, D.B. “A theory of Flammability Limits and Flame Quenching” Proc. Roy. Soc., A240: 83, 1957

[66] Kuo, K.K. “Principles of Combustion”. , John Wiley, New York, 1986

[67] Williams, F.A. “Combustion Theory” , Benjamin Cummings, Menlo Park, CA 1985

[68] Turns, S. R. “An Introduction to Combustion” Concepts and Applications, , McGraw Hill, New York, 1996, pp. 291–297

[69] Karman,V.T, and Millan. G, “Theoretical and Experimental Studies on Laminar Combustion and Detonation Waves” 4th Symposium on Combustion, 1952, pp.173-177

[70] Westbrook, C. K., Adamczyk, A. A. and Lavoie, G. A. “A Numerical Study of Laminar Flame Wall Quenching,” Combust. Flame, 1981,40, pp. 81-101

[71] Popp, P. and Baum, M. “Analysis of Wall Heat Fluxes, Reaction Mechanisms, and Unburnt Hydrocarbons during the Head-on Quenching of a Laminar Methane flame”, Combust. Flame, 1997, 108, pp. 327–348

[72] Aly, S L, Simpson, R B, and Hermance, C E “Numerical solution of the two-dimensional premixed laminar flame equations”, AIAA Journal. 1979, 17, pp. 56-63

[73] Hackert C L, Ellzey J L and Ezekoye O A. “Effects of Thermal Boundary Conditions on Flame Shape and Quenching in Ducts” Combust. Flame. 1998, 112, pp. 73–84

[74] Daou, J., Matalon, M.: “Influence of Conductive Heat-losses on the Propagation of Premixed Flames in Channels”. Combustion and Flame. 2001,128, pp. 321–339

[75] Miesse C. M., Masel R. I., Jensen C. D., Shannon M. A., and Short M. “Submillimeter-scale Combustion” AIChE J. 2004, 50, pp. 3206-14

[76] Ahmed, K. A., and Forliti. D. J. “Combustor Flowfield Measurements of a Transverse Jet Flame Holder” 47th AIAA Aerospace Sciences Meeting Including AIAA 2009-21.Orlando, Florida. January 2009

[77] Gupta, A. K., Lilly, D. G. and Syred, N. “Swirl Flows, Abacus Press, Tunbridge Wells”. U.K. 1984

[78] Kaiser, S. A., Kyritsis, D. C., Long, M. B. and Gomez, A. “The Electrospray and Combustion at the Mesoscale”, Journal Mass. Spectrum. Soc. Japan., 51, 2003, pp. 42-49

[79] Kyritsis, D. C., Guerrero-Arias, I., Roychoudhury, S. and Gomez, A. “Mesoscale Power Generation by a catalytic Combustor using Electrosprayed Liquid Hydrocarbons,” Proceeding of the Twenty-Ninth Symposium (International) on Combustion, 2002, pp. 965-972

[80] Sirignano, W. A., Dunn-Rankin, D., Strayer, B. A., and Pham, T. K., ‘‘Miniature Combustor with Liquid-Fuel Film,’’, Western States Section Fall Meeting of the Combustion Institute, paper F01-036. Salt Lake City, UT, October, 2001

[81] Sirignano, W. A., ‘‘Analysis of Miniature Liquid-Film Combustor,’’ Proceedings of the Eastern States Section Fall Meeting of the Combustion Institute, Hilton Head, SC, December ,2001

[82] Jarosinski, J and Veyssiere, B. “Combustion Phenomena: Selected Mechanisms of Flame Formation, Propagation and Extinction” CRC Press, 2009

[83] Darrieus. G., “Propagation d’un front de flamme”. Unpublished work presented at La Technique Moderne (1938), and at Le Congrès de Mécanique Appliquée (1945), 1938

[84] Landau. L., “On the theory of slow combustion”. Acta Physicochimica URSS, 1944, 19, pp.77–85

[85] Markstein. G.H., “Instability Phenomena in Combustion Waves”. Proceedings of the Combustion Institute, 1952, 4, pp.44–59

[86] Davis, S.G., Quinard.J. and Searby.G. “Markstein Numbers in Counterflow, Methane- and Propane-air Flames: A computational study”. Combustion and Flame, 2002, 130, pp. 123–136.

[87] Markstein.G.H. “Instability Phenomena in Combustion Waves”. Proceedings of the Combustion Institute, 1952, 4, pp. 44–59

[88] Markstein.G.H. “Nonsteady Flame Propagation”. Pergamon, New York, 1964

[89] Crocco. L. “Aspects of Combustion Instability in Liquid Propellant Rocket Motors: Part 1”. J. Am. Rocket Soc., 1951,21, pp. 163–178

[90] Barrère. M., and Williams. F. A. “Comparison of Combustion Instabilities found in Various Types of Combustion Chambers”. Proc. Combust. Inst., 1969, 12, pp. 169–181

[91] Lieuwen. T.C. and Yang, V. “Combustion Instabilities in Gas Turbine Engines: Operational Experience, Fundamental Mechanisms, and Modeling”. Progress in Astronautics and Aeronautics, AIAA. V. 210, , 2005

[92] Candel. S. “Combustion Instabilities Coupled by Pressure Waves and Their Active Control”. Proc. Combust. Inst., 19922, 4, pp. 1277–1296

[93] Putnam. A.A., “Combustion Driven Oscillations in Industry”. Elsevier, New York, 1971

[94] Mallard, E. E., and Le Chate1ier, H. “Recherches Experimentales et Theoriques sur la combustion des melanges gazeue explosifs.” Ann. Mines 8(4): 274-376

[95] Rayleigh. J.W.S. “The Explanation of Certain Acoustical Phenomena”. Nature, 1878, 18, pp. 319–321

[96] Palik ED. “Handbook of Optical Constants of Solids II”. Academic Press, California, USA, 1991

[97] Gaydon, A. G., “Spectroscopy of Flames”, Chapman and Hall, London, 2nd edition, 1974

[98] Gaydon, A. G., “Flames, Their structure, Radiation and Temperature”. Chapman and Hall, London, 4th edition, 1979

[99] Price, R., Hurle, I., and Sugden, T., “Optical Studies of the Generation of Noise in Turbulent Flames”. Twelfth Symposium International on Combustion. 1968, pp. 1093-1102

[100] Hurle, I., Price, R., Sugden, T., and Thomas, A. “Sound Emission from Open Turbulent Premixed Flames”. Proceedings of the Royal Society Series A. 1968, 303, pp. 409-427

[101] Shah. R and Sekulic, D. “Fundamentals of Heat Exchanger Design”, Wiley & Sons, New York, 2003

[102] Kays. W.M. and London,A.L. “Compact Heat Exchangers”. Krieger Publishing Company, FL, USA, 1998

[103] Wu, M., Hua, J. and Kumar, K. “An Improved Micro Combustor Design for Micro Gas Turbine Engine and Numerical Analysis” J. Micromech. Microeng. 2005, 15, pp.1817-1823

[104] Burmeister, L. C., “Effectiveness of a Spiral-Plate Heat Exchanger With Equal Capacitance Rates” Transactions- American Society of Mechanical Engineers, Journal of Heat Transfer, 2006, 128, pp. 295 -301

[105] Bes, T., and Roetzel, W., “Thermal Theory of the Spiral Heat Exchanger”. Int. J. Heat Mass Transfer, 1993, 36, pp. 765–773

[106] Morimoto, E., and Hotta, K. “Study of the Geometric Structure and Heat Transfer Characteristics of a Spiral Plate Heat Exchanger”. Heat Transfer-Jpn. Res. 1988, 17, pp. 54–71

[107] Zhang, N., Jiao, Z., Ni, Z., and Kung, H. C. “A Computational Method for Thermal Design of Spiral Plate Heat Exchanger," in Proceedings of the 1988 Heat Transfer Conference. Houston, TX, July 1988, Vol. 1, pp. 445–449

[108] Chowdhury, K., Linkmeyer, H., Bassiouny, M., and Martin, H. “Analytical Studies on the Temperature Distribution in Spiral Plate Heat Exchangers: Straightforward Design Formulae for Efficiency and Mean Temperature Difference”. Chem. Eng. Process. 1985, 19, pp. 183–190

[109] Jarzebski, A. “Dimensioning of Spiral Heat Exchangers to Give Minimum Costs”. Int. J. Heat Mass Transfer, 1984, 106, pp. 633–637

[110] Bes, T., and Roetzel, W. “Distribution of Heat Flux Density in Spiral Heat Exchangers” Int. J. Heat Mass Transfer. 1992, 35, pp. 1331–1347

[111] Egner, M.W. and Burmeister, L. C. “Heat Transfer for Laminar Flow in Spiral Ducts of Rectangular Cross Section” J. Heat Transfer, 2005, Vol 127, Issue 3, pp. 352-356

[112] Cashdollar K. L., Zlochower I. A., Green G. M., Thomas R. A., and Hertzberg M. “Flammability of Methane, Propane, and Hydrogen Gases.” Journal of Loss Prevention in the Process Industries. 2000, 13, pp. 327-340

[113] Weinberg F.J, Jones A.R, Lloyd, S.A. “Combustion in heat exchangers.” Proc. Roy. Soc. London. 1978, A360, pp. 97-115

[114] Metghalchi M., and Keck, J. C. “Laminar Burning Velocity of Propane-Air Mixtures at High Temperature and Pressure”. Combustion and Flame 1980, 38, pp. 143-154

[115] Suzuki Y., Saito J., and Kasagi N. “Development of Micro Catalytic Combustor with Pt/Al2O3 Thin Films”. JSME International Journal Series B. 2004, 47, pp. 522-527

[116] Ronney P. D. "Analysis of Non-adiabatic Heat-recirculating Combustors”. Combustion and Flame. 2003, 135, pp. 421-439

[117] Kuo C. H., and Ronney P. D. “Numerical Modeling of Heat Recirculating Combustors. Proceedings of the Combustion Institute. 2007, 31, pp. 3277-3284

[118] Ahn J., Eastwood C., Sitzki L., and Ronney P. D. “Gas-phase and Catalytic Combustion in Heat-recirculating Burners”. Proceedings of the Combustion Institute 2005, 30, pp. 2463-2472

[119] Sitzki L., Borer K., Schuster E., Ronney P. D., and Wussow S. “Combustion in Microscale Heat-Recirculating Burners.” Proc. 3rd Asia-Pacific Conf. on Combustion, Seoul, Korea, 2001

[120] Vijayan V., and Gupta A. K. “Combustion and Heat Transfer at Meso Scale with Thermal Energy Recirculation.” 47th AIAA Aerospace Sciences Meeting, Orlando, Florida, January 2009, AIAA 2009-443

[121] Vijayan V., and Gupta A. K. “Thermal Performance of a Mesoscale Heat Regenerating Combustor”. 7th International Energy Conversion Engineering Conference, Denver, Colorado, August 2009, AIAA 2009-4605

[122] http://webbook.nist.gov/chemistry/

[123] Prakash S., Armijo A. D., Masel R. I., and Shannon M. A. “Flame Dynamics and Structure within Sub-Millimeter Combustors” AIChE Journal, 2007, 53, pp. 1568-1577

[124] Maruta. K., Parc, J. K., Oh, K. C., Fujimori T., Minaev, S. S., and Fursenko R. V. “Characteristics of Microscale Combustion in a Narrow Heated Channel”. Combustion, Explosion, and Shock Waves. 2004, 40, pp. 516–523

[125] Pizza, G., Frouzakis C. E., Mantzaras J., Tomboulides, A. G., and Boulouchos, K. “Dynamics of Premixed Hydrogen/air Flames in Mesoscale Channels”. Combustion and Flame. 2008, 155, pp. 2–20

[126] Feldman, K. T. “Review of Literature on Rijke Thermoacoustic Phenomena”. Journal of Sound and Vibration, 1968, 7, pp. 83-89

[127] Sirignano W. A., and Rankin D. D. “UCI Liquid Film Miniature Combustor.” 45th AIAA/ASME/SAE/ASEE Joint Propulsion Conference & Exhibit, Denver, Colorado, August 2009, AIAA 2009-5317

[128] Premoli A., Francesco D., and Prino A. “An Empirical Correlation for Evaluating Two-Phase Mixture Density under Adiabatic Conditions.” European Two-Phase Flow Group Meeting, Milano, Italy, 1970

[129] Vijayan V., and Gupta A. K. “Experimental Investigation of a Mesoscale Liquid Fueled Combustor” 45th AIAA/ASME/SAE/ASEE Joint Propulsion Conference & Exhibit, Denver, Colorado, Aug 2009, AIAA 2009-5244

[130] Kline, S. J., and McClintock, F. A., “Describing Uncertainties in Single-Sample Experiments”. Mech. Eng., 1953, pp. 3-18